IEKP–KA/2005–6

ELEKTRONIK FÜR DAS WELTRAUM-EXPERIMENT AMS02 UND BILDGEBUNG IN DER STRAHLENMEDIZIN

Levin Jungermann

Zur Erlangung des akademischen Grades eines
DOKTORS DER NATURWISSENSCHAFTEN
von der Fakultät für Physik
der Universität Karlsruhe (TH)

genehmigte

DISSERTATION

von

Dipl. phys. Levin Jungermann
aus Karlsruhe

Tag der mündlichen Prüfung: 10.06.2005

Referent: Prof. Dr. Wim de Boer, Institut für Experimentelle Kernphysik

Koreferent: Prof. Dr. Thomas Müller, Institut für Experimentelle Kernphysik

Deutsche Zusammenfassung

In dieser Promotion werden zwei Anwendungen modernster Technologien für den Nachweis von Teilchen näher betrachtet. Im ersten Teil dieser Arbeit liegt der Schwerpunkt auf der Elektronikentwicklung für das weltraumgestützte Hochenergiephysik-Experiment **A**lpha **M**agnetische **S**pektrometer (AMS02). Der zweite Teil dieser Arbeit beschäftigt sich mit CMOS-Pixeldetektoren für medizinische Anwendungen. Die Untersuchungen dazu wurden im Rahmen des EU-Projektes „**S**ilicon **U**ltra fast **C**ameras for electron and gamma sources **I**n **M**edical **A**pplications“ (SUCIMA) durchgeführt.

Seit 1910, als Wulf die ersten Messungen zur Abhängigkeit der Strahlungsintensität von der Höhe gemacht hat, spielt die Untersuchung der kosmischen Strahlung eine wichtige Rolle in der Teilchenphysik. So wurden in der Höhenstrahlung das erste Mal Myonen (1937, Anderson und Neddermeyer) und Pionen (1947, Lattes et al.) gemessen, aber auch einige Hyperionen wurden in der kosmischen Strahlung entdeckt, z.B. das Ξ (1952, Armenteros et al.). In den letzten Jahrzehnten dominierten die großen Teilchenbeschleuniger (LEP, Tevatron,...) das Feld der Hochenergiephysik. Erst in den letzten Jahren hat die kosmische Strahlung wieder an Bedeutung gewonnen, da einerseits Phänomene entdeckt wurden, die in Beschleunigern auf der Erde nicht nachgestellt werden können, aber auch neue Technologien zur Verfügung stehen, die es erlauben, Teilchendetektoren zu bauen, die im Weltraum betrieben werden können.

Das AMS02-Projekt ist einer dieser neuen Teilchendetektoren zur Messung der primären kosmischen Strahlung außerhalb der Erdatmosphäre. Mit einem Prototypensystem (AMS01) konnte 1998 das Potential dieses Aufbaus während einer zehntägigen Mission im Space Shuttle (STS-91) erfolgreich demonstriert werden. Der AMS02-Detektor wird ab 2008 für mindestens drei Jahre auf der Internationalen Raumstation (ISS) das Spektrum der primären kosmischen Strahlung in einem Energiebereich von $300\,MeV$ bis $3\,TeV$ messen und hierbei eine vielfache Datenmenge aller bisherigen Experimente mit unerreichter Präzision aufzeichnen.

Der Standort von AMS02 auf der ISS und der Transport dort hin mit einem Space Shuttle stellen immense Anforderungen an den Detektor und die Ausleseelektronik. Sie müssen den Vibrationen während des Starts widerstehen können. Aber auch das Vakuum, die Temperaturschwankungen und die elektromagnetische Verträglichkeit stellen große Herausforderungen dar. Da keine Wartung des Detektors während der Betriebszeit möglich ist, müssen alle kritischen Systeme abgesichert und mehrfach vorhanden sein.

Das **I**nstitut für **E**xperimentelle **K**ern**p**hysik (IEKP) der Universität Karlsruhe (TH) ist seit 2002 verantwortlich für die Elektronik des Übergangsstrahlungsdetektors (TRD), der von der RWTH Aachen gebaut wird. Die Entwicklung der Elektronik ist in mehrere Phasen unterteilt: Prototypenstadium, Entwicklungsphase (EM), Qualifikationsphasen 1 & 2 (QM1 & QM2) sowie die Produktion der Flugelektronik. Seit der Entwicklungsphase ist das IEKP federführend an der Entwicklung der Elektronik beteiligt.

Im Rahmen dieser Promotion wurde die Firmware der Datenreduktionskarte (UDR, detektorspezifischer Teil), der Niederspannungskarte (UPSFE) und der Kontrollkarte (S9011AU) für die Stromversorgung erstellt. Dabei galt es besonders, die Anforderungen an die Verwaltung der Redundanz zu erfüllen, um einen sicheren Betrieb der Ausleseelektronik zu gewährleisten. Die Funktion der Elektronik wurde jeweils in den Phasen EM und QM1 mit einer Strahlzeit am CERN mit einem Prototypen des TRD erfolgreich überprüft.

Ein weiteres Projekt in dieser Promotion war Entwicklung und Bau einer Testumgebung für die Niederspannungskarte UPSFE. Mit Hilfe dieser Testumgebung kann die komplette Funktionalität[(1)] der UPSFE getestet werden. Nach der Erprobungsphase in Karlsruhe wurde die Testumgebung erfolgreich zur Qualifikation der Vorproduktion der Elektronik am Chung-Shan Institute of Science and Technology in Taiwan zum Einsatz gebracht und wird auch während der Produktion der Flugmodule genutzt werden.

Die Integrations- und Funktionstests auf Crate-Level sind am Institut für Experimentelle Kernphysik erfolgreich abgeschlossen worden. In naher Zukunft werden die Tests zur Validierung der Weltraumtauglichkeit (Thermo-Vakuum-Test, Vibrationstest und Elektromagnetischer Interferenztest) auf Crate-Level beginnen, hier sind jedoch keine Probleme zu erwarten.

Strahlung spielt in der Medizin eine wichtige Rolle, sowohl in der Diagnostik als auch in der Therapie. Das Zeitalter der Radiologie und -therapie begann 1895, als Wilhelm Conrad Röntgen die erste Aufnahme der Hand seiner Frau mit den so genannten „X-Strahlen“[(2)] machte. Es zeigte sich jedoch schnell, das eine sorgfältige Dosimetrie benötigt wird, um eine sichere Anwendung der Strahlung zu gewährleisten.

[(1)] Die Aufgaben der UPSFE umfassen die Regulierung und Absicherung der $\pm 2\,V$ für die Eingangsverstärker (14 Kanäle), sowie das Setzen und Überwachen von externen Kontroll- und Monitorleitungen (10 Kanäle).

[(2)] Der Name X-Strahlung stammt aus der Zeit als auch die Begriffe α-,β- und γ- Strahlung geprägt wurden und ist heute noch im Englischen als „X-ray“gebräuchlich. Im Deutschen Sprachgebrauch hat sich jedoch der Begriff Röntgen-Strahlen durchgesetzt.

Das SUCIMA-Projekt verfolgte den Ansatz, mit Wissen und Technologien aus der Hochenergiephysik die Dosimetrie in zwei Anwendungsbereichen der Strahlenmedizin, Brachytherapie (Dosimeter) und Hadronentherapie (Strahlmonitor), zu verbessern. Zwei technologische Ansätze wurden dabei verfolgt, zum einen CMOS[(3)]-Sensoren, zum anderen SOI[(4)]-Sensoren. Neben der Entwicklung der Sensoren wurde auch ein Datenerfassungssystem (DAQ) mit USB2.0-Anbindung entworfen und verwirklicht. In der Konfiguration für den Strahlmonitor kann das DAQ-System die kritischen Strahlparameter mit $10\,kHz$ überwachen und notfalls einen Abbruch der Behandlung auslösen.

Neben den Anforderungen an das räumliche Auflösungsvermögen, die Auslesegeschwindigkeit und die Größe der Detektoren spielt in diesen Anwendungen natürlich die Strahlenhärte eine besondere Rolle. Im Rahmen dieser Arbeit wurden daher Studien an SUCCESSOR-I-Detektoren durchgeführt, mit der Zielsetzung, die optimale Pixelgeometrie für einen Dosimetriedetektor zu bestimmen.

Der SUCCESSOR-I-Detektor wurde als Technologieträger entwickelt und besteht aus acht Pixelmatrizen, die jeweils 32 mal 32 Pixel umfassen und von denen jede eine andere Pixelgeometrie hat. Hierbei wurden bei allen Pixeltypen die Erfahrungen mit den älteren Prototypen berücksichtigt. Zum Beispiel sind Source und Drain der Resettransistoren im Vergleich zum alten Layout vertauscht, um parasitäre Ladungstransferpfade zu vermeiden.

Für diese Studien wurden SUCCESSOR-I Detektoren mit einer Röntgen-Anlage in mehreren Dosisstufen bis $2\,Mrad$ bestrahlt und jeweils die wichtigsten Parameter der Pixel als Funktion der Dosis bestimmt. Als Entscheidungskriterien kamen hierbei der Leckstrom, die Verstärkung im Pixel sowie die Ladungssammlungseffizienz und das Signal-zu-Rauschen-Verhältnis zum Tragen. An Hand der Pixelgeometrien 3 und 4 werden beispielhaft die Messergebnisse erklärt und bewertet. Dabei dient Pixel 3 auf Grund seines Standarddesigns als Referenz, und Pixel 4 ist als der für das finale Design ausgewählte Pixel vertreten.

In den Messungen konnte beobachtet werden, dass alle acht Pixelgeometrien im getesteten Dosisbereich unbedenklich sind in Hinsicht auf eine mögliche Degradation der Ladungssammlungseffizienz, der Verstärkung und des Signal zu Rauschen Verhältnisses. Als wichtigstes Entscheidungskriterium hat sich das Leckstromverhalten erwiesen. Pixel 4 zeigte mit den geringsten Anstieg des Leckstromes mit wachsender Dosis.

Neben den eigentlichen Messwerten werden auch Phänomene diskutiert, die während der Messungen auftraten und diese beeinflusst haben. Zum einen ist der Digitalteil des Detektors nicht strahlenhart und muss daher abgeschirmt werden, zum anderen haben sich die analogen Ausgangstreiber durch die größeren Leckströme so stark erhitzt, dass sich die Pedestals stark verschoben haben.

Zusammenfassend kann man sagen, dass Pixellayout 4 von den acht untersuchten Layouts am besten für eine Anwendung in der Brachytherapie geeignet ist: Die Ladungssammlungseffizienz bleibt von der Bestrahlung unbeeinflußt, ebenso wie die Verstärkung des Pixels und das Signal-zu-Rauschen Verhältnis. Dank seiner mittleren Verstärkung liegt die Sensitivität von Pixel 4 ebenfalls im optimalen Bereich für diese Anwendung. Ein weiteres wichtiges Merkmal von Layout 4 ist der niedrige Leckstrom, insbesondere da auch der Anstieg mit der Dosis der geringste aller untersuchten Layouts war.

Die SUCIMA Kollaboration hat einen Detektor, SUCCESSOR-V, basierend auf diesem Layout entwickelt und produziert. Im klinischen Einsatz wird dieser Detektor es erlauben mehr als 10.000 Messungen unter ungünstigsten Bedingungen (Messdauer: $10\,s$, Dosisleistung: $20\,rad/s$) durchzuführen, bevor er ersetzt werden muss. Ältere Designs hätten bereits nach einigen hundert Messungen keine zuverlässigen Daten mehr geliefert.

Das Verhalten von Detektoren in starken Magnetfeldern spielt heute sowohl in der Medizin als auch in der Hochenergiephysik eine wichtige Rolle. In einer Studie wurden daher die Signalhöhe und -breite als Funktion der Feldstärke bis $6\,T$ bestimmt. Dabei wurden zwei Konfigurationen vermessen: Magnetfeld parallel (a) bzw. senkrecht (b) zur Sensoroberfläche. Bei diesen Messungen wurde festgestellt, dass die Signalstärke in Konfiguration (a) mit zunehmender Feldstärke abnimmt, während sie in Konfiguration (b) zunimmt. Dies kann mit Hilfe eines einfachen Modells basierend auf der Lorentzkraft verstanden werden. In Fall (a) wird die Geschwindigkeitskomponente in Richtung des Kontaktes durch die Lorentzkraft verringert, während sie im Fall (b) verstärkt wird.

[(3)] **CMOS**: **C**omplementary **M**etal **O**xide **S**emiconductor

[(4)] **SOI**: **S**ilicon **O**n **I**nsulator

Space-Qualified Electronics for the AMS02 Experiment and Medical Radiation Imaging

Levin Jungermann

23rd May 2005

Contents

Introduction

This thesis takes a closer look at two applications of modern technology in particle detection. In the first part of the thesis the focus is set on the read out and slow-control electronics of the spaceborne High Energy Physics experiment **A**lpha **M**agnetic **S**pectrometer (AMS02). In the second part the emphasis is set on CMOS sensors for particle detection in medical applications. The latter was done within the framework of the EU project "**S**ilicon **U**ltra fast **C**ameras for electron and gamma sources **I**n **M**edical **A**pplications" (SUCIMA).

Ever since their discovery at the beginning of the 20^{th} century, cosmic rays have been fascinating physicists all over the world. Soon many experiments, both earthbound and airborne, were done to investigate the nature of the cosmic rays. It was evident almost from the beginning, that access to the primary particles is only possible in the upper atmosphere or above it. Due to the interaction of the incoming particles with the atmosphere of the Earth, earthbound experiments are limited to particles with low interaction probabilities, like neutrinos, or studies of secondary effects, like showers or Cherenkov light.

AMS02 is the latest experiment in a 30-year tradition of spaceborne instruments to measure the composition and spectra of the primary cosmic rays in the energy range of $300\,MeV$ to $3\,TeV$. Starting in 2008 the 3+ year long mission of AMS02 will yield an unprecedented amount of data with an unrivalled precision. This data will allow to refine the existing models for the acceleration and propagation of cosmic rays. The high precision data, especially the positron fraction and the high energy gamma spectrum, will also lead to a better understanding of the theories for Dark Matter. Additionally, the measurements will be essential for any long duration manned space mission outside of Earth's protective environment.

The location of AMS02 on the **I**nternational **S**pace **S**tation (ISS) and the transport there by a Space Shuttle impose very stringent requirements on the detector itself and its infrastructure. All components must be able to withstand the enormous vibrations during the launch, but also the temperature cycles and the vacuum. All critical parts of AMS02 have to be protected and redundant, as no maintenance is possible during the lifetime of the experiment.

Within the framework of this thesis space-grade electronics for the **T**ransition **R**adiation **D**etector (TRD) of AMS02 were developed. The Institut für Experimentelle Kernphysik at the University of Karlsruhe (TH) is responsible for the electronics of the TRD and has been actively involved in the design, qualification and production process since the engineering phase. Within the framework of this thesis the firmware codes for the data reduction card (UDR, detector specific part), the low voltage regulator card (UPSFE) and the controller card for the power supply (S9011AU) were developed. A further project was the design and construction of a testbed for the UPSFE. This testbed was used during the quality control of the pre-production of the electronics at the Chung-Shan Institute of Science and Technology in Taiwan and will be also used during the production of the flight hardware.

In chapter 1 an introduction to the detector and its subsystems is given[(1)], followed by a short review of the physics involved in the acceleration of cosmic rays. A detailed description of the electronics of AMS02 is presented in chapter 2. Here a special emphasis is put on the electronics of the TRD and the developments done within the framework of this thesis.

[(1)] Please note, that all specifications and information on AMS02 reflect the status of April 2005 and are subject to possible changes as the integration of the detector proceeds.

Radiation has become more and more important in medicine, both in diagnostics and in treatment, ever since William Conrad Röntgen took the first X-ray image of his wife's hand in 1895. This new technique induced an over-enthusiastic application of it in the years after its discovery. Through tragic events, caused by the side effects of the radiation, it soon became obvious that a thorough dosimetry had to go hand in hand with the use of radiation in medicine. From in-vivo dosimetry to digital X-ray systems, today's state of the art detectors and electronics cover an enormous field of dosimetry and imaging applications.

The aim of the SUCIMA project was to develop systems for dosimetry of extended sources and on-line beam monitoring, benefiting from the existing know-how in the High Energy Physics community and the possibilities of new technologies in the detector design and production. The two focus points of the SUCIMA project were inspired by brachytherapy, where a high activity radioactive source is used to suppress the growth of scar tissue after an angioplasty, and from hadron therapy, where an intense beam of ions is used to treat a tumour.

Two technological approaches were pursued for the detector design by the SUCIMA collaboration: CMOS[(2)] and SOI[(3)]. The CMOS technology is a standard process widely used throughout industry in different variations, where the structure is processed on top of a low resistivity wafer. The use of this technology allows to produce devices at reasonable costs while benefiting from standard designs existing in industry, even though the detectors suffer from the low signal due to the thin sensitive volume ($< 15\,\mu m$). In the SOI technology the device is made up from two wafers separated by a layer of silicon oxide. The device wafer is thinned down to a few micrometres to optimise the performance of the electronics. The handle wafer, normally a low resistivity wafer unused by industrial applications, can be replaced by a detector-grade wafer and used as fully depleted sensitive volume, overcoming the limitations of CMOS detectors, namely the low signal.

Especially in the application as a dosimeter for the brachytherapy, the detectors have to be able to withstand very high doses, as the sources have activities in the order of a few *GBq*. The second focus point of this thesis was to investigate the radiation hardness of eight pixel geometries on a prototype CMOS detector of the SUCIMA collaboration using an X-ray system. Based on the obtained results, a recommendation regarding the pixel layout was made for the final device of the SUCIMA project.

Chapter 3 gives an overview of the interaction of radiation with matter and the different technologies of position sensitive radiation detectors. In chapter 4 the SUCIMA project and its medical applications are introduced together with the detectors and the data acquisition system developed within this framework. The measurement setups used for the radiation hardness studies and the results obtained are presented in chapter 5, followed by a summary of the measurements with CMOS detectors in high magnetic fields.

[(2)] **CMOS**: **C**omplementary **M**etal **O**xide **S**emiconductor

[(3)] **SOI**: **S**ilicon **O**n **I**nsulator

Chapter 1

The AMS02 Experiment

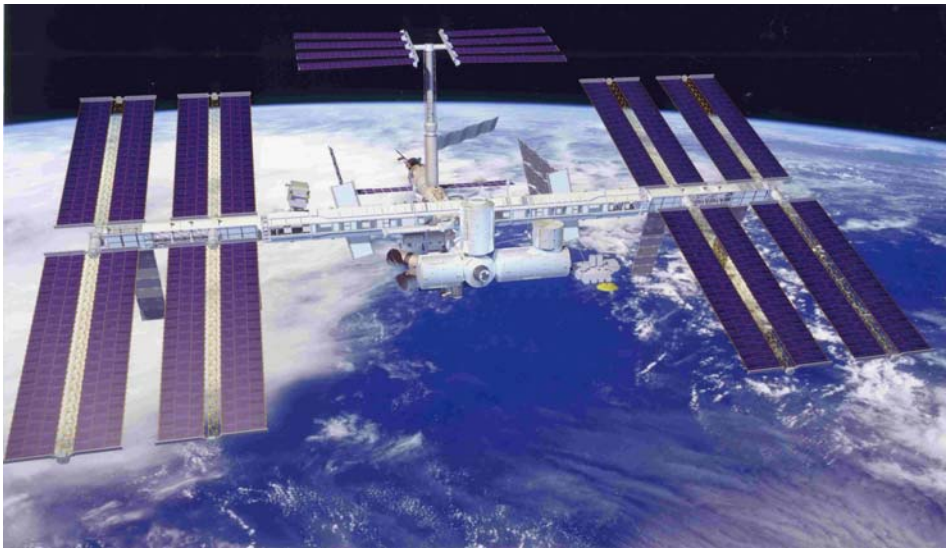

Figure 1.1: *Artist image of the International Space Station (ISS) in the final configuration. The AMS02 experiment is mounted on the S3 truss on the left hand side of the ISS, just inside of the solar panels, looking outwards into the open space. [Picture by Lockheed Martin]*

The Alpha-Magnetic-Spectrometer (AMS02) is a very ambitious high energy physics experiment which will measure the spectra of the primary cosmic rays in the energy range of $300\,MeV$ to $3\,TeV$ for 3 years starting 2008. To avoid the influence of the atmosphere of the Earth, it will be mounted on the International Space Station (ISS), see Fig. 1.1 [NAS]. The transport on-board a Space Shuttle (STS) to the ISS is provided by the NASA[(1)], as AMS02 is the only approved large scale experiment for the space station.

The size of the ISS, in its final configuration, will be $108\,m \times 80\,m$. Most of the space will be taken up by the large solar panels. These panels are capable of supplying the station with $86\,kW$ electrical power. The total weight of the space station is $420\,t$. The orbit of the ISS is $400\,km$ above the surface of the Earth, still below the van-Allen belt.

The harsh environment in space and the transport to the ISS enforce stringent requirements on all parts of the detector itself and its infrastructure, like the read out electronics and the mechanics. For example, the whole detector has to be able to withstand vibrations of up to $6.8\,g$ during launch without degrading the internal alignment by more than a few micron.

[(1)] **NASA**: **N**ational **A**eronautics and **S**pace **A**dministration, USA

On the following pages a short introduction into precursor experiments is given. In the next section AMS02, with its various subdetectors, is described in detail. At the end of this chapter the environmental conditions for a space experiment like AMS02 will be illustrated.

1.1 Precursor Experiments

From the aurora borealis to the first recorded observations of supernovas, high energetic cosmic rays have been a major motivation for scientists for quite a long time.

After some first measurements on the intensity of ionising radiation as a function of height by Wulf in 1910 on the Eifel Tower in Paris, Hess built the first balloon experiments in 1911/1912 [Hes12]. These measurements earned him the Nobel Prize in 1936.

Since then balloon borne experiments have been the choice for measurements of cosmic rays, if the influence of the atmosphere was to be minimised. Only in recent years the possibility of spaceborne high energy physics experiments has become available.

1.1.1 Balloon Experiments

Even though balloon experiments have been getting more and more sophisticated since the days of Hess, they still suffer from the same draw-backs as in those days.

Even with a maximum flight altitude of about $50\,km$, there is still $\sim 3\,g$ of atmosphere[2] above the detector, which strongly limits the access to primary cosmic rays.

The maximum weight of a balloon experiment is strongly limited as the high altitude balloons can only carry up to $\sim 3.5\,t$. This imposes very stringent requirements on the detector design, solvable in most cases only by compromises limiting the physics possibilities of the experiment, for example the opening angle.

Figure 1.2: *The BESS balloon experiment before launch. [Source: Goddard Space Flight Center]*

A third problem is the short flight time of balloon borne experiments, as the statistics that can be collected during the flight are directly proportional to the flight time. The flight time for the recent experiments varies from 1 to 14 days.

The most important balloon experiments in recent decades were BESS[3] [Wan02], shown in Fig. 1.2, and HEAT[4] [Bow99]. They were able to supply very interesting information on the spectrum and mass composition of cosmic rays. The most recent balloon flight was the Antarctica mission of TRACER[5], which lasted 14 days [TRA].

1.1.2 Space Experiments

Since the early days of spaceflight, experiments on the composition and spectra of the cosmic rays were made. For example, the moon missions, Apollo 16 and 17, carried cosmic ray detectors consisting of different absorber plates, which were analysed on Earth after the missions.

---

[2] g is the short form of g/cm^2, the remanent pressure. It is a naming convention used by the various collaborations operating balloon experiments.

[3] **BESS**: **B**alloon-borne **E**xperiment with a **S**uperconducting **S**olenoidal magnet

[4] **HEAT**: **H**igh-**E**nergy **A**ntimatter **T**elescope

[5] **TRACER**: **T**ransition **R**adiation **A**rray for **C**osmic **E**nergetic **R**ays

In recent years the main interest of satellite experiments was, mainly due to feasibility, focused on the infra-red and X-ray investigation of the universe. The best known experiments from this field are CHANDRA [CHA] and XMM-Newton [ESA]. They were able to map the sky for X-ray sources with very high precision and also measured the X-ray part of GRBs[6] and supernovas.

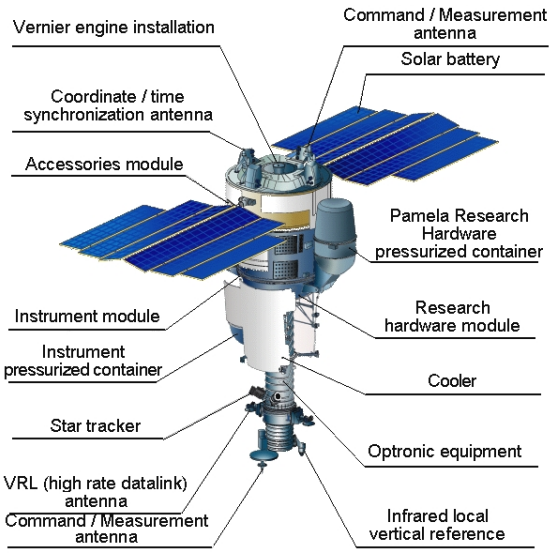

Figure 1.3: *A schematic drawing of the RESURS-DK1 satellite, that will be carrying the PAMELA experiment. [Source: PAMELA collaboration website]*

The next step in spaceborne experiments for cosmic ray particle investigation will be PAMELA[7] [Sim03]. It will be launched onboard a Russian satellite, shown in Fig. 1.3, into an elliptical orbit with an average height of $500\,km$ by a Soyuz TM2 rocket in 2005. It will be taking data for 3 years. Like AMS02 it will feature a TRD, a magnetic spectrometer and an ECAL. But compared to AMS02 it will have a rather low acceptance ($0.0021\,m^2sr$) and less separating power for high energies, as it will carry only a permanent magnet with a field of $0.4\,T$. A further problem for PAMELA is the rather small rate with which the data can be transferred to Earth. The main advantage of a satellite experiment is of course the independence of the infrastructure. It will be possible to point PAMELA at more or less any point of interest in the sky.

1.1.3 The AMS01 Experiment

NASA regulations require a proof of principle study for every experiment that is supposed to be brought into space. For AMS02 this was the precursor experiment AMS01. AMS01 flew 1998 onboard the space shuttle Discovery on the STS-91 mission and successfully collected data for 10 days. Fig. 1.4(b) shows a picture of the Discovery with open payload bay doors, exposing AMS01, taken from the MIR[8] spacestation. In Fig. 1.4(a) a schematic view of the location of AMS01 in the Space Shuttle is depicted.

A schematic drawing of the AMS01 detector is shown in Fig. 1.5. AMS01 had a six plane silicon tracker placed together with a cylinder of $1\,cm$ scintillator panels, forming the anti-counter, inside a permanent magnet (Nd-Fe-B) as the core of the detector. Above and below the tracker enclosure were two planes of scintillator on each side for the Time-Of-Flight system. This system provided also a fast trigger to the rest of the experiment. The last detector the particles passed had been an aerogel threshold Cherenkov counter.

Already this scaled down version of AMS02 was able to push the limits for the exclusion of antimatter for more than one order of magnitude [Alc99] with an acceptance of $0.3\,m^2sr$. Also limits for the flux of protons, electrons and positrons in the low orbit environment were published by the AMS01 collaboration. The results are summarized in [Agu02].

---

[6] **GRB**: **G**amma **R**ay **B**urst

[7] **PAMELA**: **P**ayload for **A**ntimatter **M**atter **E**xploration and **L**ight-nuclei **A**strophysics

[8] MIR is Russian and translates as “peace” or “world”.

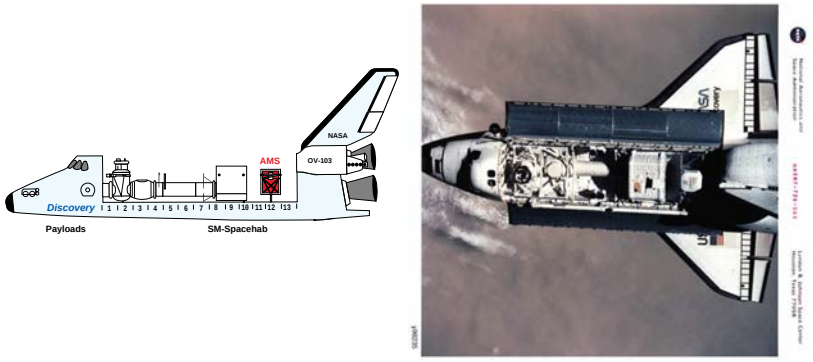

(a) (b)

Figure 1.4: *(a) A schematic drawing of the position of the AMS01 Detector on-board the space shuttle Discovery during the STS 91 mission in 1998. (b) A picture of the space shuttle Discovery with the payload bay doors open, taken from the space station MIR. [Bat99]*

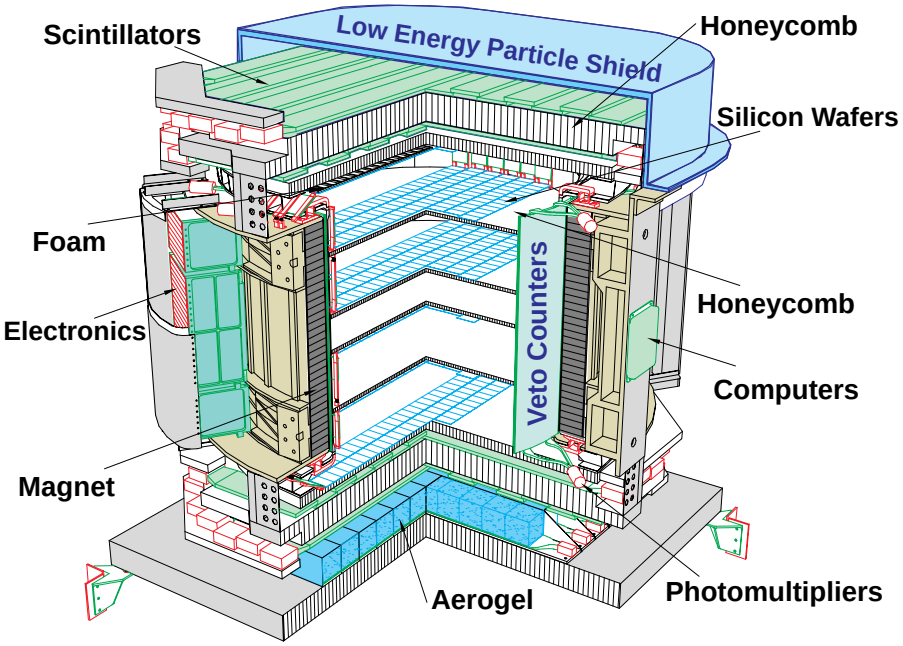

Figure 1.5: *A schematic drawing of the AMS01-Detector showing its different components. Clearly visible are the Time-of-Flight scintillator layers, the tracker planes and the magnet. [Bat99]*

1.2 The AMS02 Detector

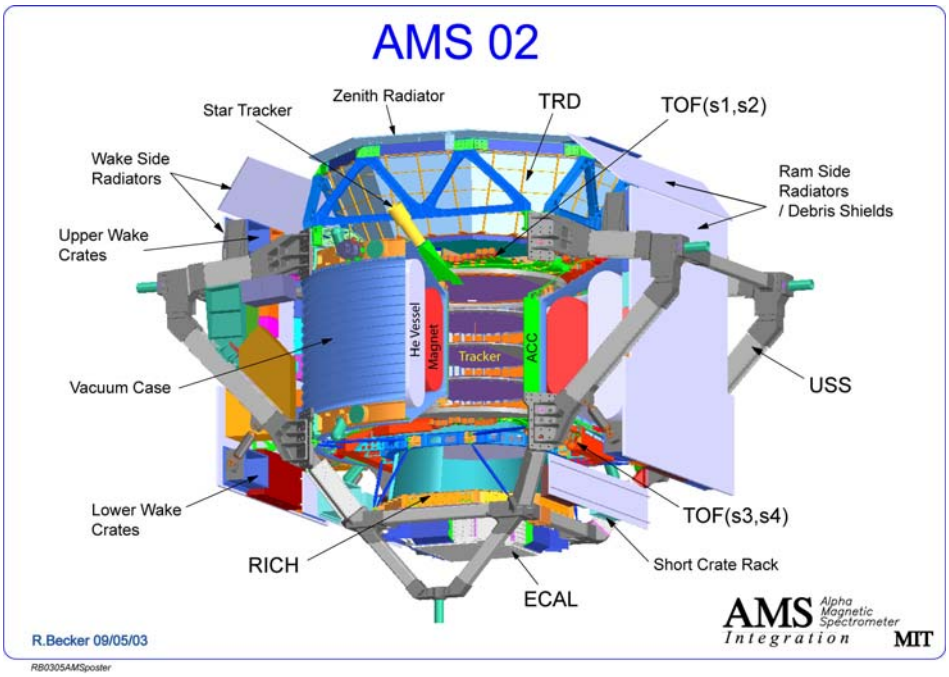

Figure 1.6: *Schematic drawing of the AMS02 Detector. The different subdetectors, the radiators and the Unique Support Structure (USS) are shown. The overall size of the AMS02 experiment is roughly* $3\,m \times 3\,m \times 3\,m$*, the total weight is 14809 lbs (=6723 kg) and the power consumption is limited to 2000 W. [Drawing by Robert Becker]*

The AMS02 experiment is a typical High Energy Physics (HEP) detector modified to the special requirements of a spaceborne experiment. A schematic cross-section is shown in Fig. 1.6. It consists of a Transition Radiation Detector (TRD), a silicon tracker inside a superconducting magnet, a Time-of-Flight (TOF) system combined with an Anti-Coincidence-Counter (ACC), a Ring Image Cherenkov Counter (RICH) and an Electromagnetic Calorimeter (ECAL). These subdetectors and their performance will be described in the following sections.

The location of AMS02 on-board the ISS imposes some very strict limits on size, weight and power budget of AMS02. The outer dimensions of AMS02 are roughly $3\,m \times 3\,m \times 3\,m$ with a weight limit of $14809\,lbs$ ($= 6723\,kg$) and power limit of $2\,kW$.

This very special environment on-board the ISS for the AMS02 detector will be described in section 1.2.8 on page 21. Also a short glimpse into the necessary measures to ensure mission safety and success will be given, which are very critical issues, as there will be absolutely no possibility of maintenance during the 3 year duration of the mission.

The space grade electronics for the read out and slow-control of the various subdetectors and the main Data Acquisition (DAQ) Computer are described in detail in chapter 2 on page 39. As the electronics of the TRD are the main focus of this thesis, they will be used as an example to explain the design philosophy used during the development of AMS02.

1.2.1 Transition Radiation Detector (TRD)

The principle of the Transition Radiation Detector (TRD), see Fig. 1.7, is based on the detection of soft X-rays generated when highly relativistic particles pass from one medium into another with $\varepsilon_1 \neq \varepsilon_2$. A more detailed description of the theory of the transition radiation principle can be found in the section *Transition Radiation* on page 37.

As the probability of the emission of a gamma quant is rather low for one transition ($\sim 10^{-2}$), the radiator material is composed of a so-called fleece ($\rho = 0.06 g/cm^{-3}$), which is made of very thin fibres ($10\,\mu m$), thus increasing the number of transitions per layer. The gamma quants are detected by proportional gas counters. The voltage applied between the central wire and the tube walls is $\sim 1600 V$. The gas mixture used for the TRD of AMS02 is $Xe : CO_2$ 80:20. In this mixture the Xe is the gas interacting with the particles (high Z), while the CO_2 absorbs the UV light emitted from the excited Xe-ions, thus preventing avalanche break-downs. The probability to detect one of the photons generated by the passing particle is $\sim 50\,\%$.

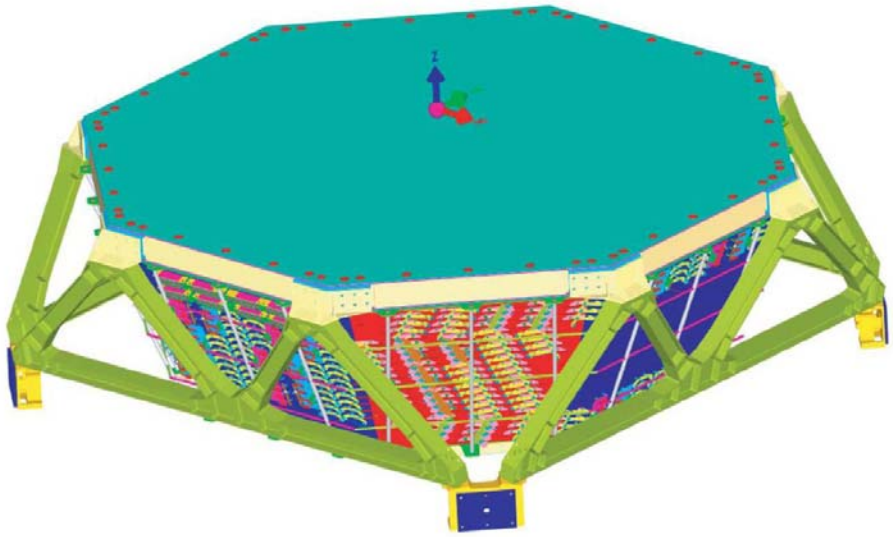

Figure 1.7: *The octagon of the AMS02 Transition Radiation Detector (TRD) and the M-structure. The octagon is the mechanical support structure of the TRD. It will keep the detector tubes at their respective positions with a precision of a few micrometres. The M-structure, named after its characteristic shape, stiffens the octagon and the Unique Support Structure (USS).*

The TRD consists of 20 layers of $22\,mm$ radiator fleece and strawtube modules placed in an octagonal support structure made from carbon fibre, as shown in Fig. 1.7. The 4 top and bottom layers are mounted perpendicular to the 12 middle ones. This configuration allows a rough track reconstruction. The carbon fibre structure is also used for mounting the gas piping and the cabling of the TRD.

To ensure that the TRD is operational for at least 3 years in space, each of the 5248 strawtubes is tested individually for gas tightness and only if it has a safety factor of at least 4, meaning that the gas supply would last 4x the planned lifetime of 3 years, it is used for the production of a module (Fig. 1.8). There are 328 modules in total, each module is made of 16 strawtubes. The length of the modules varies from $80\,cm$ to $200\,cm$. The strawtubes have walls of Kapton foil, see Fig. 1.9(a), and a gold plated central tungsten wire. A simplified cross-section of one layer of the TRD is shown in Fig. 1.9(b). More details on the TRD gas system follow on the next page.

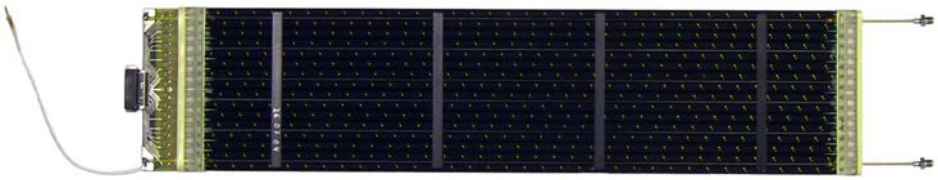

Figure 1.8: *A strawtube module of the AMS02 TRD. Each of the 328 modules of the TRD consists of 16 proportional gas tubes constantly flushed with a Xenon-CO_2 mixture (80:20). The length of the modules ranges from 80cm to 200cm, depending on their position in the octagon.*

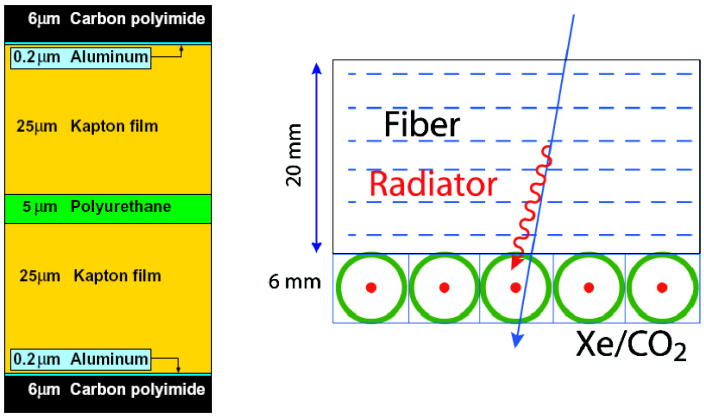

(a) Wall Cross-Section (b) TRD Layer

Figure 1.9: *(a) Cross-section of the strawtube wall. The multi-layer structure is used to ensure maximum gas tightness, which is close to the diffusion limit. The Aluminium layer in the wall is the outer electrode of the proportional tube. (b) Schematic drawing of a TRD layer. This simplified drawing shows the arrangement of the radiator, in which the X-ray photons are generated, and the strawtubes for the detection of the gamma quants.*

TRD Gas System

To ensure optimal performance of the TRD during the active time of the experiment it is absolutely vital to know the gas mixture, the temperature and the pressure at all times, as these values have a very strong influence on the gas gain and thus on the signal height. Due to this the TRD gas system plays a very important role for this detector.

The TRD has a closed circuit gas system. This means, that the gas is kept circulating inside the TRD volume and is not permanently vented to space. As no system can be absolutely gas tight, there is always the diffusion limit, the gas inside the TRD volume still needs to be replenished at a certain rate. Also a possible out-gasing of the strawtubes might contaminate the gas, leading to a change in signal height.

A CAD drawing of the main components of the TRD gas system is shown in Fig. 1.10. The gas system consists of three parts: The gas supply and mixing system (Box S, middle and bottom section of the picture), the gas control system (Box C, top section) and the control electronics (UG-crate, not shown in this picture).

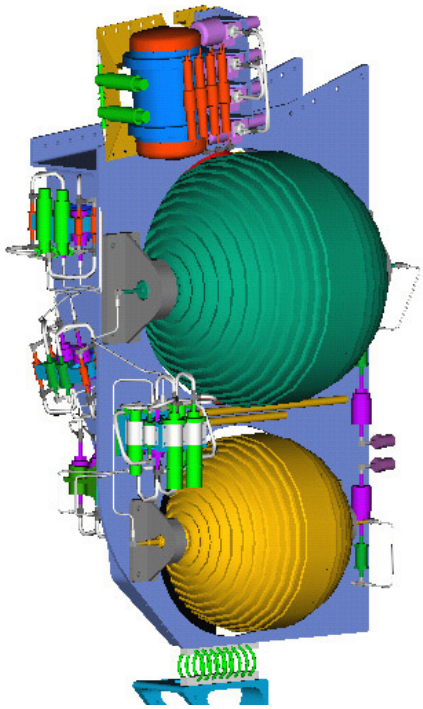

Figure 1.10: *A CAD drawing of the TRD gas system. In the so-called Box S, the main structure, the gas mixture for the TRD is prepared. In Box C (red), situated at the top of Box S, the gas gain and the gas quality is checked.*

The most prominent parts of Box S are the gas vessels. Two of them will carry the gas supply of $50\,kg$, corresponding to $8100\,l$ Xe and $2000\,l$ CO_2 at $1\,atm$. The third is the mixing tank. In it the Xe and the CO_2 will be mixed to a ratio containing slightly more CO_2 than the desired 20 %, as the CO_2 has a higher diffusion rate than Xe.

Box C features a gas gain measurement device and a CO_2 analyser. The gas gain measurement is done using a mono-energetic ^{55}Fe γ-source to generate a well-known ionisation signal, which is very close to the

signal from the transition radiation, inside a small proportional gas counter filled with the same gas as the TRD volume. The CO_2 analyser uses ultra-sonic sound waves to measure the sound speed in the gas and thus the CO_2 concentration. From these measurements the exact mixing ratio for the next injection will be calculated.

The electronics in the UG crate are constantly monitoring the pressure in the different gas circuits, the temperature and, as mentioned above, the gas gain and the mixture ratio. The information of the gas pressure is not only used for the physics analysis, but it is also vital for the detector, as in case of a sudden pressure drop due to a leak, valves can close off that section and prevent a total failure of the TRD.

Performance of the TRD

The most important contribution of the TRD to the physics data of AMS02 is the improvement of the proton rejection factor by $\sim 10^2 - 10^3$ for an energy range of up to $300\,GeV$. This can be accredited to the dependence of the transition radiation intensity on the Lorentz factor γ, see 1.3.6 for detailed description of the underlying physics. Fig. 1.11(a) shows test beam results obtained with a 20 layer TRD prototype compared to simulation data (Geant 3). The proton rejection rate as a function of the energy calculated from this data set is shown in Fig. 1.11(b).

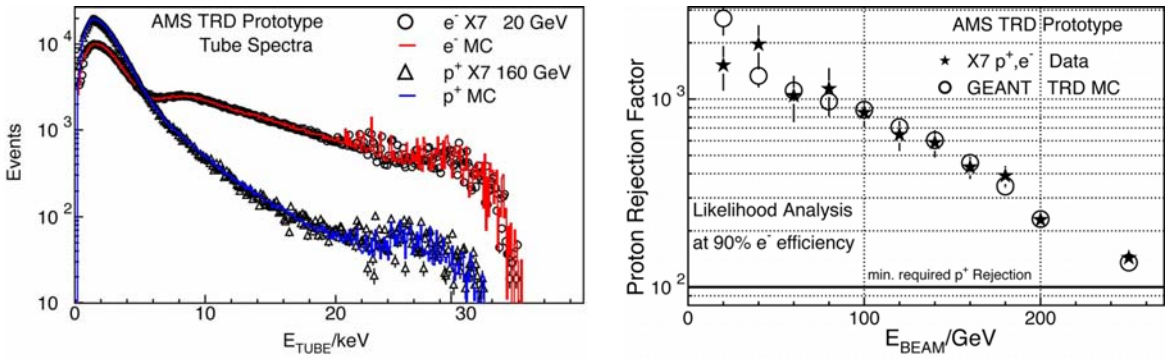

(a) Test Beam Data

(b) Proton Rejection

Figure 1.11: *The Performance of the TRD. (a) shows a data sample from the measurements with a 20 layer prototype in a test beam. In (b) the proton rejection rate is plotted as a function of the energy, as it was calculated from the data in (a). [AMS05]*

Reducing the high voltage on the proportional tubes of the TRD, thus effectively reducing the gas gain, the TRD can also be used to measure the ionisation energy loss of heavy ions, improving the precision of the heavy ion data of AMS02.

1.2.2 Time of Flight (TOF)

The Time-of-Flight subdetector (TOF) is one of the most important parts of the AMS02 detector, as it provides a fast trigger (within $1\,\mu s$) to the other subdetectors. It measures the time needed by a particle to transverse the AMS02 experiment, thus giving the velocity of the particle. A second very important information coming from the TOF is the direction of the particle, as only signals from particles passing through all subdetectors of AMS02 from top to bottom will be used for the analysis. The high resolution of this measurement, $\sim 120\,ps$, allows a separation of $1 : 10^{11}$ between particles going up or down.

The TOF also provides a dE/dx measurement in the scintillators and an absolute measurement of the charge of the passing particle, as the number of generated photons is proportional to the square of the charge of the particle ($N_\gamma \propto Z^2$). Therefore the TOF can also be used for particle identification for energies below $2\,GeV$ [Goy02].

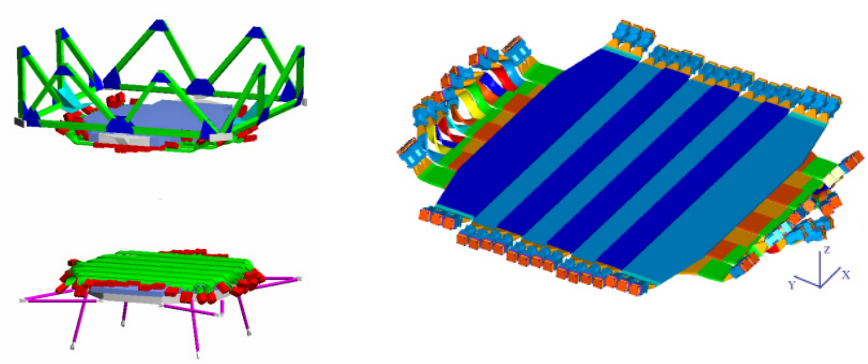

(a) TOF System (b) TOF Top Plane

Figure 1.12: *(a) The upper and the lower plane of the Time-of-Flight detector (TOF). (b) A close-up view of the upper TOF plane. Each plane consists of two orthogonal layers of segmented scintillator panels, which are read out by wave-guides and photomultiplier tubes (PMTs). As these PMTs are very sensitive to external magnetic fields, they have to be mounted along the field lines of the superconducting magnet.*

The TOF consists of two main parts, the upper and the lower TOF layers, shown in Fig. 1.12(a). A schematic drawing of the upper layer is shown in more detail in Fig. 1.12(b). The two layers are mounted directly above and below the superconducting magnet. Each layer is made of two planes of perpendicularly arranged scintillator panels which are read out on both ends with photo multiplier tubes (PMTs). The panels have a thickness of $1\,cm$, which generates a large enough signal without causing too much scattering. Each individual panel is $11\,cm$ wide.

The mesh-grid type PMTs used to read out the panels are very sensitive to magnetic fields. Nevertheless, they have to be placed close to the magnet to minimise light loss in the fibres. This problem can be overcome by aligning the main axis of the PMTs along the magnetic field lines.

Performance of the TOF

As already mentioned above, one purpose of the TOF is to supply a fast trigger for the other subdetectors. To achieve this, it is very important to reach a very high precision ($\sim 140\,ps$) for the time difference measurement between the signals from the two planes. A measurement of the resolution of the TOF as a function of the particle charge is shown in Fig. 1.13(a). A benefit of the usage of scintillators for the TOF system is the additional information on the energy deposition of the particle in the panels. The results of a test beam are shown in Fig. 1.13(b).

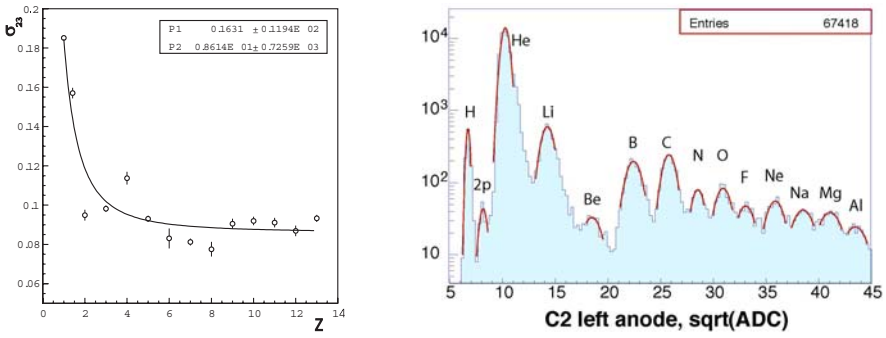

(a) Resolution (b) Mass Spectrum

Figure 1.13: *The performance of the TOF prototype. (a) shows the time resolution of the TOF as a function of the charge of the particle. In (b) a mass spectrum of the test beam obtained with the TOF prototype is depicted. [AMS05]*

1.2.3 Silicon Tracker

The silicon tracker is the central part of the AMS02 experiment. It consists of eight layers arranged in five planes inside the superconducting magnet, see Fig. 1.14. Each plane is made of a carbon fibre honeycomb structure to which the so-called ladders with double-sided silicon detectors are mounted. While the top and the bottom plane have one layer of silicon detectors, the middle planes feature two layers each with a total sensitive area of $6.6\,m^2$.

There are 7 to 15 sensors on each of the 192 ladders, which are wrapped in an EMI[9] shielding. The ladders are mounted head to head on the planes, see Fig. 1.15(a). The front-end electronics are placed on the thermal bars at the end of each ladder. A picture of a ladder is shown in Fig. 1.15(b).

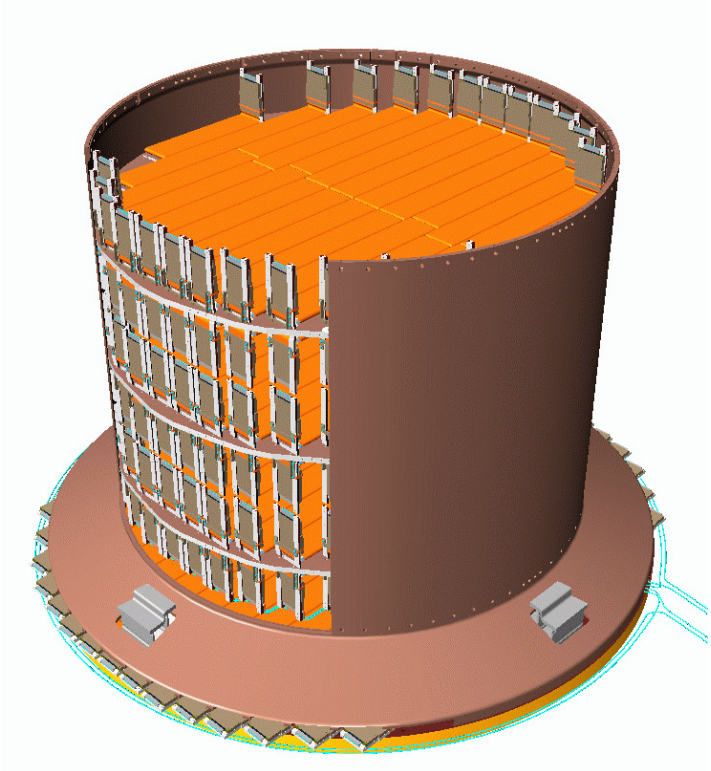

Figure 1.14: *The Silicon Tracker. The tracker, with a total sensitive area of* $6.6\,m^2$*, consists of 8 layers, which are arranged in five planes. The top and bottom planes consist of one layer of silicon each, while the middle planes consist of two.*

The silicon detectors used in the AMS02 tracker are double sided strip detectors with a position resolution of $10\,\mu m$ in the bending plane of the magnet and $20\,\mu m$ in the non-bending. The strips on the two sides of the silicon are perpendicular to each other to allow for a two-dimensional position measurement in each layer. The thickness of the silicon is $300\,\mu m$. The nominal bias voltage for the silicon detectors is $\sim 80\,V$.

To ensure the maximal position resolution during all run conditions a so-called *Tracker Alignment System* is used to monitor the relative position of the 8 tracker planes. This system is using the partial transparency of crystalline silicon for infra-red light to shine an IR laser through so-called *Alignment Holes* in all planes. Thus a signal is generated in all planes and the track can be reconstructed, defining the relative position of the planes. The system consists of 5 pairs located in the centre of the tracker.

Due to improvements in the sensor design and the higher magnetic field, the performance of the AMS02 tracker will exceed the one of its predecessor by far. It will be able to measure the rigidity

[9] **EMI**: **E**lectro-**M**agnetic **I**nterference

up to a few tens of *TeV*. With the measurement of the specific energy loss it will be possible to identify individual elements, as $dE/dx \sim |Z^2|$, for $|Z^2| \leq 28$. The tracker will also measure energy and direction of photons, which were converted in the material above.

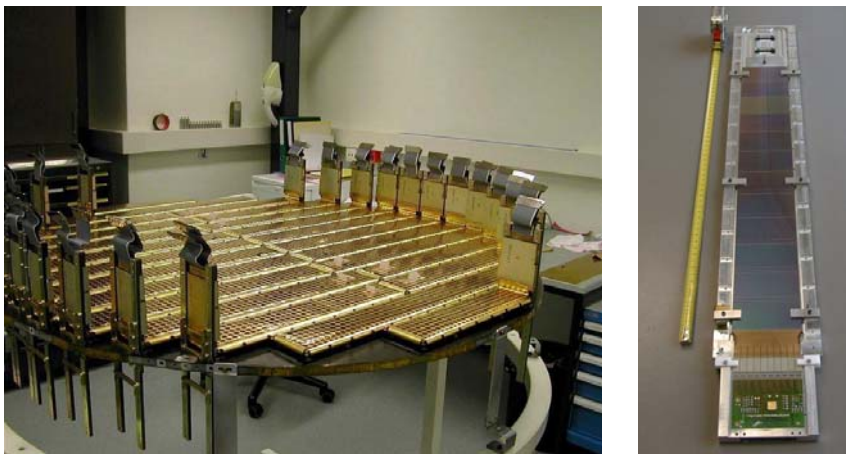

(a) Tracker Plane 2 (b) Tracker Ladder

Figure 1.15: *(a) Plane 2 of the tracker, with one side fully assembled with ladders. (b) One of the ladders of the tracker during assembly, before the EMI shielding is mounted on the ladder.*

Tracker Thermal Control System

The silicon tracker of AMS02 has by far the largest power budget of all subdetectors. In the normal run mode it consumes $800\,W$, most of this in its read out hybrids. To ensure stable operating conditions for the tracker, a thermal management is needed. The Tracker Thermal Control System (TTCS) is a closed loop cooling system designed to keep the silicon detectors and the front-end hybrids within their optimal temperature range. It is depicted in Fig. 1.16. Especially for the detectors this is very important, as the leakage current of the detectors, and thus the noise, scales exponentially with the temperature.

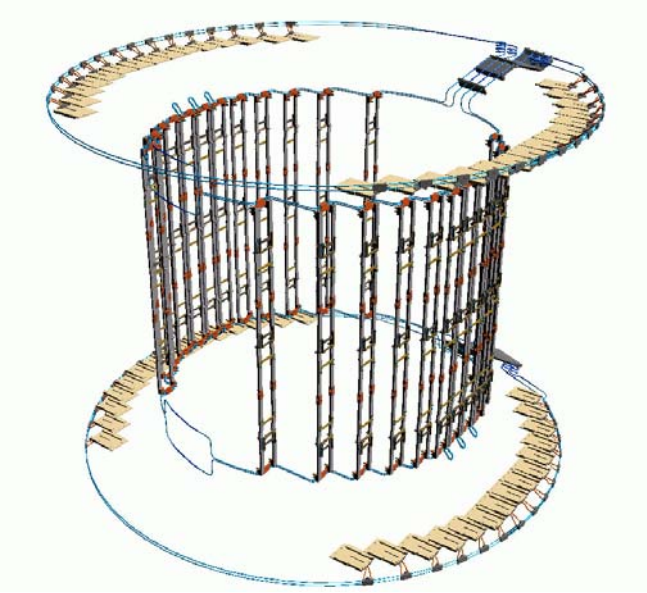

Figure 1.16: *The Tracker Thermal Control System (TTCS). The cooling pipes, the heat exchangers and the thermal bars, with which the heat is transferred from the ladders to the heat exchangers, are shown.*

The heat generated by the silicon detectors and the front-end chips is brought via thermal bars to heat exchangers of the TTCS to keep the detector and its read out within the optimal temperature range. In these heat exchangers a part of the cooling liquid CO_2 is evaporated. The two-phase mixture of liquid and gas is then pumped to the condensers, another set of heat exchangers. These are mounted on the upper radiators on wake[10] and ram[11] side. Inserted into the radiators are heat-pipes, to ensure a homogenous temperature distribution over the radiators.

The Superconducting Magnet

The silicon tracker of AMS02 is placed inside a superconducting magnet with a maximum field of $0.86\,T$, six times stronger than the permanent magnet of AMS01. The magnet of AMS02 will be the largest superconducting magnet ever to be flown into space up to now, with a height of $860\,mm$, an inner diameter of $1065\,mm$ and a total weight of $3\,tons$. A schematic view is shown in Fig. 1.17(b).

There are two dipole coils generating the magnetic field. The attractive forces between the two dipole coils ($\sim 250\,t$) are compensated inside the magnet by the support structure. As it is not possible to use a return yoke to compress the external field lines, as it is normally done in HEP experiments, due to the weight limits, a special coil configuration was chosen for the magnet of AMS02, see Fig. 1.17(a).

All coils are wound from Aluminium stabilised $NbTi/Cu$ wire and are connected in series. The total length of the superconducting wire is $55\,km$. The nominal current will be $459.5\,A$, which leads to a current density of $2600\,A/mm^2$ in the superconductor. Each coil is tested individually before the assembly.

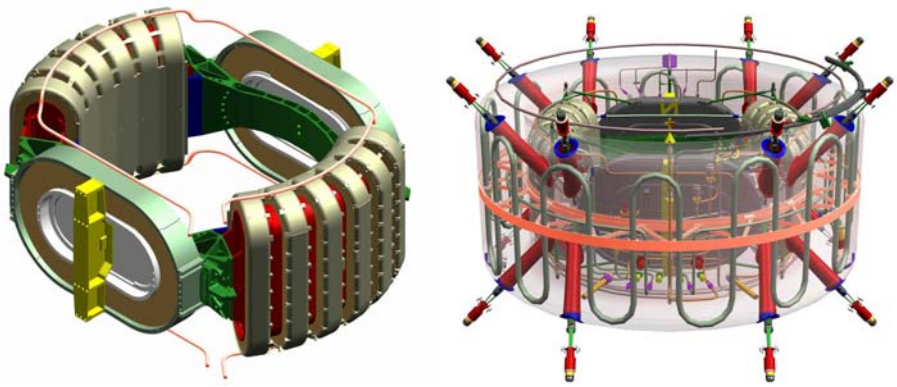

(a) Magnet Coils (b) Magnet Assembly

Figure 1.17: *The Superconducting Magnet of AMS02. (a) The coil arrangement of the superconducting magnet of AMS02 and (b) the fully assembled magnet. The very specific shape of the coils and their mounting is used to save weight, as a normal return yoke could not be used due to its extreme weight.*

The configuration of the magnet unfortunately generates a very inhomogeneous field for the tracker. Thus it is necessary to place magnetic field probes on the tracker planes to measure the magnetic field distribution.

The operating temperature will be $1.8\,K$. To keep the magnet at this temperature for the planned lifetime of 3 years, a supply of superfluid liquid Helium (LHe) of $2600\,l$ is necessary. The LHe is kept at this temperature by cryo-coolers specially designed for operation in zero gravity.

To minimise the heat transfer into the LHe tank, especially in the case of a quench, the magnet is only cooled via so-called cold fingers, and not immersed in the LHe. A second path of possible

[10] trailing side, nautical expression

[11] leading side, nautical expression

heat transfer is the mechanical fixation of the magnet. Therefore a new design is used to keep the heat transfer as small as possible while ensuring maximum safety for the magnet during launch: non-linear straps. These straps are very strong and stiff in high load situations, like the launch, but they decouple themselves during normal situations.

The magnet and the *LHe* tank are situated in a vacuum vessel. This vessel is of course only necessary for insulation during operation on ground, but in space it will also act as shield, to prevent a puncture of the *LHe* vessel in case AMS02 is hit by micro-meteorites.

Due to the limitations in power consumption imposed on AMS02 by the ISS, a special procedure is needed to ramp up the magnetic field without exceeding a maximum power of $1850\,W$. In the first stage of this process the voltage is limited, in the second part the power and in the final stage the current. After the nominal current has been reached, a superconducting switch inside the magnet composure will decouple the magnet from the external supply and it will be operating in the *persistent mode*: the current will keep cycling in the coils without any connection to the outside. No external power will be needed to keep the magnet, which stores $5.15\,MJ$ when fully charged, in operation.

In the very unlikely case of a quench of one coil, all coils will be heated above T_C to make sure, that the heat generated in the magnet will not fatally damage the quenching coil, but is spread over all coils. The magnet system is designed in such a way, that after such an event AMS02 would be fully operational again after 3 days.

As the superconducting magnet is one of the most crucial items of the AMS02 experiment, it is protected by an uninterruptible power supply (UPS), which allows to keep the magnet operational in case of a power loss on the ISS for up to 8 hours. If the nominal power is not restored within that time frame, the magnet will be ramped down.

Performance of the Silicon Tracker

The silicon tracker provides rigidity measurements, using the bending power of the magnet, for energies up to $\sim 1\,TeV$ as well as dE/dx information on the passing particle. To be able to measure the rigidity up to such energies a very high spatial resolution must be achieved. The plot in Fig. 1.18 shows the resolution, that has been achieved in a test beam on the p-side of the silicon microstrip detectors. Fig. 1.19 shows a spectrum of the cluster energy as a function of Z, making good use of the high precision measurement of dE/dx in the silicon tracker. A plot combining the information of the silicon tracker and the RICH is shown in Fig. 1.24.

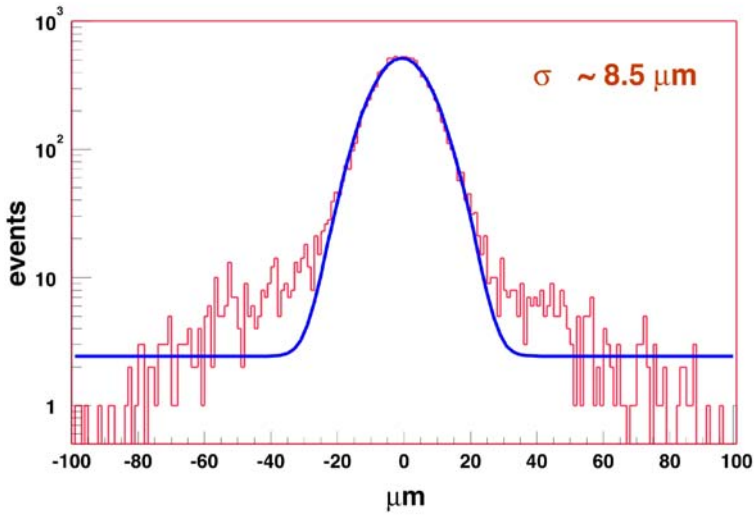

Figure 1.18: *The performance of the Silicon Tracker. The plot shows the spatial resolution measured with a particle beam using the information from the p-side of the silicon microstrip detectors. [AMS05]*

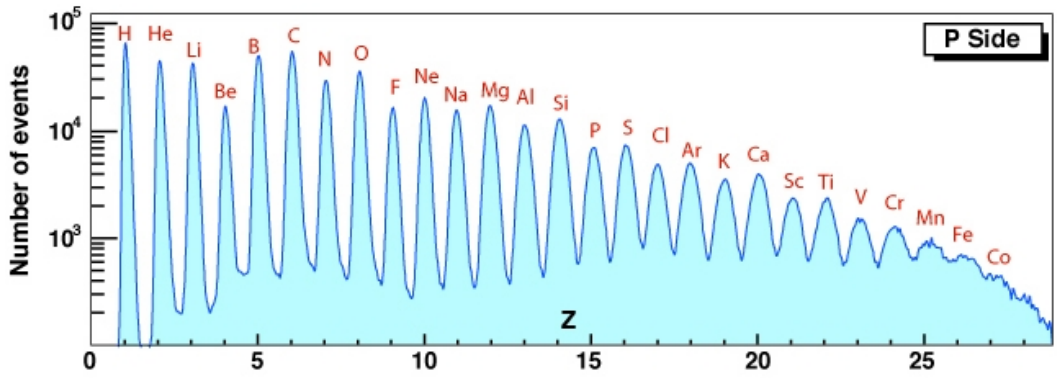

Figure 1.19: *The performance of the Silicon Tracker. The plot shows a spectrum of the cluster energy as a function of Z. [AMS05]*

1.2.4 Anti-Coincidence Counter (ACC)

The Anti-Coincidence Counter (ACC) is placed around the tracker shell, just inside the superconducting magnet. The purpose of the ACC is to veto particles entering AMS02 from the side, particles not passing through all subdetectors and back-scattering from the ECAL.

The ACC consists of 16 scintillator panels read out at both ends via wave-length shifting fibres and PMTs, see Fig. 1.20. The thickness of the scintillator panels is $8\,mm$. As the stray magnetic field is $\sim 0.16\,T$ at the position of the PMTs, mesh grid type PMTs where chosen, as they can withstand up to $0.3\,T$, when the field is parallel to the longitudinal axis of the PMT.

The signal of the ACC PMTs is brought directly into the read out electronics of the TOF to give a veto before a possible trigger signal is issued to the other subdetectors.

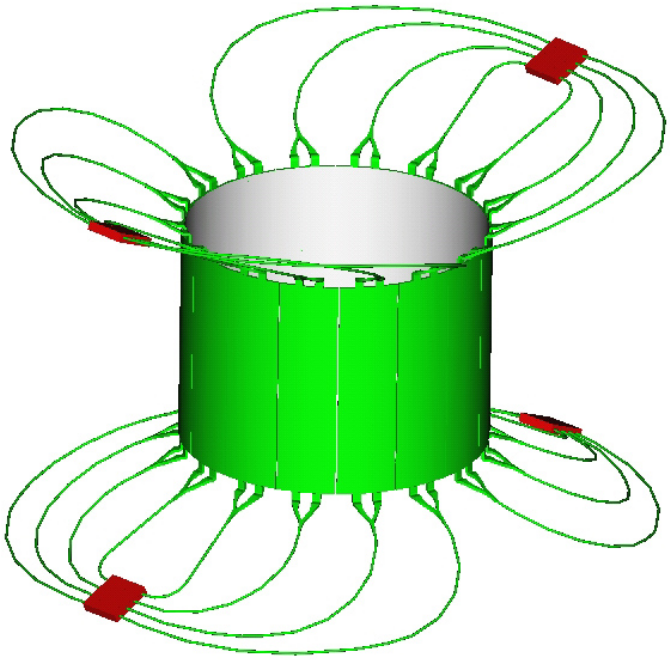

Figure 1.20: *The Anti-Coincidence Counter (ACC). The ACC is constructed like a barrel around the silicon tracker just inside of the magnet. The purpose of the ACC is to veto all particles not passing through the complete set of the AMS02 subdetectors.*

Performance of the ACC

The most important characteristic of the ACC is its inefficiency. As its purpose is to veto all particles that are not passing through the complete set of AMS02 subdetectors, it is important, that it recognises all particles hitting its panels. This was extensively tested with a 10 *GeV* particle beam. In Fig. 1.21 the pulse height spectrum is plotted on the left and the counts vs. charge for different trigger settings on the right.

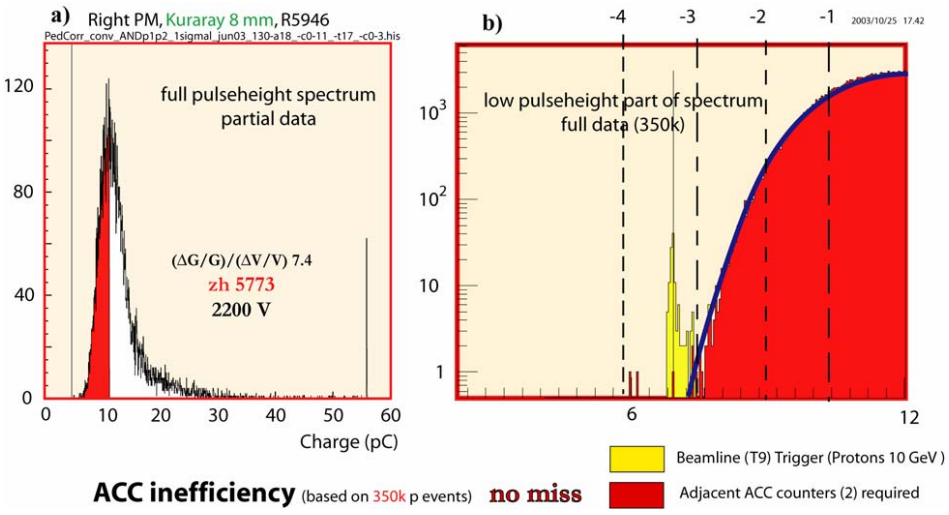

Figure 1.21: *The performance of the ACC. The plot on the left shows a pulse height distribution for a* 10 *GeV particle beam. (b) shows the counts vs. charge for different trigger settings. [AMS05]*

1.2.5 Ring Image Cherenkov Counter (RICH)

The main goals of the Ring Image Cherenkov Counter (RICH), shown in Fig. 1.22, are separation of heavy nuclei for atomic numbers ≤ 26 and the measurement of the particle velocity for $\beta > 0.95$ with a precision of $\triangle\beta/\beta \leq 1\,\%$. For energies below 4 *GeV* the RICH provides additional separation power for the e^+/p^+-ratio.

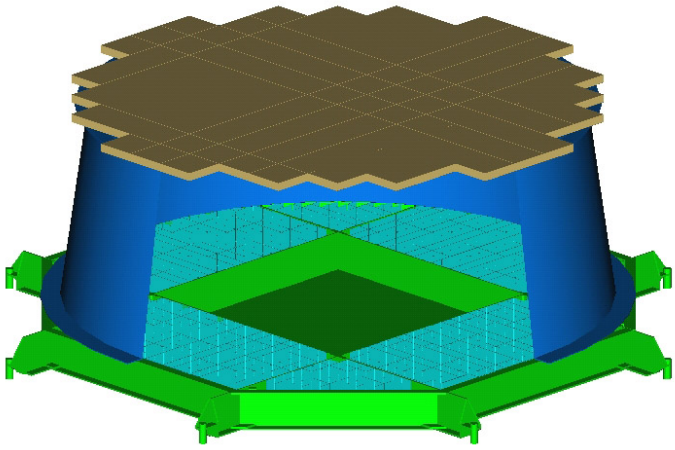

Figure 1.22: *The Ring Image Cherenkov Counter (RICH). The RICH consists of a NaF and aerogel radiator and an array of PMTs. To make sure no Cherenkov light escapes from the RICH, it is surrounded by an extremely reflective mirror. There are no PMTs in the central section of the RICH to allow particles passage into the ECAL without having to pass through too much material.*

The RICH consists of three main parts: The radiator plane, the drift space and the detection plane. The radiator plane is made from NaF and aerogel tiles with a thickness of 30 mm and a refractive index $n = 1.03 - 1.05$, embedded in an aluminium frame. The drift space has a length of 414 mm and is surrounded by an extremely reflective mirror, to make sure that no section of the Cherenkov Ring escapes from the detector. The detection plane is composed of 680 sensitive elements. Each of these elements consists of a segmented 4×4 light guide cone and a pixelated PMT. The central area ($64 \times 64\,cm^2$) of the detection plane is not equipped with PMTs to allow particles passage through the RICH into the ECAL with minimal interaction probability.

From the spatial coordinates of the PMTs, the signal height and the incoming track position the Cherenkov cone is calculated. The opening angle of the cone determines the velocity of the incoming particle. The accuracy of this measurement is $\sigma_\beta/\beta \approx 10^{-3}$. The intensity of the light detected gives an estimation on the charge of the particle. This was proven in a test beam for Z up to 40.

Performance of the RICH

The RICH will provide AMS02 with nuclear isotope identification in the energy range of up to 10 $GeV/nucleus$. Fig. 1.23(a) shows some sample Cherenkov rings obtained with an ion test beam. The corresponding spectrum is shown in Fig. 1.23(b). Combining the information of the RICH with the dE/dx data from the silicon tracker the spectrum can be improved considerably, see Fig. 1.24.

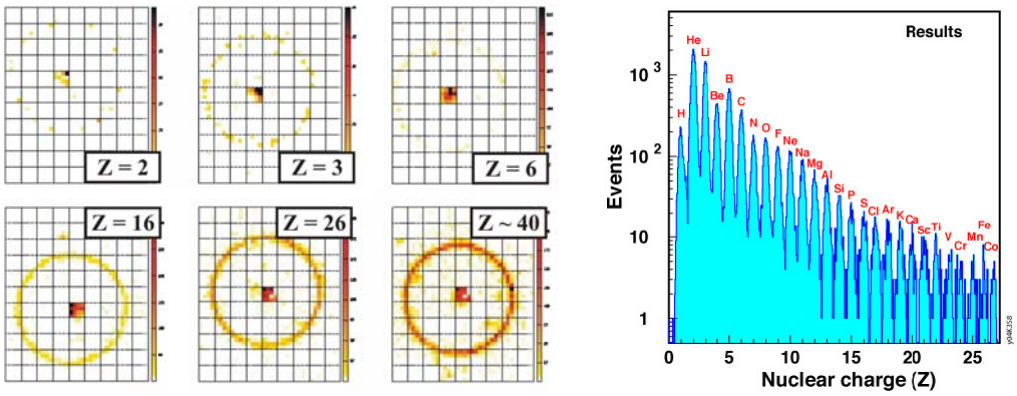

(a) Cherenkov Rings (b) Spectrum

Figure 1.23: *The performance of the ACC. The plot on the left shows a pulse height distribution for a 10 GeV particle beam. (b) shows the counts vs. charge for different trigger settings. [AMS05]*

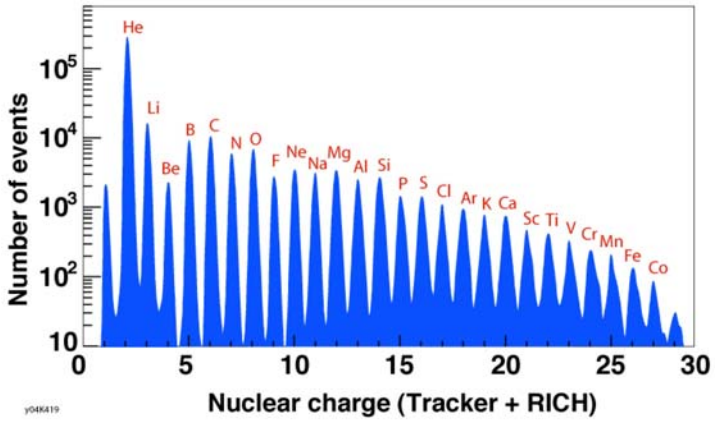

Figure 1.24: *Using the combined information from the silicon tracker and the RICH, plots 1.19 and 1.23(b) can be improved to get this plot.*

1.2.6 Electromagnetic Calorimeter (ECAL)

The Electromagnetic Calorimeter (ECAL) of AMS02 is of the so-called SpaCal[12] type (see Fig. 1.25(b)), a 3-dimensional sampling calorimeter type. It consists of 9 superlayers, each made from 10 layers of lead and scintillator fibres. The superlayers are alternately oriented perpendicular to each other. The active area has a rather small size of $64.8 \times 64.8\,cm^2$, limiting the overall acceptance of AMS02 to $\sim 0.05\,m^2sr$. This size is a direct consequence of the stringent weight limitations ($512\,kg$ for the ECAL). Nevertheless, it will have a thickness of $166\,mm$, which corresponds to ~ 16.5 radiation lengths. The showers generated by a charged particle will be sampled at 18 different depths with a granularity of $\sim 1\,cm^3$.

The scintillation fibres will be read out single sided by 324 PMTs placed on the four lateral sides of the calorimeter, shown in Fig. 1.25(a). Each PMT is divided into 16 segments. The signal strength varies from a few photoelectrons for a MIP[13] to $\sim 10^5$ photoelectrons for a TeV electron. Test beams with the ECAL prototype showed an almost perfect linearity for the energy range up to $50\,GeV$ and only small deviations ($< 5\,\%$) in the range to $180\,GeV$.

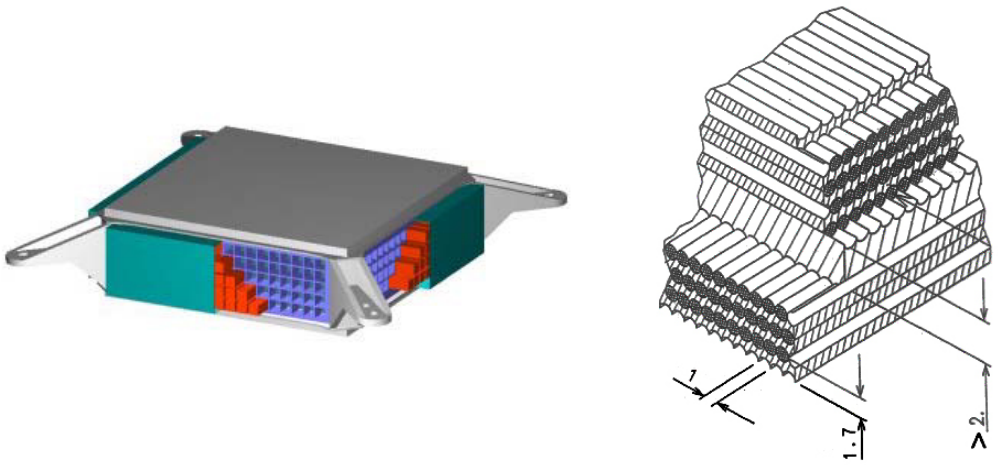

(a) The ECAL (b) Sandwich Structure

Figure 1.25: *The Electromagnetic Calorimeter of AMS02. (a) shows the assembly of the ECAL. Clearly visible are the grids for the PMTs, the top cover and the mounting brackets. (b) The internal structure of the ECAL. It consists of alternating layers of lead and scintillator fibres. The superlayers are arranged alternatingly perpendicular to each other.*

Performance of the ECAL

The 3D sampling ECAL is able to measure the energy of particles in the range of up to a few TeV. It is also able to improve the proton rejection rate in the same energy regime by a factor of $\sim 10^3$ using the dependence of the shower generation on the process involved (electromagnetic vs. hadronic). The combined proton rejection rate of the ECAL and the TRD ($10^5 - 10^6$) will allow to measure the positron fraction with unprecedented precision, which is especially important for the indirect search for Dark Matter ($\chi + \overline{\chi} \rightarrow e^- + e^+$). In Fig. 1.26(a) the relative energy resolution is plotted as function of the particle energy. Additionally, the ECAL can be used to generate a stand alone trigger for the AMS02 experiment. This is crucial for the detection of high energetic gammas, which might be missed by the other subdetectors but hold valuable information, e.g. with respect to the search for Dark Matter.

[12] **SpaCal**: **Spa**ghetti **Cal**orimeter

[13] **MIP**: **M**inimum **I**onizing **P**article

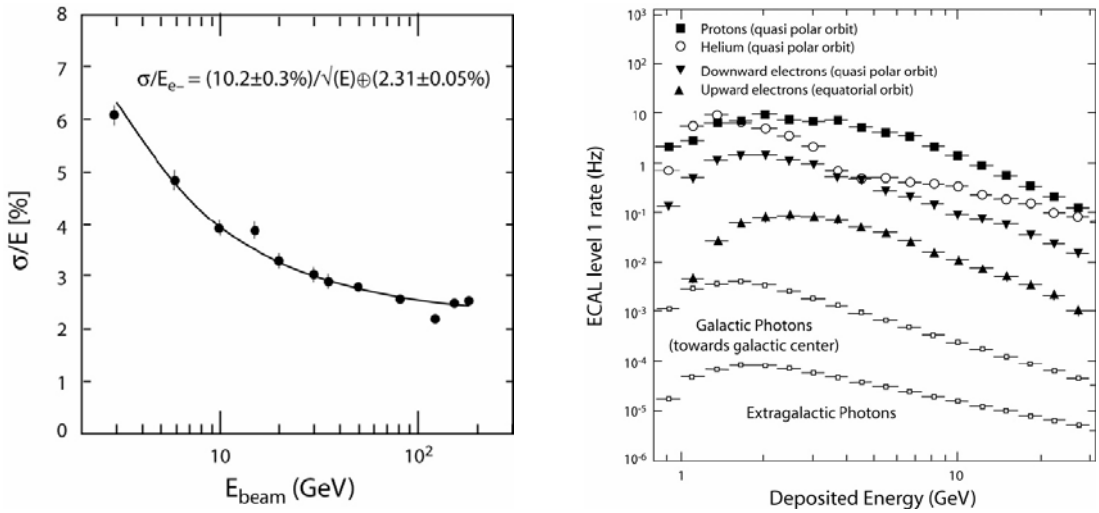

(a) Energy Resolution

(b) Stand Alone Trigger

Figure 1.26: *(a) shows the energy resolution of the ECAL as a function of the particle energy. The presented data was obtained at a test beam. The ECAL stand alone trigger rate for various particles is depicted in (b). [AMS05]*

1.2.7 Star Tracker & GPS

The star tracker, shown in Fig. 1.27, and the GPS[14] are two key elements for the physics of point source of gammas with high energies, like Gamma Ray Bursts (GRB). For precision measurements in this field, it is of extreme importance to know exactly in which direction AMS02 is pointed and the exact time of the trigger corresponding to this signal.

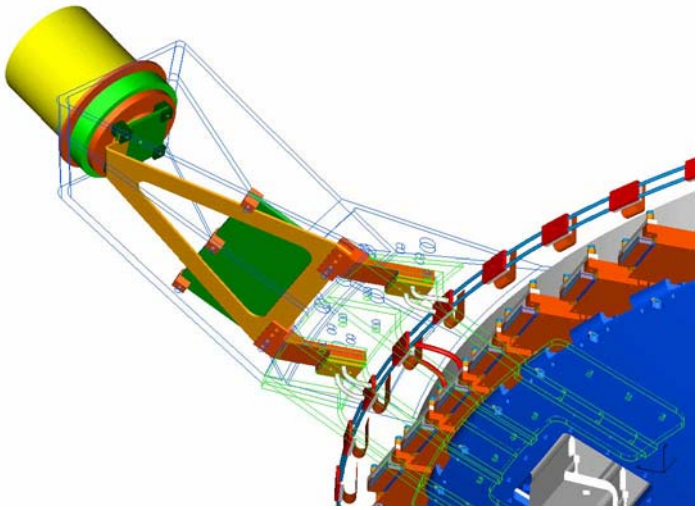

Figure 1.27: *The Star Tracker. It is a digital camera looking at the stars above AMS to measure the direction in which AMS02 is pointing. This is extremely important especially for GRB physics.*

The AMICA[15] star tracker is a commercial cooled CCD camera, made by Carso[16], with integrated read out and data processing electronics developed for space applications. To minimise the

[14] **GPS**: **G**lobal **P**ositioning **S**ystem

[15] **AMICA**: **A**stro **M**apper for **I**nstrument **C**heck of **A**ttitude

[16] C.A.R.S.O., Padriciano 99 - 34012 Trieste - ITALY, phone +39-040-3755402/3, fax +39-040-3755404

necessary amount of data to be transferred to the main computers of AMS02, these electronics are capable of calculating the direction by comparing the actual picture taken with a database of star positions in the sky. The AMICA star tracker is derived from the UVSTAR[17] telescope, that was flown three times successfully on the space shuttle.

The GPS system for AMS02 is also based on a commercially available GPS receiver, the Topstar 3000D by Alcatel. It will deliver a time stamp to the electronics of the star tracker with a rate of $\sim 1\,kHz$.

Performance of the Star Tracker & the GPS

The Star Tracker and the GPS play a very important role in the search for point-like sources of high energy gammas. Their combined information allows to measure the orientation of AMS02 with a precision in the arcsecond range. Additionally, a time profile of the event can be established. Candidates for point-like sources of high energy gammas are the Dark Matter Annihilation in galactic or extragalactic sources, GRBs, Pulsars, Active Galactic Nuclei and possible exotic events. The AMS02 experiment can detect gammas in the energy range of $10-100\,GeV$, either by conversion in one of the top layers of the TRD or by an electromagnetic cascade in the ECAL.

1.2.8 Detector Environment

One of the main challenges of the AMS02 project is to build a High Energy Physics high precision detector that can withstand the vibrations during the launch and the harsh environment in space.

The vibrations during the launch and the re-entry into Earth's atmosphere can exert forces of up to $6.8\,g$ onto the detector. Additionally, the NASA requires, that the first significant eigenfrequency of any device flown on-board a space shuttle has to be above $50\,Hz$ to prevent catastrophic resonances. As the detector should keep its precision alignment even during such extreme loads it is very important to test all components and the whole experiment for their behaviour under vibration. The standard procedure for this is the usage of finite element simulations and measurements on shaker tables to verify these simulations. This approach is also applied by the AMS02 collaboration.

As the orbit of the ISS has a height of $\sim 400\,km$, the space station is on the outer fringes of Earth's atmosphere. The remanent outside pressure at the height of the ISS is $1.45\times10^{-8}\,mbar$ [Pet03]. This low pressure is in itself already a technical challenge, but even more demanding is the fast transition from normal pressure on the ground to the vacuum in space during the launch. The design of all subdetectors has to allow the air trapped inside to escape rather fast without damaging the detector. This is especially difficult for the silicon tracker, which has a large volume but should be absolutely light tight, as any light entering the tracker would disturb its performance. In addition all components and materials used in the construction of AMS02 have to be approved by NASA to meet their requirements on out-gasing.

Temperatures in space can vary quite strongly from sunshine to shade. Therefore it is very important to calculate the time the detector spends in both, see Fig. 1.28. From this, one can compute the temperature distribution the detector will see during its lifetime. It has to be ensured that all detector components can survive this temperature range non-operating and can be active in at least 90% of it. This is especially demanding for the TRD and the read out electronics. As the TRD is a gaseous detector it is very sensitive to temperature variations and the design goal is to keep temperature variations inside the TRD below $0.5\,℃$. For the read out electronics the issue is the cooling during the operation. As there is no air available for convective cooling all heat transport has to be done by thermal conductivity. The heat is then dissipated into space by radiation.

Another issue, mainly for the electronics, is the damage done by the cosmic rays. While the total dose expected is quite low, in the range of $\sim 1\,krad/yr$, there is probability of a so-called Single Event Upset (SEU) caused by a heavy ion depositing so much charge in a silicon device, that, for example, a

[17] **UVSTAR**: **U**ltraviolet **S**pectrograph **T**elescope for **A**stronomical **R**esearch

latch-up of chip or a bit flip in a register will occur. For more details on the implications on the design of the electronics please read chapter *Space-Grade Electronics for the AMS02 Detector* on page 39.

Even though there is a very small probability of a micro-meteorite hitting the AMS02 experiment, this is quite a huge danger for the detector, as the damage done by a micro-meteorite can be tremendous. Especially the LHe tank and the TRD gas supply vessels are well protected, as a rupture of these would not only prematurely end the experiment but would also endanger the whole space station.

Unlike most experiments based on Earth, AMS02 will have no possibility for maintenance, with the exception of software updates, once it is in space. The two main reasons for this are the risks involved for the astronauts who would be servicing AMS02 and the costs. The latter are mostly caused by the training of the astronauts for a task and the transport of the spare parts, not to mention the complications in the detector design required to allow such procedures.

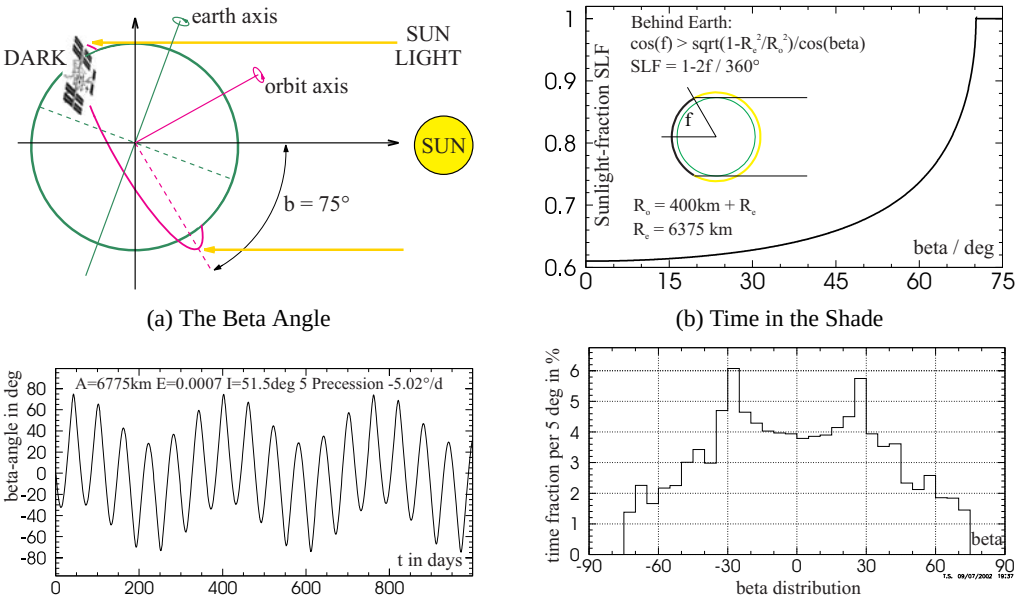

(a) The Beta Angle

(b) Time in the Shade

(c) Beta Angle Variation

(d) Beta Angle Distribution

Figure 1.28: *The beta angle of the ISS. The definition of the beta angle is shown in (a). The time the ISS is exposed to the sunshine as a function of the beta angle is depicted in (b). The variation of the beta angle vs. time is plotted in (c), the distribution of the beta angle in (d). Taken from [Sie00].*

1.3 Physics with the AMS02 Detector

The AMS02 experiment will be in space for at least three years measuring, among many other things, the composition and the energy distribution of the primary cosmic rays in the energy range of up to $1\,TeV$. This will be done with unrivalled precision and statistics for charged particles, but also for high energy gammas[(18)]. These measurements will allow the observation of time dependent phenomena, to set new limits on the matter/anti-matter and isotope ratios and to further improve the cosmological models.

In Fig. 1.29 the signatures of particles with an energy of $300\,GeV$ are shown for electrons, positrons, protons, anti-helium and gammas. One can clearly see the separation power of the combined information of the various subdetectors.

In the following sections the cosmic ray spectra, as far as they have been measured up to now, will be presented together with the models for the acceleration processes of the various particle types. Neutrinos will be excluded from this, as their interaction probability with matter is so small, that they

[(18)] High energetic gammas can only be measured by AMS02 via conversion inside the detector.

are not detectable with AMS02. After this possible candidates for the Dark Matter, which composes up to 22 % of the total matter in the universe [Ben03], will be introduced, also indicating their influence on the spectra.

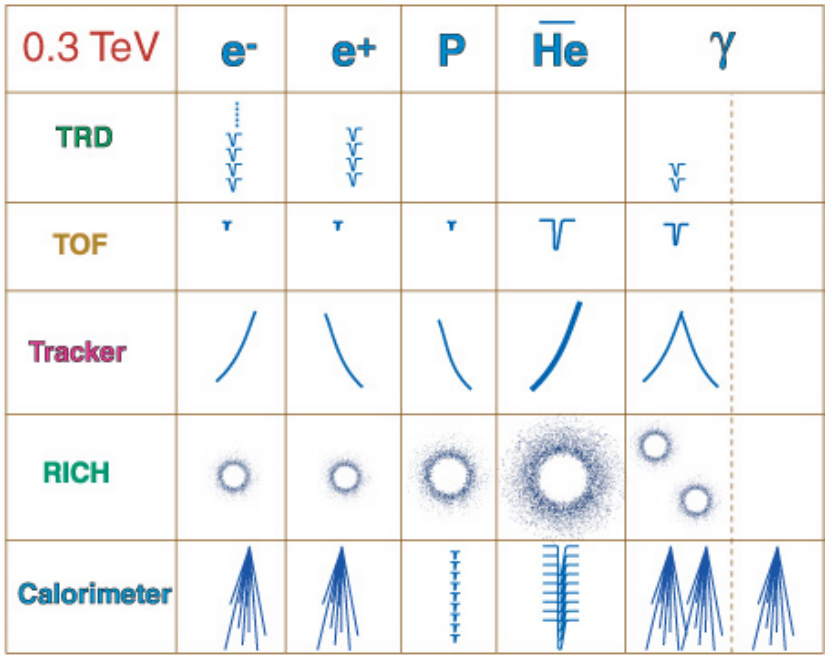

Figure 1.29: *Signatures of the electrons, positrons, protons, anti-helium and gammas with an energy of* 300 *GeV as they will be measured passing through the different subdetectors. [AMS05]*

1.3.1 Cosmic Rays

Cosmic rays have played a very important role in the early stages of particle physics in the 20th century. Particles like the positron, the anti-proton but also the pions and some "strange" particles have been discovered in the cosmic rays. They have a wide range of energies, from 0.77 meV for the neutrinos left over from the Big Bang to a few 10^{20} eV for ultra high energetic protons.

The primordial cosmic rays, that reach Earth, have already passed an average mass length of $\sim 6\,g$. Due to this and the magnetic fields in the universe, that affect the charged particles, most particles do not point back to their source and also their energy has been modified.

As Earth's atmosphere has an exponential decrease towards space, there is no real border. Most commonly the layer with $5\,g/cm^2$ remanent pressure is defined as the border region, since the cosmic rays start to produce secondary particles in the layers below. This residual pressure corresponds to a height of $\sim 40\,km$ in the atmosphere.

For a more comprehensive overview please refer to [Gru00].

1.3.2 Cosmic Rays - Charged Particles

The charged particles in the cosmic rays consist to 99 % of ions and to 1 % of electrons. The composition of the ions is dominated by hydrogen (89 %), followed by helium (10 %). All other ions only amount to 1 %. A more detailed description can be found in the next section.

Element Abundances

The composition of the elements in the Galactic Cosmic Rays (GCR) and in those originating in our solar system is very similar, see Fig. 1.30. The element with the highest abundance by far is hydrogen

(not shown in the plot), the second is helium, which is produced in vast amounts in stars during the fusion reaction.

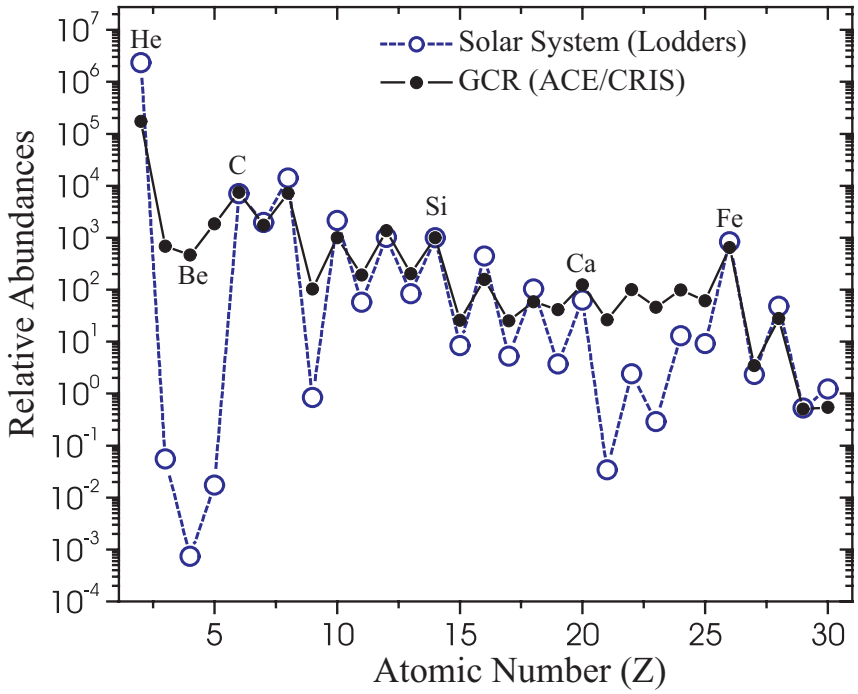

Figure 1.30: *Abundances of elements in Galactic Cosmic Rays (GCR) and in the solar system. The distributions are very similar, with the exception of the elements Li, Be, B and those below iron. [Isr04]*

The main differences in the abundances between the GCR and the cosmic rays from the solar system are at the elements Li, Be, B and at the elements below Fe. The production of these elements is suppressed in the fusion reactions in the sun, but in the GCR the elements can be produced by fragmentation of heavier elements like carbon, oxygen and iron.

For elements heavier than iron the abundance is dramatically lower. The reasons for this are again the production processes involved. The elements up to iron can be produced in the fusion processes of stars, as there is an energy gain when creating these nuclei. For heavier nuclei one has to add energy to create them. An environment for this reaction is only given in super novae explosions and in other very high energy processes.

A further observation that can be made is the high relative abundance of nuclei with completely filled shells for either protons or neutrons. These nuclei are also called magic nuclei. Especially double magic nuclei, like helium or oxygen have a rather high abundance. Also nuclei with even numbers of protons and neutrons are more stable and thus have a higher abundance than those with even/uneven or uneven/uneven proton and neutron numbers.

Cosmic Ray Energy Spectra

As already mentioned before, the particles of the primary cosmic rays have to pass some remanent mass and magnetic fields along their way. This of course affects mostly the low energetic particles and can be clearly seen in the energy spectrum of the cosmic rays in Fig. 1.31.

The flux of particles with an energy below $1\,GeV/nucleon$ is also affected by the variation of the magnetic fields of the sun in its $11\,yr$ cycle. If the sun is more active, its magnetic field is stronger and more of the low energetic particles are deflected.

As the flux diminishes for higher energies, different detectors have to be used to measure the spectrum of the primary particles. For the detection of low energetic particles balloon and satellite

experiments are used. Experiments for very high energetic particles are based on the detection of Cherenkov light in large volumes, e.g. the HESS telescope.

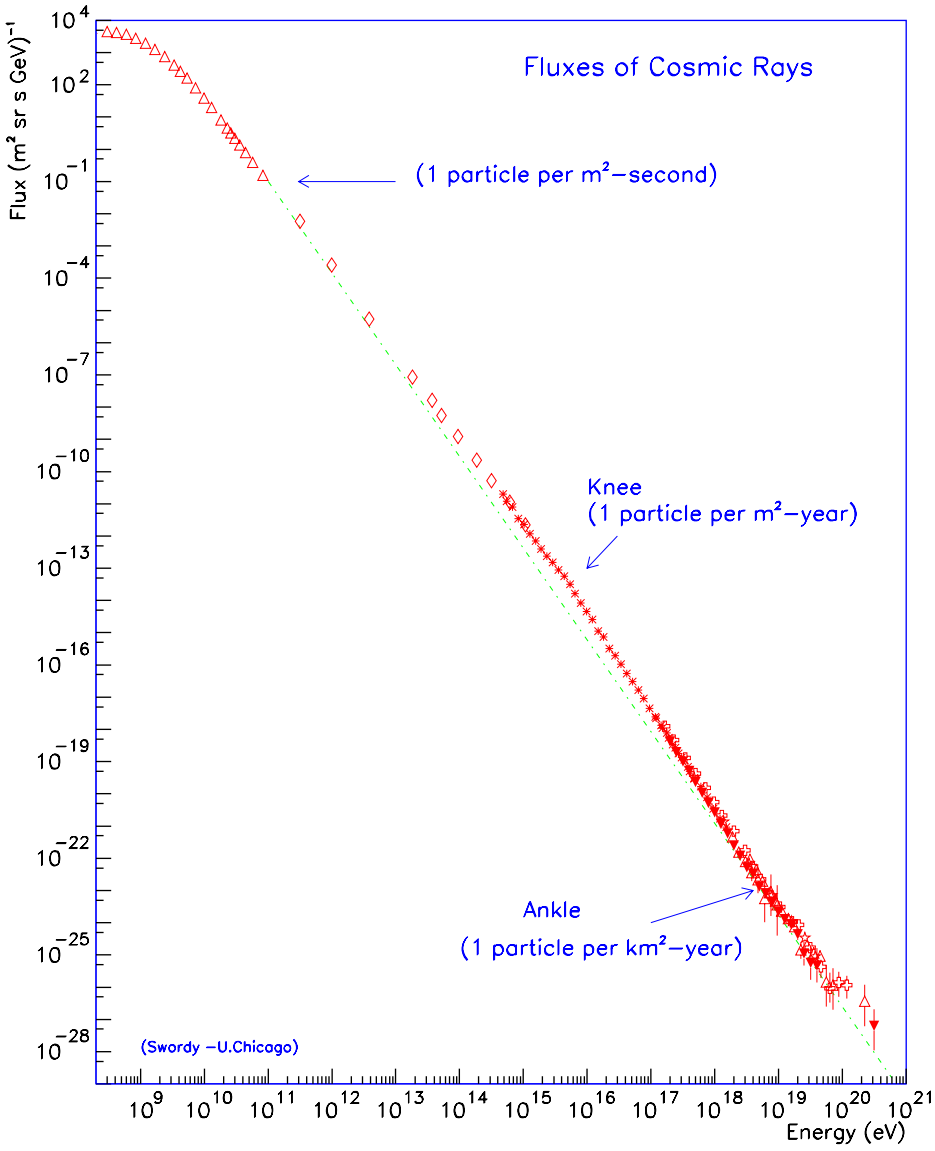

Figure 1.31: *Energy spectrum of the charged particles in the primary cosmic rays. One can clearly see the low energy particles being suppressed by the magnetic fields and the remanent matter, as well as the other two prominent features, the knee and the ankle. [Cro97]*

Most of the observed particles originate from within our galaxy. These particles dominate the spectrum up to energies of $10^{15}\,eV/nucleon$, the "knee" of the spectrum. This limit is set by the fact that the magnetic fields of the Milkyway can only keep particles inside with a gyro radius smaller or comparable to the radius of the Milkyway itself.

A second effect contributing to the slope change at the knee is, that $10^{15}\,eV/nucleon$ is the maximum energy that can be reached in super novae explosions. Particles with higher energies have to be accelerated by different mechanisms, resulting in a different energy spectrum.

The second change of slope at the "ankle" is accredited to extra-galactic components of the cosmic rays. In principle one would expect the energy spectrum to be cut off at $6 \cdot 10^{19}\,eV/nucleon$, as the predominant particles, the protons, start generating pions with the remanent photons of the black body radiation ($T = 2.7\,K$) above this threshold energy. The height of this threshold, the Greisen-Zatsepin-

Kuzmin cut-off, can be calculated using the four vector balance of the proton and the photon.

Nevertheless, some events have been observed with energies above $10^{20}\,eV/nucleon$. The attenuation length of particles with such energies is smaller than $10\,Mpc$. For photons the attenuation length at such energies is even smaller ($10\,kpc$), as they generate electron positron pairs with the photons of the black body radiation. Also neutrinos can be discarded as candidates for these events, as they would have a uniform distribution of events in the atmosphere (unlike the observed ones, that originated only from one layer of the atmosphere), due to their very low interaction probability.

Acceleration Mechanisms

How are the charged particles in the cosmic rays accelerated to such high energies? This is one of the questions in cosmology, that have not been finally answered up to now. There are many models describing mechanisms for various energy regimes, but none gives a complete picture. Some of them are introduced below.

- **Cyclotron mechanisms:** Particles with energies of up to $100\,GeV$ have been detected and traced back to our sun. These energies can be achieved by accelerating the particles in localised variable magnetic fields on the sun's surface. There are two models, both of them are based on the solar spots.

  – Single Solar Spots: Solar spots are one of the most prominent features of the surface of the sun. They can be recognised by their colour, as they are cooler than the surrounding surface and thus darker. The missing energy is "converted" into magnetic fields. These fields can reach strengths of a few T, which can be shown measuring the Zeemann effect, and sizes of up to $10^7\,m$.

    If a charged particle is moved around such an area with the diameter R with a variable magnetic field once, it is accelerated by the induced voltage and thus gains the energy:

    $$E = eU = -e\frac{d\Phi}{dt} = -e\frac{\int \vec{B}\cdot d\vec{A}}{dt} = e\pi R^2\frac{dB}{dt} \tag{1.1}$$

    The main problem of this model is, that it requires an additional force that keeps the particle on its track around the solar spot, not unlike in the accelerator rings at CERN or Fermilab.

  – Pairs of Solar Spots: In a lot of cases there is not a single solar spot, but a pair of them with opposite magnetic fields. The solar spot in these pairs move towards each other and merge later on.

    The moving magnetic dipole induces an electric field, that is perpendicular to the magnetic dipole and to the direction of the movement, $\vec{E} = \vec{v} \times \vec{B}$.

    With the typical values for the magnetic field and the velocity, the electrical field can reach strengths of $10\,V/m$. Even though this value is rather small, due to the very small friction losses in the chromosphere and the huge dimensions of the solar spots, the particles can be accelerated to energies in the GeV range.

    This mechanism is much more plausible as a model for the particle acceleration on stars, as it does not require additional forces, that keep the particle on a circular track around the solar spot.

- **Fermi mechanism:** The processes involving collisions of the particle with galactic clouds are called Fermi mechanisms. The 1st order process involves particle clouds emitted from exploding stars, the 2nd order process so-called magnetic clouds. Both processes generate very high energetic particles.

– 1st order: If a star has completely burned its hydrogen, a gravitational collapse will start, as the radiation pressure maintaining the balance is missing. This collapse increases the temperature inside the star until the helium burning starts. Once the helium is consumed the collapse continues. This process goes on till the fusion processes end at the iron group, as further fusion processes would be endothermic.

  At this moment, at the latest, the star collapses fully. During this, it emits parts of its mass into the stellar void, the rest forms a neutron star. The emitted mass acts as a shock front to the mass in the interstellar space.

  If the shock front moves at the velocity of u_1, the gas behind it moves away from it with the velocity u_2, which corresponds to $u_1 - u_2$ in the lab system. A particle with the speed v that encounters the shock front coming towards it, is reflected there and gains the energy:

$$\Delta E = \frac{1}{2} m \left(v + (u_1 - u_2)\right)^2 - \frac{1}{2} m v^2 \tag{1.2}$$

  If one takes into account the relativistic corrections and the different scattering angles and the approximation that $v \approx c$, one gets the expression, as the linear terms dominate:

$$\frac{\Delta E}{E} = \frac{4}{3} \frac{u_1 - u_2}{c} \tag{1.3}$$

  Similar expressions can be obtained for particles reflected between two shock fronts.

  In most cases the inner wave of the shock front will be moving with higher velocities (v_2) while the outer wave (v_1) will be already slowed down by interactions with the interstellar matter.

  If a particle is reflected between the inner and the outer wave of the shock front, it will gain the energy

$$\Delta E_1 = \frac{1}{2} m \left(v + v_2\right)^2 - \frac{1}{2} m v^2 \tag{1.4}$$

  at the inner front and loose the energy

$$\Delta E_2 = \frac{1}{2} m \left(v - v_1\right)^2 - \frac{1}{2} m v^2 \tag{1.5}$$

  at the outer front. Still there is a net gain in energy of

$$\Delta E = \frac{1}{2} \left(v_1^2 + v_2^2 + 2v\left(v_2 - v_1\right)\right) \approx mv\Delta v \tag{1.6}$$

  As both of these processes are linear in the relative velocity, they are called 1st Fermi-Mechanisms. Taking into account the measured values for the velocities, energies of up to $100\,TeV$ can be achieved with this acceleration processes.

– 2nd order: For collisions with magnetic clouds, one has to look at the two possibilities for such a collision: (a) the cloud is moving anti-parallel with the velocity $\overrightarrow{u}$ to the particle (velocity $\overrightarrow{v}$) or (b) parallel to it.

  In the case (a) the particle gains the energy

$$\Delta E_1 = \frac{1}{2} m (v + u)^2 - \frac{1}{2} m v^2 \tag{1.7}$$

  for (b) it loses the energy

$$\Delta E_2 = \frac{1}{2} m (v - u)^2 - \frac{1}{2} m v^2 \tag{1.8}$$

  in average there is a net gain of energy for the particle of

$$\Delta E = \Delta E_1 + \Delta E_2 = m u^2 \tag{1.9}$$

As the energy gain in this process is proportional to the square of the cloud velocity, it is called 2nd order Fermi-Mechanism. The Eqn. 1.9 is also valid in the relativistic case ($v \approx c$).

The energy gain per collision is rather small, as the cloud velocity is very small compared to the velocity of the particle ($u \ll v$). Thus the acceleration by the 2nd order Fermi-Mechanism is very time consuming.

A further point to take into account is the interaction of the particle in between acceleration steps with the interstellar matter, which slows it down again. Due to this, a minimum injection energy, e.g. given by a pre-acceleration with the 1st order Fermi-Mechanism, is required for this process to be efficient.

- **Pulsars:** Rotating neutron stars, also called pulsars, are the remains of supernova explosions. During the gravitational collapse, the radius of a star is reduced from $\sim 10^6\,km$ to $20\,km$, the density inside the star reaches values of up to $6 \cdot 10^{13}\,g/cm^3$, which is close to the density of a nucleus. As electrons and protons are compressed so much, neutrons can be produced via the weak interaction $p + e^- \rightarrow n + \nu_e$.

  As the torsional moment is conserved in a gravitational collapse, the pulsars have a very short rotation time ($\mathcal{O}(10\,ms)$). Also the magnetic flux through the surface is conserved, which leads to magnetic fields in the order of $2.5 \cdot 10^{15}\,T$. Using the relation $\overrightarrow{E} = \overrightarrow{v} \times \overrightarrow{B}$ and the fact, that the rotation axis is normally not parallel to the direction of the magnetic field, one can calculate the electric field in which particles are accelerated. With typical values for the parameters of pulsars the E field can reach values of up to $10^{15}\,V/m$. Per metre a particle can gain the energy of $1\,PeV$! Unfortunately, it is not yet fully understood how the pulsars use their rotational energy to accelerate particles.

  Even if pulsars can use only 1% of their rotational energy to accelerate particles they contribute almost 100% of the energy in cosmic rays in our galaxy. This can be calculated using the rotational energy of a pulsar ($\sim 4.4 \cdot 10^{61}\,eV$), an average lifetime of $10^{10}\,yr$, the generation rate of pulsars of $1/100\,yr$ and the size of our galaxy ($2 \cdot 10^{67}\,cm^3$). This leads to an energy density of $1.1\,eV/cm^3$, which is, allowing for de-acceleration processes and escaping particles, very close to the measured value of $1\,eV/cm^3$.

- **Double Star Systems:** Also double star systems can accelerate particles to high energies. In most cases they consist of a neutron star or pulsar and a regular star. In such systems an accretion disc is formed by the matter that is sucked from the regular star and is whirling around the pulsar. In this disc vast amounts of plasma are moved, which generates enormous electric fields, which in turn can accelerate particles.

  In addition there is also an acceleration due to the energy gain in the gravitational field of the compact star. This can be calculated from

$$\Delta E = -\int_{\infty}^{R_{pulsar}} G\frac{m_{particle} M_{pulsar}}{r^2} dr = G\frac{m_{particle} M_{pulsar}}{R_{pulsar}} \tag{1.10}$$

  A proton can gain the energy $\Delta E = 70\,MeV$ using typical values for the mass ($2 \cdot 10^{30}\,kg$) and the radius ($20\,km$) of the pulsar.

  A third effect accelerating particles in double star systems is the magnetic field of the neutron star, as it is perpendicular to the accretion disc, it can generate strong electric fields via the Lorentz force.

$$\overrightarrow{F} = e\left(\overrightarrow{v} \times \overrightarrow{B}\right) = e\overrightarrow{E} \tag{1.11}$$

Form this, one can calculate the energy of a particle as

$$E = \int \vec{F} \cdot d\vec{s} = evB\Delta s \tag{1.12}$$

using $\vec{v} \perp \vec{B}$. For realistic values of v, B and Δs, the energy of the particle can reach values of $3 \cdot 10^{19}\,eV$.

- **Active Galaxy Nuclei:** As a further source of high energetic particles also Active Galaxy Nuclei (AGN) are considered. Their acceleration mechanism is also based on the magnetic fields and the particles moving in the accretion discs. As the characteristic values of the parameters in Eqn. 1.12 are even higher than for double star systems, much higher energies can be achieved. Most of these particles are ejected from the system via the jets standing perpendicular on the accretion discs.

In the current understanding, it is assumed, that the Fermi mechanisms are responsible for the main part of the cosmic ray spectrum ($E < 10^{15}\,eV$). The higher energetic particles are believed to originate from pulsars, double star systems and AGNs.

For the acceleration in supernova shock waves one can calculate the energy spectrum of the particles accelerated there. If the particle has the starting energy E_0 and gains the energy εE in each acceleration step it has the energy

$$E_n = E_0(1+\varepsilon)^n \tag{1.13}$$

after the n$^{\text{th}}$ step. Thus to reach the final energy of E_n the particle has to undergo n acceleration steps.

$$n = \frac{E/E_0}{\ln(1+\varepsilon)} \tag{1.14}$$

Taking into account the escape probability P after each step, one can calculate the number of particles with an energy higher than E.

$$N(>E) \sim \sum_{m=n}^{\infty} (1-P)^m = \frac{(1-P)^m}{P} \tag{1.15}$$

Using the Eqns. 1.15 and 1.14 one gets the integral energy spectrum

$$N(>E) \sim \frac{1}{P}\left(\frac{E}{E_0}\right)^{-\gamma} \tag{1.16}$$

with the spectral index γ. Since the energy gain per step can be considered as very small compared to the starting energy, one can express γ as

$$\gamma = \frac{\ln(1+P)}{\ln(1+\varepsilon)} \approx \frac{P}{\varepsilon} \tag{1.17}$$

From the measurement of the spectrum one gets for γ the value 1.7 for energies below $10^{15}\,eV$ and $\gamma = 2$ for energies above. This is in good agreement with the calculation.

1.3.3 Cosmic Rays - Anti-Matter

Dirac's equation, $E^2 = m_0^2c^4 + p^2c^2$, has two solutions, one for matter, one for anti-matter. Taking this into account, one would expect from the models of the Big Bang an evenly balanced distribution of matter and anti-matter in the universe, as there is no known process favouring one or the other.

Any such process would have to be non-conserving for the baryon number. Additionally, the charge parity (CP) would have to be violated to create a matter/anti-matter asymmetry. The CP violation has been observed in the kaon decay in 1964 and is also understood from the theoretical viewpoint.

Up to now the only anti-matter particles observed are anti-protons, anti-neutrons and positrons. They contribute to the measured spectra only to a tiny fraction, which is consistent with production in secondary processes.

To prove the existence of possible anti-matter stars, galaxies or even domains in the universe one would have to measure anti-nuclei with $Z \geq 2$, as it is almost impossible to produce them in secondary processes. An annihilation gamma ray spectrum, which would have a peak around $150\,MeV$, would also be a good hint at the existence of anti-matter in the universe, but it has not been observed up to now.

In the following the anti-particles and their generation mechanisms will be described. The measured spectrum, respectively the exclusion limits, also will be presented.

- **Anti-Protons:** The most common production process for anti-protons is the interaction of a high energetic proton with the interstellar matter: $p+p \rightarrow p+p+p+\overline{p}$. The threshold energy for this process can be calculated using the centre of mass energy s.

$$\sqrt{s} = \left\{ (E_p + m_0)^2 - (\overrightarrow{p} - 0)^2 \right\}^{1/2} = \left\{ 2m_0E_p + 2m_0^2 \right\}^{1/2} \stackrel{!}{\geq} 4m_0 \tag{1.18}$$

  which has to be at least 4 times the mass of the proton. From this, one gets the minimum energy of the proton using

$$2m_0E_p + 2m_0^2 \geq 16m_0^2 \qquad \Rightarrow \qquad E_p \geq 7m_0 \quad (= 6.568\,GeV) \tag{1.19}$$

  The energy spectrum of the anti-protons, as far as it has been measured up to now, is shown in Fig. 1.32. Also included in this plot is the data expected from AMS02. For energies higher than $10\,GeV$ the anti-proton flux is 10,000 times smaller than that of the protons, which requires a detector with very good rejection rates.

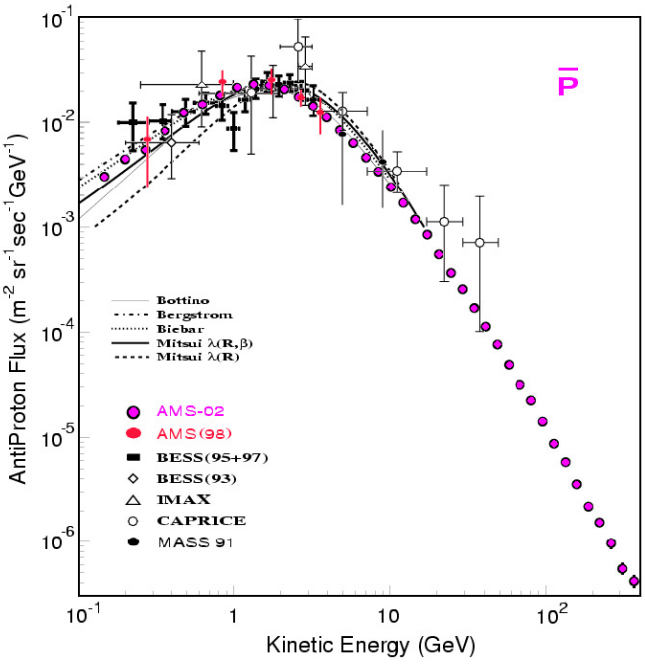

Figure 1.32: *The Anti-Proton Spectrum. The plot shows the measured data from previous experiments, including AMS01, and the data expected from AMS02 together with fits from some theoretical models.[AMS05]*

- **Positrons:** Like the anti-protons, the positrons in the cosmic rays are also generated via secondary processes. As the energy thresholds are much lower, due to the smaller mass, there are more processes, which come into play in the generation of positrons.

  The three most important processes are the e^+e^- pair production at a resting target electron by either an electron or a gamma, or the e^+e^- pair production in the Coulomb field of a nucleus.

  For the first process, $e^- + e^- \rightarrow e^- + e^- + e^- + e^+$, the energy threshold can be calculated using

$$\sqrt{s} = \left(m_e^2 + m_e^2 + 2E_e m_e\right)^{1/2} \geq 4m_e \qquad \Rightarrow \qquad E_e \geq 7m_e \quad (= 3.58\,MeV) \tag{1.20}$$

  where s is the centre of mass energy. Using the same approach, but replacing the incoming electron with a gamma, one can calculate the threshold for the process $\gamma + e^- \rightarrow e^- + e^+ + e^-$.

$$E_\gamma \geq 4m_e \quad (= 2.04\,MeV) \tag{1.21}$$

  For the third process, $\gamma + Nucleus \rightarrow e^+ + e^- + Nucleus$ the calculation is more complicated, as a virtual photon is exchanged between the electron and the nucleus.

  The spectrum of positrons in the primary cosmic rays, shown in Fig. 1.33 as the positron fraction, has been measured by many experiments. There are some deviations from the spectrum expected from pure secondary production within the Standard Model (solid line) at high energies. These deviations can be fitted by models using the MSSM[19] (Moskalenko & Strong), shown by the dashed lines.

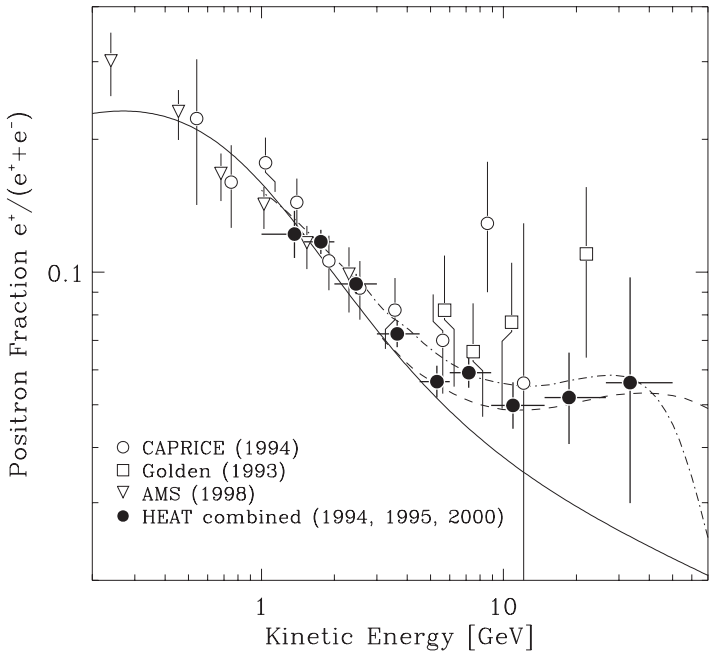

Figure 1.33: *The Positron Fraction as it has been measured by various experiments. The solid black line shows the spectrum expected from a production just via secondary processes within the Standard Model. The deviations from the SM at high energies are fitted using the MSSM (dashed lines). [Bea04]*

  The most important subdetectors for the measurement of the positron fraction are the TRD, the RICH and the ECAL, since they can distinguish between a proton and a positron and the silicon tracker, as it can separate between a positron and a electron due to the magnetic field. The total separation power of the combined subdetectors is expected to be 10^{-6}.

[19] **MSSM**: **M**inimal **S**USY extension of the **S**tandard **M**odel

The data of AMS02 will have much smaller error bars than previous data due to the much higher statistics and thus it will be possible to put much more stringent confinements on the MSSM.

- **Anti-Nuclei:** Up to now no anti-nuclei have been observed by any experiment. As it is virtually impossible to produce anti-nuclei in secondary processes, they would be a proof for anti-matter in the universe.

  Fig. 1.34 shows the limits on the helium/anti-helium ratio. These measurements were done with balloon experiments (black) and AMS01 (thin red). Also shown is the expected new limit, which AMS02 will set with 3 years of data.

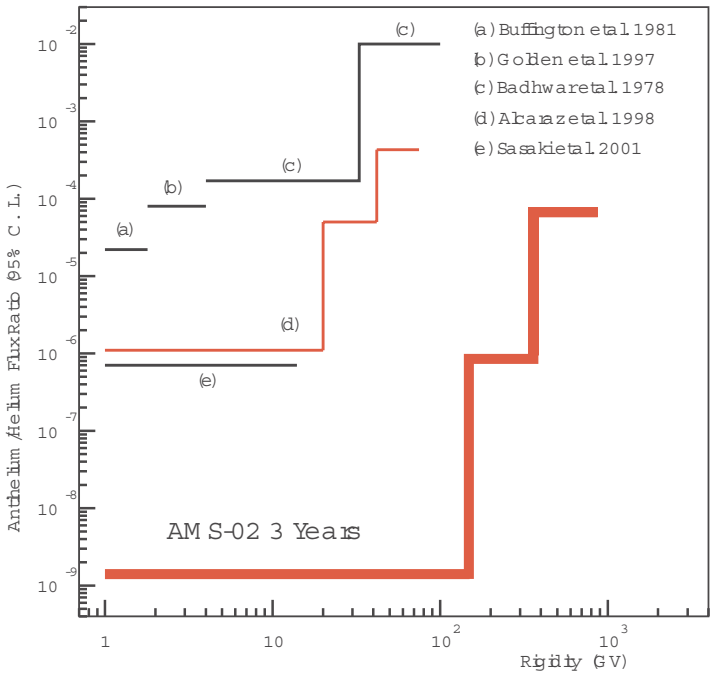

Figure 1.34: *Limits on the Helium/Anti-Helium ratio. The results from existing measurements (black , and thin red lines) are shown together with expected results from AMS02 after 3 years of data taking. [AMS05]*

1.3.4 Cosmic Rays - High Energy Gammas

The energy range of photons in the cosmic rays is almost as large as that of the charged particles. One can observe photons with energies from $10^{-7}\,eV$, used in radio and micro-wave astronomy, to $10^{15}\,eV$, for high energetic gammas.

One of the advantages of gammas is, that they are not influenced by the magnetic fields in the galaxies, thus they can be used to locate their sources, unlike charged particles. Also the attenuation length of high energetic gammas is rather large, allowing to make long distance measurements.

AMS02 can detect high energetic gammas in two ways. In the so-called low energetic mode the photon is converted into an e^+e^- pair in the top of AMS02. If the production angle between the two particles and the energy of both is measured, one can calculate the initial direction and the energy of the incoming photon. AMS02 is sensitive to photons with energies between $1\,GeV$ and $200\,GeV$ in this mode. In the high energy mode photons with energies from a few GeV up to $1\,TeV$ can be detected directly by the shower they create in the ECAL.

Acceleration Mechanisms

Like charged particles, high energetic gammas also originate from supernovae, SNRs, fast rotating objects like pulsars, neutron stars or AGNs. In these objects gammas can be produced by the mechanisms listed below.

- **Synchrotron Radiation:** A charged particle emits radiation (= photons), if it is being accelerated. This radiation is called synchrotron radiation in the case of a magnetic field causing the accelerating force. A detailed description of the synchrotron radiation can be found in [Jac98].

  The synchrotron radiation in the cosmic magnetic fields is caused by ultra relativistic particles, which means electrons, as they have a much higher β than heavier particles.

  The emitted power P for an electron of the energy E in the magnetic field B is

  $$P \propto E^2 \cdot B^2 \tag{1.22}$$

  It can be shown that the mean energy per photon is

  $$\langle \hbar\omega \rangle = \frac{8}{15\sqrt{3}} \hbar\omega_c \tag{1.23}$$

  with $\hbar\omega_c$ (in keV) $\approx 2.22 \cdot E^4/R$, where E is the energy of the electron in GeV and R the bending radius in m.

- **Bremsstrahlung:** The Bremsstrahlung is a phenomenon which is related to synchrotron radiation. Only in this case, the charged particle is not accelerated by a magnetic field, but by an electric field. Again, the charged particle can emit a photon in this process. The probability Φ for the emission of a photon is given by

  $$\Phi \propto \frac{z^2 Z^2 E}{m^2} \tag{1.24}$$

  where z, m and E are charge, mass and energy of the incoming particle and Z is the charge of the target particle.

  A more detailed description of the Bremsstrahlung can be found in [Jac98].

- **Inverse Compton scattering:** In the 1920s Compton discovered that photons scattered on free electrons can transfer a part of their energy to the electron. In the cosmos the inverse process produces high energetic gammas: An electron with very high energy scatters on a photon and transfers some of its energy to it. The photon, coming either from the black body radiation in the universe or from the star light, is then "blue shifted".

- π^0 **Decay:** A further possibility for the production of high energetic gammas is the decay of π^0s. The pions themselves are produced in the reaction

  $$p + Nucleus \rightarrow p' + Nucleus' + \pi^+ + \pi^- + \pi^0 \tag{1.25}$$

  The π^0 then decays into two gammas: $\pi^0 \rightarrow \gamma + \gamma$. If the pion is at rest the gammas are emitted anti-parallel, both with half the rest mass of the pion ($135\,MeV$) as energy. The emitted gammas can be boosted in the direction of the movement of the pion, but in most cases the energy of the pion is rather small, resulting in gamma energies around $70\,MeV$.

- **Matter - Anti-matter Annihilation:** If an anti-matter particle collides with its matter counterpart it will annihilate. Due to the conservation of the impulse, the annihilation of electrons and positrons produces two photons:

  $$e^+ + e^- \rightarrow \gamma + \gamma \tag{1.26}$$

The annihilation of protons and anti-protons generates gammas via the reactions:

$$p + \overline{p} \rightarrow \pi^+ + \pi^- + \pi^0 \qquad \Rightarrow \qquad \pi^0 \rightarrow \gamma + \gamma \tag{1.27}$$

- **Nuclear Transmutation:** During the fusion reactions in supernova explosions heavy elements are produced. Some of these nuclei are stable isotopes, some are radioactive. These radioactive isotopes can emit high energetic gammas. One well-known example is the decay of ^{60}Co with two characteristic lines at $1.17\,MeV$ and $1.33\,MeV$.

- **Gamma Ray Bursts:** Gamma Ray Bursts (GRBs) are short, non-thermal emissions of γ-rays. They were first discovered in the 1960s by the Vela satellites [Kle73]. GRBs release $10^{44} - 10^{46}\,J$ or more within a few seconds, which makes them the most luminous objects in the cosmos, with an estimated rate of one burst per million years and galaxy. The spectrum of the GRBs peaks around a few hundred keV, it is cut off below $10\,keV$ and it has a high energy tail (Photons with energies of up to $18\,GeV$ have been observed). It was shown that GRBs are located at cosmological distances, as red shifts of up to $z = 3.418$ have been observed.

  According to current understanding, the most probable source of GRBs are colliding neutron stars in a double neutron star system. Other models refer to black holes as possible sources of GRBs. A detailed description of GRBs and the so-called Fireball model can be found in [Pir99].

1.3.5 Dark Matter Search

One of the most interesting applications of AMS02 is the indirect search for Dark Matter in the universe. The first hints towards Dark Matter came up in 1933, when Fritz Zwicky measured the rotation curve of the Coma Cluster. He noted, that the galaxies in the Coma Cluster seemed to move much too fast to be held together by gravitational force of the visible mass. Since then the rotation curves of many galaxies and clusters have been measured. One example is shown in Fig. 1.35. From these curves it can be deduced, that $80 - 90\,\%$ of the matter is located in the galactic halo and is non-luminous.

The Dark Matter is also required by cosmological models of the early universe to describe the evolution of the structure of galaxies and clusters from the very small primordial density fluctuations, that can be estimated from the inhomogeneities of the microwave background radiation, which was measured by Wilkinson Microwave Anisotropy Probe (WMAP).

From these measurements it was calculated, that the total energy content in the universe is composed of $4\,\%$ baryons, $23\,\%$ Dark Matter and $73\,\%$ Dark Energy. This is in good agreement with the observed density of MACHOs[20] and other effects contributing to the baryonic matter.

The current understanding of the non-baryonic Dark Matter is, that it is made up from elementary particles. The three most discussed options are neutrinos, axions and Weakly Interacting Massive Particles (WIMP).

As the neutrino mass measurements (Tritium decay) and the WMAP results impose rather low limits on the neutrino mass, they can only contribute to a fraction in the so-called hot Dark Matter, probably in the order of $0.5\,\%$ of the total Dark Matter.

The axion, also called the Goldstone Boson of CP violation, is a very light pseudoscalar particle, that has been postulated due to the absence of CP violation in the strong interaction. According to this it should be a relic particle, that is not in thermal equilibrium. If the axion would make up most of the Dark Matter, it should have a mass of $\sim eV$. This would lead to a lifetime in the same order as the age of the universe. As axions should decay into two photons, it still should be possible to observe photons from this decay, due to the high number of axions existing. Up to now no signal has been detected. As other constraints (lifetime of stars,...) lower the limit on the mass of the axion even

[20] **MACHO**: **MA**ssive **C**ompact **H**alo **O**bject, dark star-like objects with masses in the range of $0.001 - 0.1$ solar masses.

further ($10^{-6} - 10^{-3}\,eV$), they could possibly contribute to the cold Dark Matter. At the moment they are a disfavoured candidate.

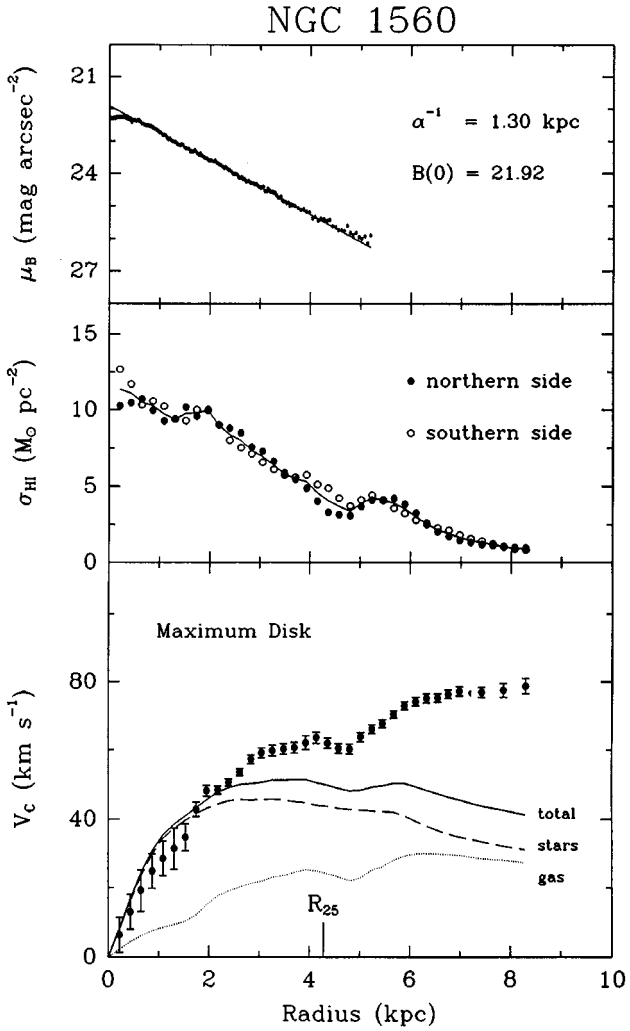

Figure 1.35: *The rotation curve of a spiral galaxy. The top panel shows the luminosity as a function of the radial distance, the middle panel the surface density of H_I. The expected rotation curves from the gas (dotted line), the stars (dashed line) and the total visible mass (solid line) are shown in the bottom panel. The measured values are given by the dots.[Bro92]*

The third candidate for the Dark Matter is the so-called WIMP, which is the most popular hypothesis at the moment. Several reasons lead to the assumption, that supersymmetric particles are the most likely contestants for WIMPs. The supersymmetry theory (SUSY) postulates, that there is a symmetry between fermions and bosons. Thus it postulates a supersymmetric boson (fermion) partner to each fermion (boson) from the Standard Model. The heavier SUSY particles decay into lighter ones and end up in the lightest SUSY particle (LSP). This LSP, also called neutralino, is stable, but it can annihilate in the collision with its anti-particle. This annihilation process would lead to a characteristic signal in the spectrum of positrons, anti-protons and gammas. In Fig. 1.33 the positron fraction is plotted. The standard model prediction (solid line) is not able to describe the measured data very well. Models including SUSY fit the data much better. With the high precision measurements of AMS02, especially with the high proton suppression ($\sim 10^5 - 10^6$) from the combined information of the TRD and the ECAL, it will be possible to improve the quality of the data points by orders of magnitude and to strengthen (or rule out) the contribution from SUSY.

AMS02 will also be able to measure any anomalous effects in the anti-proton spectrum caused by Dark Matter annihilation, but there the interpretation of the data will be much more challenging due to the high background from secondaries in the interesting energy range.

A more promising candidate for the indirect search for Dark Matter is the high energy gamma spectrum, in which a significant contribution to the signal is expected from the annihilation of WIMPs into mono-energetic quarks [Boe04]. AMS02 is well suited to complement the measurement data of EGRET ($0.1 - 30\,GeV$) with its sensitivity to gammas in the energy range of $1 - 200\,GeV$. Already the data from EGRET shows an excess in the spectrum of the diffuse galactic gammas, which is consistent with the annihilation spectrum of WIMPs, considering the mSUGRA[21] model. The excess is detectable in all directions, see Fig. 1.36, but increases towards areas where a higher density of Dark Matter is expected, namely the galactic centre and the ring of stars at $14\,kpc$ from the galactic centre. Assuming a halo profile as it is shown in Fig. 1.37(a) (deduced from the ring of stars at $14\,kpc$), one can fit the EGRET data for the longitudinal distribution of the gamma ray intensity, see Fig. 1.37(b), and the rotation curve of the Milkyway, see Fig. 1.37(c).

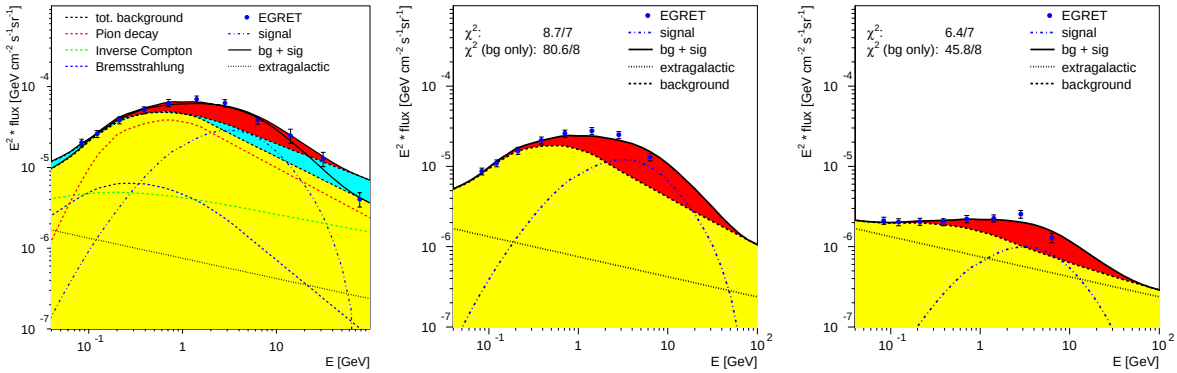

(a) Galactic Centre (b) Outer Disc (c) Galactic Pole

Figure 1.36: *The diffuse gamma ray spectra measured by EGRET for different directions. (a) was measured towards the galactic centre, (b) towards the outer disc and (c) towards the galactic pole. [Boe04]*

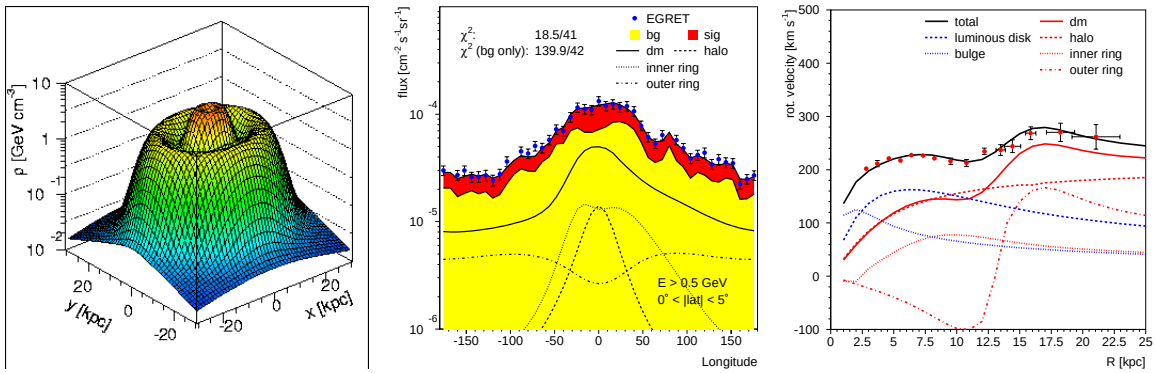

(a) 3D Halo Profile (b) γ Distribution (c) Rotation Curve

Figure 1.37: *(a) From the EGRET data this halo profile can be deduced, which has a concentric ring at $14\,kpc$ from the centre of the galaxy. (b) The longitudinal distribution of the gamma ray intensity can be fitted well using the halo profile from (a). This profile explains the change of slope in the rotation curve at $10\,kpc$ (c). [Boe04]*

[21] **mSUGRA**: **m**inimal supersymmetric model with **SU**per**GRA**vity inspired symmetry breaking

1.3.6 Transition Radiation

The idea of the Transition Radiation (TR) was first discussed by Ginzburg and Frank in 1945 [Gin45]. They showed that a uniformly moving electron will emit radiation when crossing the border from one medium (vacuum) into another one (ideal conductor). In 1957 Garibian predicted, that for ultra-relativistic charged particles the TR depends on the Lorentz factor γ [Gar57]. Due to this feature the TR became a very helpful tool for the lepton identification in HEP experiments. Among today's experiments using Transition Radiation Detectors (TRDs) are ATLAS, Hermes and AMS02.

In the following a short introduction into the TR and its characteristics will be given. For more details please refer to [Gin45, Gar57, Ego00, Wak04].

It was shown that for a single interface the spectral dependence of the TR intensity is:

$$\frac{d^2W}{d\omega d\theta} = \frac{2\alpha\hbar\theta^3}{\pi}\left(\frac{1}{1/\gamma^2+\theta^2+\omega_1^2/\omega^2} - \frac{1}{1/\gamma^2+\theta^2+\omega_2^2/\omega^2}\right) \tag{1.28}$$

and the total intensity of the radiation emitted from one interface is:

$$W = \frac{\alpha\hbar}{\pi}\frac{(\omega_1-\omega_2)^2}{\omega_1+\omega_2}\gamma \tag{1.29}$$

with the plasma frequencies ω_1, ω_2 of the two media, the emission angle θ of the photon with respect to the particle track and the fine structure constant $\alpha = e^2/\hbar c$.

From these equations one can derive the most important features of the transition radiation:

- The energy loss of a particle crossing a boundary between two media is proportional to the Lorentz factor of the particle. The linear dependency on γ allows to use the TR to discriminate between particles of the same charge but different mass. This is used in AMS02 to separate between positrons and protons.
- Most of the radiation is emitted in a cone with an opening angle of $1/\gamma$. As this opening angle is very small for electrons and positrons, the TRD of AMS02 can be used for a coarse tracking of the incoming charged particles.
- Due to the electromagnetic properties of the TR, the effect is symmetric for the crossing of the media: There is no difference between crossing from media 1 into medium 2 or from medium 2 into media 1. Both times the probability to radiate a photon is in the order of $\alpha = 1/137$. Combining these two effects, one can enhance the TR by using multiple interfaces in the radiator material. For AMS02 this is done by using a fleece material.
- The spectrum of the TR, shown in Fig. 1.38, has its maximum in the X-ray region for highly relativistic particles. In order to be able to detect these X-rays AMS02 uses proportional wire chambers flushed with $XeCO_2$, using the high Z of the Xenon to increase the probability to measure the photons.

For a stack of foils, Eqn. 1.28 becomes more complicated, as one has to take into account the coherent emission from the multiple layers and in addition also the re-absorption in the radiator material due to its finite thickness.

$$\frac{d^2W_N}{d\theta d\omega} = \frac{d^2W}{d\theta d\omega} 4\sin^2\left(\frac{l_1}{z_1}\right)\frac{\sin^2\left[N\left(l_1/z_1+l_2/z_2\right)\right]}{\sin^2\left(l_1/z_1+l_2/z_2\right)}\cdot\left|\frac{1-C^N}{1-C}\right|^2 \tag{1.30}$$

with the absorption coefficient C and the formation zone z:

$$C = \exp\left(\frac{il_1}{z_1}+\frac{il_2}{z_2}-l_1\sigma_1-l_2\sigma_2\right) \qquad \text{and} \qquad z_{1,2} = \frac{4c}{\omega}\left(\frac{1}{\gamma^2}+\theta^2+\frac{\omega_{1,2}}{\omega}\right)^{-1} \tag{1.31}$$

where l_1 is the foil thickness, l_2 the spacing and N the number of foils. $\sigma_{1,2}$ are the absorption cross-sections of the media. As these cross-sections are a function of Z^5, one has to use low Z material for the radiator. For AMS02 the radiator fleece is made from polypropylene.

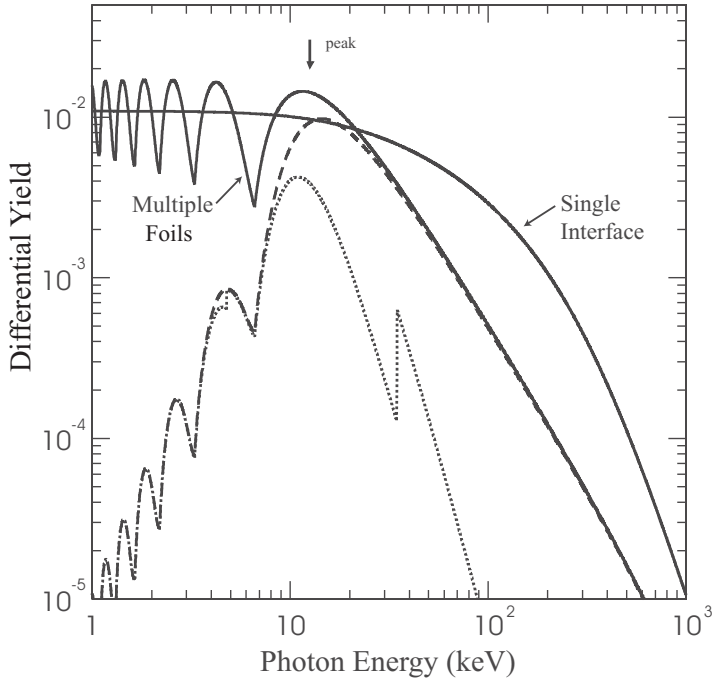

Figure 1.38: *The differential yield of the Transition Radiation ($dW/d\omega$). The solid black lines indicate the single and multi-foil TR spectra without corrections. The dashed line shows the effects of the self-absorption, and the dotted line shows the observed spectrum if* 1 *cm of Xenon is used in the detector. The data is plotted for* $\gamma = 2 \cdot 10^4$. *[Wak04]*

From this equation one can derive more parameters of the transition radiation, which are a function of the foil thickness and spacing.

- If $l_1 \ll z_1$ the $\sin^2$ term goes to zero, suppressing the transition radiation. On the other side, if both l_1 and l_2 are larger than z_1 and z_2 the yield will approach $2N$ times the one of the single foil.
- The multi-foil spectrum peaks around the characteristic energy $\omega_{peak} \approx \omega_1^2 l_1 / 2\pi c$.
- The transition radiation yield does not increase indefinitely with γ. A saturation effect limits the yield as the Lorentz factor rises, since the formation zones z_1 and z_2 depend strongly on γ and will eventually become larger than l_1 and l_2. This leads to a plateau in the TR emission. The calculated saturation value for the Lorentz factor is $\gamma_{sat} \approx 0.6\omega_1 \sqrt{l_1 l_2}/c$.

Chapter 2

Space-Grade Electronics for the AMS02 Detector

The location of AMS02 on-board the ISS places stringent requirements on the detector and of course also on its electronics, shown in Fig. 2.1. This chapter will give an introduction into problems of electronics, when they are used in such hostile environments like space. A detailed overview of the electronics of the AMS02 TRD will be given. For these electronics the responsibility lies with the Institut für Experimentelle Kernphysik at the University of Karlsruhe (TH). Following these remarks, the design and production process will be described as well as the testing and verification.

The description of the electronics and related issues will be quite detailed, as the system design, programming of the firmware of two slow-control cards and the testing of the electronics according to space-qualification rules was a major focus point of this thesis.

All abbreviations will be explained, as far as possible, on their first occurrence. For a complete list of the abbreviations used in this thesis please refer to the glossary on page 203.

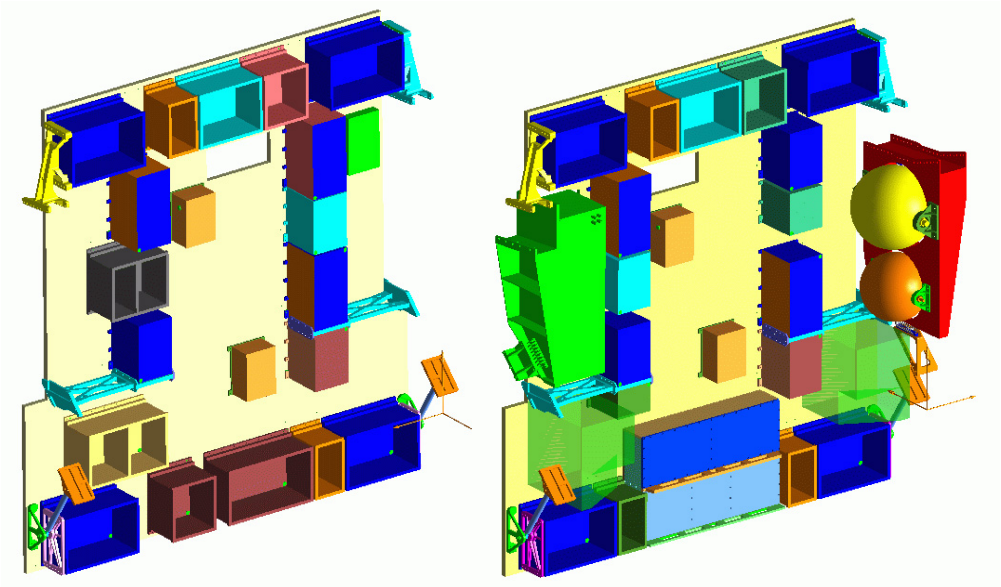

(a) Wake Radiator (b) Ram Radiator

Figure 2.1: *The wake (a) and ram (b) radiators of the AMS02 electronics. (wake and ram refer to the ISS direction of travel) [AMS05]*

2.1 Overall system design

With the experience of six decades of spacecraft engineering and operation, NASA has set up a system to ensure the safety of the involved astronauts and to maximise the chances for a successful mission.

This system consists of many different parts, e.g. there are large databases containing information on components that can be used for spacecrafts, but there are also review boards looking into the project along its way at various critical stages to make sure that all NASA regulations are fulfilled.

For the electronics production AMS02 relies heavily on the existing know-how of NASA and space technology companies. But in some areas AMS02 is also using new components, that were not used before for space applications. Each of these new parts was thoroughly tested by the collaboration before being allowed to be employed in the design.

As it is extremely difficult and dangerous to do maintenance on any spacecraft while it is on orbit, the design of such a spacecraft has to be done thoroughly and proven reliable before launch. Some of the tests involved in the verification of the design will be described in detail in section 2.5, as they also apply to the electronics of AMS02.

For a system such as AMS02, where the costs of training astronauts for maintenance would be very high due to the immense complexity of the detector, this option is only chosen for vital systems like the life support equipment. Due to this consideration, the AMS02 experiment was designed as a zero maintenance system. With the exception of the ACOP[(1)], there will be no astronaut intervention once AMS02 is mounted on its designated position on the S3 truss.

So the key point in the design of AMS02 is to protect all components where necessary and to use redundancy for all safety and mission success critical items. A good example for this is the main DAQ computer of AMS02. It is fourfold redundant and each of the four computers is protected against over-current, over-voltage and over-temperature.

2.2 AMS02 Electronics

In this section an overview of the electronics of the AMS02 experiment will be given. First the architecture of the DAQ chain will be discussed, followed by a description of the slow-control and monitoring system.

The general overview of the electronics of the AMS02 experiment is shown in Fig. 2.2 together with a scheme of the interfaces of AMS02 to the International Space Station.

For both the data and the slow control chain AMS02 uses tree-like architectures with a clear master and slave structure. Schematic drawings of both trees are shown in Fig. 2.3 and Fig. 2.4.

[(1)] **ACOP**: **A**MS **C**rew **O**perations **P**ost. The ACOP is a computer inside the ISS, which stores all data coming from the experiments and acts as a back-up slow-control and monitoring station.

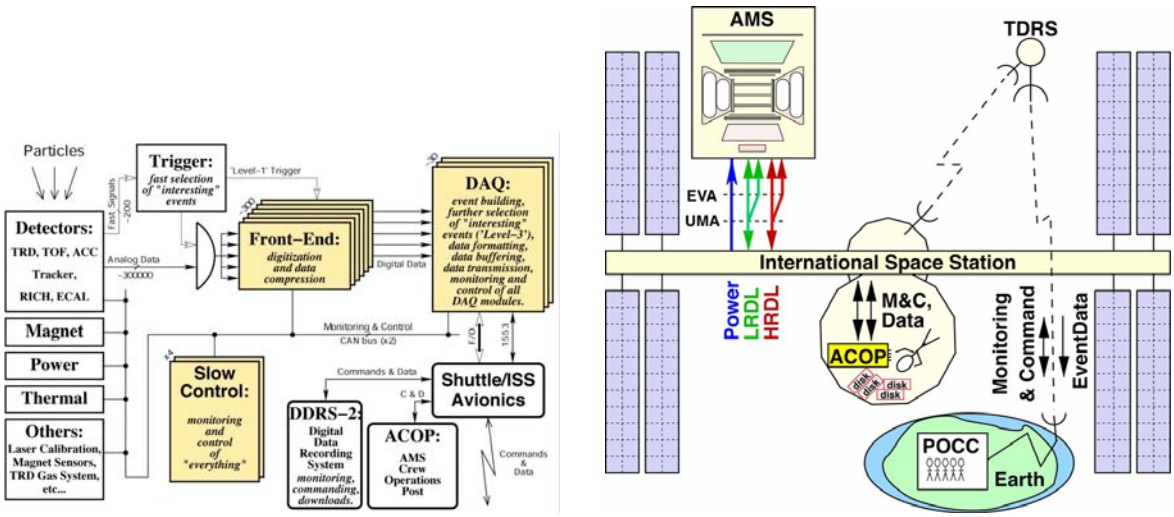

(a) Electronics Overview (b) Connections to ISS

Figure 2.2: *(a) Overview of the AMS02 electronics and their connections to the ISS and the Space Shuttle. (b) The electrical interfaces of AMS02 to the ISS. (TDRS: Tracking and Data Relay Satellite, POCC: Payload Operations and Control Centre, M&C: Monitoring and Control)[AMS05]*

2.2.1 DAQ systems

The DAQ chain of the AMS02 experiment, shown in Fig. 2.3, is well adapted to the specific requirements imposed by the operation in space: e.g. all critical parts are at least twofold redundant.

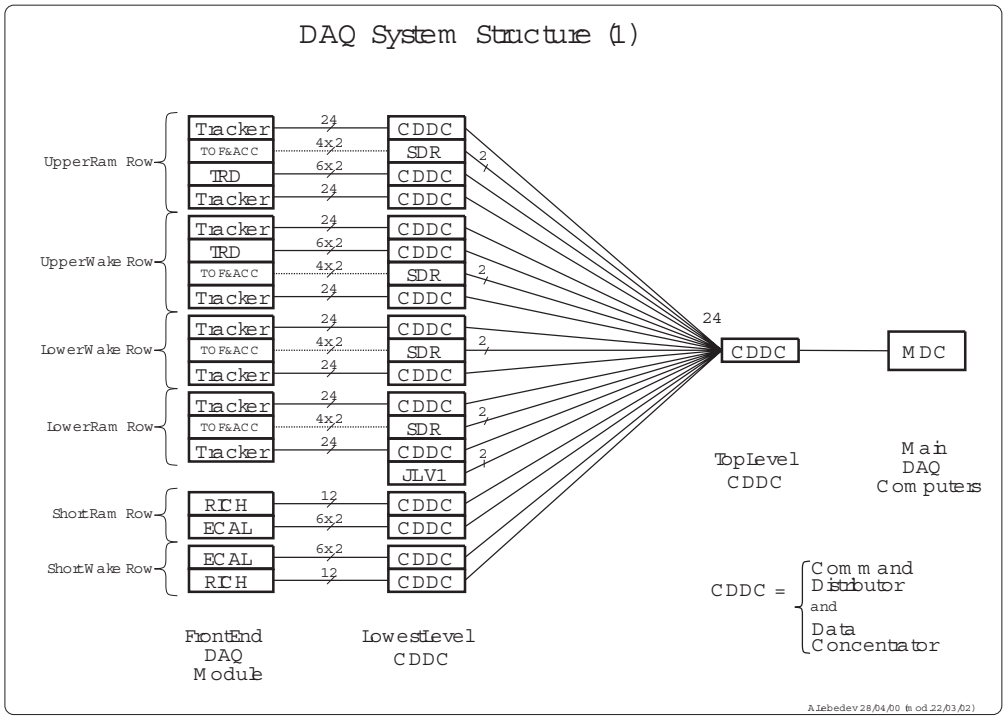

Figure 2.3: *The DAQ structure of the AMS02 experiment. This picture shows the tree-like structure of the data flow in AMS02. The subdetector crates are grouped according to their position on the radiators. The numbers close to the connecting lines indicate the number of data reduction cores (first number) and their redundancy (second number), if existing. For the abbreviations please refer to the glossary at the end of this thesis. [Drawing by Alexei Lebedev.]*

As the raw data rate of the AMS02 Detector is about $7000\,Mbit/s$ for the expected $2\,kHz$ trigger rate and the averaged downlink data rate from the ISS to the ground stations is only $2\,Mbit/s$, it is clear that the data has to be compressed as early as possible in the DAQ process. Even then it is not possible to transfer all data in real time to the ground stations.

The first data compression and event building is done inside the xDR boards, where x stands for the subdetector and DR for data reduction.

In the next stage of the read out chain, the JINF, the data from all xDRs in one crate is collected and combined according to the event number. After this, the JINJ collects the data from all JINFs, combines it and passes it on to the JMDC, the main DAQ computer. At all stages of the data handling, a CRC[(2)] is added to the data to ensure that no data is compromised due to a bad communication link.

From the main DAQ computer the data is then transferred to the ISS data bus. One system connected to this data bus is the ACOP, the AMS Crew Operations Post. This computer is used mainly as data storage system. It stores all data coming from the AMS02 on hard discs, which are taken down to Earth on regular intervals.

Only a small part of the events can be transferred down to Earth in, more or less, real-time. These events are then used to check the performance of the detector and in case of problems to change settings via the slow-control system.

2.2.2 Slow-Control & Monitoring

The slow-control and monitoring system of AMS02, depicted in Fig. 2.4, has to be highly reliable and partly autonomous, as the transfer rate for commands and monitoring data guaranteed by NASA is only $1\,kbit/s$ upstream and $10\,kbit/s$ downstream.

Like the scientific data all slow-control commands and monitoring data pass through the JMDC. The JMDC collects all monitoring data, like temperatures and voltages, from the slow-control cards. Some of the most critical data are sent in real-time to the control centres on Earth.

Together with the scientific data, all slow-control information is recorded and stored in the ACOP. For some of the subdetectors, this information, like temperature and gas pressure, is extremely important for the correct analysis of the scientific data.

As the data rate for commands sent to the experiment is extremely low, the JMDC has to react autonomously for some re-occurring events. In most cases this is done using look-up tables. A second option to minimise the bandwidth used for commands is to use high-level commands, like “prepare a new gas mixture for the TRD” and “insert it into the sensitive volume”, which are then translated by a programme in the JMDC into a complex scheme of single commands, like “open the Xenon valve 2 for 10 seconds”.

The slow-control system of AMS02 uses various different types of buses. The 3 most important ones are the CAN bus, the LeCroy bus and the AMSwire. The CAN bus is a communication system developed for commercial applications. It is widely used in the automotive industry. The LeCroy bus is a two wire serial bus, developed by LeCroy for the control of the MHV100 high voltage generator ASIC, which is used in the high voltage generator of the TRD. This bus was adopted by AMS02 for slow-control purposes in the TRD and Tracker crates, as well as for the high voltage systems of the ECAL and the RICH. The AMSwire, based on the commercial SpaceWire, is a high speed data link, that was designed for the transfer of the scientific data, but due to weight reduction measures is now also used in the slow-control system.

[(2)] **CRC**: **C**yclic **R**edundancy **C**heck

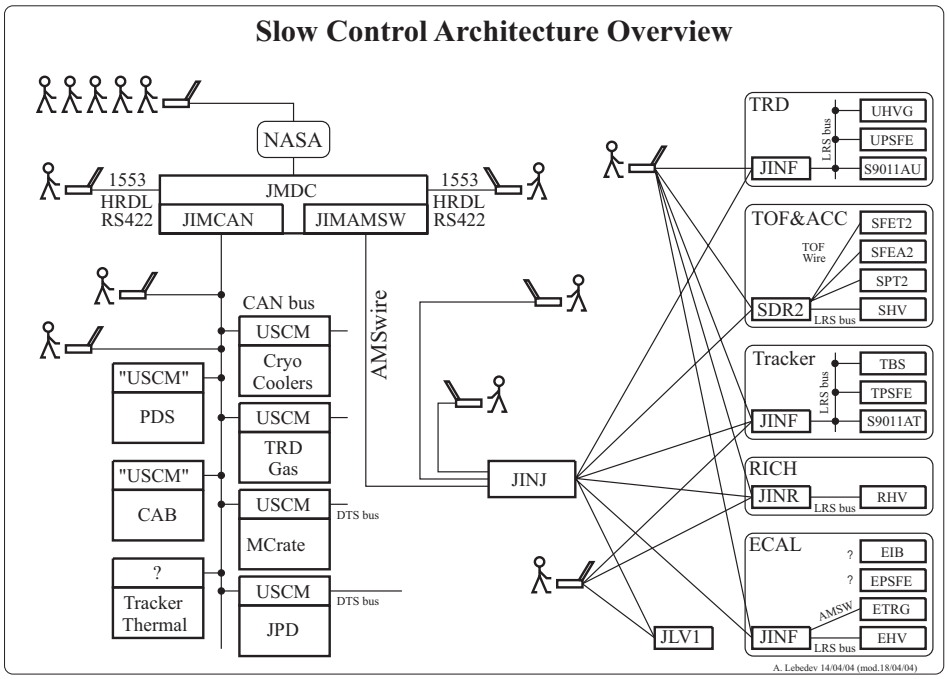

Figure 2.4: *The slow-control structure of the AMS02 experiment. This picture shows the various subsystems of the slow-control system: In the top-left corner is the ground control and the JMDC. Beneath the JMDC is a group of subsystems that is connected via the CAN bus. These subsystems are mainly thermal, magnet and gas systems. The subdetectors slow-control systems are shown on the right side. They are connected via AMSwire. Inside the crates various buses are used, but mainly the so-called LeCroy bus. The matchstick men indicate the various points at which the user can connect to the system to control the respective functions. With the exception of the ground control (top left) and the ACOP (left of the JMDC) these points are only accessible before and during the detector integration.[Drawing by Alexei Lebedev.]*

2.2.3 Trigger

A schematic overview of the trigger system that drives the physics data flow is shown in Fig. 2.5. The purpose of this system is to recognise, when a particle has passed through the detector, and to start the read out sequence of the complete system.

For charged particles a trigger signal is given, when coincident fast signals from both TOF planes and a clean track through the complete detector (signal from ECAL and no signal from ACC) are observed.

For gamma rays there are two possibilities to generate a trigger. One possibility is a pair production in the TRD. These particles are then recognised by the standard trigger procedure. For non-converted gammas above $1\,GeV$ there is a second possibility to cause a trigger signal. This is done by a stand-alone pattern recognition in the ECAL.

A LV1 signal is sent to the various subdetectors $\sim 1\,\mu s$ after the particle has passed through the detector. This is in good agreement with the signals of the other detectors, as the peaking time of their amplifiers is in the range of $2.4\,\mu s$.

The expected trigger rate, the estimations are based on the measurements of AMS01, varies from 200 to $2000\,Hz$ depending on the geomagnetic latitude. The design of the electronics allows for rates twice as high as this without any degradation on the physics data.

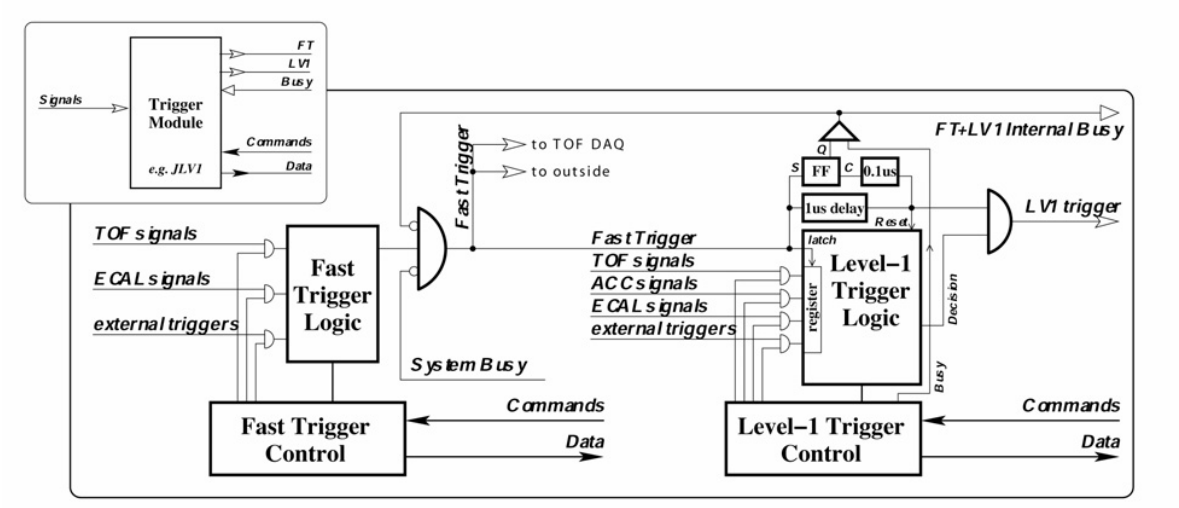

Figure 2.5: *The Fast (FT) and Level-1 (LV1) Trigger scheme of the AMS02 experiment. The inputs from the TOF, the ECAL and external lines as well as the interfaces to the other detectors (LV1 out & Busy out) are shown.[Drawing by Alexei Lebedev.]*

2.3 Electronics for the TRD

As the electronics of the TRD, especially the programming of the slow-control cards, was one of the main focus points of this thesis, they will be described in detail in the following sections, together with the development of the firmware and the testing of the various electronic cards.

The design and production of the electronics for the TRD followed the general scheme of the AMS collaboration, using a four step process (EM, QM1, QM2 & FM/FS)[3], which is explained in detail in section *Production and Qualification* on page 75.

To optimise the electronics of the TRD subdetector with regard to noise, power dissipation and weight, they are segmented into 3 parts, as shown in Fig. 2.6.

The part closest to the detector is the front-end board. The U-Front-End board (UFE) contains the front-end amplifier ASICs and some control circuitry. The signals from the detector are already digitised on the UFE. The U-crate holds the data reduction boards, the low voltage regulators and the high voltage generators. The power-supply electronics are housed in the U power distribution box (UPD).

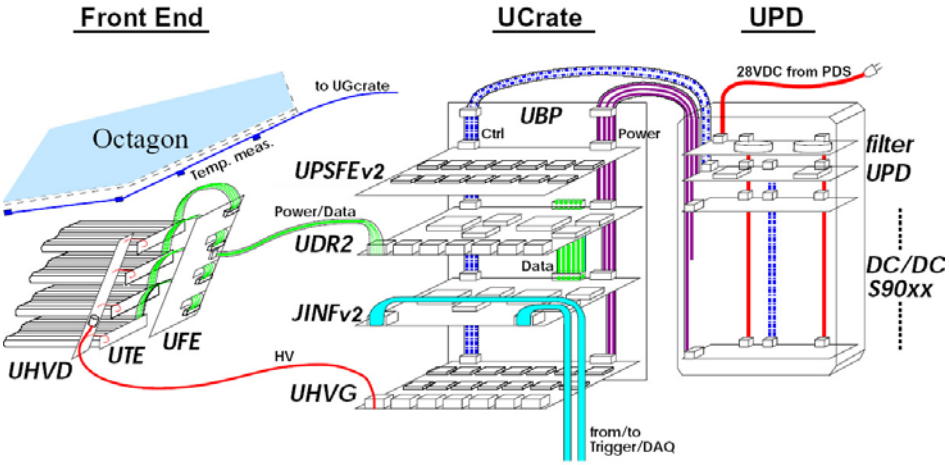

Figure 2.6: *This scheme shows a general overview of the read out electronics of the TRD, which is segmented into three parts. A more detailed view of the data connections can be found in Fig. 2.7, of the power connections in Fig. 2.8. Taken from [AMS05], updated.*

Convective cooling is not available for the electronic systems of AMS02 in space as there is no air. Thus all cooling has to be done using thermal conductivity to transport the heat and radiators to dissipate it into space. Due to this, all electronic crates are placed directly on the main radiators.

Fig. 2.7 shows the connections of the data lines in the electronics of the TRD. Both the scientific data lines and the slow-control lines are shown. The number given beside each line specifies the number of redundant lines for that connection.

A schematic picture of the power connections inside the TRD electronics is shown in Fig. 2.8. Again the number of redundant lines used for each connection is given beside each connection.

In the following sections the various boards housed in the U-crate and the UPD will be described: First the boards for the scientific data handling, then the slow-control cards and finally the power systems. See Tab. 2.1 for a complete list of logic boards of the TRD electronics.

[3] **EM**: **E**ngineering **M**odule
QM1: **Q**ualification **M**odule version **1**
QM2: **Q**ualification **M**odule version **2**
FM/FS: **F**light **M**odule, **F**light **S**pare

name	functionality
UBP	backplane of the crate
UDR	data reduction card, reads 7 front-end hybrids
UFE	front-end hybrid
JINF	collects data from the UDRs and interfaces to higher level DAQ chain
UPSFE	power supply card for the front-end hybrids
UHVG	high voltage generator for the strawtubes
USCM	slow-control card (removed)
S9011AU	controller card of the U Power Distribution box

Table 2.1: *A list of the boards in the U-Crate and the UPD with name and functionality of each board.*

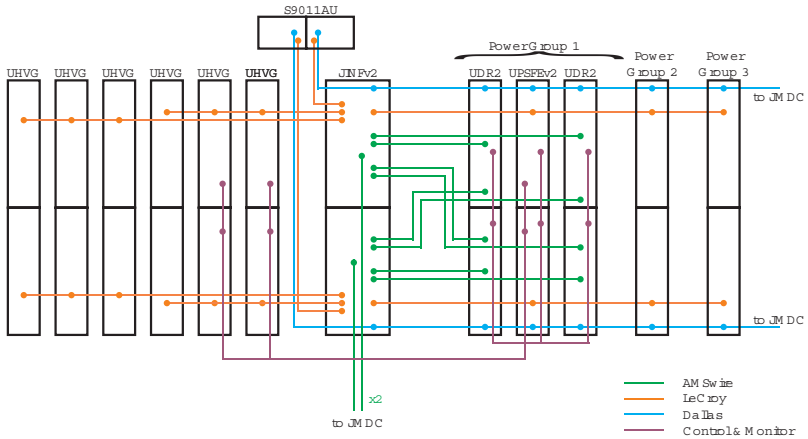

Figure 2.7: *The data connections inside the TRD. The scientific data, slow-control and control & monitor lines are shown at the example of the Power Group 1. For maximum safety the communication with all cards is at least twofold redundant. The same is true for the control & monitor lines.*

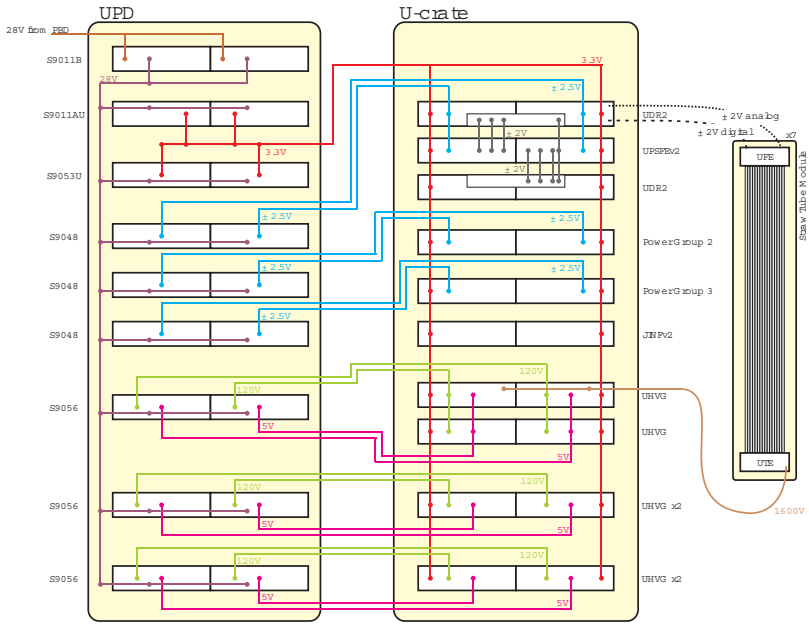

Figure 2.8: *The power connections inside the TRD. Both the low voltage and the high voltage lines are shown, using Power Group 1 as an example. All power lines between the UPD and the U-crate are twofold redundant. The connections from the U-crate to the modules are single lines.*

2.3.1 The TRD electronics crate - U-Crate

The U-Crate houses the electronics for the read out of the TRD and the high voltage supplies for the strawtube modules. A picture of the QM1 version of the U-Crate is shown in Fig. 2.9.

Due to the weight reductions on the electronics of AMS02 the number of boards inside the U-Crate was reduced from 21 (see Fig. 2.10(a)) to 16. Fig. 2.10(b) shows the new layout used. Clearly visible are the 3 power groups into which the U-Crate is segmented in both versions.

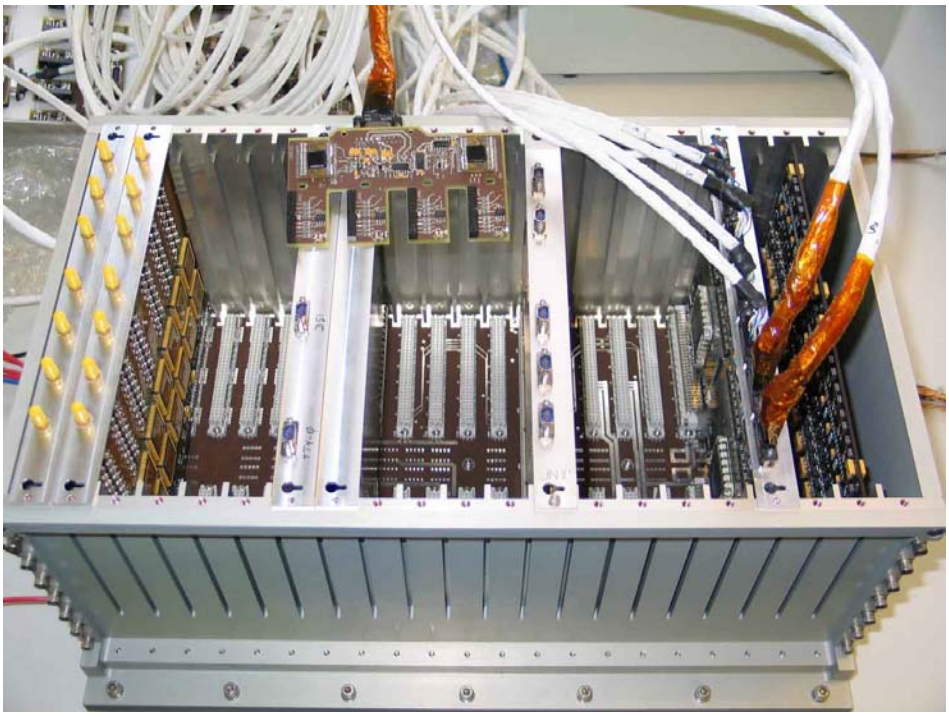

Figure 2.9: *The U-Crate QM1 version. Due to the weight reductions, the flight version of the crate will be smaller (5 cards were removed). The following cards are inserted into the crate (from left to right): 2 UHVGs, 2 USCMs, 1 JINF, 1 UDR and 1 UPSFE. The cables from the UD2 go to the UFEs, of which one is lying on top of the crate.*

2.3.2 U-Backplane - UBP & UBPv2

The UBP acts as an electrical interconnection between the various cards in the U-crate. The UBP has no active components, only some resistors for LVDS line terminations.

All electronic cards in the crates of AMS02 have the mechanical dimensions of 6U VME[(4)] cards. The pin-out on the backplane connectors is optimised for each card in AMS02 and is not compatible with the VME bus specifications.

Figs. 2.10(a) and 2.10(b) show the arrangement of the electronic cards inside the U-crate before and after the weight reduction. The basic unit, the so-called power group, is still there, but the number of cards per power group was reduced. Also the USCMs were removed.

A more detailed description of the consequences of the weight reduction will be given in the corresponding section for each card affected.

[(4)] **VME**: **V**ersa **M**odule **E**uropa. An industrial standard first defined in 1981 by Motorola, Phillips, Thompson, and Mostek. It is also known as IEEE 1014-1987.

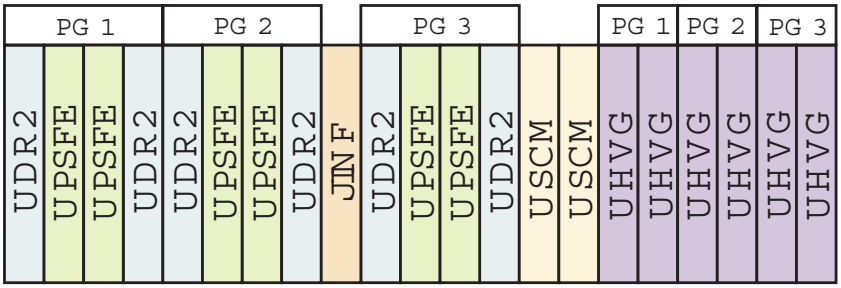

(a) QM1 Crate

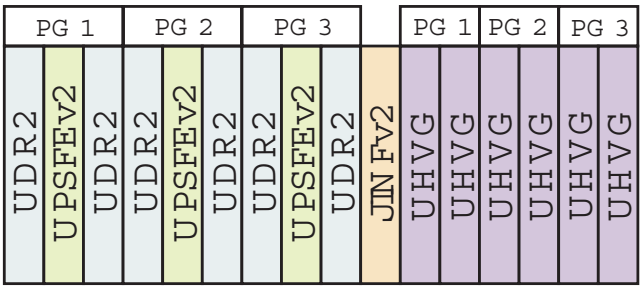

(b) QM2 Crate

Figure 2.10: *(a) The UBP QM1 version. It was designed for 21 cards, but was too heavy. (b) After the weight reduction this new scheme of arranging the remaining 16 cards is used in the U-Crate from the QM2-version onwards. In both versions of the UBP the cards are grouped in 3 so-called power groups (PG).*

2.3.3 J-Interface - JINF

The JINF, see Fig. 2.11, is a card common to many DAQ crates. It is the highest level of the DAQ chain inside the U-crate, acting as a two-way interface between the JMDC and the UDR2s. It receives commands via AMSwire from the main computer, passes them on and assembles the replies.

In the first iteration of the DAQ design the JINF was only meant to handle scientific data. After a decision made by the collaboration to save weight on the electronics, the JINF was modified, not only to handle the scientific data and the commands with regards to this, but also to act as an interface for the slow-control system.

The JINF consists of two Command Distributor & Data Concentrators (CDDC), of which one is kept as cold redundant spare, and of the line drivers, which are connected either to lines inside the crate or via cables to the JMDC. Due to the high number of lines going out to the other cards in the crate, the JINF uses a 512 pin cPCI[5] type connector to interface to the backplane.

A schematic drawing of a CDDC is shown in Fig. 2.12. It consists of an Anti-Fuse FPGA[6], a DSP[7] together with its 512 kB FlashROM and a 512 kB SRAM chip. The FPGA features a memory controller and handles the interfaces to the AMSwire links. The DSP is used for command interpreting and event building. The FlashROM contains the programmes for the DSP in threefold redundancy.

One of the most important functions of the JINF is the handling of level 1 trigger and busy signals. It receives a level 1 trigger from the trigger crate and passes it on to the UDR2s. The UDR2s themselves emit a busy signal for the time they need to read out the front-end ASICs, which is send back to the trigger crate by the JINF. Both trigger and busy signals can be masked in the JINF for single UDR2s in case of problems with one of the boards.

---

[5] **cPCI**: **c**ompact **P**eripheral **C**omponent **I**nterface, a standard for connections often used in industrial computers

[6] **FPGA**: **F**ield **P**rogrammable **G**ate **A**rray

[7] **DSP**: **D**igital **S**ignal **P**rocessor

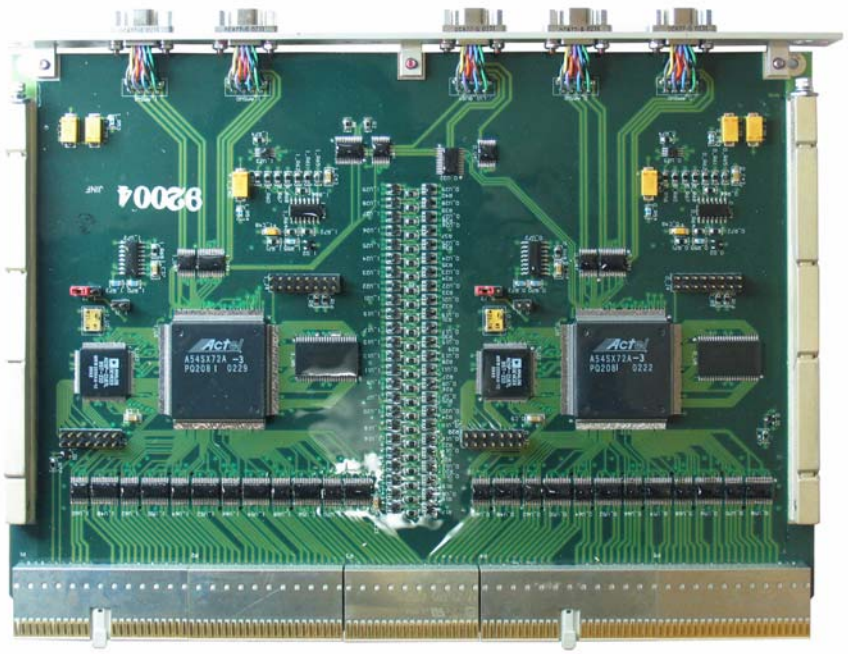

Figure 2.11: *JINF: J Interface. The JINF collects the data from the UDRs and combines it according to the event number. Since the weight reduction, the JINF is also the slow-control master card in the U-Crate. One can clearly distinguish the two redundant CDDCs.*

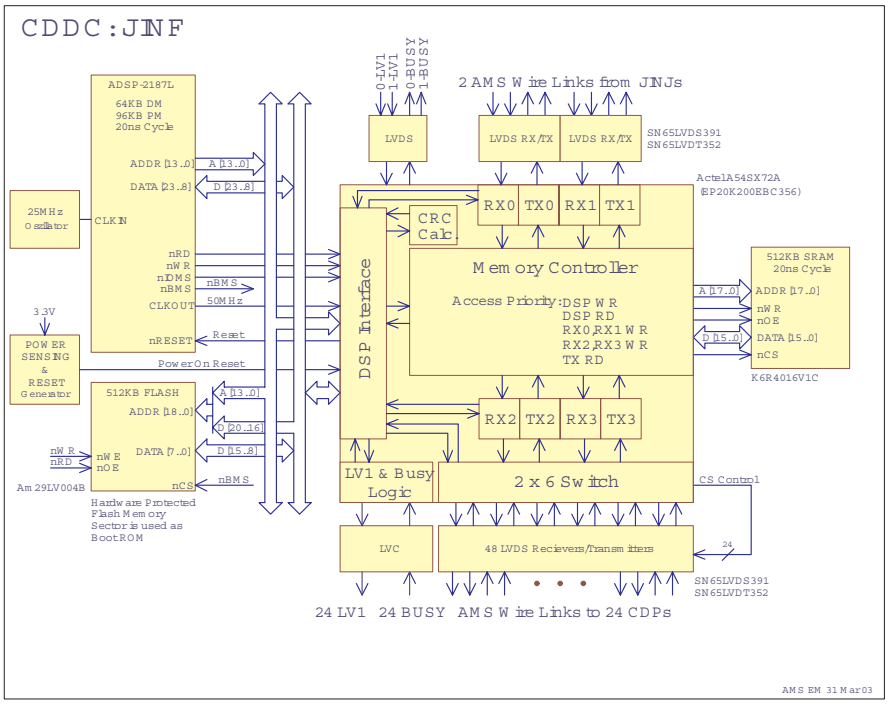

Figure 2.12: *CDDC: Command Distrubutor & Data Concentrator. The 4 main parts of the CDDC are shown in this drawing: the FPGA, the DSP with its FlashROM and the SRAM chip. [Drawing by Vladimir Koutsenko.]*

The main function of the JINF is to collect the data from all data reduction cards in the crate via the AMSwire lines on the backplane, to combine the data from the same event, to calculate and attach

a CRC[8] and keep it in the on-board memory until the JMDC asks for the data.

The slow control functionality of the JINF is handled by the DSP. It receives the commands via AMSwire, converts them to LeCroy and sends them via one of its serial ports to a UHVG, a UPSFE or a S9011AU. The single serial port of the DSP is multiplexed to the 8 LeCroy lines using external ICs, which are controlled by the FPGA. Both LeCroy clock and data signals are converted from LVTTL[9] levels to LVDS[10] before they enter the backplane.

2.3.4 U-Data-Reduction - UDR2

The UDR, see Fig. 2.13, is the data reduction card of the TRD. The UDRs control the front-end cards of the TRD, perform an online data reduction and store the event data in a FIFO till the JINF collects it.

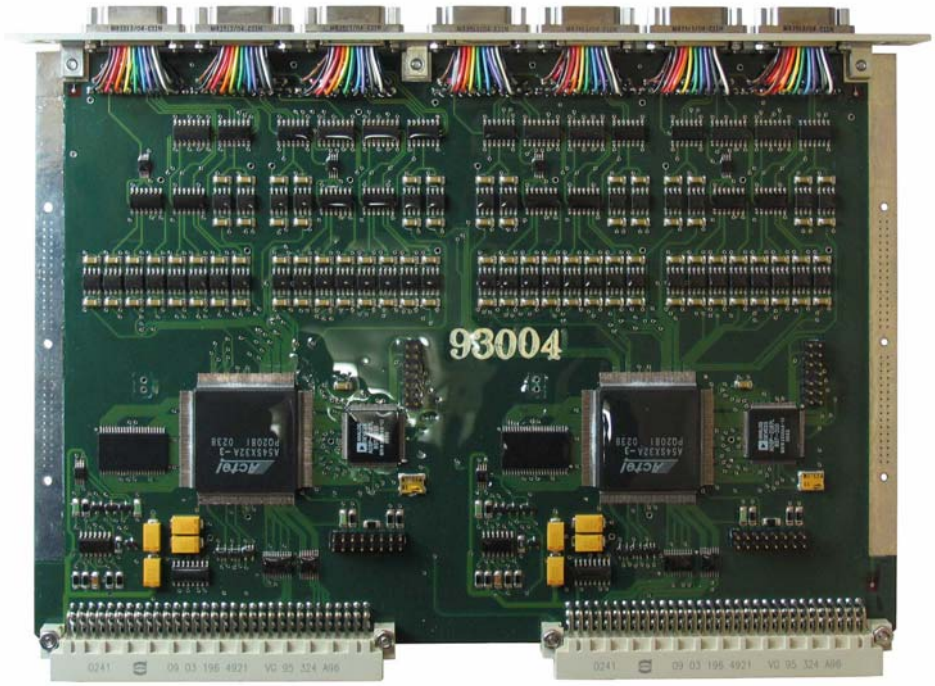

Figure 2.13: *UDR2: U Data Reduction, version 2. The different parts of the UDR2 can be clearly distinguished: The two redundant CDPs and the detector specific part, which is located close to the connectors for the front-ends.*

Each UDR is connected to 7 UFEs. In both DAQ crates of the TRD there are 6 UDRs. With 64 channels per UFE, this amounts to a total of 5376 read out channels. As this would be already more than enough data to saturate the data downlink of the AMS experiment, the data has to be reduced online in the UDRs. This is done using an algorithm, that subtracts previously acquired pedestals from the data and then compares the data content to a threshold based on the noise of the pedestals. This is done separately for each channel.

Each UDR consists of 2 Common Digital Parts (CDP) and a set of detector specific components. Like the CDDC the CDP is made of an Anti-Fuse FPGA, a DSP with its FlashROM and a 512kB SRAM, see Fig. 2.14. The main difference between the CDP and the CDDC is, that the FPGA of the CDP contains detector specific code: the sequencer. This sequencer controls the ADC and the ASIC

[8] **CRC**: **C**yclic **R**edundancy **C**heck

[9] **LVTTL**: **L**ow **V**oltage **T**ransistor to **T**ransistor **L**ogic

[10] **LVDS**: **L**ow **V**oltage **D**ifferential **S**ignal

on the front-end. It also steers the Digital to Analog Converters (DAC), that sets the voltage for the test pulse, if the front-end ASIC is run in calibration mode.

As already hinted above, the UDR has two read out modes. The standard read out mode is used during data taking. It collects data from all 7 UFEs connected and stores it in a 4 event deep FIFO. The second mode is the calibration mode. It allows to measure the optimal peaking time of the ASIC and its linearity. The first is accomplished by varying the delay between the injection of the test pulse and the "sample & hold" signal from 0 to 6.4 μs with a precision of 100 ns. In an offline analysis the pulse height measured is then compared for the various settings and the optimal timing can be used for the next set of measurements. The linearity of the read out is measured by setting the peaking time to its optimum and varying the height of the test pulse from minimum to saturation level using the DACs on the UDR.

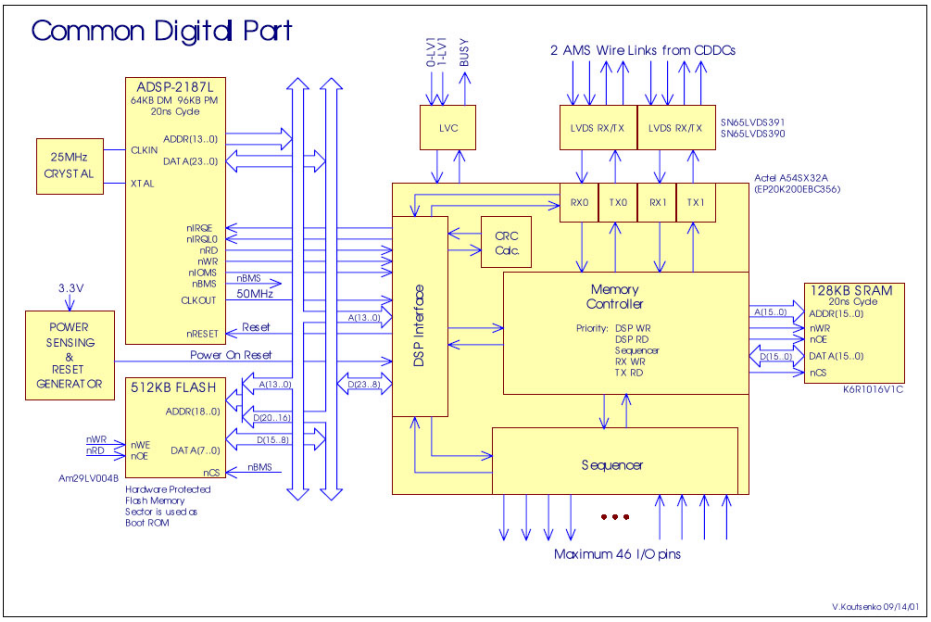

Figure 2.14: *CDP: Common Digital Part. The CDP is a circuitry widely used throughout the AMS02 electronics. It consists of an FPGA, a DSP with its FlashROM and a 512kB SRAM. The UDR2 is used for data taking, data reduction and communication. [Design & Drawing by Vladimir Koutsenko.]*

2.3.5 U-Front-End - UFE

The U-Front-End hybrid (UFE) is the first stage in the read out chain of the TRD. The UFEs are located directly on the octagon walls of the TRD itself.

A picture of a QM1 UFE is shown in Fig. 2.15. Clearly visible are the four connectors for the cables to the straw tubes, the two pre-amplifiers and the cable, which links the UFE to the UDR.

The UFE consists of two Viking VA32HDR ASIC pre-amplifiers [IDE00], a fast 12 *bit* serial ADC and some control logic that receives the control signals from the UDR and steers the two ASICs.

The analog signal from the 64 straw tubes is amplified and multiplexed by the two ASICs. The analog output of the 2 pre-amplifiers is connected to the ADC, where the signals are converted to digital values before they are sampled by the UDR. A schematic view of the UFE and its connections is shown in Fig. 2.16.

The design of the UFE is optimised for low noise and minimum EMI[(11)] emission.

[(11)]**EMI**: **E**lectro-**M**agnetic **I**nterference

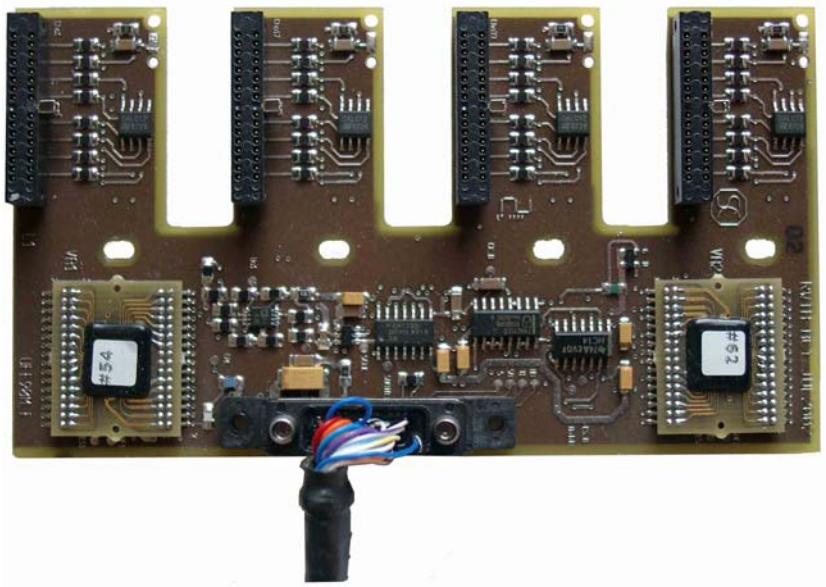

Figure 2.15: *UFE: U Front-End. The UFE is attached directly to the octagon walls of the TRD. The signals from 4 strawtube modules are multiplexed by 2 VA32HDR ASICs and digitised by a fast* 12 *bit ADC.*

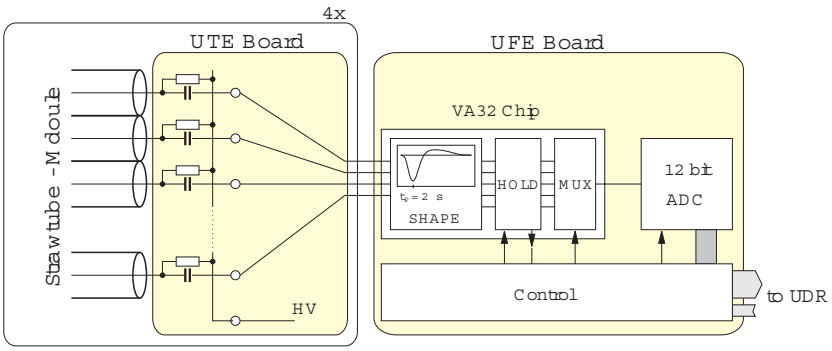

Figure 2.16: *A schematic overview of the UTE (U-Tube End) and the UFE. After [Sch01]*

2.3.6 Universal Slow Control Module - USCM

The Universal Slow Control Module (USCM), shown in Fig. 2.17, was designed as a multipurpose slow-control card. Its main purposes are temperature monitoring of the electronics and the detector itself and the role of a slow-control master inside the crate. As the USCM is not redundant in itself as all other cards in the U-crate, there are two of them in the QM1 design. A detailed description of the USCM can be found in [Cam03].

The USCM communicates via the CAN bus with the JMDC. The slow-control commands are passed on to the UPSFEs and the S9011AUs via 16 LeCroy bus links. In addition to the already mentioned communication lines, the USCM also features serial ports, ADCs and DACs.

Another important function of the USCM is the reading of Dallas DS1820 digital thermometers. In principle 8 single wire Dallas buses can be connected to the USCM with a total number of 255 temperature sensors. In reality this number is far smaller due to the capacitance and resistance of the wire, which leads to a smearing of the digital signals.

A more detailed description of the bus protocols used in AMS is given in section 2.3.13 *Communication Protocols*.

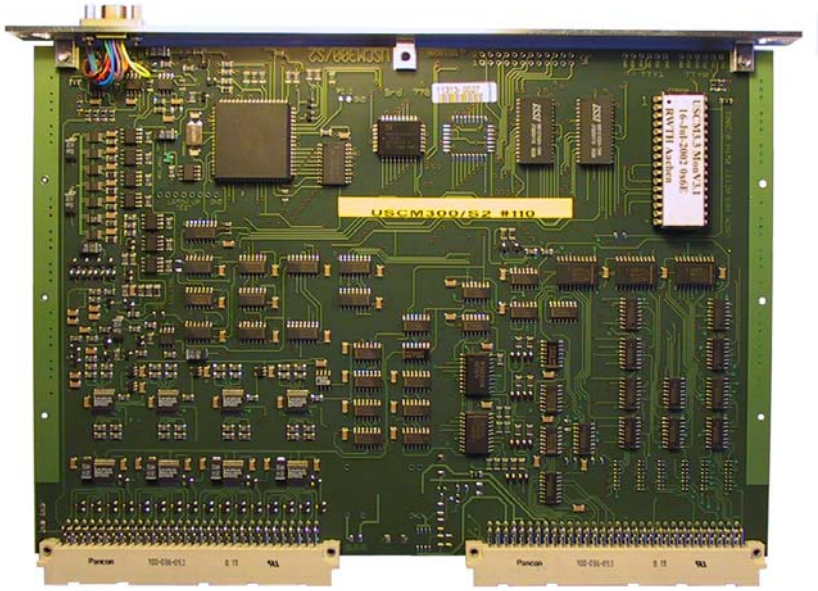

Figure 2.17: *USCM: Universal Slow Control Module. Before the weight reduction, the USCM was the slow-control master for the U-Crate. It acted as interface from CAN bus to LeCroy bus and read the DS18S20 temperature sensors on the various cards and in the TRD itself, now these functionalities are taken over by other cards.*

As stringent limits on the weight of the electronics of the experiment were exceeded, it was necessary to save weight by omitting some cards in the various read out crates. One of the cards that was removed from the crates was the USCM. Only very few USCMs located in critical places of AMS02 remained.

The functionality of the USCMs removed from the DAQ crates was transferred to other cards. The temperature monitoring is now done by the few remaining USCMs. The slow-control functions were moved to the JINF. For a more detailed description please refer to the section on the JINF on page 48.

2.3.7 U-High-Voltage-Generator - UHVG

The UHVG generates the high voltages for the strawtube modules from a $120V$ input coming from a S9056 DC/DC converter. The output voltage can be set from a few Volts up to $\sim 1850V$ with $14bit$ precision. The principle used on the UHVG is a 16 stage charge pump based on the Cockroft-Walton multiplier [Coc32]. Each of these charge pumps is controlled by a LeCroy MHV100 chip [LeC97], a custom development for the AMS experiments. The Cockroft-Walton multipliers and the control chips are clearly visible in Fig. 2.18.

One UHVG has 14 independent HV channels, which are organised in two groups with seven channels each. One of these halves is kept as cold redundant spare during nominal operation. This is controlled and monitored by the UPSFEv2. The communication with the two parts of the UHVG is done via two independent LeCroy links coming from the JINFv2.

Due to the many features of the MHV100 chips the UHVG has a lot of functionality. For each channel the UHVG has the possibility to set over-voltage and over-current limits with $16bit$ precision, which can be also used for an automatic power down of a channel in case of a spark in the strawtube. The actual voltage and current can be read back, as well as the temperature of the device.

The communication with the MHV100 chips on the UHVG is done using the so-called LeCroy protocol. This protocol uses one data and one clock line for the data transfer. A more detailed description of the protocol can be found in section 2.3.13 and in [LeC97].

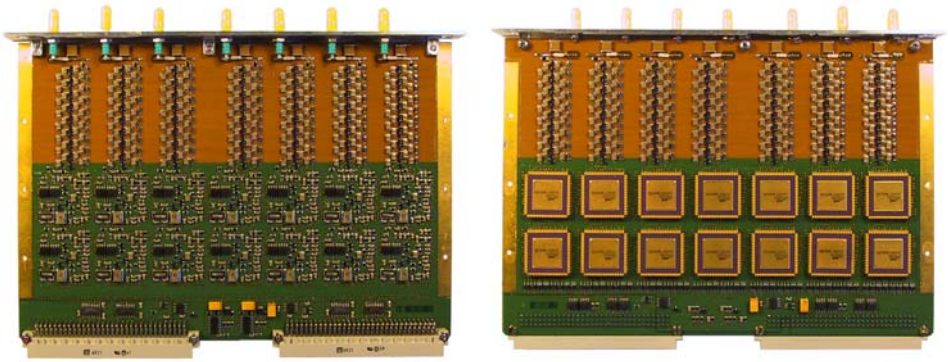

(a) Front Side (b) Back Side

Figure 2.18: *UHVG: U High Voltage Generator. The UHVG generates, regulates and monitors the high voltage for the strawtube modules. Each UHVG has 14 independent HV channels, which are grouped in 7 pairs. (a) front side of the UHVG with 7 charge pumps (b) back side of the UHVG with the MHV100 controller chips and the second set of charge pumps. [Design by Vladimir Koutsenko.]*

Due to variations in the MHV100 DACs each channel of the UHVGs needs to be calibrated separately. Fig. 2.19 shows such a calibration curve. Even though the deviations between the set value and the measured value are quite small ($< 3\%$), the calibration is required, as the gas gain in the straw tubes is a function of the applied high voltage.

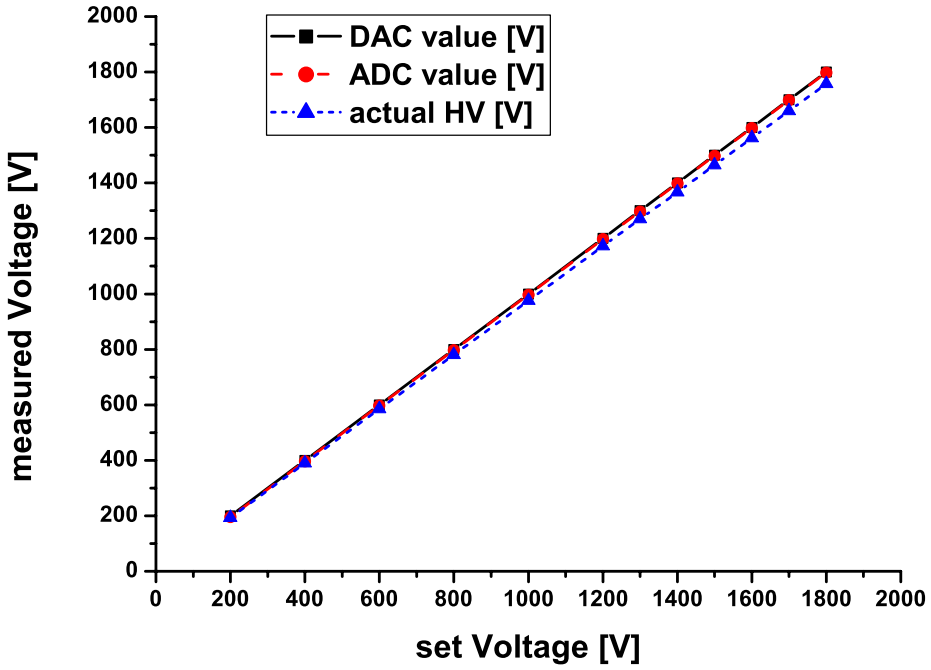

Figure 2.19: *Calibration curve of one MHV100 chip on a QM1 UHVG. One can clearly see the relatively good agreement between set value and measured value with only a small non-linearity. But, as the gas gain in the detector is a function of the applied HV, all UHVG channels must be calibrated. The curve of the DAC and the ADC values are in perfect agreement, as expected. [Measurement by Thomas Krynicki]*

2.3.8 U-Power-Supply-for-Front-End - UPSFE

The main function of a UPSFE, depicted in Fig. 2.20, is to supply 14 UFEs via two UDRs with stable $\pm 2V$. In addition to this the UPSFE features safety functions for the linear regulators and some external control and monitor lines.

Each UPSFE has 14 linear regulators. These regulators are grouped in seven pairs. In each pair one is kept as cold redundant spare in nominal operation. The linear regulators convert the incoming $\pm 2.6V$ to stabilised $\pm 2V$.

Each linear regulator has a self-protection circuit. This circuit disables the regulator in case of over-current or over-voltage for $\sim 220\,ms$ and then tries to power-up again. In case the limits are still exceeded the power is cut again after $\sim 50\,ms$. The current limits for (+) and (-) are asymmetric: $300\,mA$ and $340\,mA$.

The linear regulators are controlled and monitored by the two FPGAs on the UPSFE. Again, one of them is kept as cold spare during nominal operation. These FPGAs receive their commands via LeCroy-bus connections from the slow-control interface on the JINF.

The UPSFE has no external clock. The LeCroy clock and data lines drive the communication block in the UPSFE firmware and thus the main entity. The monitor lines drive $4\,bit$ counters, which record the number of errors reported.

The external control and monitor lines of the UPSFE are connected to two UDRs, two UHVGs and the JINF. These lines are directly connected to the solid-state fuses on these cards. The FPGAs on the UPSFE can switch between the two redundant parts of the UDRs, the UHVGs and the JINF and also monitor their status.

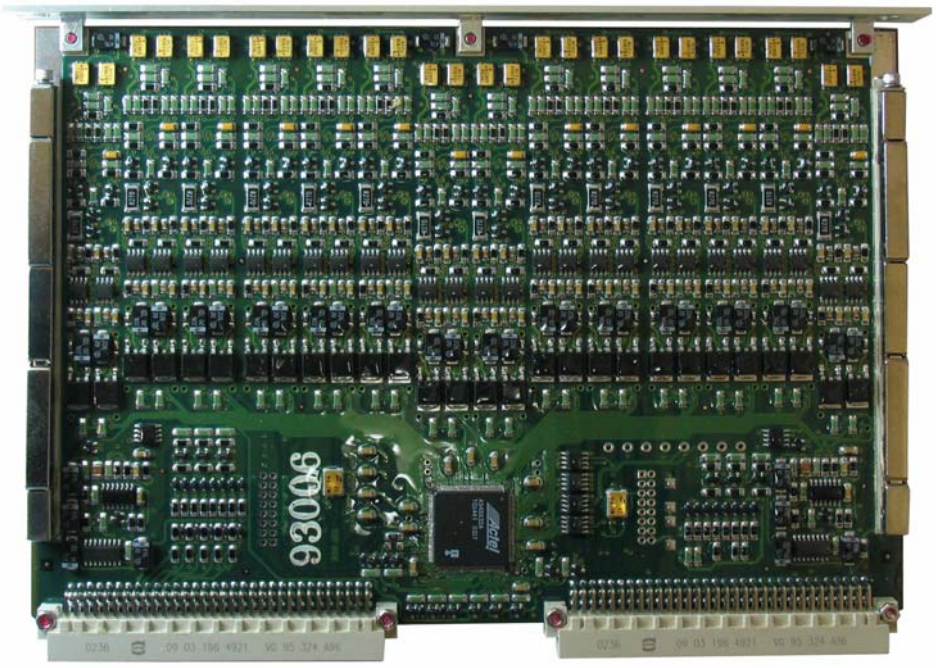

Figure 2.20: *UPSFE: U Power Supply for Front-End. The UPSFE regulates the low voltage supply lines for the 14 UFEs, which are connected to the two UDRs in its power group. It also controls and monitors the solid-state fuses on the UDRs and the UHVGs. The UPSFE can be controlled via the LeCroy bus.*

UPSFEv2

The UPSFEv2 is an updated version of the UPSFE, which was required to meet the new specifications after the weight reduction was implemented. The major changes are:

- linear regulator assignment: Before the weight reduction the two halves of the UPSFE were assigned to digital and analog supply lines for the UFEs. As one UPSFE was removed per power group, it was not possible to keep this assignment anymore, if the redundancy of the linear regulators was to be kept. With the new assignment one linear regulator now supplies both, analog and digital part of the UFE, and the two halves of the UPSFEv2 act as redundant spares.

- increased power limits: The new assignment of the linear regulators also required a change in the implementation of the linear regulators, as now a higher current is required per regulator. The load limits are asymmetric. The limit is $300\,mA$ for the positive voltage and $340\,mA$ for the negative.

- JINF: The functionality to control and monitor the solid-state fuses on the JINF is still there, but as the JINFv2 acts now as a slow-control interface in the crate, it was decided, that the JINF should control its solid-state fuses by itself.

- Oscillator: On the QM1 backplane some reflections were observed on the clock and data lines of the LeCroy buses, see Fig. 2.36.

  One way to minimise the risk of communication failure due to glitches is to oversample the signals on the clock and data lines using an external clock signal provided by a quartz resonator. On the UPSFEv2 a $2\,MHz$ oscillator was included for this purpose. This oscillator is also used to oversample the monitor lines from the linear regulators and the external signals.

  No significant increase in the power consumption of the UPSFE, due to this modification, was observed.

- LVDS line drivers: As the LVDS line driver chips used on the UPSFE and the USCM were designed for point to point connections and not bus operation, they were not able to drive a load of only $50\,\Omega$, as it would be required by a bus correctly terminated at both ends. On the UPSFEv2 a different driver chip is used for the LVDS lines. This new IC is optimised for the operation on LVDS buses, see Fig. 2.21. Thus on the UBPv2 the LVDS lines of the LeCroy clock and data are terminated on both ends with $100\,\Omega$.

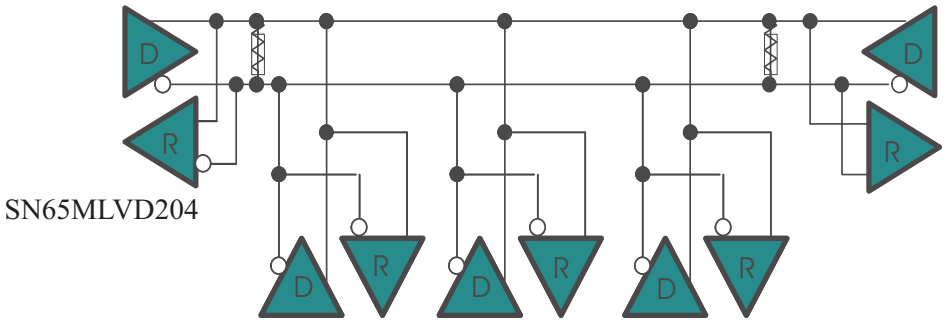

Figure 2.21: *LVDS transceivers in a bus configuration, as is it implemented on the UBPv2 for the LeCroy-buses for the UPSFEv2, the UHVG and the S9011AU. Taken from [Tex03].*

The modifications of the UPSFE did not affect the power consumption of the board. With both FPGAs operational, the power consumption on the $3.3\,V$ supply line for the digital part is $239\,mW$. In the nominal operation, where one FPGA is kept as cold spare, the power consumption reduces to $176\,mW$.

A more detailed description of the firmware of the UPSFEv2 can be found in Appendix B.

2.3.9 The U Power Distribution Box - UPD

The U Power Distribution Box contains the DC/DC converters, which generate the required voltages from the $28V$ delivered to the UPD and their controller card, the S9011AU. The $28V$ input is filtered by the S9011B using mostly passive components.

(a) The UPD

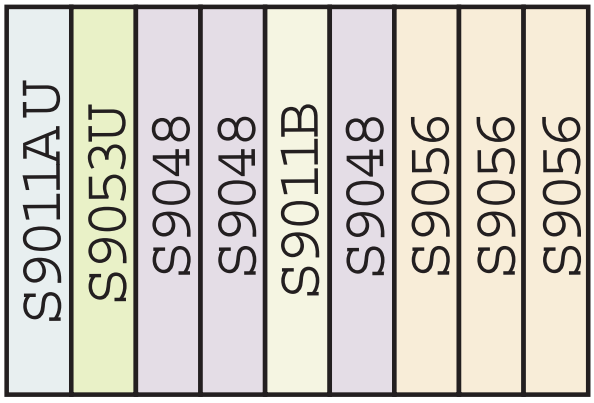

(b) UPD scheme

Figure 2.22: *(a) A picture of the QM2 version of the UPD without its top cover. (b) The layout of the final UPD for the flight. It contains the control board (S9011AU), the input filter (S9011B) and the 3 types of DC/DC converters (S9053U, S9048 & S9056) needed for the TRD.*

Fig. 2.22(a) shows a picture of the assembled UPD. One can see the connectors for the cables to the U-crate, the i-frames holding the DC/DC converters and the bus bars, which distribute the $28V$ inside the UPD. The schematic drawing in Fig. 2.22(b) shows the arrangement of the controller card, the filter and the DC/DC converters in the UPD.

With the exception of the communication and temperature sensor cables, all wires between the UPD and the U-Crate are redundant in themselves. As there are two redundant FPGAs and temperature sensors, the redundancy for the communication is kept by connecting the two FPGAs via separate cables.

On the following pages the components of the UPD will be described in detail.

2.3.10 UPD Electronics - S9011AU

The S9011AU, shown in Fig. 2.23, is the controller board for the DC/DC converters in the UPD. Like the DC/DC converters it is housed inside the UPD. The communication between the S9011AU and the U-crate is done via two LeCroy links, each connected to one of the two FPGAs.

The S9011AT, the controller board of the Tracker Power Distribution box, is physically identical to the S9011AU, but it uses a slightly different firmware, which is based on the code of the S9011AU.

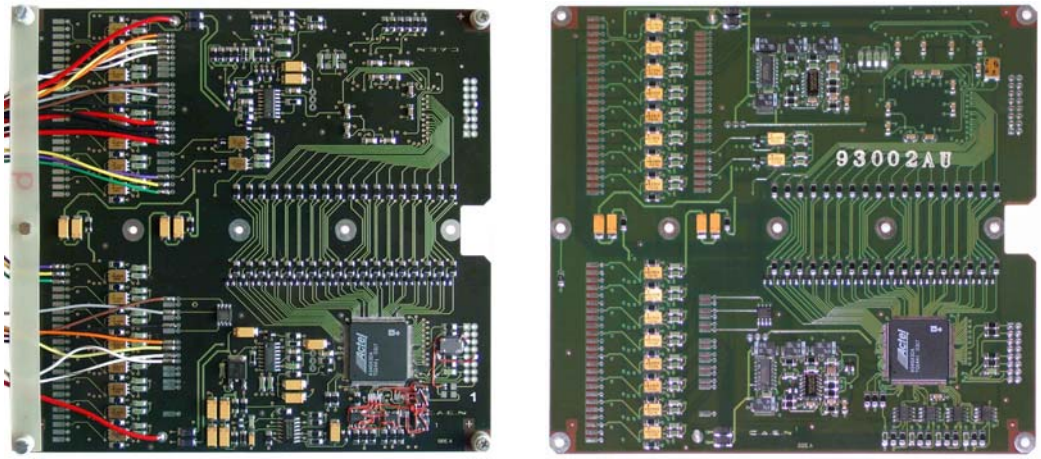

(a) QM1 w/ hotfixes (b) QM2

Figure 2.23: *S9011AU: Slow control board for the UPD. The picture shows a QM1 version of the S9011AU cabled for testing. A closer look to the area below the FPGA (bottom right corner) shows the changes, that were done to accommodate for the new LVDS drivers and the oscillator, which is used for over-sampling the incoming signals to prevent malfunction due to glitches.*

The S9011AU can control and monitor 18 DC/DC converters. As the DC/DC converters are built of two redundant halves, these 18 channels are grouped in the firmware in two sets of 9. For each channel the S9011AU has a differential control signal (OFF+ & OFF-) and a status input.

Both the output and the input lines to the DC/DC converters are galvanically decoupled using opto-couplers. For the control lines the opto-couplers are located on the converters, while for the monitor lines they are on the S9011AU itself.

The two redundant FPGAs (Actel A54SX32A-TQ144), each of them protected by a solid-state fuse, handle the communication and the signals for the DC/DC converters. After power-on both FPGAs are powered. To keep one FPGA as cold spare or to disable a malfunctioning FPGA, each FPGA has the possibility to switch the solid-state fuse of the other.

Via the FPGAs the DC/DC converters can be switched on and off. They also register possible trips of the DC/DC converters and set a corresponding register in the firmware, which can be read via the LeCroy bus.

Like on the UPSFEv2 the LVDS drivers originally foreseen for the LeCroy clock and data lines were replaced with ones able to operate on a bus. Also a $2\,MHz$ oscillator was added, which is used by the firmware for over-sampling incoming signals to prevent malfunction due to possible glitches or reflections on the lines.

The S9011AU has two DS18S20 temperature sensors. They are located close to the solid-state fuses of the FPGAs. The solid-state fuses are the parts dissipating the most heat on the S9011AU.

A detailed description of the firmware of the S9011AU and the corresponding control software can be found in the manual in Appendix C. A more detailed technical description of the S9011A and S9011B can be found in [CAE04].

2.3.11 UPD Filter 28V - S9011B

The S9011B is the EMI filter for the $28V$ supply line for the UPD. Its purpose is to suppress all high frequency noise on the $28V$, both incoming and outgoing. A picture of a S9011B is shown in Fig. 2.24.

The S9011B, made from mostly passive components, is, like all critical parts in AMS02, built in a redundant way. In Fig. 2.24 one can clearly see the two parts (top and bottom half) of the S9011B. Each half is dimensioned for a maximum current of $2.5A$, thus the maximum power that can be drawn in the UPD is $140W$.

The main functionality of the S9011B is achieved by using a low-pass RLC group, which strongly damps frequencies above $10kHz$. The circuit was designed according to the specifications in [Eri99].

Due to the strong magnetic field in AMS02 generated by the superconducting magnet, which does not allow the use of high A_L cores, the inductance of the filter is rather small.

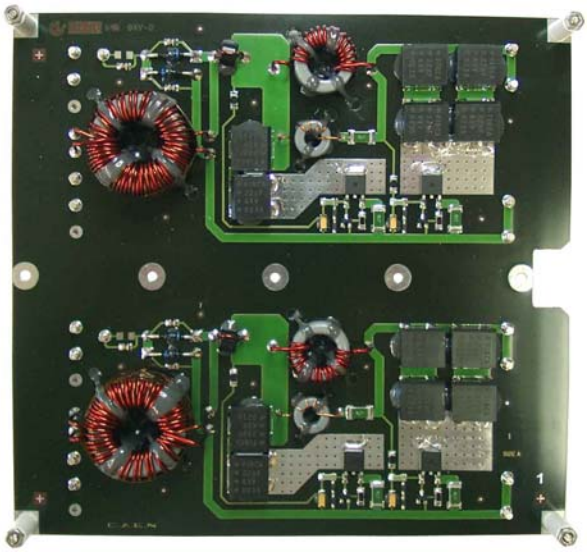

Figure 2.24: *S9011B: The S9011B acts as a filter for the 28V line. It also limits the inrush current to protect the PDB.*

The second important feature of the S9011B is the limitation of the inrush current. The large capacitance of the second filter stage otherwise could cause the main supply to go into self-protection mode, which in itself would make it impossible for the UPD to start up.

2.3.12 DC/DC-Converter

The main power feeds from the ISS to AMS02 supply the experiment with $120V\ DC$. This voltage is converted in the main power system of AMS02 to $28V$ and then distributed to the xPDs of the various subdetectors.

The DC/DC converters in the UPD convert the incoming $28V$ (allowed range: $26.5V - 30.5V$) to the specific voltages needed in the TRD. These range from $\pm 2V$ for the front-ends to $+120V$ for the high voltage generator for the strawtubes.

Fig. 2.25 shows one of the DC/DC converters used in the UPD from the QM1 production. One can clearly distinguish the two redundant halves of the converter. Both halves have separate in- and outputs, as well as control and monitor lines.

The incoming $28V$ are distributed inside the UPD via so-called bus bars. These bus bars are nickel-plated copper bars. The secondary voltage is brought via cables to connectors in the side walls of the UPD.

All DC/DC converters are specified to withstand a total absorbed dose of $30krad$ and a magnetic field of $500G$. The operational temperature range is $-40℃$ to $+70℃$. The mechanical dimensions of the DC/DC converters is $160mm \times 150mm$. The thickness varies from $19.6mm$ to $24.6mm$ depending on the size of the inductors, which is related to the maximum output power.

The efficiency of the DC/DC converters is a function of the load. Around the nominal load, 80% of the maximum load, they reach their maximum efficiency, which is for the low voltage converters $\sim 80\%$ and 65% for the high voltage ones.

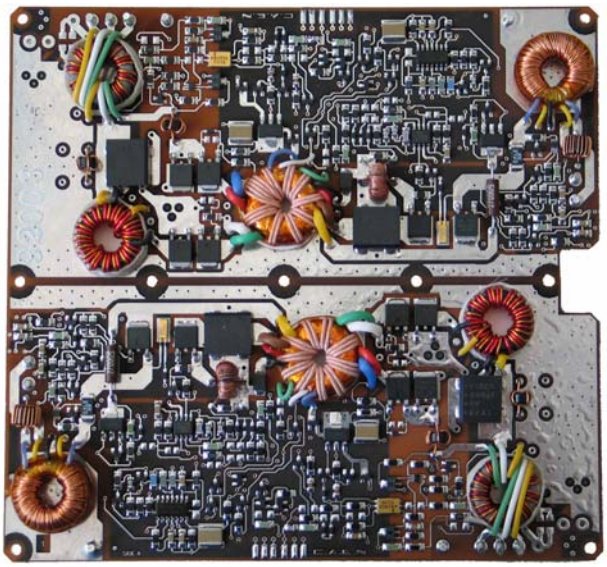

Figure 2.25: *The DC/DC converters in AMS02 transform the 28V delivered to the subdetector electronics to the voltages required in the specific system. All outputs are protected against over-voltage and over-current.*

The following DC/DC converters are used in the electronics of the TRD:

- S9048: Output voltage: $\pm 2.6V$
  This converter generates the voltages for the supplying of the UFEs. The $\pm 2.6V$ are regulated on the UPSFE to $\pm 2.0V$. The maximum output power of the S9048 is $12W$. A more detailed description can be found in [CAE03a].

- S9053U: Output voltage: $+3.7V$
  These DC/DC converters supply all digital circuits in the electronics of the TRD including the S9011AU. The maximum output power is $24W$. For more information on this converter please refer to [CAE03c].

- S9054: Output voltage: $+5.6V$
  The S9054 was designed to supply the USCM and the S9011AU. As the USCM was removed due to the weight reduction, it was decided to change the supply of the S9011AU to $3.3V$ and also remove the S9054. The maximum output power of the S9054 is $25.2W$. A more detailed description can be found in [CAE03b].

- S9056: Output voltage: $+5V$ & $+120V$
  This converter generates the $120V$ for the UHVG. The $5V$ are also used on the UHVG. They are needed for the control circuitry of the high voltage generator. Detailed information on this converter is available in [CAE03d].

	S9048	S9053U	S9054	S9056
voltage [V]	± 2.6	$+3.6$	$+5.6$	$+5/+120$
efficiency [%]	77	78.5	82	65
maximum output power [W]	12	24	25.2	6
maximum output current [A]	2.4	7	4.5	150m / 35m
maximum input current [A]	0.575	0.55	1.1	0.28
weight [gr]	273	340	340	256

Table 2.2: *An overview of the most important features of the various DC/DC converters used in the TRD electronics. [CAE03a, CAE03c, CAE03b, CAE03d].*

2.3.13 Communication Protocols

In the AMS02 experiment various types of communication protocols are used: From the high speed data link AMSwire to the low speed LeCroy bus for slow control functions. In the following sections a short description will be given for each of the 3 protocols used in the TRD. For a more comprehensive reading please refer to the references given for each protocol.

AMSwire

AMSwire is a point-to-point serial link operated at $50\,MHz$ in a master and slave mode. It is used on all levels of the DAQ chain in AMS02. The Double-Data-Rate and a small overhead in the protocol allow for a net data transfer rate of $10\,MByte/s$. Together with the very low latency this makes the protocol ideal for transferring the scientific data inside the experiment.

AMSwire uses four wires for the data transfer. Two wires are used for the receiver (RX) and two for the transmitter (TX). For each direction there is one data line and one strobe line. The clock is reconstructed in the receiver by "XORing" the signals from the data and the strobe lines. There are also separate buffers for RX and TX.

To ensure maximum safety for the transmission, the lines are implemented as LVDS connections and there are always at least two independent links between to partners.

Since the weight reduction in the electronics of the AMS02 electronics, the AMSwire protocol is not exclusively used for the data acquisition any more, but also for the slow-control data.

The AMSwire protocol and implementation [LIN03] are a development of the AMS collaboration based on the SpaceWire [ECS03], which itself is based on the IEEE-1355 standard [IEE95].

CAN-Bus

The CAN-bus[(12)] was defined in the 1980s by the Robert Bosch GmbH [Bos91]. It was designed for real-time safety-critical applications like in the automotive environment. By now it has become an industrial standard (ISO 11898) and is used in a lot of different applications.

The CAN-bus is a multi-master bus specified for a maximum length of $40\,m$ and a data rate of up to $1\,Mbit/s$. In the AMS02 experiment it is used in the slow-control system to connect the USCMs in the various crates to the main DAQ computer.

Using 2-wire differential connections and a set of error detection mechanisms the CAN-bus is extremely failure safe and can "survive" even a failure on one of the two wires.

As the USCMs were removed from the U-crate during the weight reduction and the functionality was taken over by the JINFv2, the CAN-bus is not used anymore in the TRD read out electronics from the QM2 version of the electronics onwards. All slow-control data is now transmitted using the AMSwire protocol. In other subdetectors, where there is still a USCM, the CAN-bus is still in usage.

LeCroy bus

The LeCroy bus was designed by the LeCroy Corporation for the digital data interface of the high voltage chip MHV100 [LeC97], which is used on the UHVG. In AMS02 the LeCroy bus is used for the communication on the lowest level of the slow-control system in various places.

In the TRD electronics the LeCroy bus is used for the communication between the USCM / JINFv2 and the slow-control slaves: UHVG, UPSFEv2 and S9011AU. The bi-directional LeCroy bus consists of one data and one clock line.

The communication is always initiated by the bus master (e.g. JINFv2). In the first 32 bits of the communication a command is transmitted to the slave (e.g. UPSFEv2), in the second 32 bits the slave either sends an echo of the command or the reply in case of a read request. A detailed overview of the bit usage in the LeCroy bus communication can be found in Appendix A and in [LeC97].

[(12)] **CAN**: **C**ontroller **A**rea **N**etwork

Dallas 1-wire Bus

The 1-wire bus was developed by Dallas Semiconductor for connecting sensors, like thermometers or pressure probes, to μControllers. The communication in this master-slave bus runs at $16\,kbps$ at regular speed and at $140\,kbps$ in overdrive mode using CMOS/TTL logic levels.

The 1-wire bus consists of a data line and a ground line. If the bus is operated in parasitic mode, the data line is also used to power the slave devices. This is done using the half-wave rectifiers which are present in each slave. As buses with a lot of slaves would draw to much power from the master driving the line, the slaves can also be powered externally.

As the 1-wire bus has no separate clock and data line, the data transfer is done using the time slot method. A system clock is not required for this, as there is an internal oscillator in each device on the bus, which is synchronised to the falling edge of the master.

At the beginning of each command the master resets the bus by pulling it low for at least $480\,\mu s$, after this it waits for the presence pulses from the slaves. In order to write a logic "1" the master pulls the bus low for $15\,\mu s$ or less. For a logic "0" the master pulls the bus low for $60\,\mu s$ or more. The time margin is used to counter any issues due to worst case conditions.

Each 1-wire device is identifiable by a $64\,bit$ Device ID. This ID contains a $48\,bit$ unique serial number, an $8\,bit$ device family code and an $8\,bit$ CRC.

2.4 Firmware Programming

Firmware programming for read out and slow-control cards was a major part in the scope of this thesis. After a short introduction into FPGA programming, the three projects, namely UDR, UPSFE and S9011AU, will be described in the following sections.

2.4.1 FPGA and Fuse/Anti-Fuse basics

The short cycles in electronics production require fast and cheap development procedures. For most applications it is too time consuming and too expensive to design and manufacture custom ASICs[13]. Modern CMOS technology allows the use of so-called FPGAs[14].

FPGAs are re-programmable logic devices that can feature up to a few million logic cells in a single chip. The newest generation of FPGAs are clocked with frequencies up to $1\,GHz$. Some even feature a complete DSP[15] or CPU[16] core, making them extremely powerful devices for system-on-a-chip applications.

The internal architecture of the Altera APEX20k, a chip used for some of the developments described below, is shown in Fig. 2.26(a). The left part of the picture shows the logic cells and their interconnect scheme. On the right the overall chip is shown, with its two main parts, the block with the logic cells and the electronics for the switching of the interconnections. Fig. 2.26(b) shows the approach of Actel for the interconnects between the logic cells.

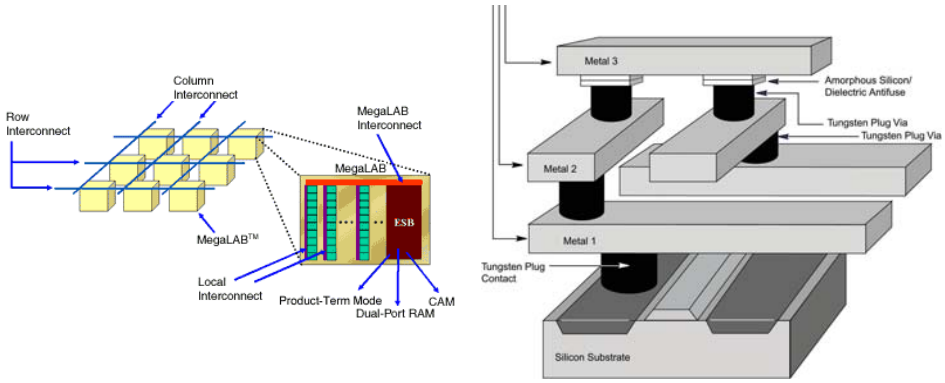

(a) Altera APEX20k (b) Actel Anti-Fuse

Figure 2.26: *(a) Architecture of the Altera APEX20k FPGA. On the left hand side the logic cells with their interconnections are shown. On the right the overall structure with the block of logic cells and the switching electronics are depicted. [Alt05] (b) Schematic drawing of an Actel Anti-Fuse. The tungsten vias form the main interconnections. The amorphous silicon anti-fuse is shown between the metal 2 and 3 layers. [Taken from [Act01]]*

Unfortunately, common FPGAs have two major drawbacks that hinder their use for space applications. The first issue is that the configuration programmed into the device is volatile. After a power cycle of the device it needs to be re-programmed. This can be overcome by the introduction of an EEPROM[17] from which the FPGA loads its configuration at power-up. But this will add at least one more component to the design, which will increase its failure probability.

[13] **ASIC**: **A**pplication **S**pecific **I**ntegrated **C**ircuit

[14] **FPGA**: **F**ield **P**rogrammable **G**ate **A**rray

[15] **DSP**: **D**igital **S**ignal **P**rocessor

[16] **CPU**: **C**entral **P**rocessing **U**nit

[17] **EEPROM**: **E**lectronically **E**rasable **P**rogrammable **R**ead-**O**nly **M**emory

The second problem of common FPGAs is far more severe. Due to the CMOS technology that is used for their production they are not radiation hard. A SEU[18] can cause a bit flip. There are two possible consequences of such an event: data integrity might be corrupted or the programming of the device might be changed. Both of which are very dangerous for space experiments.

Only very recently a re-programmable radiation hard FPGA was introduced on the market. Unfortunately, the design of the electronics of the AMS02 experiment was by far too advanced to be adapted to this new device.

AMS02 followed the classical approach to solve this problem: Use standard re-programmable FPGAs during the development phase and radiation hard once programmable FPGAs for the final production. In the technology of once programmable FPGAs the interconnections between the logic cells are made either by fusing the connection (Fuse-Logic) or "burning" the connection (Anti-Fuse Logic) with the use of rather high voltages and currents. A cross-section of an Anti-Fuse device, as it is used in AMS02, is shown in Fig. 2.26(b).

To make things easier during the final steps of the firmware development the Anti-Fuse FPGAs are not soldered directly onto the PCB, but they are clamped in a socket which has a compatible footprint. A close-up picture of the socket is shown in Fig. 2.27(a). On the UPSFE and the S9011AU due to the limited space a different socket was used, see Fig. 2.27(b).

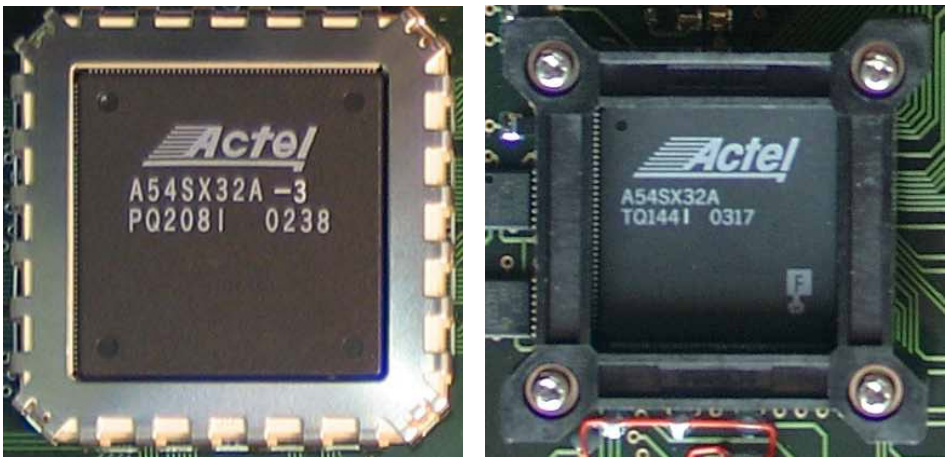

(a) ET S-QFP-SM-208-A (b) ET S-QFP-SM-144-A

Figure 2.27: *A close-up picture of the socket for the Anti-Fuse FPGA on the UDR2 (a) and on the S9011AU (b). These sockets allow easy replacement of FPGAs during the firmware development.*

A second advantage besides the easy exchange of the FPGAs is, that the usage of sockets circumvents the problem of the maximal number of re-soldering on a PCB. This number is rather low (< 10) compared to the maximal cycle number of the sockets (~ 50).

The final versions of the PCBs are not equipped with sockets anymore, as these would not be able to withstand the vibrations during the launch of the spacecraft.

The transition from common FPGAs to Anti-Fuse FPGAs is only possible as both worlds use the same high-level programming languages, like VHDL[19], and only after synthesis the outcome is device specific.

2.4.2 Introduction into VHDL & Design Flow

In this section a short introduction to the programming languages and tools used in the scope of this work is given. The development for the re-programmable FPGAs (Altera APEX20K) was done with

[18] **SEU**: **S**ingle **E**vent **U**pset

[19] **VHDL**: **V**ery **H**igh Scale IC **D**escription **L**anguage

the IDE[20] Quartus II®. For the Actel A54SXA series FPGAs the Libero IDE 5.2 gold version was used. In the following only the parts of the Libero IDE will be described, as the final design was done with this tool set.

Introduction into VHDL

VHDL and Verilog®HDL are high level description languages[21] for system and circuit design. They can be used for different abstraction levels of the design. For optimal performance, device dependent coding has to be used, but with a more abstract level designs can be created that can be used on different architectures. In this way designs can be tested with re-programmable FPGAs before using Anti-Fuse FPGAs for the final production.

```
library IEEE;
use IEEE.std_logic_1164.all;

entity dff_async_rst is
port (
    data  : in   std_logic;
    clk   : in   std_logic;
    reset : in   std_logic;
    q     : out  std_logic
    );
end dff_async_rst;

architecture behav of dff_async_rst is

begin

process (clk, reset) begin
  if (reset = '0') then
    q <= '0';
  elsif (clk'event and clk = '1') then
    q <= data;
  end if;
end process;

end behav;
```

(a) VHDL Code

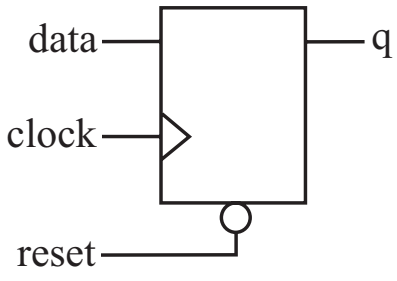

(b) Logic Cell

Figure 2.28: *Rising Edge Flip-Flop with Asynchronous Reset. (a) shows the VHDL code and (b) the logic symbol created from it. The output value q of the Flip-Flop is* 0 *for reset* $= 0$ *and becomes data for reset* $= 1$ *and clock* $=\uparrow$*. From [Act02].*

VHDL was chosen by the collaboration as the programming language for the firmware projects of the AMS02 experiment. As all firmwares are written in the same language, parts can be re-used in different projects, shortening the design process very much. An example of a simple VHDL programme and the corresponding logic block is shown in Fig. 2.28.

The example given shows the clear structure of the VHDL code. This allows to easily identify the most important parts of the modules, like the input / output connections of the module and the different subroutines.

For more detailed information on system design and VHDL please refer to [Ash02] and [Cha99].

[20] **IDE: I**ntegrated **D**evelopment **E**nvironment

[21] Even though they are called high level description languages, manipulations of data are on the bit level. See Fig. 2.28 for an example.

Design flow

In the following section the design flow from the conceptual draft to the final file programmed into the FPGA will be explained.

- **Conceptual design:** This is the first stage of the design of a new firmware. As a first step the necessary functions and communication protocols are defined on a very abstract level. After this the most important parts and their connections to each other and the outside world are identified. These major parts define the structure of the VHDL code.

- **VHDL design:** The main entity and its different sub-components are put into VHDL code. In this step the project is still device independent and can be used on many different chip architectures.

- **Synthesis:** When the first iteration of the VHDL code is ready for further processing the synthesis is started. In this process the functionality described in the VHDL code is mapped to device specific logic cells and gates in the FPGA. In case of too little resources in the FPGA, a possible optimisation is to allow the synthesis tool to re-use the same logical cell for different purposes, thus decreasing the total number of cells needed.

  The log file of the synthesis tool gives very detailed information about the number of logical cells used in the project. It also provides first timing estimates on the design allowing reconsiderations before going to the next stage of the design.

- **Compilation:** In this stage the result of the synthesis is used to extract the information on the number of IO pins and logic cells used in the design. Also the use of the various clock networks is verified.

- **Pin Assignment:** Once the software has extracted the information on the IO signals used, these signals have to be assigned to pins of the FPGA to connect the internal functions of the design to the outside world, the PCB.

  But not only has the signal to be assigned to the correct pin, but also the corresponding IO standard (e.g. LVTTL, CMOS or PCI) has to be selected. As an additional setting it is also possible to select the default value of a pin after powering the device. Also the external clocks are connected to the corresponding internal clock networks in this stage of the design flow.

- **Layout:** After selecting the pins, the development tool can assign the logic cells from the synthesis to the physical cells in the FPGA.

  Different optimisation levels can be selected for this process. The development tool used for the Actel Anti-Fuse FPGAs has three optimisation levels: Incremental placement, timing driven placement and multiple iterations. These three optimisations can be combined to achieve better results.

- **Netlist:** The netlist is a result from the layout process. It can be used to check if the IDE assigned the correct logical cells to the desired functions and if they are connected accordingly.

- **Back Annotation:** The timing extractor generates the back annotation file from the output of the layout. It uses an internal database to calculate the delays of the different logical cells and the interconnects along the paths of the internal signals.

- **Stimulus:** Using a waveform generator a stimulus file is created. In this stimulus file the values of the external signals going into the FPGA are listed as a function of the time. The achievable precision is 1 *ps*.

- **Simulation:** One of the most important stages in creating a firmware is the simulation of the project. During this process a software tool calculates the response of the FPGA to the stimulus according to the timing data provided by the back annotation.

- **Fuse File Creation:** Once the simulation gives the expected results, the fuse file can be generated. It contains the information required to programme the firmware into the FPGA.

- **Programming:** Depending on the type of FPGA different approaches can be used to programme the code into the device.

  For re-programmable devices the most common interface for loading the code into the FPGA is the so-called JTAG[22]. This standard allows to programme the device on the PCB.

  Anti-Fuse FPGAs cannot be programmed on the PCB as the voltages and currents needed are much too high for standard electronics designs, thus special devices are needed.

- **Silicon Explorer:** The Actel Anti-Fuse FPGAs feature a proprietary debugging interface, the Silicon Explorer. This tool can be used to do a boundary scan via the JTAG interface once the FPGA is mounted on the PCB to check the correct programming of the device. More important is the possibility to do an online debugging of the processes inside the FPGA while it is running. This allows to watch the different signals on the level of the logical cell as if a digital oscilloscope was connected to the cell.

2.4.3 UDR Sequencer

The firmware for the xDRs is comprised of 5 major parts, see Fig. 2.29. All of these parts are common to all subdetectors with the exception of the sequencer. The sequencer has to be detector specific as different pre-amplifier chips are used in the various subdetectors.

In the case of the TRD two VA32HDR12 pre-amplifier chips by IDEAs [IDE00] are used on each of the front-end hybrids. Due to some particularities of the chip, the sequence used in our firmware was slightly modified from the one specified in the data sheet of the device.

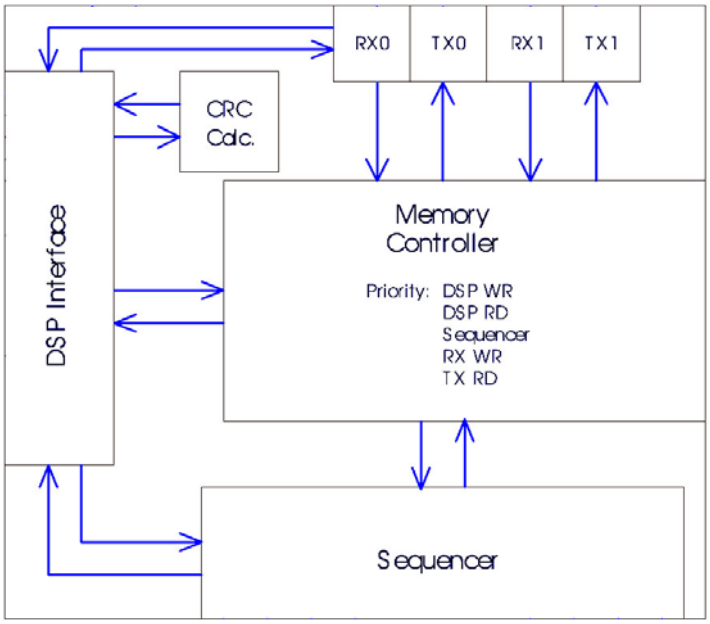

Figure 2.29: *A schematic view of the architecture of the UDR firmware.*

[22] **JTAG**: **J**oint **T**est **A**ction **G**roup of IEEE. Standards are published in IEEE1149.x

The development process for the sequencer code was separated into 3 phases. In the first phase, the prototyping stage, the code was developed and tested on the S9007. The S9007 has a complete CDP on-board and detector specific add-ons were connected as piggy-backs, see Fig. 2.30(b).

The communication to the PC was done using an EPP[23] cable. The setup used for this first stage is shown in Fig. 2.30(a). On the Linux-PC the data was read into a LabView 6i VI via a C++ library.

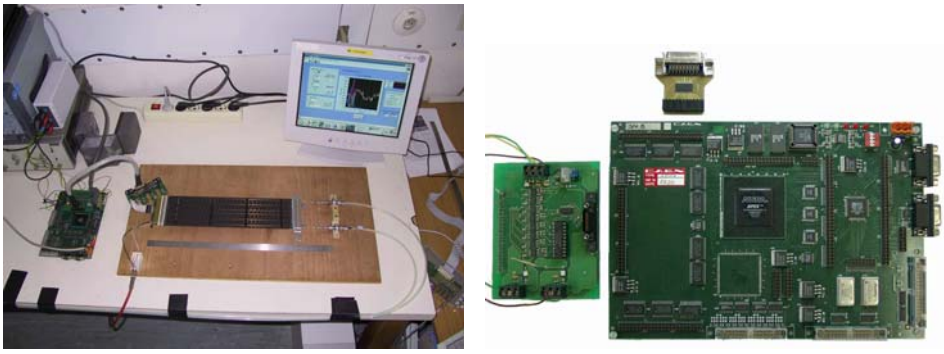

(a) Table Top Setup (b) S9007 “Guidoboard”

Figure 2.30: *(a) The table top setup for developing the sequencer code. (b) The S9007, often called the “Guidoboard”. With the help of this setup the sequence for the read out and calibration of the front-end amplifier ASIC was implemented in VHDL. The measurements done include timing and linearity scans and energy spectra of various radioactive sources like* ^{55}Fe *and* ^{90}Sr *.*

The second stage of the development was done using the Engineering Module (EM) version of the UDR. Again the FPGA was re-programmable, thus allowing for easy modifications of the code.

The finale phase was done on a QM1 UDR2. As the UDR2 uses an Anti-Fuse FPGA it was decided to use a footprint compatible socket for the FPGA to allow easy replacement of the once programmable FPGA during finalisation of the firmware code. A close-up picture of the socket is shown in Fig. 2.27(a).

Two modes are implemented in the UDR2 for reading out the front-end chips: The standard read out mode and the calibration mode. The first mode is used to read the chips during normal data taking. The second mode allows to inject charge via an external capacitor into the input stages of the pre-amplifier chip and thus to calibrate the gain and the linearity of the read out chain.

Fig. 2.31 shows an example of a read out cycle as it is implemented within the firmware of the UDR sequencer. After an incoming trigger the *sample & hold* signal is sent to the front-end chip. Then the output multiplexers of the pre-amplification chip are clocked to all 64 channels of the 2 chips. During each of the 64 steps the analog signal is sampled with an ADC[24] on-board the UFE. At the end of the sequence a reset is sent, to put the front-end chips in a defined state, ready to receive the next trigger.

Due to the signal propagation time in the cable ($\sim 20\,ns/m$) from the UDR2 to the UFE, the sample time has to be artificially delayed with respect to the clock and control signals for the ADC for some nanoseconds to read back the correct data.

[23] **EPP**: **E**nhanced **P**arallel **P**ort

[24] **ADC**: **A**nalog to **D**igital **C**onverter

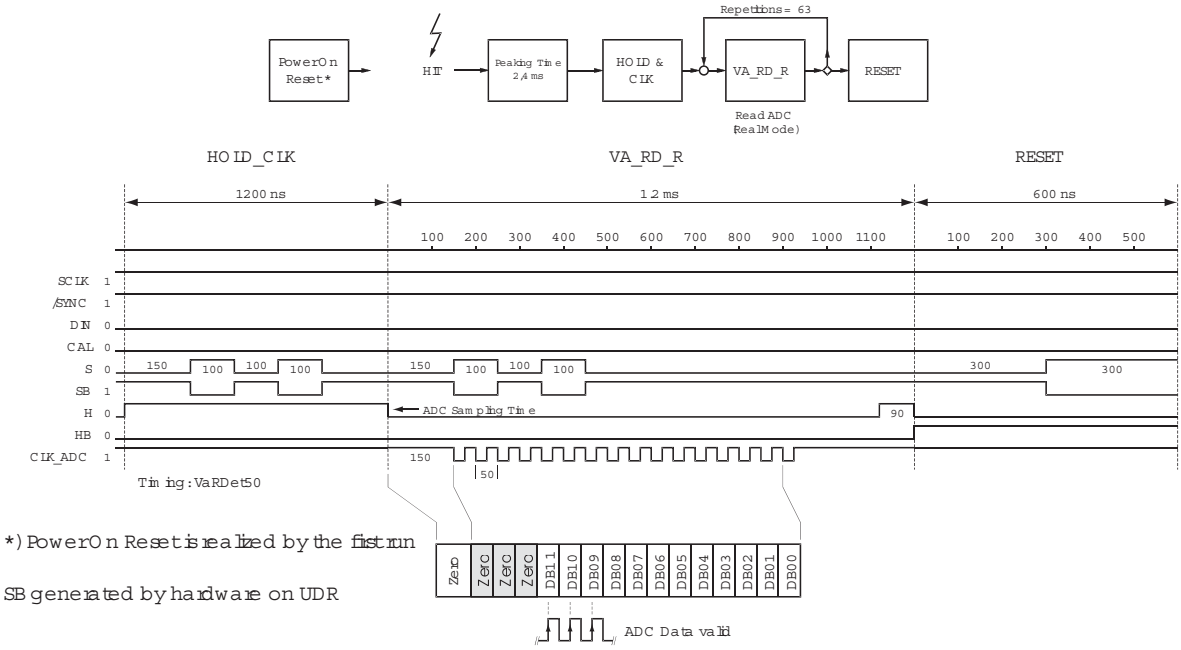

Figure 2.31: *UDR read out sequence in normal mode. After an incoming trigger a "sample & hold" is sent to the VA32HDR12. Then the output multiplexer is clocked to each channel. During the time the analog signal is stable at the output of the VA, it is sampled by the ADC. After all 64 channels of the 2 VAs have been sampled the VA is reset. The standard read out cycle lasts 78 µs. [Drawing by Wacek Karpinski.]*

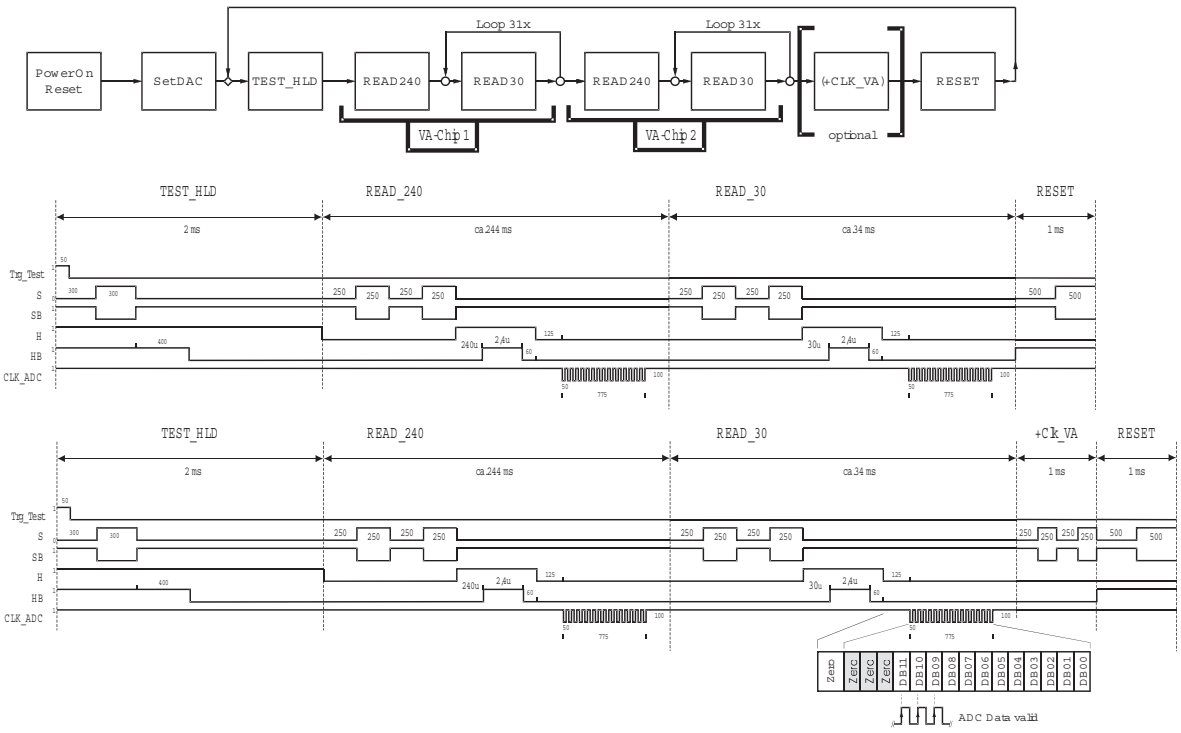

Figure 2.32: *UDR read out sequence in calibration mode.[Drawing by Wacek Karpinski.]*

The second mode implemented in the sequencer of the UDR2 is the calibration mode, shown in Fig. 2.32. In this mode the external inputs of the VA32HDR12 are disconnected and a well-known charge can be injected into each input stage. The amount of the injected charge can be varied using a

DAC on the UFE which is connected via a capacitor to the calibration input of the VA32HDR12.

A second feature of this mode is the variable delay between *sample & hold* and the clocking of the multiplexer. This allows to check if the internal timing of the VA32HDR12 has changed due to external effects like temperature and radiation damage.

This sequence is much more complicated than the normal read out, as the VA32HDR12 can only connect one input stage at a time to the external calibration pulse and needs to be reset before the next channel can be calibrated. Thus the calibration procedure is the following:

First the DAC is set to the desired value. As the setup time of the DAC is not negligible, one has to wait at least $5\,ms$ before starting the calibration sequence of the VA32HDR12.

In the beginning of the calibration sequence the VA32HDR12 is set to the test pulse mode. After a short hold time the input multiplexer is clocked to the desired channel. A short preparation time is required before the test pulse can be generated. An adjustable delay (0 to $6.3\,\mu s$) allows to sample the output of the shaper and select the optimal timing for the normal read out. After reading out a channel in the calibration mode a long delay ($20\,\mu s$) is required before the chip can be reset and the calibration sequence for the next channel can be started.

First measurement results

In order to verify the proper behaviour of the VA32HDR12 when using a specific sequence, extensive studies were done. These studies include e.g. pedestal taking, timing and linearity scans. Furthermore, long-term tests were performed. In the following part some of the results from these tests will be presented.

The first test with a new sequence is always to read a sufficient number of cycles and calculate the pedestals and their noise distribution. Some of the problematic features of the VA32HDR12 can be already observed in this measurement. For example, a problem with the first channel of a UFE was noticed, when using the same timing for all channels. The obvious solution was to use a slightly longer hold time ($1200\,ns$) for the first channel and standard timing ($600\,ns$) for all the others.

Both with the normal read out mode and with the calibration mode a timing scan can be performed. While this requires for the normal read out mode a special method for injecting charge into the inputs of the VA32HDR12 and an external adjustable delay unit, the calibration mode allows to do this without external hardware.

For this timing scan a constant signal is applied to the inputs of the VA32HDR12 and the time between the trigger and the read out is varied. The expected peaking time of the VA32HDR12 is $2.4\,\mu s$ [IDE00]. In the calibration sequence the delay can be chosen from 0 to $6.3\,\mu s$ in steps of $100\,ns$. A measurement performed using the S9007 setup is shown in Fig. 2.33.

A second feature of the calibration mode is the possibility to scan the input range of the VA32HDR12 with a test pulse and thus check the linearity of the VA32HDR12 and the ADC. The result of a measurement performed with the S9007 is shown in Fig. 2.34. It can be clearly seen that the VA32HDR12 has a linear range till ~ 3000 ADC counts. After this a slight deviation from the linear behaviour can be observed. This non-linearity is caused by the starting of the saturation of the VA32HDR12. The cut-off of the input range at 4096 ADC counts is caused by the upper limit of the input range of the $12\,bit$ ADC.

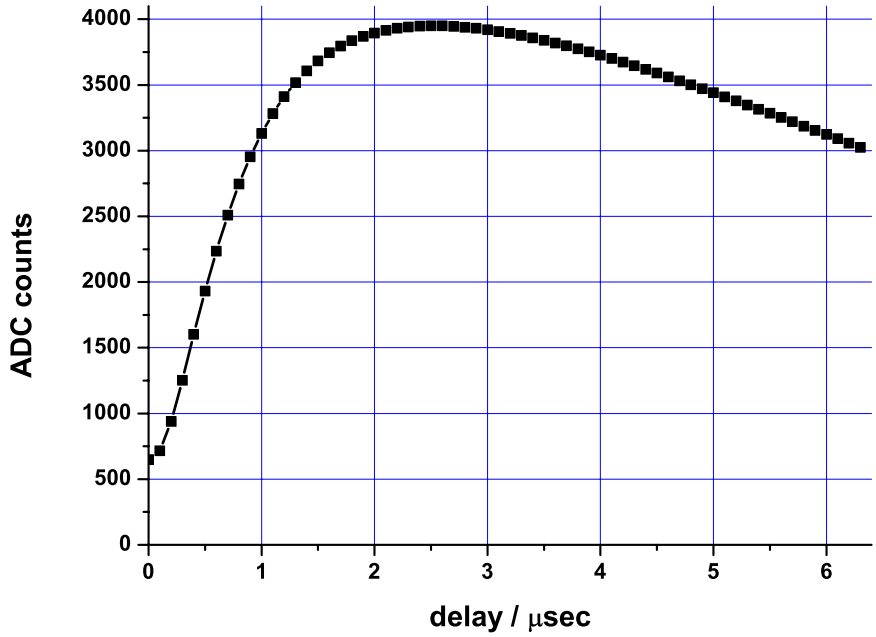

Figure 2.33: *The graph shows the output of channel 20 of a VA32HDR12 with different delays between the injection of the test pulse and the read out. The height of the test pulse was kept at a constant value during this measurement. This measurement was done using the S9007 setup. The maximum output of the VA32HDR12 was measured with a delay of* 2.4 *µs, as was stated in the data sheet of the ASIC.*

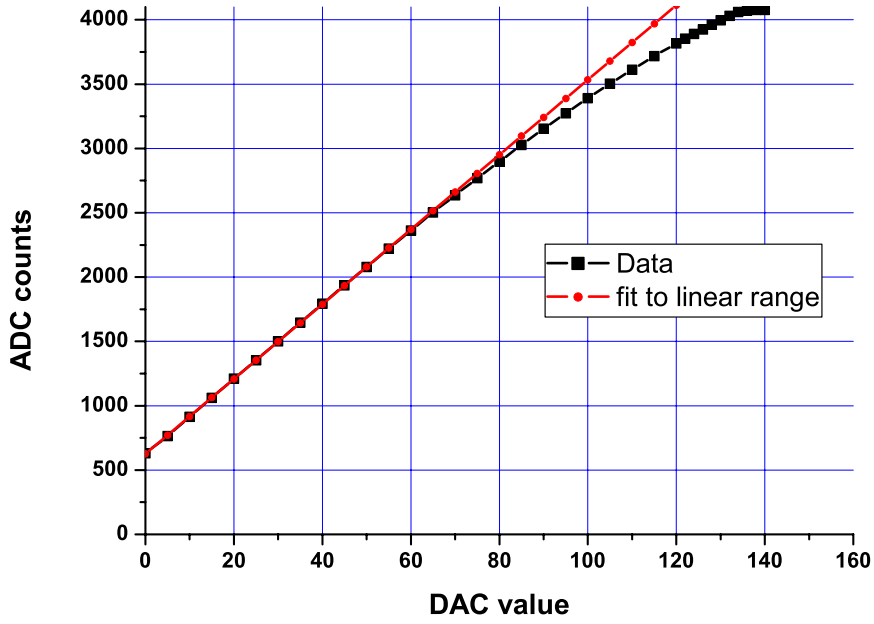

Figure 2.34: *The graph shows the output of channel 20 of a VA32HDR12 with different signal heights of the external test pulse set by the DAC on the UFE. The peaking time was kept at a constant value of* 2.4 *µs during this measurement. This measurement was done using the S9007 setup.*

The final check for a new sequence is the acquiring of a spectrum of either a radioactive source, cosmic rays or a beam test. All three methods have been used during the design and validation of the electronics and the software.

In the early stages of the development of the sequencer the spectra of radioactive sources like ^{55}Fe

and ^{90}Sr were acquired and compared to the expected distributions. An example for such a spectrum measured with the S9007 setup is shown in Fig. 2.35.

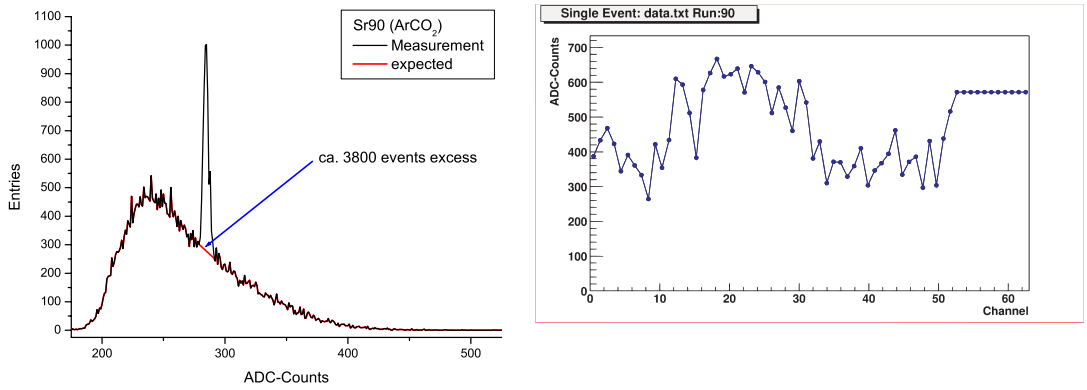

(a) Histogram

(b) Single Event

Figure 2.35: *This ^{90}Sr spectrum (a) was acquired with the S9007 setup using the optimal read out parameters. Due to a problem with the data transfer from the S9007 to the EPP port of the read out PC, some events showed a behaviour as depicted in (b). This problem never occurred with the UDR read out system.*

During the EM and the QM stages, beam tests (October 2002 and 2003) at CERN PS T9 were used to check the data acquisition system. During these measurements data was taken with different particles at various energies. The results from these tests will be presented in more detail in section 2.5.10. No data reduction was used during these measurements.

In spring 2004 a long-term setup was built in Karlsruhe to measure cosmic rays spectra. The main purpose of this setup was to check the long-term behaviour of the read out system and to verify the on-board data reduction in the UDR.

2.4.4 The UPSFEv2 Firmware Programme

In the scope of this thesis, a firmware for the Actel A54SX32A-TQ144 on the UPSFE and the UPSFEv2 was developed using the tools described in section 2.4.2. The main tasks of the firmware are the communication with its slow-control master via the LeCroy bus and the control and monitor functions for the linear regulators and the external lines of the UPSFE.

To achieve maximum portability to other slow-control cards in AMS02, e.g. TPSFE & S9011AU, and to allow multiple instances of the same code sequence for similar tasks a modular design approach was chosen. In Fig. 2.37 a schematic overview of the firmware and its modules is shown.

A schematic overview of the firmware is shown in Fig. 2.37. It consists of the *main entity*, which uses the *LeCroy Interface* to communicate with the slow-control master, the modules for the redundant set of linear regulators (*Linear Regulator A* & *Linear Regulator D*), the module for the second Actel (*Actel*) and those for the external control and monitor lines (*JINF*, *UDR* & *UHVG*).

All inputs into the firmware, with the exception of the geometrical address and */reset*, are sampled using the external 2MHz oscillator to prevent any malfunctioning due to unwanted short term level changes on the lines, as shown in Fig. 2.36. The LeCroy clock is sampled using a more sophisticated "deglitch" algorithm, which checks and compares the level for two master clock cycles.

The external signal */reset* is provided by the solid state fuse on the UPSFEv2 and is used to set all registers and outputs of the UPSFEv2 FPGA in a defined state after power-on.

The *LeCroy Interface* (LCI) handles the communication with the JINFv2 using the LeCroy protocol, see 2.3.13. The LCI is connected to the outside world via the LeCroy clock and data lines as well as the geometrical address. The geometrical address is equal to the slot number in which the

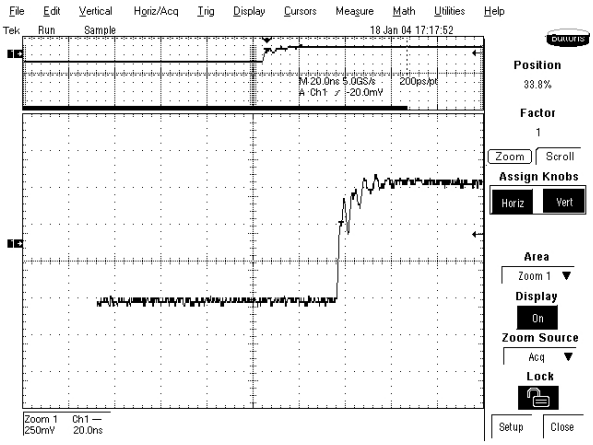

Figure 2.36: *This screenshot shows some of the oscillations observed on the LeCroy lines on the UBP. These oscillations due to reflections caused problems in the non-clocked logic. Therefore all inputs are sampled using an external* 2 *MHz quartz oscillator.*

UPSFEv2 is placed. It is 5 bit wide, but only 4 bits are used in the firmware, as the U-crate has only 16 slots.

Even though the LeCroy bus is only specified for 100 *kHz*, the communication with the UPSFEv2 is still fully operational at 500 *kHz*. This is especially important, since it minimises the occupancy of the JINFv2, which has taken over the slow-control functionality after the weight reduction.

The *main entity* (ME) and the LCI communicate via a set of lines. One of the lines, *sample*, tells the ME when it should read the actual status of the monitor lines and provide this information in the *reply*. This *reply* can also hold other information, like counter values. The *R/W* tells the ME, if the LeCroy transfer was a read-request or a command. Parameters for commands are set via the *data* lines. And *commit* tells the ME when a command should be executed.

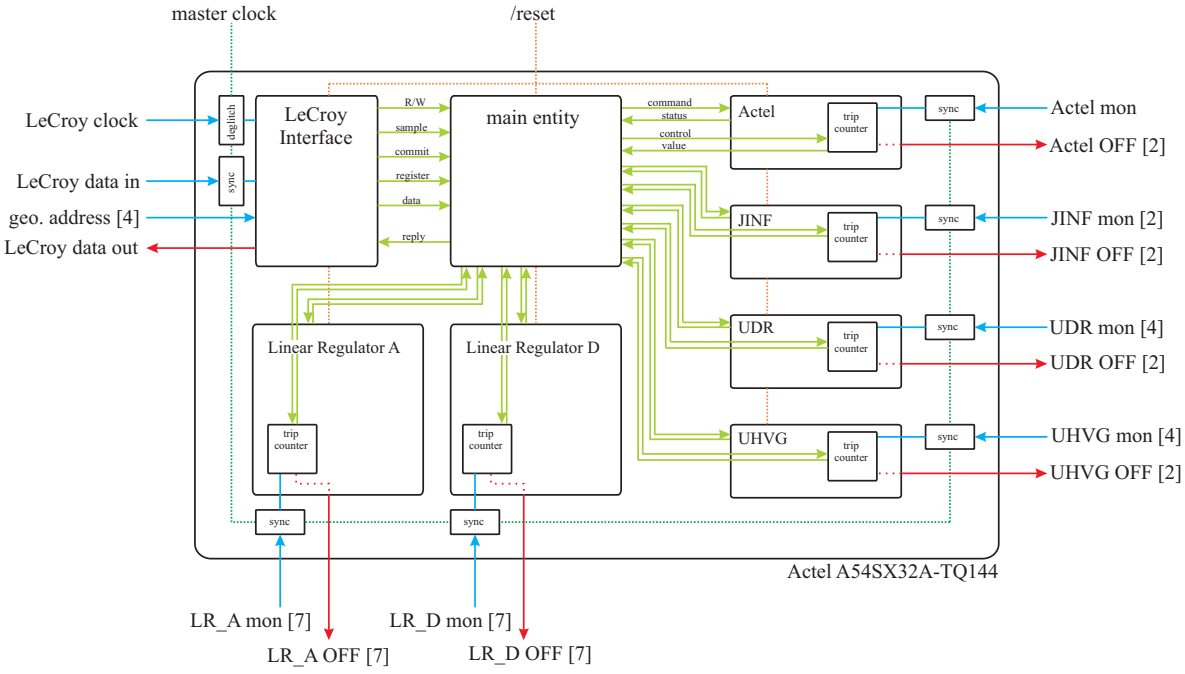

Figure 2.37: *A schematic drawing of the firmware of the UPSFEv2, showing the various submodules and the respective interconnections as well as the I/O ports.*

The control and monitor features of the UPSFEv2 are grouped in 3 different classes in the firmware

according to their functions. One class for the linear regulators, one for the second Actel and one for the external lines for JINF, UDR and UHVG.

Each of the modules for the linear regulator controls and monitors one of the two redundant sets of regulators. For each regulator the modules feature one control and one monitor register and a 4 *bit* trip counter, which is driven by the monitor line of the regulator. The values of the counters are mapped to registers in the ME, which can be read back via the LeCroy bus resetting them at the same time.

The modules *Actel*, *JINF*, *UDR* and *UHVG* have the same functionality as the modules for the linear regulators, but they control and monitor both sets of redundant parts.

The major difference between the *Actel* module and all others is the automatic disable feature, which is implemented in all modules, but not in the *Actel* module. This automatic disable feature, which is by default not active, allows the firmware to switch off a device if the trip counter has reached its maximum value of 15.

A detailed manual for the UPSFEv2 firmware can be found in Appendix B, together with an introduction into the commanding software for the UPSFEv2 written by Alexei Lebedev.

2.4.5 The S9011AU Firmware Programme

The firmware of the S9011AU is based on the code for the UPSFEv2. Since the S9011AU has much less functionality than the UPSFEv2 the firmware has been adapted to this and is much simpler.

For the S9011AU firmware the modular approach was used again. This allowed to re-use some parts of the UPSFEv2 code without or with only minor modifications. The firmware consists again of a *main entity*, the *LeCroy Interface*, the *Actel* module and two modules (*DC/DC converter L* & *DC/DC converter H*) for controlling and monitoring the two redundant halves of the DC/DC converters connected to the S9011AU. The schematic drawing in Fig. 2.38 gives a good overview of the firmware of the S9011AU and its modules.

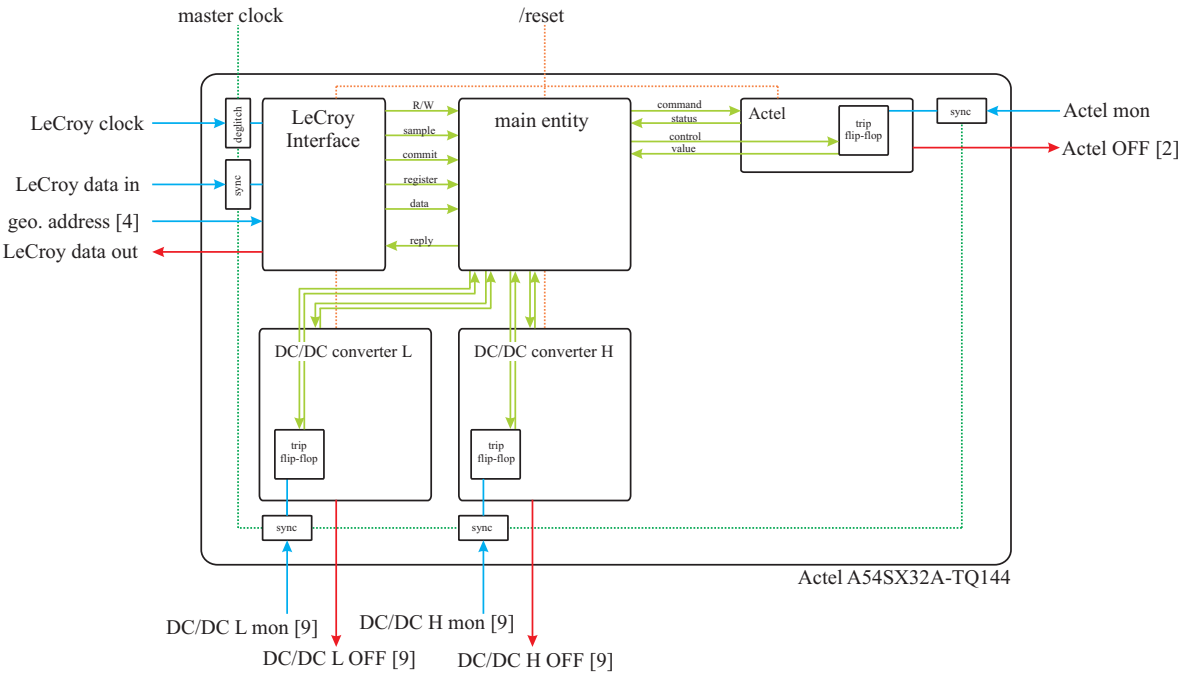

Figure 2.38: *A schematic drawing of the firmware of the S9011AU, showing the various submodules and the respective interconnections as well as the I/O ports.*

In the S9011AU, like in the UPSFEv2, all inputs, with the exception of the geometrical address, are sampled using the external 2 *MHz* oscillator to prevent problems originated by short term fluctuations on the lines. Again, the LeCroy clock line is protected by a more sophisticated “deglitch”

module, as this line drives most of the logic in the FPGA.

As the *main entity* and the *LeCroy Interface* are almost identical to the code of the UPSFEv2, they use the same links for data exchange and synchronisation. In principle a second LeCroy Interface is foreseen for each FPGA on the PCB of the S9011AU, but this option is not used, as there are no free LeCroy links available in the U-crate. The second LeCroy link would also require additional logic to prevent malfunctioning if both links are active at the same time.

Like for the UPSFEv2 the LeCroy clock frequency for the communication with the S9011AU can be operated at up to $500\,kHz$, exceeding the specifications by a factor of 5.

Unlike in the UPSFEv2 there are no trip counters in the S9011AU firmware. In the occurrence of a trip of either a DC/DC converter or the solid-state fuse of the other Actel a flip-flop is set. The status of these flip-flops can be read back via the LeCroy link, which also resets the flip-flops.

Together with a short description of the commanding software for the S9011AU, written by Alexei Lebedev, a detailed manual for the S9011AU can be found in Appendix C.

2.5 Production and Qualification

2.5.1 Design Process & Production Procedures

The design process of the electronics for the AMS02 experiment is divided into four parts. The first stage is the prototyping. After this an engineering model is built, before the qualification model is produced. The final product flown into space is the flight model.

In the following paragraphs this design process will be described with the help of the example of the data reduction board (UDR) for the TRD.

Prototyping

The first stage of the design flow is the prototyping phase. In this phase the principle design is chosen and a first version of the board, often a multi-purpose board, is built.

In the case of the data reduction boards this prototype board was the S9007. It consists of the same core components as the final device, namely a DSP, an FPGA and a memory chip. All detector specific components were connected to the S9007 as piggy-back PCBs. A picture of this board is shown in Fig. 2.30(b).

With this prototype a set of functional tests is performed in order to verify that the performance of the design is within the requirements.

Engineering Modules - EM

The next stage of the design process is the engineering phase. In this stage the PCB design is as close as possible to the final design. The main difference to the following stages is the usage of non-space-qualified components on the PCBs.

With these Engineering Modules (EM) a first integration test is performed to verify the system design. In the example of the UDR, these boards were also used during a beam test, see section 2.5.10, to check the performance of the detector modules and the front-end hybrids.

Qualification Modules - QM

The qualification stage is one of the most important phases of the design process of space-grade electronics. This is the first time an electronics module is built exactly the way it will be flown during the mission.

The PCB design is frozen before the Qualification Module (QM) production. Only minor changes are allowed from QM to the final production. The qualification modules are submitted to the full spectrum of tests to verify the design of the individual board.

The tests performed on the QM boards include thermo-vacuum tests, vibration and integration tests. A part of the integration tests can be beam tests. These tests allow not only to test the individual board, but also the complete system.

As some of the electronic boards are produced in Taiwan, the production and design flow of AMS02 has one peculiarity: it has 2 qualification module steppings. The first one (QM1) is produced in Europe and is used to verify the design of the electronics. The second iteration (QM2) is produced in Taiwan by the institute that will also produce the final flight electronics. The QM2 is used to qualify the production in Taiwan.

The QM2 level is the first time in the production line, that a crate fully equipped with boards will be available for system integration and qualification tests.

Flight Modules - FM

In the final phase the Flight Modules (FM) and the Flight Spares (FS) are produced. These boards will also undergo some qualification tests, but not to the level of the QM boards, as this would pose too high a risk of damaging the boards before they are integrated into the experiment.

Production Procedures

A diagram of the production procedure is shown in Fig. 2.39. Once the electronics boards have successfully undergone all space qualification tests the schematics and the layout of the PCBs are transferred to the institute producing the PCBs together with the bill of material (BOM). The file format chosen for this transfer is an industrial standard format called Gerber. It contains all information on the lines like position, thickness and width.

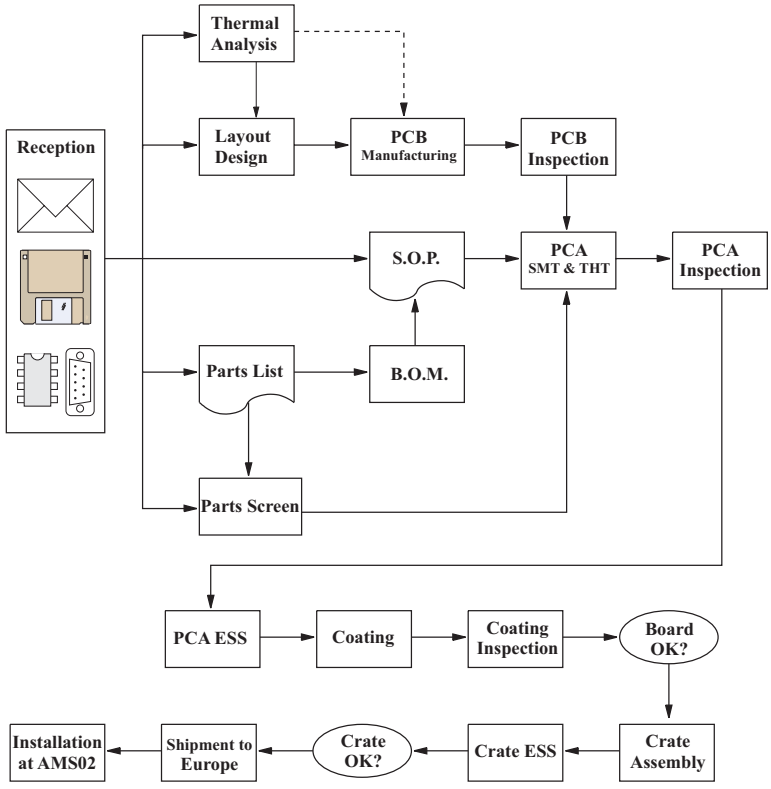

Figure 2.39: *The production scheme of the electronic boards, as it is implemented for the AMS02 experiment. The various production steps and the quality assurance tests are shown. [Drawing by Georg Schwering]*

As all PCBs used in AMS02 are of multi-layer type, the PCBs are produced by manufacturing all layers separately and laminating them together. Each layer is optically inspected after production. The complete stack of the layers is then checked after the laminating using X-ray systems. Once the boards have passed this test, vias are drilled and the contacts are grown.

When the naked board is completed, the assembly of the board (PCA) starts. All components used are either space-grade or they are specially screened before the PCA.

The fully assembled board then has to pass a functional test to verify that it is fully operational. After this test the board is coated. The next step in the production is the environmental stress screening (ESS). During this test, the temperature of the board is varied from the minimum non-operational to the minimum operational on to the maximum operational and finally to the maximum non-operational temperature. This cycle is done a few times. After the ESS the boards have to pass a second functional test to verify they still work within the specifications. Finally the boards are put into a climate controlled clean storage, where they are kept till the assembly of the detector.

2.5.2 Space Qualification Procedure

All electronics boards must undergo a qualification procedure after their production. These tests can be classified into two groups: the single board level test and the crate level tests.

Single Board Level Tests

The single board level tests are done directly after the production of the electronics boards, as shown in Fig. 2.40. The first step of the testing is an inspection of the boards by the Chung-Shan Institute of Science and Technology (CSIST) using visible light and X-rays.

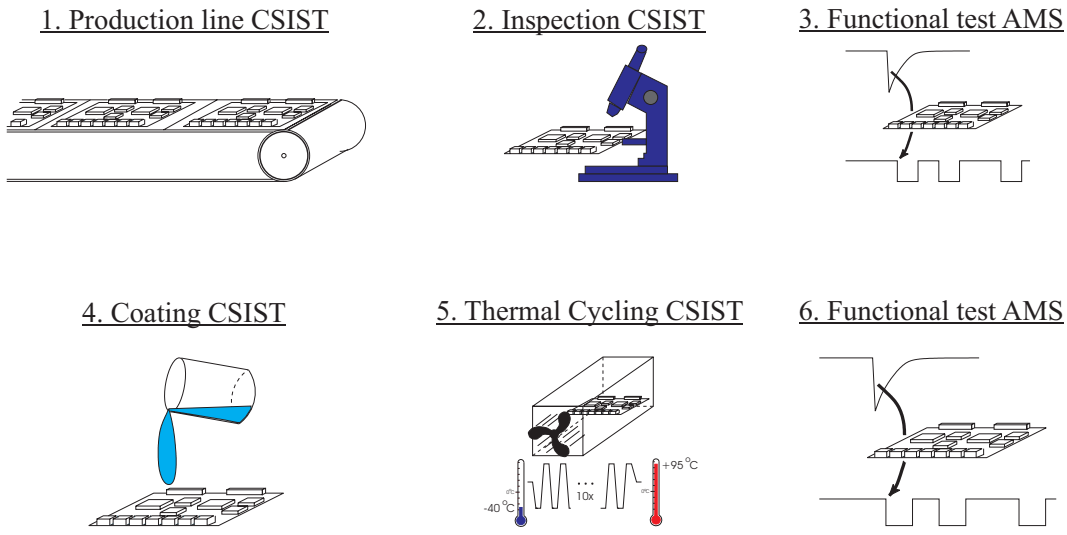

Figure 2.40: *The qualification scheme, on single board level, implemented by AMS for the electronics production at CSIST. [based on a drawing by Georg Schwering]*

The second stage is a functional test of the board. Depending on the type of board this step requires quite a lot of additional equipment, e.g. a test backplane as it is described later on in this section.

During these functional tests all features of the various cards must be tested. For the UPSFEv2, for example, this means testing the communication with the FPGA, all linear regulators on the board and all external control and feed-back lines.

If the boards pass this first round of functional testing, they are protected by the application of conformal coating. Afterwards they are put into a climate chamber and thermally cycled. After this

environmental stress test (ESS), the boards have to undergo the functional testing again. At the end of these tests, the boards are stored in clean-room conditions till the assembly of the box/crate.

Crate Level Tests

Once all boards required for a full crate are produced and have passed the single board level tests, a crate is assembled and will undergo careful testing. The set of tests is depicted in Fig. 2.41.

The first test for the full crate is a system test. In this test all functionality of the crate is studied in great detail to minimise the risk of a system failure during the following tests or even during the mission.

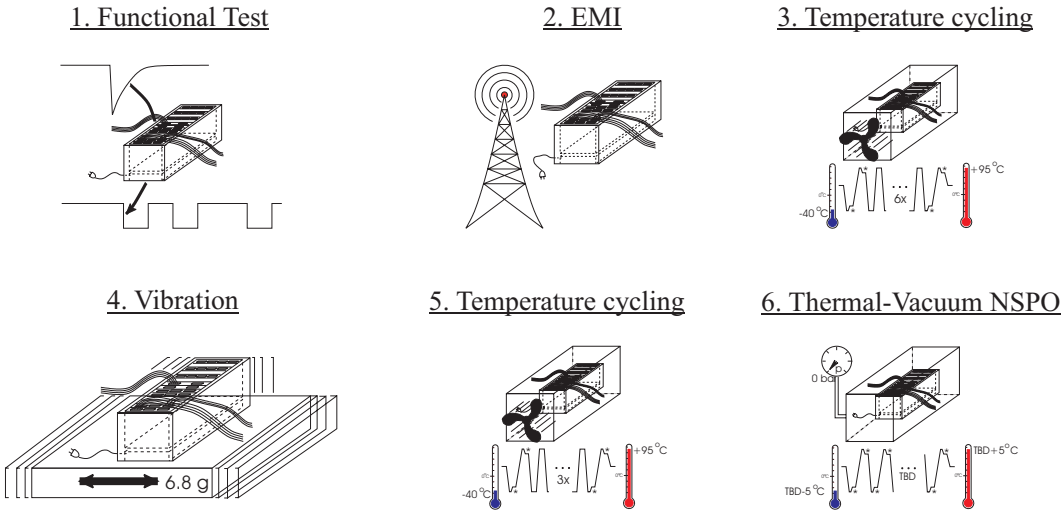

Figure 2.41: *The qualification scheme, on crate level, implemented by AMS for the electronics production at CSIST. Each step includes functional testing, both during and after stress test. [based on a drawing by Georg Schwering]*

After the initial system test, the crate is put into an electromagnetically shielded chamber and subjected to an EMI test. This test is followed by a first thermal stress test. Then a vibration test is done. The crate is again thermally cycled afterwards. The final test for the crate is a thermo-vacuum test. During all these tests the crate is operated, at least partially, and the availability of all functions at all times is tested.

2.5.3 Electro-Magnetic Interference Test - EMI Test

In this test the conformity of a device with the stringent requirements by NASA for the use inside the Space Shuttle and on the ISS on the electromagnetic sensitivity and amount of emitted electromagnetic radiation is checked.

To do this the device is placed in a room, which is electromagnetically shielded, together with an emitter and a receiver. The setup used is shown in Fig. 2.42. Using the emitter a well defined spectrum is sent and the response of the device under test is recorded using the receiver while at the same time the functionality of the device is monitored.

This receiver is also used to record the spectrum emitted by the device during different modes of operation. The spectrum of interest ranges from $10\,kHz$ to $1\,GHz$ and the electrical field strength from 5 to $100\,V/m$.

Figure 2.42: *The picture was taken during the EMI test of a TRD prototype at the MPE in Garching. From left to right one can see the electric field sensor (black globe), the TRD prototype (wrapped in MLI) and the antenna of the emitter. [S. Schael, AMS02 TIM April 2003]*

2.5.4 Environmental Stress Screening Test - ESS

The Environmental Stress Screening Test is used to find problems in the electronics related to thermal issues. It is a rather fast test done in a thermal chamber under normal atmospheric conditions. The profile of the thermal cycle is shown in Fig. 2.43.

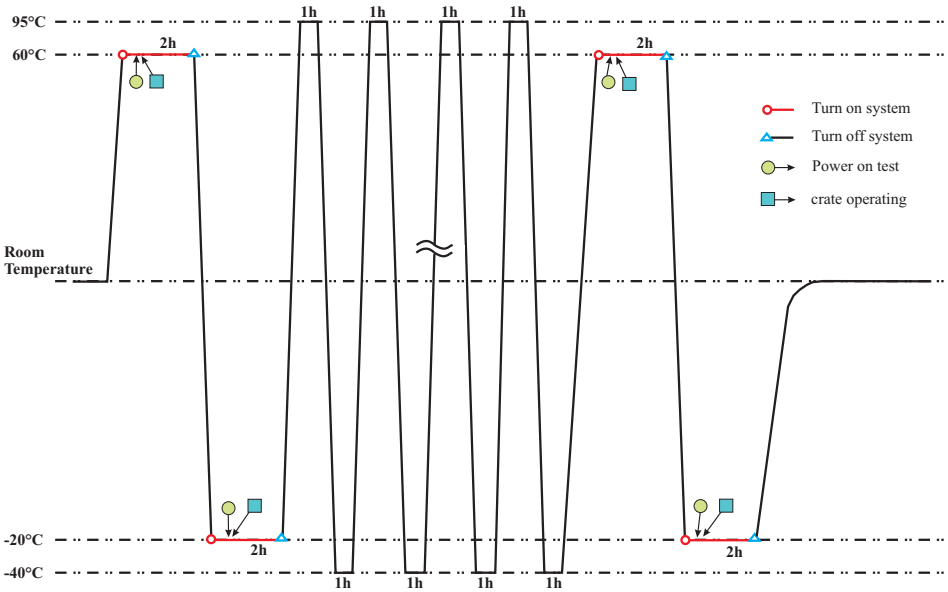

Figure 2.43: *This plot shows the thermal cycle as it is used for the ESS tests for the qualification procedure at CSIST. The board is brought ten times to the maximum and the minimum storage temperature and is operated at the beginning and at the end of the ESS for some time at the maximum and the minimum operational temperature. [after Yuan T. Ting, AMS02 TIM July 2004]*

This test is used on the single board level to find possible problems due to bad contacts or problems in the PCB. The board is only operated if it can be run as a stand-alone system, like the DC/DC converters. All other boards undergo a functional testing before and after the ESS.

On the crate level the tests are more thorough. Not only is the crate thermally cycled, but it is also powered on at maximum and minimum operational temperatures to verify the system can be started after being outside the operational temperature limits. Also a full functional test is done once the crate is powered up successfully.

2.5.5 Vibration Test

The vibration test is used to simulate the mechanical stress on a device, that is imposed on it during the launch of the carrier vehicle, e.g. the Space Shuttle. The mechanical load can be divided into two parts: the constant load, due to the acceleration of the rocket, and the vibrations.

The acceleration of the Space Shuttle is limited by the on-board guidance systems to $3g$. This constant load is simulated using a centrifuge-like construction.

On top of the constant load there are random vibrations. These vibrations are simulated using a so-called shaker. Fig. 2.44 shows such a shaker, in a horizontal configuration, as it was used for the tests of the DC/DC converters.

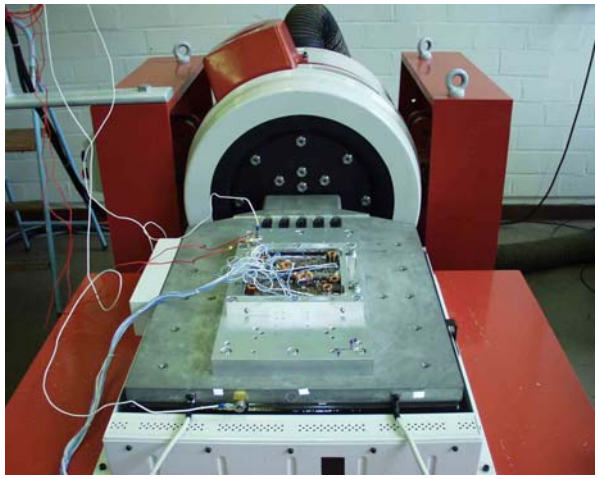

Figure 2.44: *Vibration test of a QM1 DC/DC converter at the vibration facility of the RWTH in Aachen. [Hau05]*

The device is vibrated along all three spatial axes in two different modes. The first mode is the so-called sine sweep, in the second mode random vibrations are used.

In the sine sweep the device is vibrated using sine waves. The frequency of these waves is varied from 10 to 2000 Hz with a constant acceleration of $0.5g$. This mode is used to find the eigenfrequencies of the system under test. According to the regulations of NASA the first significant eigenfrequency has to be above $50\,Hz$, as most of the vibrations at the launch have a frequency below this value.

The second mode, the random sweep, simulates a more realistic scenario. The device is vibrated with a spectrum of waves ranging from 80 to $500\,Hz$ with a RMS value of $6.8g$ for $90\,s$ and the response of the system is recorded. In this mode the Acceleration Spectral Density has a value of $0.04\,g^2/Hz$.

2.5.6 Thermo-Vacuum Test - TVT

In the TVT the environment in space is simulated, with regards to atmosphere and temperatures. This is especially important, as it will show for the first time if the crate will be operational under space conditions.

Fig. 2.45(a) shows one of the TVT chambers at NPSO in Taiwan. This TVT chamber will be used for the crate level tests of the TRD electronics. The crate will be mounted on the heat exchanger plate inside the vacuum chamber and the temperature will be varied according to the specifications shown in Fig. 2.45(b). The pressure inside the chamber will be $10^{-5}\,mbar$. During this test the crate will be operational for most of the time.

In the thermal model of the crate and the detector, a lot of assumptions and predictions about the heat generation and transfer are used. Based on these the temperatures of the crate during the various situations on the ISS are calculated. One of the main purposes of the TVT is to compare the thermal model of the crate with the reality.

To achieve good measurement results for the thermal properties of the crate, quite a lot of temperature sensors are used. They are located in the critical places in the crate (most temperature sensitive & power consuming components) and on the contact to the heat exchanger. The last set of sensors is used for reference points and for the thermal balance measurements.

(a) TVT Chamber

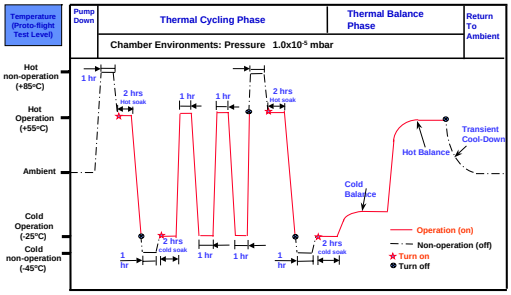

(b) Thermal Cycle

Figure 2.45: *(a) One of the TVT chambers at the NSPO in Taiwan. This one will be used for the TVT of the TRD crate. (b) The temperature profile used for the TVT at the NSPO facility. [Jih-Run Tsai, AMS02 TIM July 2004]*

2.5.7 EM test backplane

The EM test backplane, shown in Fig. 2.46, was developed to verify the design of the engineering modules of the UDR and the UPSFE, as well as that of the UFE. It was successfully used during a beam test in October 2002 at the Proton Synchrotron (PS) facility at CERN for data acquisition.

The EM test backplane has one slot for an UDR and two slots for a pair of UPSFEs. This configuration allows to test the functionality of the UDR and the redundant power supply via the two UPSFEs.

One of the features of the EM test backplane is, that it has shunt resistors in all power lines, to and between the cards, thus it allows to accurately measure the power consumption of each card. These values are very important for the estimation of the total power consumption of the TRD electronics crates.

This setup was also used during the firmware development of the UDR and the UPSFE. As the EM boards were not required to be space grade, the FPGAs used on both types of boards were reconfigurable, thus making the development easier and faster.

After the initial tests of the UDR and the UPSFE in this configuration were passed successfully, the final test before the “go ahead” for the development of the QM1 boards was a beam test in October 2002 at the PS facility at CERN.

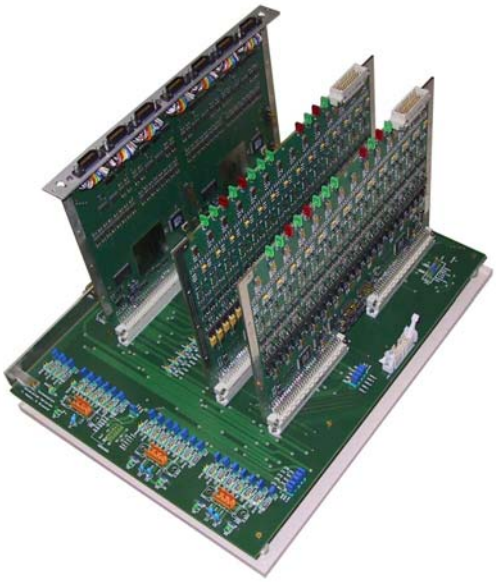

Figure 2.46: *The EM test backplane.*

During this beam test some minor issues, e.g. with the timing sequence for the front-end hybrid, where discovered and solved in the months afterwards.

A more detailed description of the EM test backplane can be found in [Brü02].

2.5.8 QM1 test backplane

The QM1 test backplane was developed to verify the design of the qualification modules of the UDR and the UPSFE, as well as the system design. It was successfully used during a beam test in October 2003 at the PS facility at CERN for data acquisition together with QM1 versions of the UDR and the UPSFE. A picture of the test backplane with a UDR and a UPSFE plugged in is shown in Fig. 2.47.

The QM1 test back plane allows for the first time to test a full power group, the basic unit of the TRD DAQ crate. This power group consisted, before the weight reduction, of two UDRs and two UPSFEs and will consist of two UDRs and one UPSFE in the flight configuration.

Like in the EM version, the QM1 test backplane allows the measuring of the currents on all power lines to and between the cards via shunt resistors. The currents measured on the QM1 & QM2 boards allow a very precise prediction of the power consumption of the final boards for the flight.

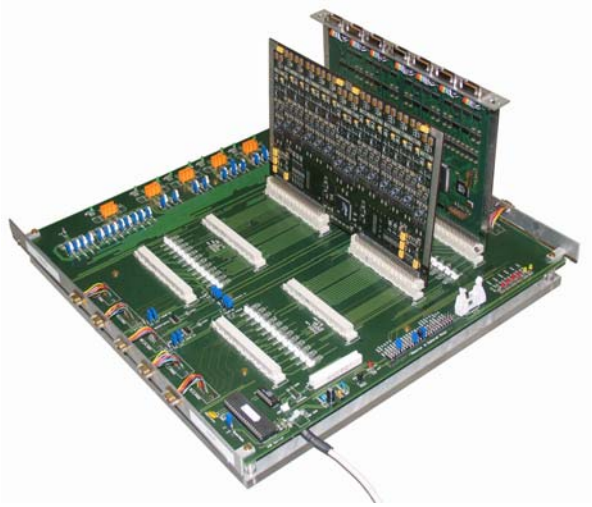

Figure 2.47: *The QM backplane was developed to verify the design of the qualification modules of the UDR and the UPSFE. It was used during a test-beam in October 2003 at the PS at CERN for data acquisition.*

Most of the functionality of the UPSFE can be tested on the QM1 test backplane. All vital lines of the UPSFE are connected. The LeCroy links of the FPGAs can be accessed via flat band cable connectors. Also the digital temperature sensors on the UPSFE can be accessed via such a connector. The external control & monitor lines for the UDRs are directly connected, while the lines for the UHVGs and the JINF are connected to jumpers or LEDs. The geometrical (= slot) address of the UPSFE can be set via five jumpers.

For both UDRs the 4 AMSwire links and the Trigger and Busy lines can be accessed separately. The Trigger and Busy signals are converted from LVDS (external) to LVTTL (internal) on the test backplane.

The QM1 test backplane also features a variable load circuitry, that can be used to test the solid state fuses on the UDR, which protect the CDPs. This circuitry can be controlled by a computer via a IO-Warrior40 IC located on the test backplane.

In October 2003 the QM1 test backplane was successfully used for the data acquisition system during a beam test at the PS facility at CERN.

In the same time frame the collaboration made the decision, that a weight saving effort was to be done for the electronics of the AMS02 experiment, to get back inside the weight budget. One of the suggestions was the removal of one UPSFE from each power group. This opened some concerns, like “Would the increased power consumption per linear regulator pose a problem?” or “Would the powering of analog and digital parts from the same source increase the noise?”. These issues were checked using the test backplane and the outcome showed that no significant performance loss was observed due to this modifications.

Another application of the QM1 test backplane is the quality control of the production in Taiwan. There the board was used to do the functional testing of the QM2 UDRs and will be used again for the FM/FS production.

2.5.9 UPSFEv2 test backplane

The requirements for the functional testing of the UPSFEv2 called for a specific setup for this purpose. Within the framework of this thesis and a master thesis [Egg04] a test backplane, see Fig. 2.48, was designed that allows to test all features of the UPSFEv2.

The communication from the Linux control computer to the UPSFEv2 is established via an EPP-CAN box, designed by Vladimir Koutsenko, and an USCM sitting in a miniature backplane [Cam01]. The USCM acts as an interpreter converting the CAN-bus commands to LeCroy commands for the

UPSFEv2. The software used for controlling the UPSFEv2 is described in Appendix B. The connectors on the test backplane are placed close to the UPSFEv2 slot in the top left corner of the PCB.

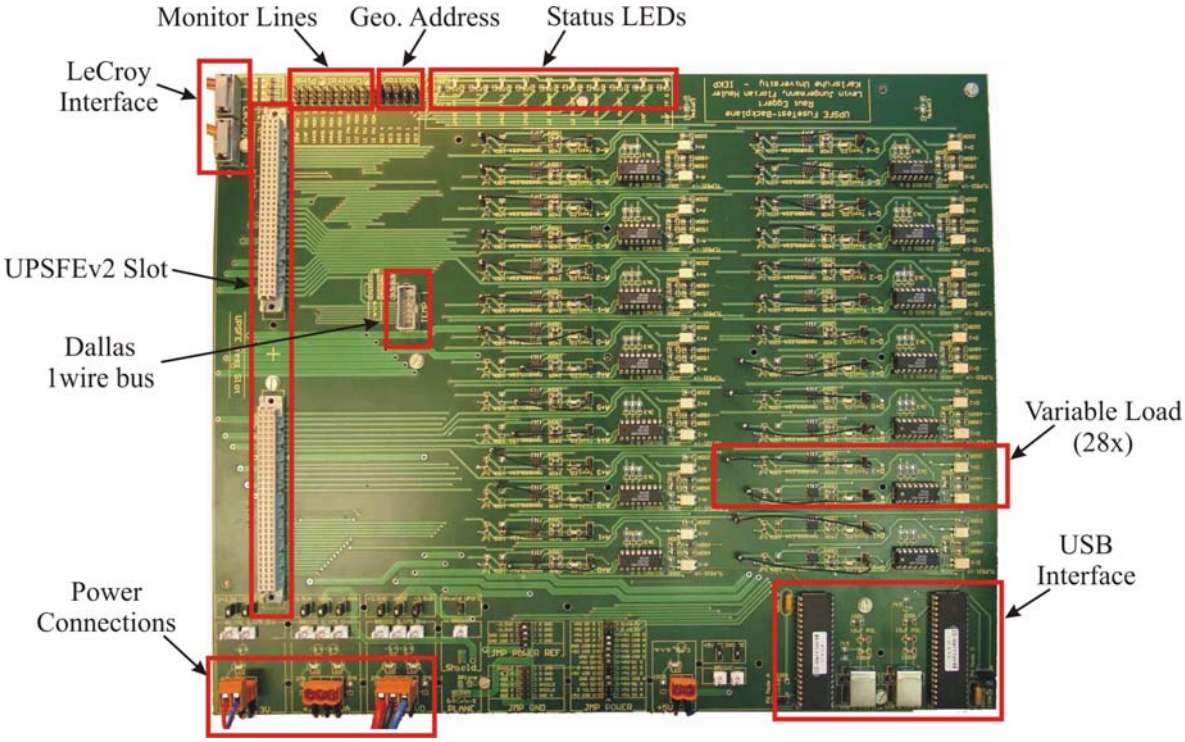

Figure 2.48: *The UPSFEv2 test backplane. Clearly visible are the slot for the UPSFE on the left and the MOSFETs, used as variable loads, on the right side of the PCB. The actual load resistors are mounted on the bottom of the test backplane. One can also see the power connections (bottom left corner) and the computer interface ICs (bottom right corner).*

The two digital temperature sensors (DS18S20) on UPSFEv2, located close to the linear regulators, can also be accessed from the computer via the EPP-CAN box and the USCM. The flat band cable connector is situated to the right of the UPSFEv2 slot.

The status of all external control lines can be checked with the LEDs on the test backplane. In Fig. 2.48 they are located on the top side in the middle. The jumpers left of the status LED block allow to set the external monitor lines of the UPSFEv2.

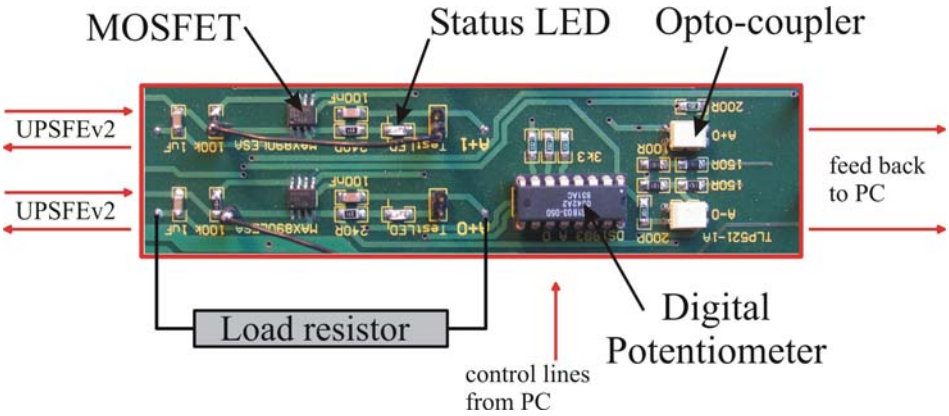

Figure 2.49: *A close-up picture of the Linear Regulator test circuitry as it is implemented on the UPSFEv2 test backplane. As the digital potentiometer is a two-channel device, the variable loads are always grouped in a pair.*

The most important function of the test backplane is the testing of the linear regulators on the UPSFEv2 and their self protection systems. For all 14 linear regulators the (+) and the (-) branch can be tested independently. This is necessary because the over current protection of the linear regulators is implemented separately for the two branches. In total 28 test circuits are required.

Due to this high number of channels, which were causing addressing problems on the control bus, it was decided to organise load circuits on the test backplane in two completely independent parts. Both parts, clearly visible in Fig. 2.48, consist of seven 2-channel potentiometers each controlling two MOSFETs.

The design of the test circuitry, see Fig. 2.49, for the linear regulators is based on an application note for an adjustable load using the MAX890L by Maxim [Dal00]. This MOSFET IC can be controlled via an external potentiometer. In our case this was implemented using a digital potentiometer. This potentiometer can be interfaced to a μController using a 2-wire serial bus compatible with I^2C, an industrial standard defined by Philips Semiconductors [Phi00].

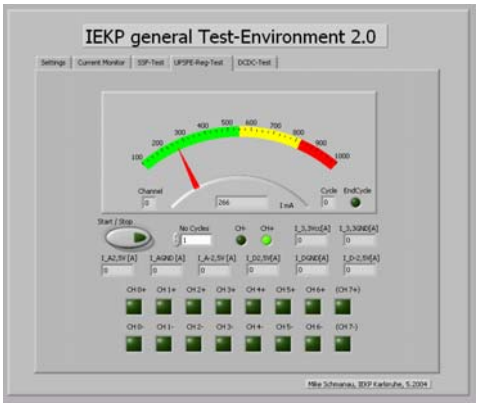

Figure 2.50: *A screen shot of the Software for controlling the UPSFE test backplane.*

The status of each channel, (+) and (-) of one linear regulator, is indicated by LEDs and can be read back into the computer controlling the test backplane via opto-couplers and the μController. Fig. 2.50 shows a screenshot of the LabView software on the PC.

Figure 2.51: *The UPSFEv2 test setup, as it was used during the quality control of the QM2 production at CSIST in Taiwan. The setup from left to right: The laptop computer was used to control the USPFEv2 via an EPPCAN box and an USCM. The oscilloscope is needed for the measurement of the timing of the solid-state fuses and the linear regulators. Next is the UPSFEv2 itself, sitting in the UPSFEv2 test backplane. On its right are two power supplies, one for the digital part, one for the analog part together with the digital multi-meter used for monitoring the currents. The computer used to control the DMM and to log the data from it is located right next to it.*

The two μControllers used on the test backplane are of the type IO-Warrior40 produced by Code Mercenaries. These μControllers have one USB link, and 32 IO pins. Due to the limitations of the USB port the communication data word rate is $\sim 120\,Hz$. Two of the IO pins can be used in a special

mode as I^2C interface, which is much faster. The implementation of the PC interface is based on an article in the *c't* [Mey03] and the data sheet of the IO-Warrior40 [Cod03].

This setup was also used during the quality control of the production of the QM2 modules at CSIST in Taiwan. Fig. 2.51 shows the setup in the lab in Taiwan.

A detailed description, including all schematics, of the UPSFEv2 test backplane can be found in [Egg04].

2.5.10 Beam Tests

The optimal test for the verification of a read out system and its software is to acquire "real" data in a well understood setup and compare it to previous measurements and simulations. For the TRD electronics this was done twice, once with the EM setup and then again with the QM1 setup.

Both tests were done at the PS-T9 facility at CERN [Dur93]. The particles used during the tests were electrons and protons with energies ranging from $3\,GeV$ to $15\,GeV$. The results obtained were compared to simulations done with GEANT3 (Fortran based) and GEANT4 (C++ based) [Ago03].

EM beam test - October 2002

The first beam test for the TRD electronics was done in October 2002 at the PS/T9 facility at CERN. The setup is shown in Fig. 2.52. The read out of the detector modules was done using the EM versions of the UDR, the UPSFE and the UFE. Since at this moment no full backplane was available, a mini-backplane designed at the IEKP was used (see section 2.5.7). This mini-backplane housed 2 UPSFEs and 1 UDR. The connection to the PC was established via the S9007, which acted as EPP to AMSwire interface. The high voltage for the TRD prototype modules was generated using a LeCroy HV system, as the UHVG was not yet available.

Figure 2.52: *The setup used during the beam test at the PS facility at CERN in October 2002. The beam entered from the right side of the picture and then passed through a set of trigger scintillators, prototype scintillators for the anti-counters of AMS02, hidden beneath the cloth, through the two TRD jigs and finally through a Multi-Wire Proportional Chamber (MWPC), which was not used during our measurements.*

Two detector prototype jigs were used for this test. Both jigs housed 4 strawtube-modules with 16 tubes each and radiator fleece between the layers. The upstream module was the so-called “EMI-jig”, which is built from carbon-fibre plates like the final large scale detector. The so-called “vibration jig” was placed downstream, as it contains a lot of aluminum.

The trigger for the read out system was generated using the coincidence of 4 scintillators, placed before and after the TRD jigs, together with the coincidence or anti-coincidence of two Cherenkov counters upstream of the setup.

A second purpose of this beam test was to evaluate the physics performance of strawtube modules, which were built using tubes that had an additional $9\,\mu m$ Parylene-C coating, which was thought to improve the gas tightness [Kir02]. The results of these measurements are shown in Fig. 2.53. All strawtubes were constantly flushed with $ArCO_2$ in a 80:20 mixture. Gas pressure and temperature were constantly monitored and recorded.

The chambers built with the Parylene coated strawtubes showed, as expected, a smaller response to the transition radiation photons, while not improving gas tightness as much as hoped. Thus this modification of the strawtubes was discontinued.

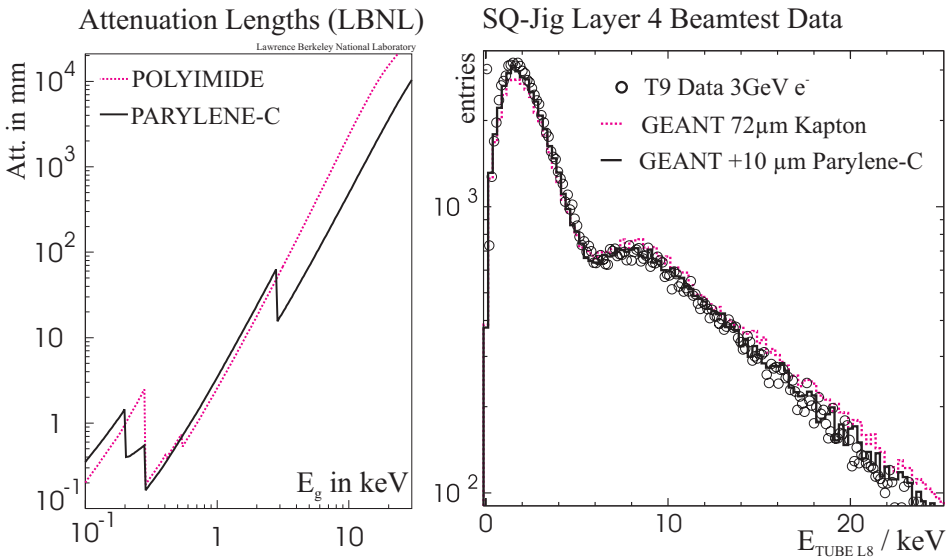

Figure 2.53: *(Left) A comparison of the attenuation lengths of Polyamide and Parylene. (Right) Data from the beam test in October 2002, taken with the Parylene coated chamber, compared to the simulations done with Geant3. [Kir02].*

QM1 beam test - October 2003

The purpose of the beam test in October 2003 was to check the QM1 version of the TRD read out electronics. For the first time physics data was taken with a complete set of cards on a full-scale backplane. The electrical power was supplied using EM versions of the DC/DC converters.

In Fig. 2.54(a) the setup used for the measurements is depicted. One can clearly distinguish the EMI jig housing the strawtube modules connected to the read out, the trigger scintillators and the gas supply system. The path of the beam is indicated by the white arrows.

Fig. 2.54(b) shows the QM1 backplane (UBP) with the following cards plugged in (from left to right): UDR2, UPSFE, JINF, USCM and UHVG. The connection from the “crate” to the DAQ computer (not shown) was established via AMSwire using a PCI-AMSwire card [Lin02].

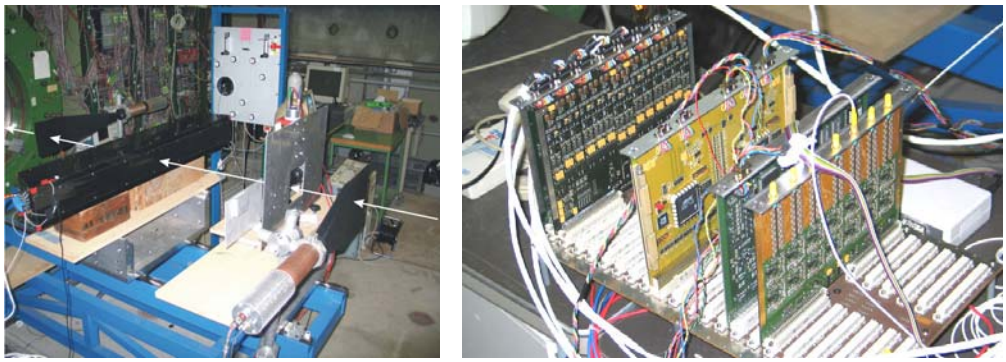

(a) Detector Setup (b) DAQ Electronics

Figure 2.54: *The setup used during the beam test at the PS facility at CERN in October 2003. (a) shows the detector prototype and the scintillators, (b) shows the read out electronics. The path of the beam is shown by the white arrows. The trigger for the DAQ chain was made by a coincidence of the four scintillator counters up and down stream of the TRD prototype and the two Cherenkov counters in the beam line.*

During the setup the chambers were flushed with $ArCO_2$, as during the beam test in October 2002. To simulate the conditions of the TRD detector on the ISS as close as possible, the strawtubes were flushed with $XeCO_2$ mixed in a ratio of 80:20 during the final phase of the data taking.

Since during the beam test in October 2002 the trigger was generated by a coincidence of two large scintillator panels and two small scintillators mounted perpendicular to each other and the coincidence or anti-coincidence with the two Cherenkov counters upstream of the setup. The Cherenkov counters were used to select particle type and energy.

The beam was slightly de-focused for the measurements to decrease the number of tracks in the jig per event. This was done to achieve a maximum separation between the tracks and prevent pile-up.

Plots illustrating the measurement results from this test beam period can be found in [Hau05].

Chapter 3

Silicon Sensors

In this chapter, after an introduction into the interaction of radiation with matter, the most important features of position sensitive semiconductor radiation detectors will be presented, with a special emphasis on CMOS Pixel Detectors, as these played a major role in the framework of this thesis. Following this is a section on the influence of radiation on the performance of the detection device.

An in-depth description of the properties of the semiconductor material silicon and detectors made from it can be found in [Lut99, Die03].

3.1 Interaction Of Radiation With Matter

A charged particle travelling at high speeds will lose energy, when it traverses matter. This happens in independent stochastic processes, in which the incident particle interacts with either the electrons of an atom of the target or its nucleus. In both types of interactions different processes contribute to the total loss of energy of the incident particle. In the following sections the mechanisms of energy loss will be described for charged particles and photons.

Unfortunately, the energy deposition of incident particles can also affect the detector itself. The effects of radiation on the detector and its performance will be introduced in section 3.4 at the end of this chapter.

3.1.1 Charged Particles

The principle mechanisms of energy loss are the same for light and heavy particles, even though some processes (e.g. bremsstrahlung) only appear at relativistic velocities and thus mainly affect light particles, like electrons. The most important process for the energy loss of charged particles is an inelastic process in which the incident particle scatters at an orbital electron. In case the energy transfer to the target electron is large enough, it can be removed from the potential well of the atom and leave behind an ionised atom. If the energy transfer onto the target electron is above a few keV, the knocked out electron is also called δ-electron[(1)]. These δ-electrons cause themselves substantial secondary ionisation. The second case, in which the energy transfer is not sufficient to ionise the atom, leads to excited states of the atom. In semiconductor materials these excited states can also be described by a process in which an electron is lifted from the valence band to the conduction band, the creation of an electron-hole pair. In both cases the atom returns from its excited state to its default state by the emission of photons or phonons.

The generation of free charge carriers via the above mentioned processes in the target material by the incident particle is exploited in solid state and gaseous sensors for the detection of particles. In most solid state application this is done by depleting the sensitive volume from free charge carriers by

[(1)] In some books the δ-electrons are also called knock-on electrons.

applying an electric field and subsequently measuring the current induced by removing the generated charge.

Scattering on the nucleus of a target atom is also possible. In most events though the energy transfer to the target is very small, as the mass of the target, the nucleus, is much larger than that of the incident particle. More details on the inelastic scattering of incident particles on the nuclei of the target can be found in section 3.4, which deals with the effects of radiation on the detector material.

Even though the energy loss of a particle traversing matter is a stochastic process on the microscopic scale, and thus is subject to fluctuations, on a macroscopic scale it can be approximated by an average energy loss $-dE/dx$. The unit of dE/dx is commonly given as $MeV/(g/cm^2)$, which corresponds to the energy loss per unit of length in a material with a given density. The average energy loss is described well by the Bethe-Bloch formula [Gro00]:

$$-\frac{dE}{dx} = Kz^2\frac{Z}{A}\frac{1}{\beta^2}\left[\frac{1}{2}\ln\left(\frac{2m_ec^2\beta^2\gamma^2T_{max}}{I^2}\right)-\beta^2-\frac{\delta}{2}\right] \tag{3.1}$$

where Z is the atomic number of the medium, A its atomic mass, m_ec^2 the mass of the electron, I the mean excitation energy and T_{max} is the maximum kinetic energy which can be transferred to a free electron in a single collision. For a particle with the mass M and the momentum $M\beta\gamma c$, T_{max} can be calculated as:

$$T_{max} = \frac{2m_ec^2\beta^2\gamma^2}{1+2\gamma m_e/M+(m_e/M)^2} \tag{3.2}$$

The Bethe-Bloch formula in this form describes the average energy loss of an incident particle in a large range of energy. Still, it needs to be adjusted at low energies for tightly bound atomic electrons and other effects. At high energies radiative corrections have to be taken into account. Fig. 3.1 shows the stopping power of copper for μ^+, including the corrections at low and high energies.

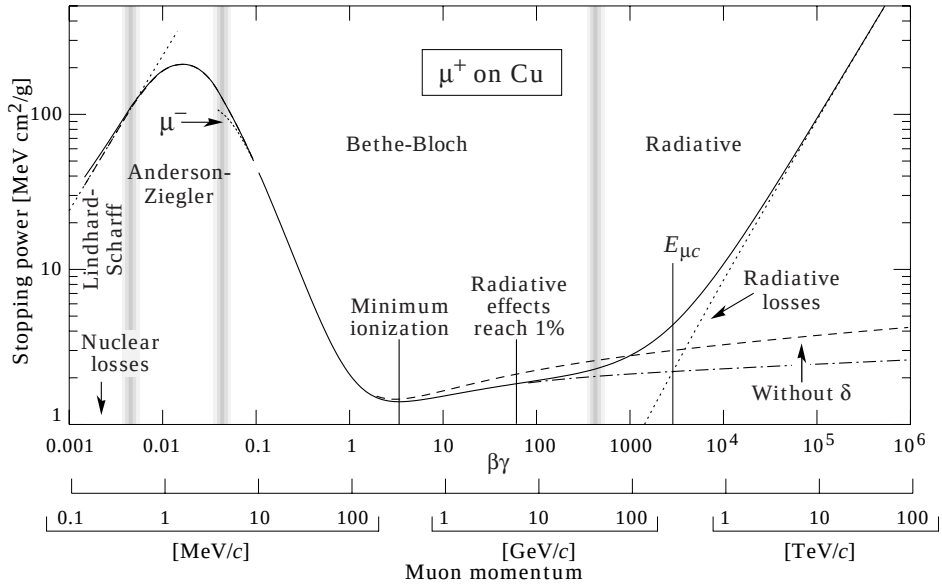

Figure 3.1: *The stopping power of copper for μ^+ in the momentum range of $0.1-10^8\,MeV$. The plot includes the corrections to the Bethe-Bloch formula at low and high energies. [Eid04]*

For electrons and other light particles as incident particles the Bethe-Bloch equation has to be slightly modified. Especially the small mass of the electrons plays an important role in the modification of the formula, as the maximum energy transfer in a single collision is now limited to half of the kinetic energy of the incident particle.

The signal measured with a detector depends on the energy deposited by the traversing particle along its track. This is not necessarily equal to the total energy loss of the particle in the detector

material, as some of the energy is removed from the track vicinity and thus escapes the measurement. This is mainly caused by δ-electrons, photons either emitted by excited atoms or radiated by the incident particle itself. The Cherenkov radiation contributes to this effect only to a very small part. Taking these effects into account, a new formula can be derived for the restricted energy loss:

$$-\frac{dE}{dx} = Kz^2 \frac{Z}{A}\frac{1}{\beta^2}\left[\frac{1}{2}\ln\left(\frac{2m_e c^2\beta^2\gamma^2 MIN\left(T_{cut},T_{max}\right)}{I^2}\right) - \beta^2\left(1+\frac{MIN\left(T_{cut},T_{max}\right)}{T_{max}}\right) - \frac{\delta}{2}\right] \quad (3.3)$$

Where T_{cut} is a cut-off energy, which describes the limitation of the energy loss along the track taking into account the generation of δ-electrons. For silicon the experimentally measured value for T_{cut} is $\sim 140\,keV$.

If one considers not the average energy loss in a thick layer, but the energy loss in a thin layer δx, fluctuations in the energy loss have to be taken into account. There are two sources for fluctuations in the energy loss. One is the variation of the energy transfer during the scattering process, the second is the number of collisions in the thin layer. The number of collisions is distributed following the Poisson formula. Thus for N collisions the distribution has a width of $\sqrt{N}$. As the relative variation of the number of collisions is proportional to $1/\sqrt{N}$, the fluctuations in the energy loss due to the variation in the number of collisions vanishes in the limit of the thick absorber.

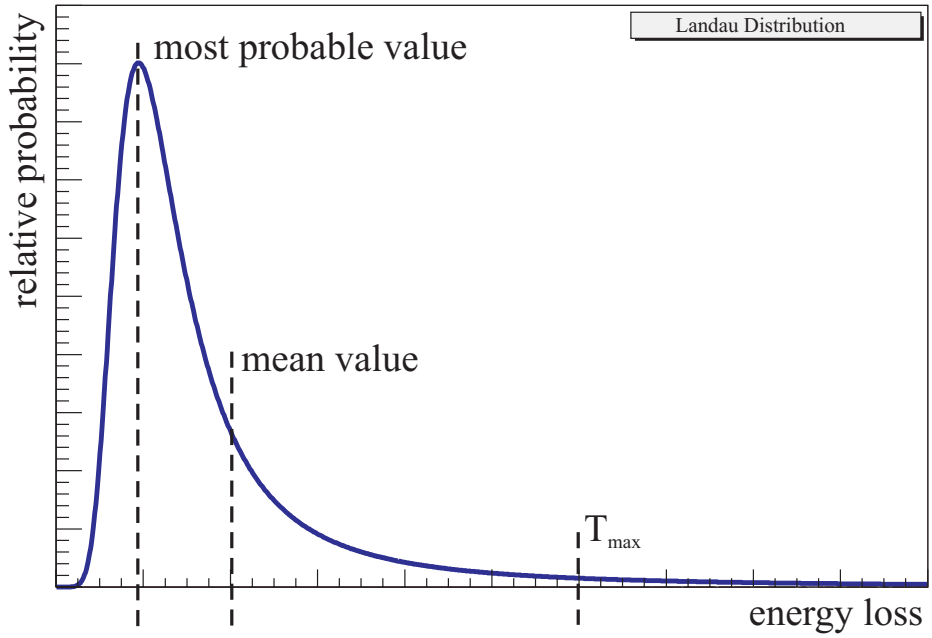

Figure 3.2: *The Landau Distribution: The typical energy loss of particles in a thin absorber.*

The function describing the variation in the energy loss is called the "straggling function". Only for thick absorbers, $(dE/dx)\delta x \gg T_{max}$, it can be approximated by a Gaussian. In the general picture the function is non-symmetric, shifted towards higher values and has a long tail towards higher energies. The first description of the straggling function was given by Landau in the 1940s. He made three assumptions in his work:

- It is possible to transfer all kinetic energy of the incident particle on an electron in the target material.
- The electrons in the shell of the target atoms can be considered as free charge carriers.
- The velocity of the incident particle is not changed during the passage through the target material, which is only true for thin absorbers.

The last postulate requires that the mean energy loss in a thin layer x is much smaller than the maximum energy transfer per interaction T_{max}.

$$\rho K z^2 \frac{1}{\beta^2} \ll T_{max} \tag{3.4}$$

As a result of this, the energy loss spectra of systems which fulfil the formula above can be described using the so-called Landau distribution, which is shown in Fig. 3.2. For a MIP[(2)] the most probable number of electron hole pairs generated in $1\,\mu m$ of silicon is 76 (average 108).

3.1.2 Photons

The interaction of photons in the target material, and thus the detection mechanism, is based on processes different from those involved for charged particles. The total attenuation coefficient is the sum of a whole set of processes with energy dependent cross-sections: photoelectric effect, Compton scattering, Rayleigh scattering and pair production. These processes lead to either a deflection of the photon or its complete absorption. In Fig. 3.3 the attenuation is shown for silicon as absorber material.

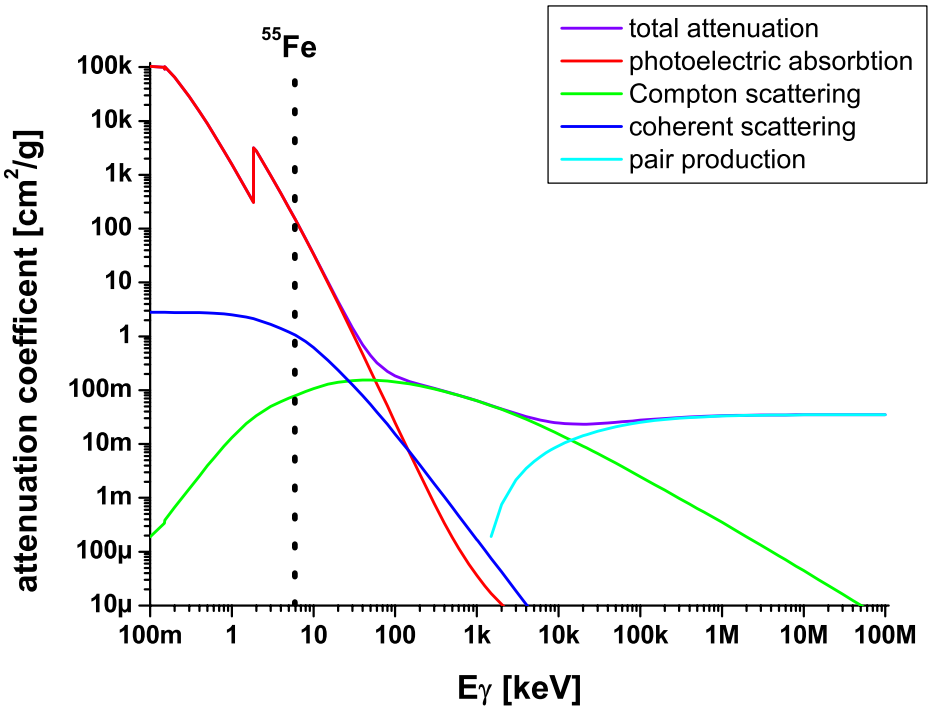

Figure 3.3: *The attenuation coefficient for photons in silicon as a function of the photon energy shown in a double logarithmic scale. The vertical dotted line shows the energy of the photons of* ^{55}Fe *. [Source: PhotoCoeff]*

In the following the effects contributing to the total attenuation will be described in more detail:

- Photoelectric Effect
  The energy of the photon is transferred completely onto an electron of the inner shell. This electron is then ejected and flies away as a free electron. The kinetic energy of the electron is equal to the energy of the photon minus the binding energy of the electron. The recoil is

(2) **MIP**: **M**inimum **I**onising **P**article, a particle with an energy such that it lies in the minimum of the Bethe-Bloch formula.

absorbed by the nucleus to which the electron was bound. If the resulting photoelectron has enough kinetic energy, it will produce secondary ionisation along its track. As the complete energy of the photon is absorbed in one step, this process can be used for the calibration of the detector. Nevertheless, the result may be smeared by escaping photons. These photons are produced, when the hole in the electron shell of the nucleus is filled again by an electron from an outer shell "falling down". The energy of the second generation photons is much smaller than that of the incident one.

- Compton Scattering
  In the Compton effect, also called the incoherent scattering, the incident photon scatters on a free electron[(3)] in the absorber material. In this process the photon transfers some of its energy onto the electron, but it is not fully absorbed, it continues its path albeit under an angle to its incident trajectory. The target atom is partially ionised after a Compton scattering, as the "free" electron flies away.

- Rayleigh Scattering
  The Rayleigh scattering (or coherent scattering) is also based on the interaction of an incident photon with an electron of the shell of the atom. Unlike in the Compton scattering, in this effect no energy is transferred onto the medium, neither is the atom excited nor ionised, only the photon is deflected from its original path.

- Pair Production
  During the process of pair production a photon is transformed into an electron and a positron. Since momentum has to be conserved in this process, it can only happen in the presence of a third body, to be more exact, in the Coulomb field of a nucleus or an electron. As two particles are produced in this process, the energy of the incident photon has to be larger than the threshold, which is given by two times the rest mass of the electron ($\sim 1.02\,MeV$).

The most commonly used soft X-ray photons for detector calibration are those from the two decay lines of ^{55}Fe . With a characteristic energy of $5.9\,keV$ (branching ratio 24.4 %) and $6.49\,keV$ (branching ratio 2.86 %) they have an absorption length in silicon of $26.95\,\mu m$ and $35.35\,\mu m$ respectively. In CMOS detectors, this allows to probe the whole depth of the active volume which has a typical thickness of $< 15\,\mu m$ beneath a dead layer of $< 10\,\mu m$, which consists of the integrated electronics and passivation layers. A typical ^{55}Fe spectrum measured with a CMOS detector is shown in Fig. 3.9.

The size of the charge cloud generated by the absorption of a X-ray photon is given by the range in the detector material of the secondary electrons produced in the absorption process. The range R of a secondary electron with the energy E_{e^-} is given by [Bro61]:

$$R = 40.8 \cdot 10^{-3}\,\mu m \cdot E_{e^-}[keV] \tag{3.5}$$

Thus for secondary electrons generated during the absorption of ^{55}Fe gammas, the range is smaller than $1\,\mu m$, which leads to a charge cloud confined very closely around the absorption point of the X-ray photon.

3.1.3 Charge Carrier Generation in Semiconductor Materials

In semiconductor detectors the generation of electron-hole (e-h) pairs by the incident particle itself or secondary effects, due to its passage through the material, is used for the detection of high energetic particles. The energy W required to generate one e-h pair depends strongly on the material used, as

(3) Actually, it is an electron bound to a nucleus, but if the energy of the incident photon is large compared to the binding energy, the electron can be considered approximately as free.

it is a function of the band gap and thus slightly depends on the temperature of the device. Eqn. 3.6 gives a linear fit to the data measured for various materials [Ali80].

$$W = 1.76\,eV + 1.84 \cdot E_{gap} \tag{3.6}$$

As one can see from the equation above, the energy needed to create an e-h pair in a semiconductor is always larger than the band gap. This is due to the fact, that there is a distinct possibility to invoke additional processes involving the excitation of phonons[(4)] and plasmons[(5)]. While the measurable effect of phonons in the detector is an increase in the temperature of the device, plasmons end up producing e-h pairs with relatively high energies. The electrons created in this process are called "hot electrons" due to the higher energy.

The mean energy required to produce one e-h pair in silicon was measured to be $W = 3.658\,eV$ at $170\,K$ with a temperature dependence of $dW/dT = -0.1\%/K$ [Fra94]. This corresponds to $W = 3.645\,eV$ at room temperature.

The intrinsic energy resolution ΔE is given by the following expression:

$$\Delta E = 2.36\sqrt{N} \qquad \text{with} \qquad N = \frac{E}{W} \tag{3.7}$$

Where N is the number of primary e-h pairs produced in the absorption, E the total energy absorbed and W the energy required to produce an e-h pair. This equation assumes a Poisson distribution of the number of interactions where $\sigma_n = \sqrt{n}$ is the variation of a given number n. The statistical accuracy is improved by the introduction of the Fano factor f, which was experimentally determined to be $f = 0.155$.

$$\Delta E = 2.36\sqrt{N \cdot f} \tag{3.8}$$

For the total energy resolution of the detector, one of course has to take into account further effects, e.g. variations in the detector material, in the gain of the read out channels and the noise of the device itself and its read out system.

3.2 Position Sensitive Detectors

Charged particles travelling at relativistic velocities generate charge carrier pairs when traversing condensed matter along their track and small clouds of charge carriers at the position where they are stopped, see section 3.1 for more details. Thus a segmented detection device allows to determine the position where the particle interacted in the sensitive volume. In the following sections various types of position sensitive devices will be introduced.

3.2.1 Microstrip Detectors

Silicon microstrip detectors, see Fig. 3.4, are the most commonly used position sensitive radiation detectors in High Energy Physics. In experiments like DELPHI and CDF they have proven their reliability. As a consequence, they are also used in the next generation of experiments (CMS, ATLAS,...) at CERN.

Microstrip detectors are large area diodes, with a sensitive area of up to $100\,cm^2$, operated in reverse bias mode with a typical thickness of $300\,\mu m$. The implants and contacts of the diode are segmented into multiple thin strips to obtain a high spatial resolution. The pitch, the distance from one

(4) Phonons are the quanta of the lattice oscillations. They are classified in two groups: the acoustic and the optical phonos. The acoustic phonos are related to the propagation of sound waves in the lattice, the second class of phonons can interact directly or indirectly with photons and thus are named optical phonons. They occur in crystals with more than one atom per unit cell.

(5) The quanta of the longitudinal oscillations of the free electron gas in the semiconductor crystal are called plasmons. The typical energy range for plasmons is $3-20\,eV$. In silicon they have an energy of $16.8\,eV$.

strip to the next, is typically in the range between $50\,\mu m$ and $200\,\mu m$. The base material for microstrip detectors is mostly high resistivity n-type silicon into which the p^+ read out strips are implanted.

As the strips have a rather high capacity ($\sim 1\,pF/cm$), the read out has to be done using very low noise circuitry. The two most important connection schemes are the so-called AC- and DC-coupling. In the DC-coupling the implanted strip is directly connected to the read out amplifier. In this scheme the dark current has to be absorbed by the read out amplifier, which can be a problem for highly irradiated detectors, as there the current can become very high. In the second case, the AC-coupling, the implant of the strip is not directly connected to the read out amplifier, but through a coupling capacitance. This capacitance, mostly implemented in form of an oxide layer between the implant and the metallisation, prevents the dark current from reaching the amplifiers. The disadvantage of this scheme is the need for additional bias resistors to get rid of the dark current. In modern designs they are implemented as poly-silicon resistors at one side of the detector.

In order to obtain two-dimensional information on the position of a hit on the detector one has to use either two single-sided detectors back-to-back or one double-sided detector. There are two different types of double-sided detectors: stereo-angle and 90° detectors. The stereo angle detectors have only a small angle ($1-5°$) between the strips on the top and the bottom side. The advantage of this design is, that both sets of strips can easily be connected on the same side of the detector. 90° detectors have a better spatial resolution, but this comes at the cost of a more complicated connection scheme for the read out on one side, which is the preferred geometry: One has to use a second metal layer to route the signals from the perpendicular strips to another edge for the connection to the read out amplifiers. This increases the capacitance and thus the noise dramatically. The major advantage of double-sided detectors over back-to-back mounted single-sided ones is the reduced material budget and thus a reduced probability for multiple scattering.

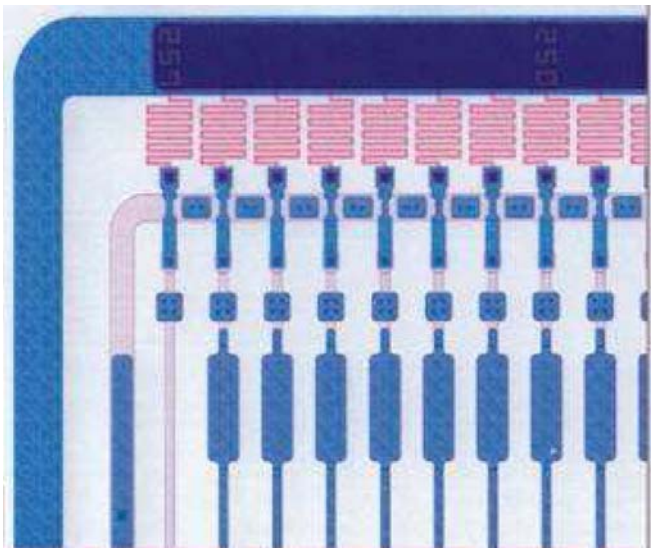

Figure 3.4: *A close-up picture of a corner of a CDF silicon sensor. One can clearly see the bias resistors (red, wiggled line), the bias ring (blue, thick line), the AC- and DC-pads (blue, rectangular shapes) and the strips (blue, thin lines). The strips are connected by vias and "bridges" to the bias resistors [source: Micron Semiconductor]*

3.2.2 Pixel Devices

A different approach to obtain two-dimensional information on the hit position is the usage of pixel devices. These devices come in different techniques, one of which, namely the CMOS detectors, will be described in more detail.

Pad Detectors

Pad Detectors are the simplest approach to pixel detectors. They consist of an array of independent diodes produced on the same substrate. Each of the diodes is connected, via routing lines, to a separate read out channel. Today pad detectors are still used in Hybrid Photo Diodes. With a diode size of $\sim 1\,mm$, their spatial resolution is quite limited, but they can cover rather large areas ($\varnothing 5\,cm$).

Hybrid Pixel Detector

Hybrid pixel detectors allow to separately optimise the substrate material for the sensor and the read out electronics. One can use for example high resistivity silicon or CdZnTe for the detector itself and low resistivity silicon for the electronics. Hybrid pixel sensors have been used successfully at experiments like DELPHI and will also be used in the next generation of experiments at the LHC. A schematic cross-section of such a pixel detector is shown in Fig. 3.5.

In this picture one can already see some of the major drawbacks of the hybrid pixel design. The additional electronics mounted on the sensor increase the probability of multiple scattering. This effect is enhanced by the solder bumps, which normally consist of a high Z metal (e.g. indium or gold). The process of mounting the read out chip on the detector wafer, the so-called bump bonding, is also quite troublesome due to technical difficulties and yield issues. A further problem is the limited granularity of the hybrid pixel detectors. This limitation is mainly caused by the size of the solder bump.

Originating in the need to integrate a lot of functionality in each pixel cell a further enlargement of the pixel size, even when using deep sub-micron CMOS technologies, is inevitable. The most important circuitry in addition to the in-pixel amplifier is the current compensation circuit, which is required to counter the dark current of the pixel, as an AC-coupling is very difficult to implement. In more advanced pixel designs DACs are included to compensate for the pixel to pixel spread in pedestals and gain. Depending on the purpose, also discriminators, counters and even data sparsification can be included in each pixel cell. Due to the large amount of circuitry per pixel cell and the high read out frequencies, hybrid pixel detectors have a high power consumption, in the order of a few hundred mW/cm^2.

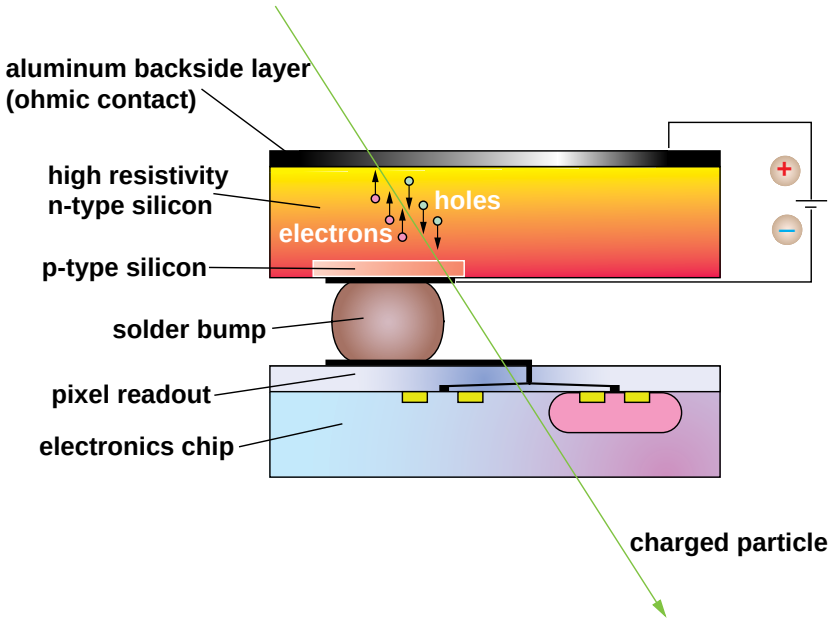

Figure 3.5: *The classical configuration of the hybrid pixel detector. The top part is the sensitive volume, formed by a fully depleted high resistivity silicon substrate. In the middle is the solder bump connecting the diode to the electronics at the bottom. [source unkown]*

Charge Coupled Device - CCD

Originally the design of CCDs was driven by the need for position sensitive detectors for visible light [Boy70], an application in which they are still widely used, for example in digital cameras. Apart from visible light detection, it soon became obvious, that they can be used in a wide field of applications, from cooled down back-illuminated detectors for infra-red light in astronomy to high resolution pixel detectors for high energy particle physics [Dam81]. While the spatial resolution of the first CCDs used in particle physics was in the range of 40 μm, newer detectors have reached values of a few micrometres.

A schematic cross-section of a CCD is shown in Fig. 3.6. The electrons generated in the epitaxial layer by a traversing particle are trapped in potential wells arranged in a two-dimensional matrix. The potential of each well is controlled by a gate contact on top of it, with every third row being connected to the same potential. To read out the device, the charges are shifted row by row towards one side of the device. This is done by applying sequentially a potential change on three neighbouring rows. At the edge of the device the charge is transferred into a linear register, in which it is then shifted towards the charge sensitive output amplifier located at one end.

With this read out scheme the CCD has essentially no dead time. On the other hand it is the reason for some of the major drawbacks of the CCD. Shifting the data from all potential wells to just one read out contact requires a lot of time. Additionally, the large amount of charge transfers inside the device makes it very sensitive to radiation damage. This can easily be understood, as the traps created in the material by the radiation allow the electrons to recombine and thus influence the charge transfer efficiency. For large arrays, a few million pixels, even a small loss of the charge transfer efficiency in the range of a few per mill can cause quite a problem as it easily amounts to a charge loss of 10 % at the end of the array.

To overcome the technical limitations of the CCDs new approaches have been studied. To reduce the read out time, the so-called column parallel read out has been introduced. In this read out scheme the charge is transferred via bond wires from a pad at the end of each of the columns into a front-end chip. Additionally, the charge transfer speed can be enhanced by cooling the device. This has the beneficial effects of reducing the leakage current (and thus the noise) and freezing out the radiation induced traps, making the CCDs more radiation hard. A further modification regards the thickness of the CCDs. New CCDs will be thinned down to 50 μm (from 300 μm),which reduces the back scattering significantly.

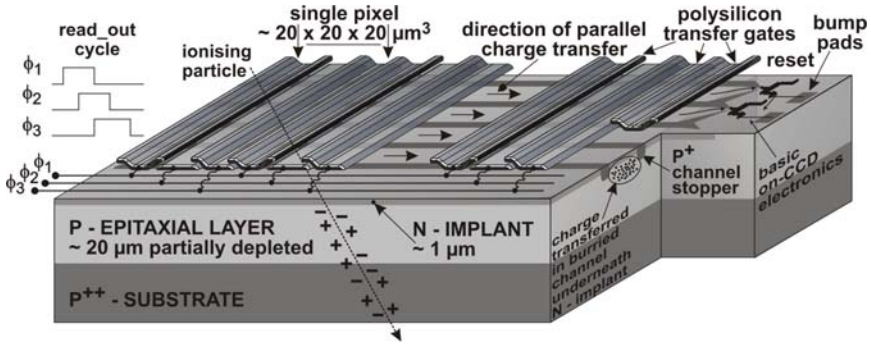

Figure 3.6: *A schematic cross-section of a CCD matrix. Clearly visible are the epitaxial layer (in which the electrons are generated), the transfer gate contacts and the bond pads for the column parallel read out. [Dep02]*

Monolithic Pixel Detectors

A pixel detector is called a monolithic detector if the signal processing circuitry is included on the device itself. This can be done in different ways. The most common way is to use low resistivity

bulk material and to place the electronics inside wells next to the charge collecting diode. A second possibility is the usage of the Silicon On Insulator (SOI) technology in which the electronics are separated from the sensitive volume by a thin layer of oxide. Another way is the usage of high resistivity material in which then the electronics are included, but this requires special, non-standard processing and is thus much more expensive. In the following three of the various possibilities will be introduced: DEPFET[6], CMOS[7] and SOI[8].

- **DEPFET**
  The DEPFET design (a schematic cross-section is shown in Fig. 3.7) uses a fully depleted high resistivity substrate as sensitive volume [Kem87]. The read out is realised in form of Field Effect Transistors (FET), that are implemented on the surface of the device. The internal gate of the FET serves as a collecting diode for the electrons generated by traversing particles. The potential change due to the accumulated charge at the internal gate modulates the current flowing through the FET. To save power, this current is only flowing during the read out phase of the pixel.

  As the read out does not remove the charge from the internal gate, it is possible to re-read the device without influencing the measurement. The disadvantage of this is the need for a "clear" contact, to which a rather high potential ($15-20\,V$) has to be applied to remove the charge from the internal gate. This problem can be overcome using the so-called constant clear design, in which a punch through contact removes the charge from the internal gate.

  A correlated double sampling can be achieved with this detector by reading the signal, sending a clear and then reading the device again. The difference then contains the signal. Detectors using the DEPFET design have been proven to be very low noise devices with an ENC in the order of a few e^- per pixel.

  In order to facilitate the design of the DEPFET and to shorten the read out time of the device, in most cases the DEPFET is run with the help of auxiliary chips: one gate and one reset switcher and front-end chip.

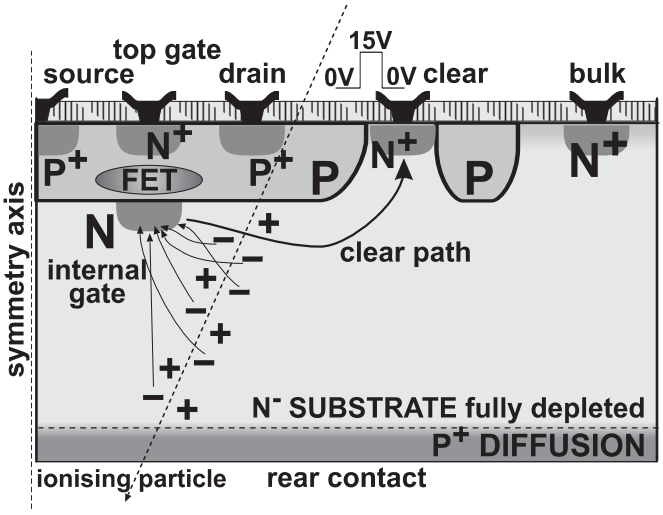

Figure 3.7: *This picture shows a schematic cross-section of a DEPFET pixel. The most prominent features are the field effect transistor with its internal gate and the "clear" contact, both being surrounded by a guard ring. The bulk material is contacted and depleted via the implant on the right side. [Dep02]*

[6] **DEPFET**: **DE**pleted **P**-channel **F**ield **E**ffect **T**ransistor

[7] **CMOS**: **C**omplementary **M**etal **O**xide **S**emiconductor

[8] **SOI**: **S**ilicon **O**n **I**nsulator

- **CMOS Detectors**
  The concept of detectors produced in a standard industrial CMOS process has been successfully pursued by various groups in the High Energy Physics community for a number of years as a competitor to CCDs [Tur01]. The concept of CMOS arrays originates from the industry as detectors for visible light, an application in which they have already replaced CCDs to some extent. The basic concept is the same in both applications.

  The usage of an industrial standard process comes at the price of short lifetimes, as the processes are constantly optimised for applications other than particle detectors. Thus for each new device iteration, one has to adapt the design of the device to the new rules of the foundry. The benefits of the new processes like the smaller feature size ($0.35\,\mu m$), which allows to integrate more electronics into the device, are often paired with unwanted modifications, like a thinner epitaxial layer, which reduces the signal heights. The increased usage of CMOS devices by industry for visible light detection has led to the development of processes from which also particle detectors could benefit, as they have a rather thick epitaxial layer ($15-20\,\mu m$) and are optimised for low dark current.

  A simplified cross-section of a CMOS pixel is shown in Fig. 3.8(a). In this picture one can already see the major difference between the CMOS detector and other solid state detector types used in HEP: Only a very small part of the sensitive volume, the low doped epitaxial layer, is depleted. Nevertheless, CMOS detectors have an extremely high detection efficiency, as the electrons generated in the epitaxial layer (see Fig. 3.8(b) cross-section 1) have a very long lifetime and drift towards the collecting diode (see Fig. 3.8(b) cross-section 2), where they then contribute to the signal. This geometry allows CMOS detectors to achieve a fill factor of 100 % and a tracking resolution of $1.5\,\mu m$. Even though the amount of charge generated by a traversing particle is very small, as the sensitive layer has a thickness of only a few micrometres, signal to noise ratios of > 30 can be achieved. This is made possible by placing the first amplification stage inside the pixel itself and by the very small capacitance of the pixel, which leads to a very small noise.

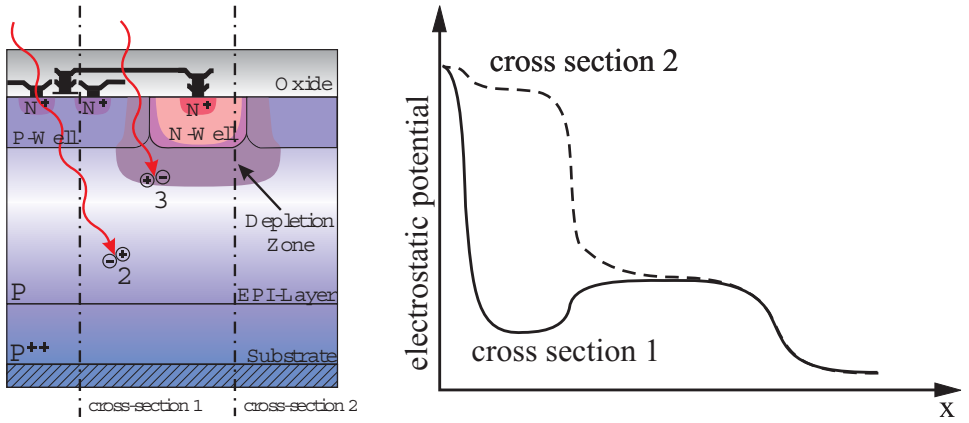

(a) Cross Section (b) Potential

Figure 3.8: *(a) shows a schematic drawing of a CMOS pixel cell with the electronics at the top, the collecting diode (top, middle), the epitaxial layer (middle) and the substrate at the bottom. In (b) the electrostatic potential along cross-sections 1 & 2 is shown. One can clearly see the potential well formed by the diode and the barrier formed by the substrate. [Dep02, Jun02]*

Fig. 3.9 shows the typical seed pixel[(9)] histogram of the measurement of a ^{55}Fe source with a CMOS detector, in this case matrix 0 of a SUCCESSOR-I chip. The shape of this histogram

[(9)] Seed Pixel: The seed pixel is defined as the central pixel of the cluster of pixels, that has detected a signal from one hit.

can easily be understood when looking at the geometry of the CMOS pixel. The peak on the left (1) is caused by the noise of the device. Photons converted in the epitaxial layer and in the substrate close to the epitaxial layer contribute to the middle part of the spectrum (2). In this layer some of the charge is lost due to recombination, the rest is shared between neighbouring pixels. The two peaks on the right (3), the 5.9 *keV* and the 6.49 *keV* line of ^{55}Fe , are created by events where the photon converted in the small depletion zone close to the collecting diode.

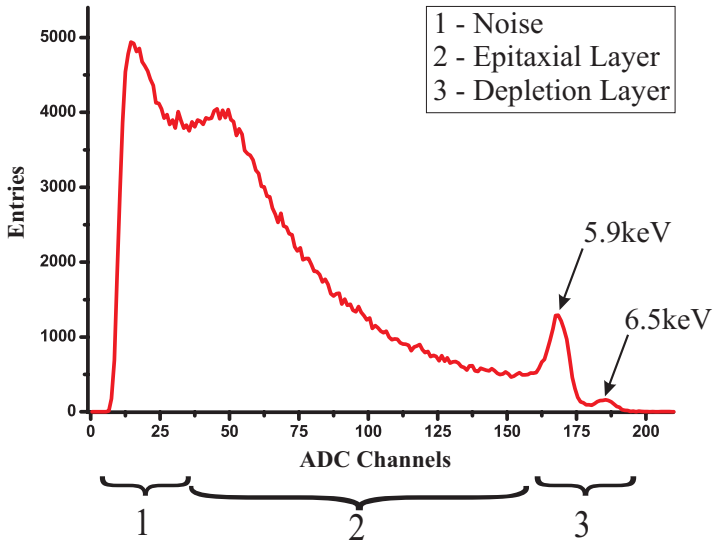

Figure 3.9: *A ^{55}Fe single pixel spectrum measured with matrix 0 of a SUCCESSOR-I chip. The noise peak (1) is caused by baseline fluctuations. The broad peak (2) is a product of conversions in the epitaxial layer, where the charge is shared between some pixels. The two peaks on the right (3) are created by photons converting directly in the small depletion layer underneath the collecting diode.*

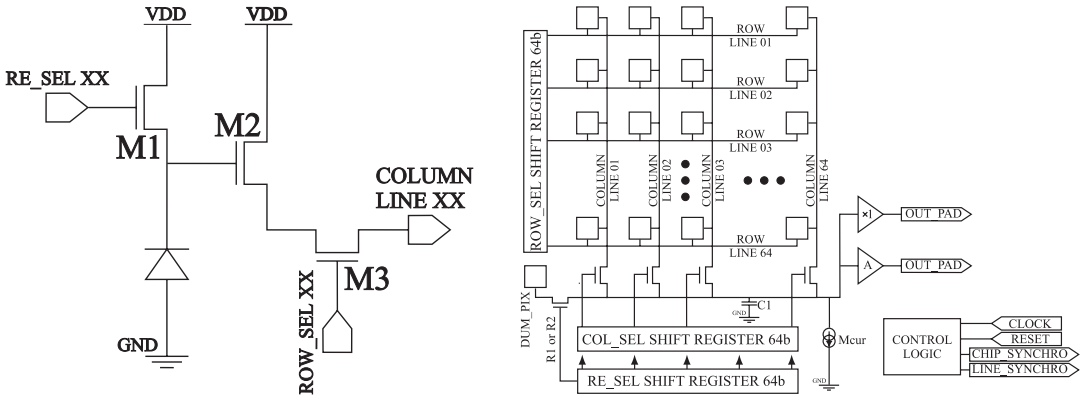

(a) Pixel (b) Matrix

Figure 3.10: *Schematic drawing of a CMOS pixel read out. (a) shows the logic inside a pixel cell. M1 is the reset transistor, M2 one part of the source follower of the amplifier and M3 the select switch for the read out. In (b) the layout of the complete sensor is shown. Taken from [Tur01].*

The first amplification of the signal is done inside the pixel itself. A schematic drawing of the standard approach for the circuitry used is shown in Fig. 3.10(a). Due to the number of transistors (three) in this design, it is also called the *3T*-approach. The transistor *M1* is the so-called reset switch. When it is enabled, the charge collecting diode is connected to the reverse bias and the accumulated electrons (dark current and signal) are removed. Transistor *M2* is one part of the source follower, which does the first stage of amplification of the signal. *M3* is the

row select switch. This switch is enabled during the read phase to connect the output of *M2* to the second part of the source follower. As depicted in Fig. 3.10(b), the column select switch and the current source for the source follower are located outside of the pixel and are shared between many pixels. This configuration allows to integrate charge in the pixel continuously between two consecutive reset operations.

The read out scheme to be used with this type of read out circuitry is described as follows: At the beginning of a read out cycle the detector is reset. This is done by applying the reset signal (typically 2 clock signals long) and clocking it through the detector ([number of rows + 1] clock signals). After this the detector can be read out for the first time. To read out one frame the detector has to be clocked (number of pixels + X) times, where X is the number of clocks required for the external logic. This read out of frames is then repeated until the diodes of the detector have accumulated enough charge to reach the saturation point. After this the process starts over with another reset of the detector. With this type of read out, pixel frequencies of up to $40\,MHz$ have been achieved even for large prototypes with one million pixels.

The dominant source of noise in a CMOS detector is the resetting of the pixel at the end of the integration time. The average noise can be calculated for the steady state using an expression describing thermodynamic fluctuations:

$$\overline{V_{n,res}^2} = \frac{kT}{C_{conv.}} \tag{3.9}$$

Due to insufficient time to reach the steady state condition during the reset phase the so-called kTC noise is close to one half of this value in real applications. Fortunately, the kTC noise can be easily removed applying the Correlated Double Sampling (CDS) technique. However, this causes a small increase in the white noise.

A further noise source is correlated to the leakage current of the diode. This is the most important noise during the integration phase. It is called the shot noise. The mean square value of the noise sampled on the conversion capacitance at the end of the integration time is given by:

$$\overline{V_{n,res}^2} = \frac{q i_{leak}}{C_{conv.}^2} t_{int} \tag{3.10}$$

One of the major drawbacks of CMOS detectors is the relatively high threshold for low energetic particles. This reflects the geometry of the pixel. The passivation oxide and the wells for the electronics and the collecting diode form a rather thick dead layer, which defines the threshold level. To overcome this problem a new approach, the so-called back-thinning, has been successfully adapted to CMOS detectors and tested within the SUCIMA collaboration. In this process the detector is illuminated from the backside, once the substrate has been removed down to the epitaxial layer. A more detailed description of the back-thinning process can be found in section 4.2.2 on page 118.

Another constraint of this approach is the limitation to the use of NMOS transistors in the sensitive volume, since the n-wells of PMOS transistors would act as competitive charge collecting paths to the diode. Nevertheless, as both types of transistors, P- and NMOS, can be used at the periphery of the chip, all necessary logic can be implemented on the device.

- **Silicon On Insulator - SOI**
  The SOI technology aims to combine the best of two worlds: the high resistivity substrate giving a high signal for the sensitive volume and the low resistivity material better suited for electronics for the read out circuitry. Originally SOI came to the attention of the industry in recent years, as a solution to the issues of the enormous leakage currents of the high density CMOS devices, like processors. In Fig. 3.11 a schematic cross-section of a SOI pixel is depicted. The SOI detector is segmented into three layers: the device layer, the buried oxide and the substrate.

In the first step of the production the SOI wafer is prepared. At the moment there are three competing techniques for this step. In the so-called SIMOX[10] process a layer with a high dose of oxygen is created by ion implantation. From this layer the BOX[11] is then formed by annealing of the wafer at high temperatures.

Alternatively, a SOI wafer can be fabricated by the so-called wafer bonding. In this process two wafers are "glued" together by oxidising them and bringing them into close contact, so that van der Waals forces keep them together. An annealing at this stage can improve the mechanical stability. Afterwards the low resistivity device wafer is thinned down to the necessary level. This is done either by wet etching or by splitting. The second method, the splitting of the wafer, requires the introduction of a weak layer in the device wafer. This can be achieved by the implantation of light ions or by anodic etching and annealing.

A further, but somewhat disfavoured, approach is ZMR[12], a process in which first an oxide is grown on top of the wafer and then an amorphous layer of silicon on top of the oxide. This amorphous layer is then crystallised by heating the wafer locally above the melting point.

From the SOI wafer the pixel detector is then produced by etching the vias through the device layer and the BOX to the substrate for the pixel contact, the implantation of the pixel diodes and finally the production of the electronics in the device layer. During all these steps the parameters of the process, especially the temperature, must be monitored closely.

While the production of SOI detectors is not a standard process, and not all parameters are fully understood up to now, the SOI technique allows to employ both P- and NMOS transistors in the device layer, which makes it feasible to use much more complex electronics inside the pixel, than with only one type of transistors as in the CMOS pixel detector design.

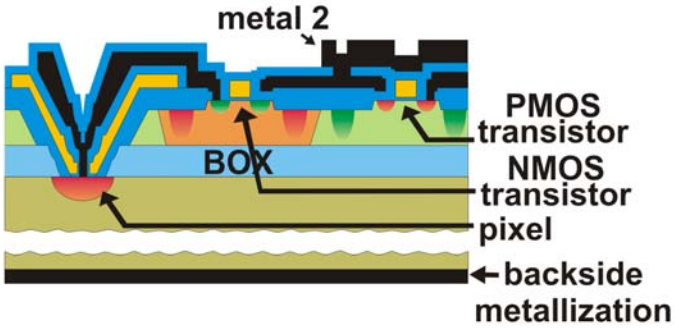

Figure 3.11: *A schematic cross-section of a SOI pixel. From top to bottom the following parts are visible: the electronics layer, the buried oxide (BOX) and the high resistivity substrate with the diodes and the backside metallisation. [Mar04]*

3.3 A Comparison of Detector Technologies

In order to select the best detector for a given purpose it is very important to carefully weigh the advantages and disadvantages of each technology available against each other. Tab. 3.1 tries to give a comprehensive overview of the most popular technologies for particle detection. Based on considerations like these, SUCIMA decided to go for the CMOS technology for its main device and SOI as candidate for the next generation of devices.

[10] **SIMOX**: **S**eparation by **IM**planted **OX**ygen

[11] **BOX**: **B**uried **OX**ide

[12] **ZMR**: **Z**one **M**elt **R**e-crystallisation

	PROs	**CONs**
Silicon Microstrip	+ large sensitive area ($10 \times 10\,cm^2$) + thick → high signal ($25000\,e^-/MIP$) + very radiation hard ($> 1 \cdot 10^{15}\,n/cm^2$) + short read out time ($40\,MHz$) + lots of existing know-how	- only 1D information, 2D possible but complicated - high strip capacitance - very expensive - amplification & logic external - only few suppliers
Hybrid Pixel	+ 2D hit information + sensor and electronics separately optimisable + fast	- large pitch for pixel device - requires bump bonding (yield issues) - heavy on material budget (2 wafers)
CCD	+ 2D hit information + integrated amplification + large area + high spatial resolution + low noise + back-thinned devices available	- external logic - not radiation hard - limited dynamic range - not very fast ($\sim 10\,MHz$) - signal has to shifted to one end → charge loss - needs many different voltages - high power consumption
DEPFET	+ 2D hit information + integrated amplification + low power consumption + low noise + multiple reading of cell content	- external logic - only small devices - not radiation hard - requires $10-20\,V$ for clear, → high voltage CMOS process - not very fast read out
CMOS	+ 2D hit information + integrated amplification + integrated logic + fast read out ($40\,MHz$) + standard process → cheap + radiation hard (ionising, $> 3.5\,Mrad$) + high spatial resolution ($1.5\,\mu m$) + small capacitance → small noise + back-thinned devices available → light on material budget → low threshold energy + high signal to noise ratio (40+) + low power consumption	- limited sensitive area ($2 \times 2\,cm^2$) - small signal - subject to fast technology changes - not radiation hard (non-ionising, $< 1 \cdot 10^{12}\,n/cm^2$) - only NMOS logic (in sensitive area) - high kTC noise → need CDS
SOI	+ 2D hit information + high signal + integrated amplification + integrated logic + P- & NMOS logic + fast read out + low power consumption	- non-standard technology - needs vias through BOX - little existing know-how

Table 3.1: *A comparison of available detector technologies for particle detection. The advantages (PROs) and disadvantages (CONs) of the most popular technologies are listed. The table claims in no way to be complete and has to be understood as a guideline.*

3.4 Radiation Damage

In HEP experiments, as well as in other applications, the ability to withstand increasing radiation doses has become a very important criterium for the design of solid state detectors, especially for those made from silicon. The most severe requirements up to now on the radiation hardness are imposed on the detectors by the new generation of experiments at the LHC at CERN. There, a flux of $1 \cdot 10^{15}$ hadrons[(13)] and a total absorbed dose of $35\,Mrad$ is expected for the innermost layer of the vertex detector. But also in medical applications, like those envisaged by SUCIMA, the detector performance under the influence of radiation plays an important role.

Semiconductor devices are affected by three main effects under the influence of radiation: displacement of atoms from their positions in the lattice, transient and long term ionisation in insulator layers and formation of interface defects. The displacement of atoms is an issue, especially for lower doses, primarily in the bulk material of the detector and not in the read out electronics and thus it is also called "bulk damage". The inducing of locally fixed charge carriers by ionisation and the creation of interface defects is summarised under the term "surface damage". Especially the trapped charge carriers, but also the interface defects, are responsible for the deterioration of electronic devices. Both, bulk and surface damage, can affect the performance of the device, decreasing the signal height and increasing the leakage current and the noise in the device, thus leading to a smaller signal to noise ratio.

In the following two sections both types of radiation induced damage in the device will be introduced. Also their influence on the performance of a device will be described, with an emphasis on CMOS detectors. For a more detailed reading please refer to [Lut99, Die03, Dep02].

The surface damage is by far the dominant effect of radiation damage in the applications of SUCIMA. The radioactive sources used in clinical treatment emit only electrons and gammas of low to medium energy. Thus the probability of bulk damage is extremely small. Nevertheless, the effect of neutron irradiation has been studied by Lepsi for doses up to $10^{12}\,n/cm^2$.

3.4.1 Bulk Damage

To displace a silicon atom from its position in the lattice, a minimum recoil energy of $15\,eV$ is needed. Elastic scattering of incident high energetic charged or neutral particles at the lattice atom is the source of the required energy. As the recoil energy needed to dislocate an atom is different in the direction of a neighbouring atom than in a direction between two atoms, the threshold is not sharp and the displacement energy E_d is introduced. For a value of $E_d = 25\,eV$ the probability to displace an atom is 0.5. For values below, lattice vibrations will dominate, while for values above, additionally interstitial-vacancy pairs will be formed. For recoil energies far above E_d, the displaced atom can cause further formation of interstitial-vacancy pairs.

If the recoil energy is below $1-2\,keV$, only isolated point defects will be created. For recoil energies between 2 and $12\,keV$, a defect cluster will be formed. These clusters consist of a dense agglomeration of point defects. Simulations give a diameter of $5\,nm$ of the cluster with roughly 100 interstitial-vacancy pairs in it. They are formed at the end of the track of the recoil silicon atom, where it loses its last $5-10\,keV$ and the cross-section increases by several orders of magnitude.

In Fig. 3.12 an example is shown for a recoil energy much larger than $12\,keV$. In this case the knock-on atom has an energy of $50\,keV$. As one can see, the simulation predicts the formation of many clusters and additional point defects along the track of the knock-on atoms.

Depending on the type of the impinging particle and its energy, different mechanisms are involved in the generation of the primary knock-on silicon atom, resulting in different probabilities for the interaction. In the inset of Fig. 3.12 the two possible interactions are shown. Charged particles scatter at the (partially screened) electric potential of the nucleus, while neutral particles scatter elastically at

[(13)] The flux of hadrons (any kind, any energy) is normalised to neutrons with an energy of $1\,MeV$ using the NIEL hypothesis, where NIEL stands for Non-Ionising Energy Loss, and is given in units of $1 MeV\ neutrons/cm^2$.

the nucleus itself. The mass of the incident particle is responsible for the kinematics of the interaction and the maximum possible energy transfer onto the silicon atom. For example, a low mass particle like an electron has to have a kinetic energy of at least $260\,keV$ ($4.6\,MeV$) to generate a point defect (cluster). For a neutron it is only $190\,eV$ respectively $15\,keV$.

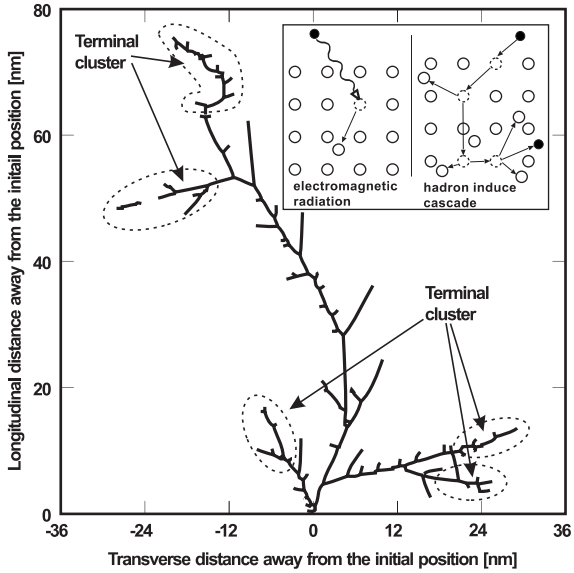

Figure 3.12: *The picture shows the model of the development of atom displacement and cluster formation due to the impact of a high energetic particle ($E_{kin} = 50\,keV$). In the inset the two different effects leading to atom displacement, electromagnetic and hadronic interaction, are shown. [Dep02]*

As for most point defects where the interstitial atom and the resulting vacancy are nearby, there is a high probability of the atom moving back to its place in the lattice. Thus only about 2% of the defects generated in the first place remain electrically active. The point defects introduce additional energy levels in the band structure of the semiconductor. These can act like acceptors, donors or charge traps and thus affect the lifetime τ of the charge carriers.

$$\frac{1}{\tau} = \frac{1}{\tau_0} + \frac{1}{\tau_{def}} \qquad \text{with} \qquad \tau_{def} \propto \frac{1}{\sigma_{def} N_{def}} \tag{3.11}$$

where τ_0 is the lifetime of the charge carriers before irradiation, σ_{def} the cross-section of the defect for charge capture and N_{def} the concentration of the defects. In a simple model the lifetime of the charge carriers becomes inversely proportional to the flux Φ, as the damage can be considered as linear to the flux.

$$\frac{1}{\tau} = \frac{1}{\tau_0} + \kappa_\tau \Phi \tag{3.12}$$

As the effects of point defects include the increase of the capture, generation and recombination rates of non-equilibrium charge carriers, they affect the internal electrical field of the detector. This may lead to effects, which bring the detector even beyond the type inversion point[14]. Additionally, the damage leads to an increase of the dark currents and to charge collection losses. It also affects the capacitance and the resistivity of the detector material. The increase of the dark currents in the bulk is mainly due to defects with energy levels close to mid band gap. As an irradiation is per default not necessarily homogeneous, this may lead to the formation of so-called hot pixels. These are pixels with an above average dark current.

[14] The defects in the crystal introduced by the irradiation act as acceptors. In n-type bulk material this will lead to an effective doping concentration which is p-type, thus causing type inversion. This described by the so-called Hamburg Model

Problems due to an increased dark current are primarily troublesome at room temperature. Cooling the device reduces the dark current to negligible values. Traps capture charge carriers and only release them after a time which is often beyond the time needed for one complete read out of the detector, they cannot contribute to the signal and thus the Charge Collection Efficiency (CCE) is decreasing. At higher temperatures, the trapping time is reduced, and the charge carriers will be released in time to be collected for the read out, resulting in a higher CCE. At lower temperatures, the trapping time increases dramatically and can reach values up to a few seconds. In this case the traps will be filled at the beginning and then will not accept further charge carriers, as they are already occupied. Thus, at lower temperatures, the CCE remains at rather high values. The effect on the radiation hardness of low temperature operation of silicon detectors and read out electronics has been the focus of many research efforts [Col00].

3.4.2 Surface Damage

Ionisation by charged particles or photons with sufficient energy to create e-h pairs in the medium may also lead to effects deteriorating the performance of the device. These unwanted effects are concentrated around the interfaces of two different materials, e.g. Si↔SiO_2. The concentration of these effects on the interfaces results from the rather high number of traps in the interface ($10^9 - 10^{10}/cm^2$) due to lattice mismatch and dangling bonds. The number of interface states depends strongly on the process parameters used when creating the interface, e.g. the temperature during the oxidation. In addition to the generation of charge carriers, ionising radiation can also break chemical bonds in the interface and thus increase the number of traps available.

The incident particles generate e-h pairs not only in the silicon bulk material of the detector, but also in the SiO_2 layers on top of it, even though a much higher energy of $17 \pm 1 eV$ is needed to produce an e-h pair there. Most of the generated e-h pairs recombine, for those not recombining the electron and the hole are separated by the electric field across the oxide. The actual recombination rate depends strongly on the quality of the oxide and ranges from almost all (for rad-hard oxide) to only a few percent (standard oxide). As the mobility of electrons in the oxide is five to twelve orders of magnitude higher than that of holes and the trapping cross-section is much smaller, in the case of the n-MOS transistor, most of the generated electrons will be collected by the positively biased gate contact. The holes will drift via a hopping process towards the Si-SiO_2 interface and will be stuck in traps already there changing their electrical behaviour and thus affecting the functionality of the device. A simplified cross-section of an NMOS transistor and an illustration of the charge trapping in the gate oxide - silicon interface of the NMOS transistor is shown in Fig. 3.13. In both drawings a positive gate voltage is applied to the MOSFET.

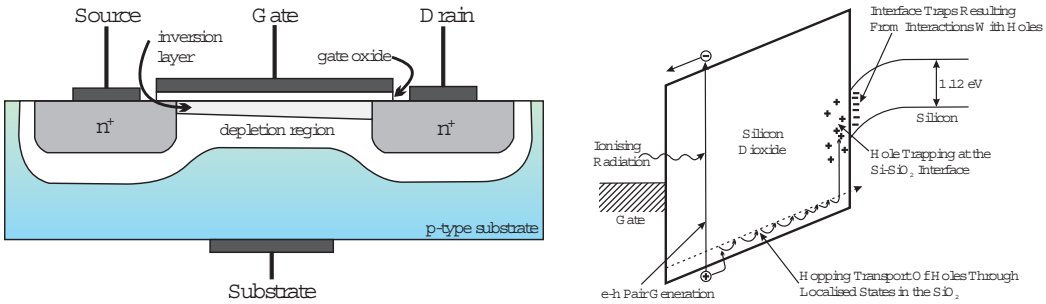

(a) MOS Transistor (b) Band Structure

Figure 3.13: *(a) A simplified cross-section of a NMOS transistor, with a positive gate voltage applied. (b) The band structure in the MOS contact, also with a positive gate voltage being applied, used to illustrate the hole capturing in the Si-SiO_2 interface. Modified from [Ane00]*

The increased amount of energy levels in the band gap close to the interface, which can also act

as recombination centres for the charge carriers, lead to a decreased carrier lifetime in this region. Macroscopically, this effect can be noticed as an increase in the leakage current of the device. The charge-up of the oxide due to the increase of interface states is also a limiting factor for read out electronics. Both, NMOS and PMOS transistors, are affected by this. Primarily this leads to a shift of the threshold voltage V_{th} of the transistor. The shift of V_{th} is proportional to a power n of the oxide thickness t_{ox}: $V_{th} \propto (t_{ox})^n$. The power factor n depends on the processes used to grow the oxide and its thickness. It has been measured to be in the range of 1 to 3.

Those holes that are trapped very close to the interface can recombine with electrons tunnelling into the oxide from the silicon beneath. The probability of this tunnelling process is a function of the oxide thickness: the thinner the oxide, the higher the probability for the tunnelling. Thus processes using a thin oxide, like the new deep sub-micron technologies, are more radiation hard.

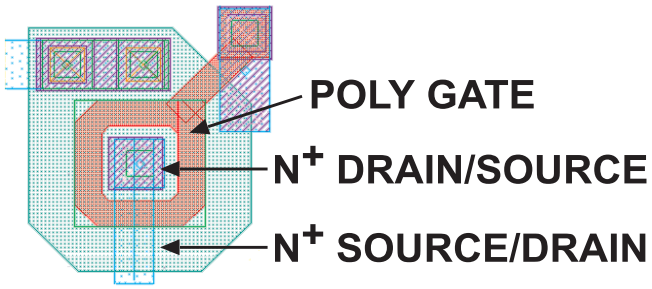

Figure 3.14: *A radiation tolerant NMOS transistor in the so-called "enclosed transistor" design. The name of this design is derived from the circular gate contact enclosing either source or drain. [Dep02]*

An additional effect of the accumulation of positive charges in the oxide, especially in thick oxides, is the formation of parasitic charge transfer paths, by creating inversion layers between n-wells in the p-type substrate, that may lead to a decrease in the signal to noise ratio or even to short circuits in the chip. In the case of NMOS transistors, the charge-up of the oxide may reach a concentration, that makes it impossible to completely switch off the transistor. A commonly used approach to overcome this issue is the so-called "enclosed transistor" design, an example is shown in Fig. 3.14. In this layout the circular gate contact encloses either source or drain of the transistor, preventing the formation of parasitic charge transfer paths to neighbouring transistors.

Using the above mentioned "enclosed transistor" design and the new deep sub-micron process, read out chips can be produced, that are able to withstand several tens of *Mrad*. One example is the APV25 front-end chip used in the LHC experiments for the read out of silicon microstrip detectors.

For more detailed information on the transfer of holes in the oxide, the generation of interface states and other effects of the irradiation on MOS structures please refer to [Ane00, Dep02, Lut99] and the references therein.

Chapter 4

Medical Radiation Imaging

Ever since Wilhelm Conrad Röntgen took the first X-ray image of his wife's hand in 1895, radiation has become more and more important in medicine, both in diagnostics and in treatment. After the first enthusiastic years, it soon became obvious that a thorough dosimetry had to go hand in hand with every application of radiation. Today's state of the art detectors and electronics cover an enormous field of dosimetry and imaging applications, from in-vivo dosimetry to digital X-ray systems.

The goal of the SUCIMA project was to transfer know-how from the HEP community to medical applications, namely dosimetry of extended sources and online beam monitoring. In the following sections the project itself will be introduced together with its two main applications and the requirements on the sensors resulting from these, as well as the sensors developed within this project.

4.1 SUCIMA

SUCIMA[(1)] is a project, supported by the European Commission within the Fifth Framework Programme (contract no. G1RD-CT-2001-00561), addressing the development of an imaging technique of extended radioactive sources based on monolithic and hybrid position sensitive silicon sensors, where "imaging" has to be understood as the record of a dose map. The detector characteristics are constrained by the two main applications, namely intravascular brachytherapy and real time monitoring of a proton beam for oncology.

The SUCIMA collaboration consists of eleven partners from five European countries. Among these partners are not only universities, but also four research centres and two companies.

4.1.1 Intravascular Brachytherapy

Brachytherapy is the medical term describing a radiation treatment in which a radioactive source is brought close to the target volume. The name "brachy" is derived from the Greek "brakhus", which translates as "short" or "close by".

Originally, Brachytherapy is an oncological treatment, in which the radiation is used to destroy the DNA of malignant cells to prevent further growth of the tissue. The applications range from permanent implantation of low-activity, short half-life time seeds (e.g. ^{125}I or ^{103}Pd) when treating prostate cancer to short term insertions of high-activity sources (e.g. ^{192}Ir) when treating laryngeal cancer. The second type of brachytherapy is also called afterloading.

In recent years a second field became more and more important for the Brachytherapy: coronary artery diseases (CAD). CAD are often linked to an artery narrowing (stenosis). This narrowing, caused by the build-up of plaque, will lead to an oxygen lack in the heart muscle which in turn increases the risk of a heart attack. There are two possible treatments for this: surgery, a bypass to the blocked

[(1)] **SUCIMA**: **S**ilicon **U**ltra fast **C**ameras for electron and gamma sources **I**n **M**edical **A**pplications

artery is introduced, and angioplasty, the lumen of the artery is re-established by inflating a balloon introduced by a catheter.

Re-stenosis, i.e. re-narrowing of the artery cross-section, is the main limitation of angioplasty and it affects $\sim 40\,\%$ of the patients treated with this method within 6 months from the intervention. There are three contributing effects: *elastic recoil* of the artery; *intimal proliferation*, growth of new tissue at cracks and tears of the vessel wall; *remodelling*, a mechanism similar to wound contraction.

To avoid the elastic recoil, a slotted stainless steel tube, a so-called stent, is mounted on the balloon catheter and inserted together with it into the constriction of the blood vessel, as shown in Fig. 4.1. After deflating and removing the catheter, it keeps, like a scaffolding, the vessel walls from closing in again. The major drawback of stents is the added proliferation, especially at the stent ends, due to damage to the vessel wall, see Fig. 4.2.

The stents range from 10 to $40\,mm$ in length and come in diameters of 3, 4 and $5\,mm$.

A reduced probability, 4% instead of 30-40%, for re-stenosis can be achieved by intravascular brachytherapy [Ver01]. Two ways of delivering the dose are used. One, by now disfavoured, possibility is the usage of a radioactive stent (low dose rate, short half-life time isotopes), which remains in position. The other is to use a non-active stent and temporarily implant radioactive seeds or wires (high dose rate).

In the second case there is a choice between two different source types. One is a train of radioactive seeds, with a typical length between 30 and $60\,mm$, the other is a coil wound from radioactive wire. In both cases the source is brought to the constriction inside a catheter.

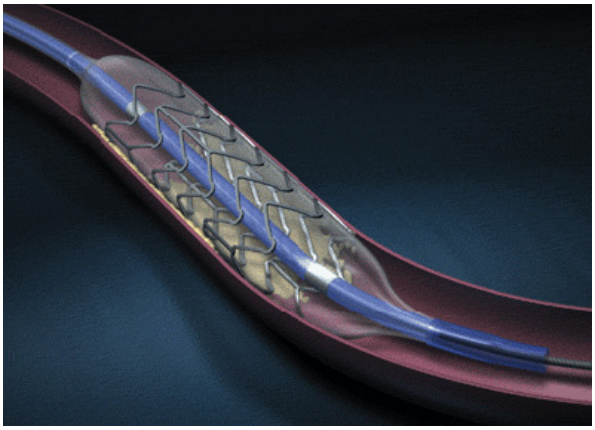

Figure 4.1: *A picture of a balloon catheter with a stent mounted on it, as it is used for angioplasty. [Cap05]*

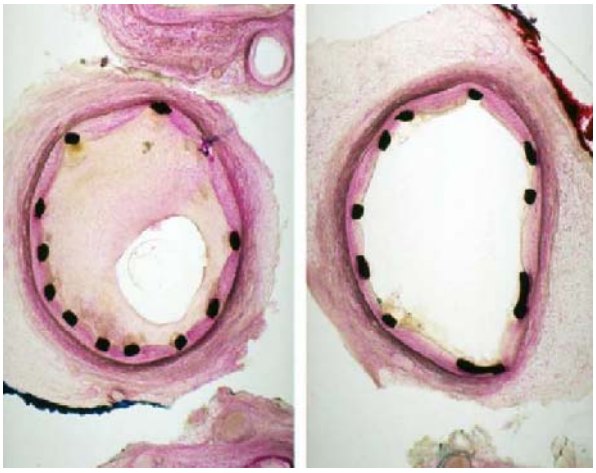

Figure 4.2: *Two cross-sections of arteries with implanted stents (black). The one on the left is affected by re-stenosis, the one on the right is not. This was achieved by the application of brachytherapy after implanting the stent. [Cap05]*

As the catheter with the source reduces the blood flow in the arteries quite a lot, the time for the treatment has to be kept as short as possible, $3-4\,min$. As the desired dose is in the range of $15-20\,Gy$, the sources have to have an activity of a few *GBq*.

The radionuclides used for the afterloading are mainly β emitters (^{90}Sr/^{90}Y, ^{144}Ce or ^{22}P) and not γ emitters, due to the steep dose gradient and the easier protection of the staff handling the source during the treatment.

The usage of high-activity sources requires of course a very thorough dosimetry and quality assurance for the treatment planning and the application itself. Up to now this is done using thermoluminescent dosimeters (TLD), semiconductor diodes or ionisation chambers, which lack the necessary spatial resolution, or with radiochromic films, which are not real-time and require expensive equipment for the analysis.

An advantage of the radiochromic films, which are not sensitive to visible light, is the very good

linearity over many orders of magnitude of dose ($0.1 - 400\,Gy$). These films consist of photomonomer molecules which change colour due to chemical changes induced by the absorbed dose, a process that requires many hours. A further advantage of the material is, that it is tissue equivalent and thus can be easily used in phantoms.

The SUCIMA collaboration aims to build cameras allowing for real-time imaging of brachytherapy sources during production and everyday usage at hospitals. To be competitive with existing dosimeters the following requirements have to be met:

- Size: In order to be able to measure the seed trains, which can be up to $60\,mm$ long, in one go the sensor has be at least $30 \times 70\,mm^2$.

- Granularity: The granularity of the dosimeter has to be below $50\,\mu m$, to allow a precise planning of the treatment and an exact measurement of the dimensions of the source.

- Radiation Hardness: The dosimeter has to able to withstand a dose rate of $2 - 20\,rad/s$ for an extended time frame.

- Sensitivity: The sensor should be able to detect single low energetic particles, but it should also be able to cope with $1 - 10\,MIPs/(pixel \times 100\,\mu s)$[(2)].

The efforts of the collaboration will allow for improvement of the quality control of brachytherapy sources, but also for better simulations, treatment planning and customised sources. Another benefit of this will be higher safety conditions for patients and personnel.

4.1.2 Hadron Therapy

A second field of work for the collaboration is a beam monitor for hadron therapy. This device is being developed together with the Hadron Therapy Centre, of which TERA[(3)] [Ama93] is a part of SUCIMA.

In cancer treatment, radiotherapy with X-ray or electron beams is used in $\sim 50\,\%$ of the cases in addition to chemotherapy and/or surgery. The energy released by the beam in the tissue destroys the genetic material, mostly by creating single strand breaks (SSB), of the tumour cells and thus prevents them from growing further.

One of the major features of the X-ray and electron beams is the exponential depth-dose curve, see Fig. 4.3. The further the beam goes into the tissue, the less intensity is left. This, together with the problem, that the beam is not stopped in the tumour but passes on, leads to serious issues for the protection of the healthy tissue around the tumour and results in complicated treatment plans for a large number of cases.

Beams of protons or light ions have many advantages over the conventional treatment techniques. The first and most important is the stopping behaviour of hadrons: They deposit almost all their energy when they reach the end of the penetration range in the so-called Bragg peak. The penetration range strongly depends on the energy of the incident particles. A second advantage is, that the hadrons are charged particles: The beam can be focused and steered using magnets in the beam line.

---

(2) **MIP**: **M**inimum **I**onising **P**article, more information can be found in section 3.1 on page 89

(3) **TERA**: **TE**rapia con **R**adiazioni **A**droniche, Therapy with Hadronic Radiations

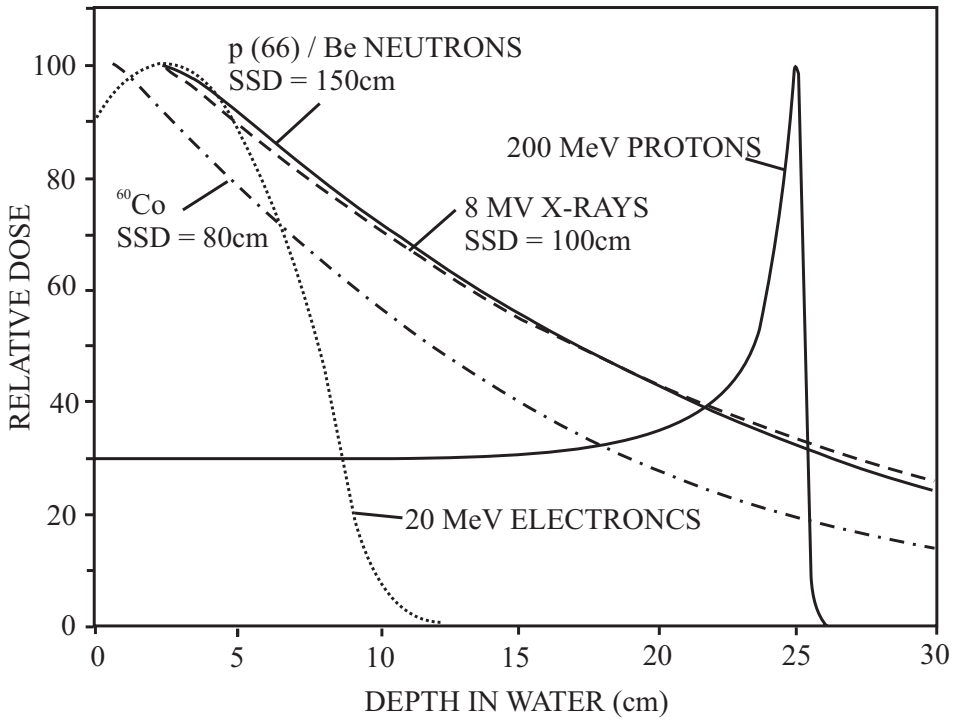

Figure 4.3: *Depth-Dose curves for various radiation types, that are used in oncological treatments. One can clearly see the exponential losses of the X-ray and the electron beams and the Bragg-peak of the proton beam. [Ama95]*

The combination of these two factors allows to scan the tumour with the beam during the treatment in all three dimensions with a precision in the range of a millimetre, as shown with a phantom in Fig. 4.4. With this a very precise dose application to the tumour can be achieved, without the risk of damaging the healthy tissue around.

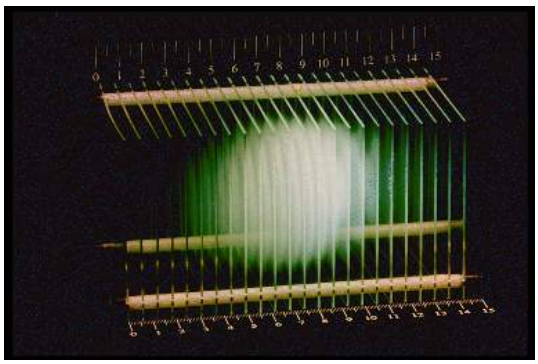

Figure 4.4: *3D scanning of a target volume with a hadron beam. [GSI]*

A further advantage of the cancer treatment with hadron beams is the biological effect of hadrons in the tissue. Unlike X-ray or electrons, they create double strand breaks (DSB) and multiple damaged sites (MDS), which are more difficult for the cell to repair and which thus more efficiently stop the tumour growth.

To ensure maximum safety for the patient and optimal performance of the accelerator complex, online measurement of the beam profile is mandatory.

Beam Monitor

To ensure a safe and efficient treatment with a hadron beam, the characteristics of the beam (spot size, dose rate,...) have to be monitored constantly, ideally without disturbing the beam. There are some well established techniques, that are used in HEP and in medical applications. But all of them have their disadvantages.

- Wire Scanner: A beam monitor based on a wire scanner consists of two major parts. One part is a carbon wire, which is mounted in a movable fixation, so that the wire can be moved across the beam with precision in the micrometre range. The second part is a detection system. In most

cases this is a scintillation screen (see below) that is observed using a CCD camera. The major drawback of this system is, that one has to use many bunches to obtain a profile of the beam and it is not possible to get a "single-shot" image. A further disadvantage is the need for a linear motion system with very high precision, that is UHV[(4)] compatible. Due to the measurement principle it is of course not applicable during the treatment.

- Multi-Wire Proportional Chamber (MWPC): MWPCs have a long standing tradition of more than 30 years in HEP applications and they are widely used in clinical accelerators. They work well in the energy range of interest and also the intensity is within the limits of the MWPC. The main problem of the MWPC is the rather complicated production procedure. Also the operation of the device is not without problems, as it constantly has to be flushed with gas and needs high voltage. The MWPC is also destructive for the beam and only reaches a spatial resolution of $0.5\,mm$.

- Scintillation Screens: The material of choice for scintillation screens in medical accelerators is CsI(Tl) with a thickness of $1\,mm$ and a decay time of $< 1\,\mu s$. The light output of the scintillator is observed using a CCD camera. Due to the fast decay time of the scintillator material, time dependencies of the beam can be observed. With these systems a spatial resolution of $50\,\mu m$ can be achieved. They are also able to cope with flux variations over 4 orders of magnitude. Scintillation screens are easy to produce and they can withstand enormous amounts of radiation. As the material thickness has to be rather large to obtain enough light output, even though image intensifiers can be used, the beam is strongly perturbed. For low beam energies also the number of scintillation screens possible in one beam line is limited.

- Secondary Emission Monitor (SEM): When a hadron beam passes through a wire or a foil, low energetic electrons are emitted from the surface layers. The ratio of emitted electrons to incoming particles is in the order of 1:100. The localisation is conserved, meaning this effect can be used to measure the beam profile. The secondary electrons are collected by segmented anodes. This presents also the main drawback of the SEM, the spatial resolution is very limited due to the size of the read-out strips. A second negative effect is the large signal and gain variation from strip to strip. A further limitation comes from the high impedance of the collecting anodes which leads to a quite high threshold on the signal, even if low-noise electronics are used. As the secondary emission is a surface effect, the foil in the primary beam can be very thin, leading to the main advantage of the SEM, the low interception of the beam.

The only possibility to monitor the beam during the treatment, at least to some extent, is the usage of so-called halo monitors. These consist of scintillator panels that are mounted on linear tables around the beam in an iris shape. They collect $0.1 - 1\,\%$ of the particles of the beam from the halo. Due to the unprecise measurement principle, the halo monitors can only be used as watchdogs, terminating the beam in case of unexpected beam parameters.

SLIM

At low beam currents, standard measurement devices are interceptive respectively pertubative and thus they are not usable during treatment. The SUCIMA approach is: Secondary emission for Low Interception Monitoring (SLIM), a real-time high precision beam monitor using the secondary emission of electrons from a thin foil in the path of the primary beam [Fer03]. This system overcomes the main limitations of the standard SEM systems and will allow to check the beam in multiple places even during the treatment.

[(4)] **UHV**: **U**ltra **H**igh **V**acuum, residual pressure $< 10^{-9}\,mbar$

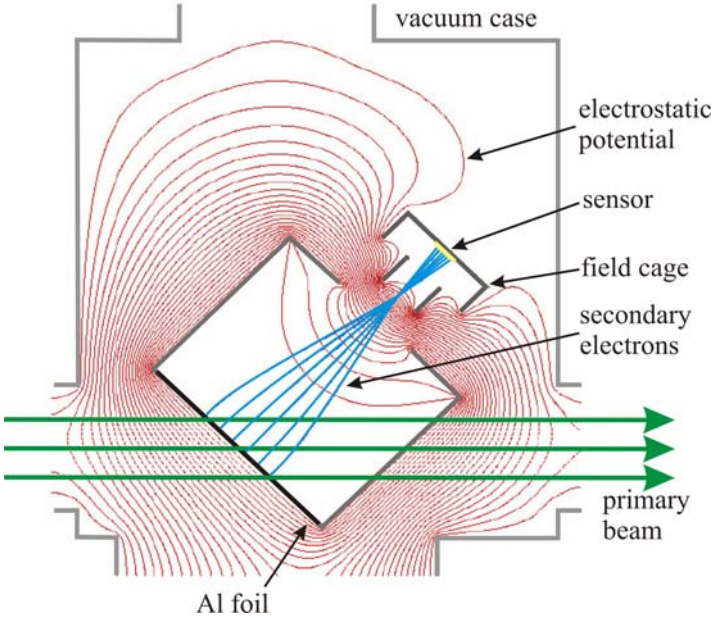

Figure 4.5: *SLIM: Secondary emission for Low Interception Monitoring. The picture shows a cross-section of the beam monitor of SUCIMA from a simulation.*

Fig. 4.5 displays the measurement principle. The primary hadron beam (green) passes through a thin Al foil (thickness: $0.2 - 0.4\,mm$). The secondary electrons (blue) emitted from the foil are accelerated and focused by the electric field (red) of the SLIM optics towards the sensor. In the first test runs, the sensor was a pad detector. In the final device it will be a back-thinned CMOS sensor, the SUCCESSOR-IV.

A CAD drawing of the implementation of the chamber is shown in Fig. 4.6(a), a picture of the first prototype in Fig. 4.6(b). In the CAD drawing the beam passes along the tube from left to right through SLIM. The secondary emission Al foil is located in the centre of the front plate of the optical system of SLIM. One can also see the wire mesh through which the beam leaves SLIM, once it passed through the foil.

The picture of the prototype shows the SLIM optics from a slightly different angle. Here one can see the mounting frame for the electron detector, the wire mesh and the hole for the Al foil, which is not yet mounted.

The electrostatic optics of SLIM accelerate the electrons from the secondary emission to energies of up to $20\,keV$. A second effect of the optics is a demagnification by factor 5 and the focusing of the electrons onto the detector. The optics preserve the beam position, shape and intensity, thus allow a full characterisation of the beam parameters.

As the energy of the electrons, even after the acceleration, is only $20\,keV$, the penetration depth in silicon is extremely short. To be able to detect these electrons, a sensor with a very thin entrance window has to be used. For this purpose the SUCCESSOR-IV sensor was designed. After the production it is back-thinned down to the epitaxial layer and then illuminated from the back side in the SLIM setup. This has the beneficial effect that the electrons will be fully stopped in the sensitive layer and will not reach the electronics on the other surface, which they would otherwise damage over the time.

The beam size, position and intensity are measured with a rate of $10\,kHz$ in order to observe any time dependent fluctuations in intensity and/or position. The system will allow for online correction of the beam parameters or a fast beam dump, if there are serious problems. In addition, it will serve as a cross check for the dosimetry system, thus it will help to maximise safety.

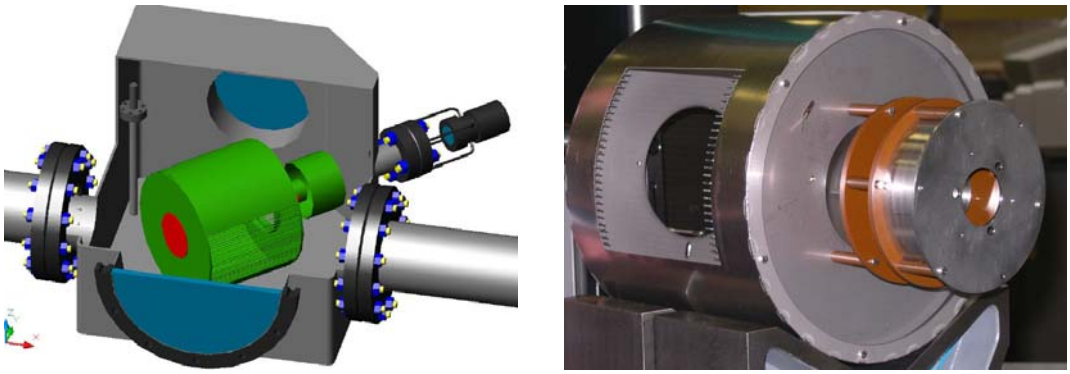

(a) CAD Drawing (b) Prototype

Figure 4.6: *The Implementation of the SLIM system. (a) shows a CAD drawing. The aluminum foil is located in the centre of the front plate of the optical system. Also visible is the mesh grid in the side of the optical system through which the beam exits. In (b) the optical system of the prototype is depicted from the reverse angle compared to (a). Source: SUCIMA Collaboration.*

In order to fulfil the requirements for a fast and precise beam monitor (uncertainty in the delivered dose $< 2.5\,\%$) for medical applications, the sensor has to meet the following standards:

- Size: The primary beam has a diameter of a few centimetres before entering the quadrupole magnet focusing it into the target. Even with the demagnification of the focal system the size of the sensor still has to be larger than $15 \times 15\,mm^2$.
- Granularity: The requirements on the granularity of the sensor are not as high as for the dosimetry: $200\,\mu m$
- Radiation Hardness: Radiation hardness is not an issue in this application, as the low energetic electrons ($20\,keV$) are all fully stopped in the sensitive layer of the detector and do not reach the electronics layer, which they might damage over time.
- Sensitivity: The low energy of the secondary electrons, even after the acceleration, is somewhat of an issue, but this can be overcome by using back-thinned CMOS sensors, which have a negligible dead layer. The dynamical range, a sensor has to be able to cope with, is $0.2 - 2000\,MIP/(pixel \times 100\,\mu s)$.
- Speed: As time dependent phenomena of the beam should be detected by the system, the frame rate has to be at least 10000 fps[(5)].

4.1.3 SUCIMA – Summary Detector Specifications

Specification	Brachytherapy	Hadron Therapy
Size $[mm^2]$	30×60, stitched	15×15
Granularity $[\mu m]$	50	200
Rad. Dose $[rad/s]$	$2 - 20$	0
Sensitivity $[MIPs/(pixel \times 100\,\mu s)]$	$1 - 10$	$0.2 - 2000$
Speed [fps]	10-100	10000

Table 4.1: *This table summarises the requirements on the detectors for the two applications of SUCIMA, brachytherapy and hadron therapy.*

[(5)] **fps**: **f**rames **p**er **s**econd

4.2 SUCIMA Medical Detectors

In the SUCIMA project a variety of sensors has been used for different applications. This chapter will give an introduction to the sensors themselves and to the read out electronics developed within the SUCIMA collaboration.

The main purpose of radiation sensors in medical applications are either imaging, e.g. radiography, or quality control of treatment procedures. The sensors used up to now are either very slow (GAFchromic films) or have a very poor spatial resolution (ionisation chambers). Also most of the systems are very expensive.

The approach of SUCIMA to use state-of-the-art silicon devices for some very specific applications allows to combine high granularity with fast acquisition times. The devices are cross-calibrated against well established systems to ensure the conformity with medical regulations.

There are many silicon devices that can be used as detectors for radiation. There are some technologies that have been used in High Energy Physics for decades, but also some interesting new developments. SUCIMA concentrated its efforts on three of these technologies: Silicon Micro-Strip Detectors, CMOS[6] pixel sensors and SOI[7] pixel sensors.

In the following sections the sensors designed and/or used by the SUCIMA will be introduced, with the emphasis on the CMOS pixel detectors. A detailed insight into the various development stages and prototypes will be given on that matter, while the silicon micro-strip and the SOI detectors will only be shortly introduced.

4.2.1 Silicon Micro-Strip Detectors

Silicon micro-strip sensors have a long-standing tradition in High Energy Physics. They have been successfully used for many years in large scale experiments like DELPHI[8] [Cho98] or CDF[9] [Sil00] and will be used in even bigger experiments like CMS[10] [Kra04].

As the development from scratch and the production of a silicon micro-strip detector is time consuming and expensive, SUCIMA chose to use off-the-shelf components for the sensor and the read out system, especially since the strip detectors were only regarded as a backup in case the development of the pixel devices would have failed. Nevertheless, they proved to be very valuable to better understand the requirements on the pixel sensors and for dosimetric measurements with highly active seeds.

The sensors used by SUCIMA, see Fig. 4.7, were developed for the AGILE[11] experiment [Tav03] and are produced by Hamamatsu Photonics K.K. The sensors are $9.5 \times 9.5\,cm^2$ large and have 768 read out strips with a pitch of $121\,\mu m$. The full depletion voltage is $\sim 80\,V$ with a leakage current of $0.1\,nA$ per strip.

The read out system is based on a VA pre-amplifier ASIC by IDEAs ASA. The data acquisition is either done by a VME based system or by the SUCIMA Imager, a USB2.0 read out board. More information on the SUCIMA Imager can be found in section 4.3.1 on page 126.

The strip sensors were mainly used in dosimetry setups where the dose of a radioactive source was measured as a function of the radian around the catheter or the depth of a water equivalent material.

A detailed description of the silicon micro-strip sensors, the setup and their performance can be found in [Cap05].

---

[6] **CMOS**: **C**omplementary **M**etal **O**xide **S**emiconductor

[7] **SOI**: **S**ilicon-**O**n-**I**nsulator

[8] **DELPHI**: **DE**tector for **L**epton, **P**hoton and **H**adron **I**dentification

[9] **CDF**: the **C**ollider **D**etector at **F**ermilab

[10] **CMS**: **C**ompact **M**uon **S**olenoid

[11] **AGILE**: **A**stro-rivelatore **G**amma a **I**mmagini **LE**ggero

Figure 4.7: *A picture of the silicon micro-strip detector of SUCIMA mounted on its hybrid.*

4.2.2 CMOS pixel detectors

This pixel detector type, the CMOS pixel detector, has been discussed as an alternative to CCDs[(12)] for some applications since the early 1990s. Today it is used in a wide field of products ranging from digital X-ray systems to web cameras.

Most CMOS pixel detectors use a concept called Active Pixel Sensor (APS). Besides the sensitive element, either a photodiode or a photogate, they feature in each pixel cell the first amplification stage plus a reset transistor and a selection switch. Please refer to Fig. 3.10 for an example of the implementation of this read out for both, pixel and chip level. This basic scheme was implemented in the MIMOSA-I chip and is still used, with only minor modifications, in the most recent MIMOSA and SUCCESSOR chips.

In the following sections, the various prototypes used in the context of this thesis will be introduced, with an emphasis on the SUCCESSOR-I chip, which was used intensively for the radiation hardness studies presented in chapter 5.

MIMOSA-V

The MIMOSA-V chip, originally designed as a detector prototype for a possible linear collider experiment, was used in the SUCIMA collaboration. Its main purpose was to be the reference device during the development of the DAQ system, when the SUCCESSOR chips were not yet available.

A second very important application of the MIMOSA-V was to test the process of the back-thinning of the sensors on wafer basis, which was applied to this kind of chips for the first time. As this proved to be very successful it will be applied also to the final detector for the SLIM application.

A picture of the die of the MIMOSA-V chip is shown in Fig. 4.8(a), a schematic overview in Fig. 4.8(b). The MIMOSA-V sensor was produced in an $0.6\,\mu m$ technology. It has a surface of $19400 \times 17350\,\mu m^2$ and is segmented into 4 different sectors, each having its own analog output. The sub-matrices consist of 510×512 pixels with a pitch of $17\,\mu m$. The digital part of the chip and the output buffers are all located on one side of the detector. This allows to place up to 7 sensors next to each other on the wafer with a dead band between them of only $200\,\mu m$.

The charge collecting diodes of the pixels are n-well/p-epi devices, see Fig. 3.8(a). Depending on the sub-matrix their dimension is either $3.1 \times 3.1\,\mu m^2$ or $4.9 \times 4.9\,\mu m^2$. The electronics of the pixels are based on the standard three transistor ($3T$) approach, see Fig. 3.10, allowing for a maximum clock frequency of $40\,MHz$.

[(12)] **CCD**: **C**harge-**C**oupled **D**evice

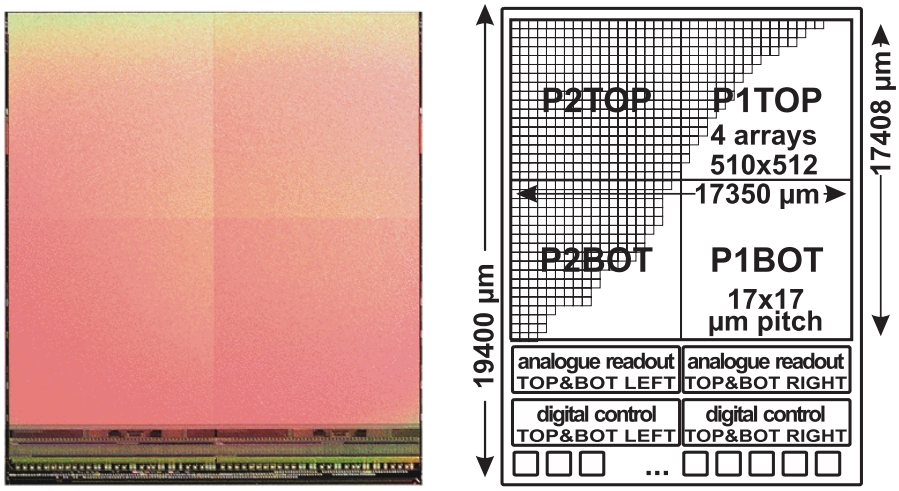

(a) Die (b) Layout

Figure 4.8: *(a) shows a picture of the actual die of a MIMOSA-V detector. The arrangement of the sub-matrices and the analog and digital read out parts on the sensor are depicted in (b). [Dep03a]*

The MIMOSA-V offers a set of different operation modes. It can be read out in the standard way, with a rolling shutter[(13)] or in a so-called fast scan mode[(14)]. In the last mode only every ninth pixel, in both directions, is read out. In order not to lose signal in this mode, the signal from the interleaved pixels can be summed.

A more detailed description of the sensor and its performance can be found in [Dep03a].

MIMOSA-V back-thinned

For the detection of low energetic particles one has to use a sensor with a very low threshold energy. In silicon sensors this threshold is defined by the thickness of the dead layer above the sensitive volume and the characteristic stopping power for this particle.

The thickness of the dead layer is typically in the range of a few μm, which corresponds to a threshold on the energy of a few tens of keV for electrons. The metallisation layers intrinsic to the CMOS sensors increase the problem even further.

The apparent approach to solve the issues caused by the dead layer is to flip the sensor over and shine it from the backside. Unfortunately, this does not help immediately for CMOS sensors, as they have a few hundred μm insensitive bulk material beneath the active layer, the epitaxial layer.

The idea is then, roughly spoken, to glue a handle wafer on top of the sensor for mechanical stability and etch the backside down to the sensitive volume. This process will be described in more detail in the following:

- Fig. 4.9(a) shows the CMOS pixel sensor in its standard configuration. One can immediately see the first problem of this process. The surface of the chips is not even. At places where there are many interconnection layers, the sensor is higher, at the locations of the bond pads it is much lower. Thus before glueing the handle wafer onto the sensor wafer[(15)], these inhomogeneities have to be evened out. Especially the “holes” above the bond pads have to be filled up, as the bond pads will be later on used from the other side.

[(13)] In the rolling shutter mode only a few rows are kept active and are read out while all others are kept at reset level. This set of active rows constantly moves in a cycle through the detector.

[(14)] This is an interleaved read out mode. Only every 81^{st} pixel is read out (every 9^{th} in both dimensions).

[(15)] This has to be done on the still un-diced wafer. Previous tests had proven that back-thinning on an individual sensor basis was not achievable.

- Once a homogeneous surface has been achieved, the handle wafer is glued onto the wafer, as shown in Fig. 4.9(b). After this the bulk material of the sensor wafer is etched away. The process used for this, is designed in such a way, that it stops when it reaches the surface of the epitaxial layer. The exact etching process is kept a corporate secret by Atmel.
- After finishing this process step, a passivation layer of a $100 - 300\,nm$ silicon oxide is grown on the new surface. The thickness of this passivation layer, together with the depth of a very shallow doping to restore the potential increase towards the edge, defines the dead layer and thus the energy threshold. As the total thickness is still very small, the threshold is now in the order of a few *keV*, where it was before a few tens of *keV*.
- Another problem of this method is the bonding of these flipped-over chips, see Fig. 4.9(c). One has to "drill" a hole down to the metal layer of the bond pad through the epitaxial layer. In order not too get to close to the sensitive volume, the holes have very steep edges. Thus the bonding can only be done using very narrow deep-access bonding tools and a very thin bond wire. In Fig. 4.21(a) a back-thinned MIMOSA-V is shown, mounted onto a standard hybrid.

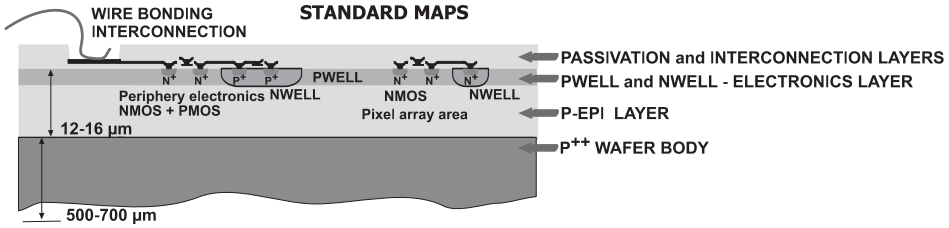

(a) Standard MAPS

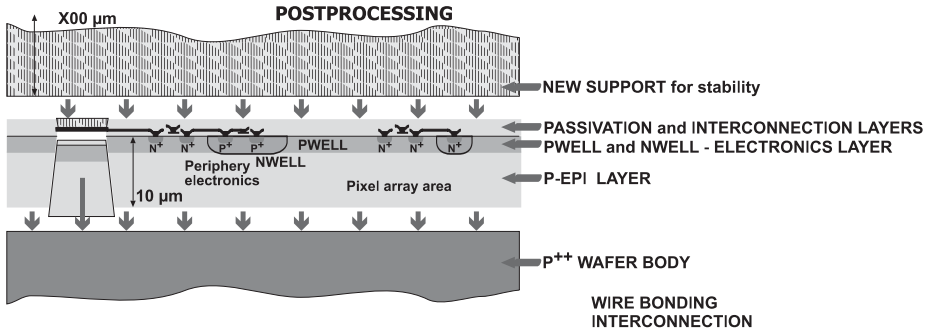

(b) Back-Thinning

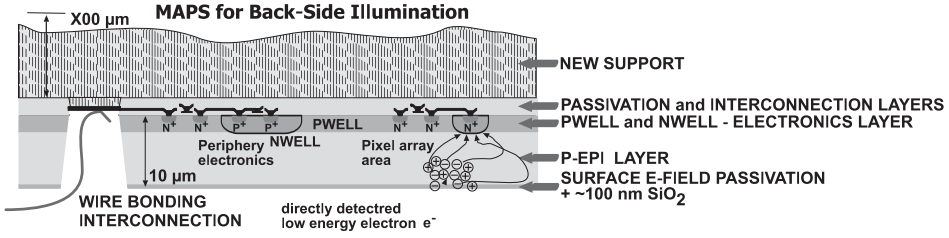

(c) Back-Side Mounting

Figure 4.9: *These drawings illustrate the back-thinning process used on the MIMOSA-V and the SUCCESSOR-IV chips. (a) shows the CMOS pixel sensor in its standard configuration. In (b) the steps of the process are depicted: the creation of a homogenous surface, the glueing of the handle wafer, the removal of the bulk material and the "drilling" of the access holes to the bond pads. In (c) the final product, a CMOS sensor with a very thin entrance window, is shown.*

To demonstrate that the back-thinned CMOS sensors work according to expectations, two tests were done on back-thinned MIMOSA-V sensors. One test was a set of measurements in an HPD[16]-like configuration [Dul04], the other was an autoradiography measurement with a Tritium source [Dep04].

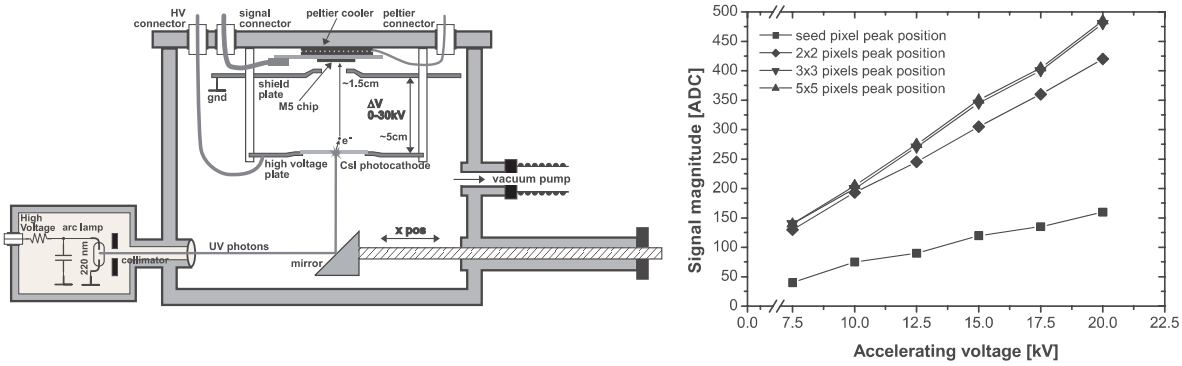

(a) HPD Setup (b) Result Plot

Figure 4.10: *The HPD setup (a) for the back-thinned MIMOSA-V and one of the result plots (b) from the measurements with this setup. The performance of the chip was very close to the expectations. As the cluster generated by an incoming electron is larger than one pixel, the seed pixel has a lower peak than the sum over the cluster. Taken from [Dul04]*

Fig. 4.10(a) shows the setup used for the measurements in the HPD-like system. The sensor is placed in a vacuum chamber beneath a photocathode. The electrons emitted from the photocathode due to the light shone onto it are accelerated towards the sensor with an adjustable electrical field. One of the results of these measurements is shown in Fig. 4.10(b). The plot shows the signal magnitude for various cluster sizes as a function of the acceleration voltage.

SUCCESSOR-I

SUCCESSOR-I was the first chip to be designed within the SUCIMA collaboration. The layout of the SUCCCESSOR-I is shown in Fig. 4.11(a), a picture of the die in Fig. 4.11(b). Its main purpose was to evaluate the performance of 8 different pixel geometries, especially with regard to the radiation hardness. Based on the measurements described in chapter 5, the design for the final chip was chosen.

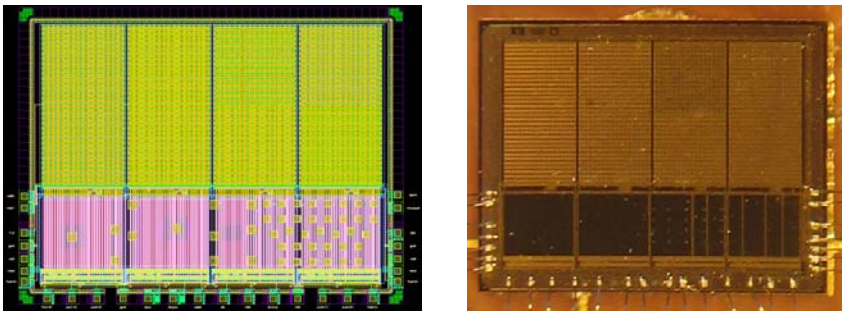

(a) Layout (b) Die

Figure 4.11: *The SUCCESSOR-I CMOS sensor. (a) shows the layout of the chip. One can distinguish the 8 different pixel matrices (top / yellow), the test structures (middle / pink), the digital part (bottom / green) and the bond pads. A picture of the actual die is shown in (b). Here one can also easily see the different parts of the sensor.*

[16] **HPD**: **H**ybrid **P**hoto **D**etector - a PMT like photon detection system in which a silicon detector is used for the read out instead of a standard cathode

The chip was produced using the AMIS 0.35 μm technology, which has a 4 μm epitaxial layer. The overall dimensions of the chip are $4600 \times 3600\,\mu m^2$. As already mentioned, the chip features 8 different pixel arrays, which can clearly be seen in Figs. 4.11(a) and 4.11(b). Each of them consists of 32×32 pixels arranged in clusters of 4 pixels, the so-called super-pixels (see Fig. 4.12). The pixel pitch is 30 μm for the basic pixels and 60 μm for the super-pixels.

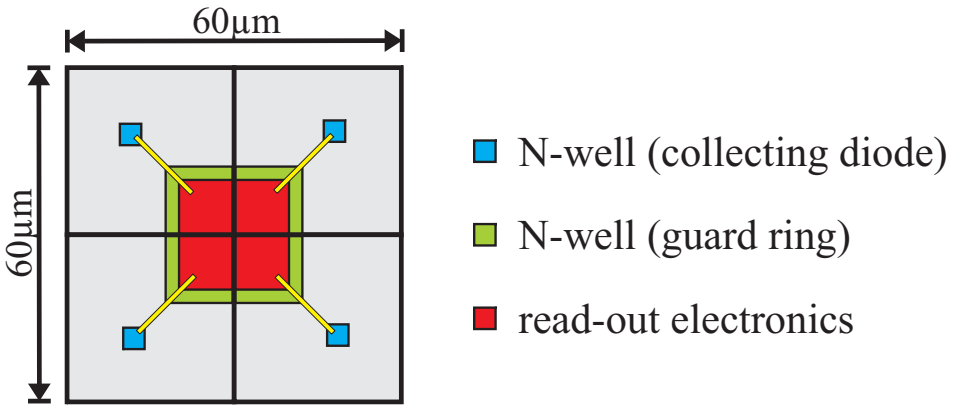

Figure 4.12: *The so-called super-pixel of the SUCCESSOR-I. One super-pixel contains 4 pixels which are arranged in such a way, that the read out electronics are located in the centre and can be separated from the sensitive volume by a guard ring.*

To increase the radiation hardness of the pixels, especially to counter the loss of charge collection efficiency due to parasitic collection paths, source and drain of the reset transistor were swapped in this design. Additionally, a radiation hard "enclosed" design was chosen.

The 4 channel parallel output allows to clock the chip with a maximum read out frequency of 40 MHz. The digital part of the chip is designed using non-radiation-tolerant standard cells. This required the use of shielding during the irradiation to protect the digital part, see section 5.2.1.

In the following each of the 8 different pixel types will be introduced briefly. A picture of each pixel schematic is shown in Figs. 4.13 and 4.14. Their most important features are summarised in a comparison table at the end of this section.

Pixel 0: This pixel has a C-shaped collection diode, which is rather large with $\sim 34\,\mu m^2$. Nevertheless, the capacitance of the pixel, 32 fF, is only 50% larger than that of the pixels with smaller diodes. A guard ring separates the collecting diode from the read out electronics. Another feature of this pixel is the metal field plate on top of the junction which can be biased with a negative voltage. The fill factor (definition see below) of this pixel is 85%

Pixel 1: The design of this pixel is very similar to that of Pixel 0. The collecting diode has the same size, $\sim$ 34 μm^2 and almost the same capacitance, 30 fF. The major difference between Pixel 1 and Pixel 0 is, that Pixel 1 has no field plate on the junction. Again, the fill factor is 85%, as Pixel 1 also has a guard ring between the electronics and the diode.

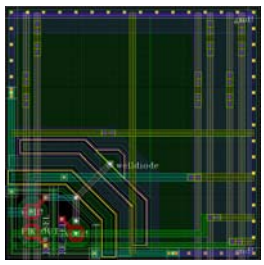

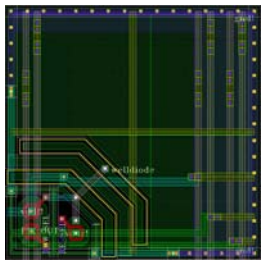

Figure 4.13: *Pixel Layout*

Pixel 2: The collecting diode of this pixel is quadratic with an area of $\sim 10\,\mu m^2$. Due to the rather small size of the diode in this layout, the capacitance of the pixel is also quite small with $18\,fF$. Pixel 2 features both, a guard ring and a field plate on top of the junction. The fill factor of this pixel geometry is therefore rather small with $20-30\,\%$.

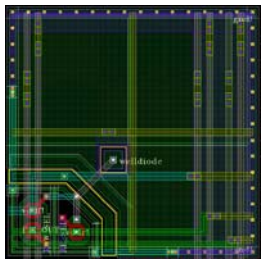

Pixel 3: The layout of this pixel is the closest to the "standard pixel" of all the pixels on this chip. It is very much like that of Pixel 2. Its square diode has the same size of $\sim 10\,\mu m^2$ and thus the same capacitance of $18\,fF$. It also features a field plate, but no guard ring. This makes the complete area of the pixel sensitive and thus gives a fill factor of $100\,\%$.

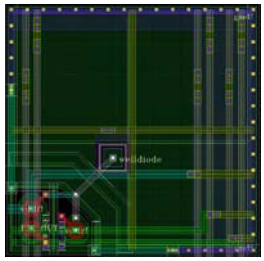

Pixel 4: The design of this pixel has some peculiarities. Its collecting diode is also square, but uses the minimum feature size of this process, which leads to an area of less than $3\,\mu m^2$. Still it has the same capacitance of $18\,fF$, like Pixel 2 and Pixel 3. This design features neither a guard ring nor a field plate. Instead there is a large poly silicon pad with metal covering. As there is no guard ring, this configuration has a fill factor of $100\,\%$.

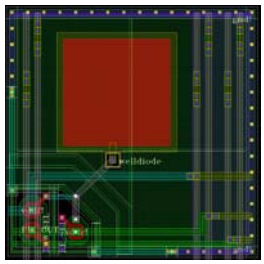

Pixel 5: This pixel also has the minimum sized diode with an area of $< 3\,\mu m^2$. As the oxide of this design uses the minimum thickness it is not possible to calculate the capacitance precisely. This pixel also has no guard ring. The field plate of this pixel is placed on top of the oxide and not on the junction, as it was done for the other designs. The fill factor of this pixel geometry is $100\,\%$.

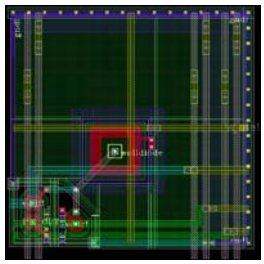

Pixel 6: Using a C-shaped collecting diode of $\sim 34\,\mu m^2$, this pixel was designed with thin oxide, which should increase the radiation tolerance, resulting in a capacitance of $93\,fF$. A guard ring separates the electronics from the collecting diode. Due to this the fill factor is $85\,\%$.

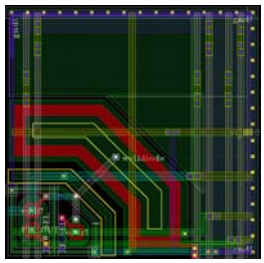

Pixel 7: The unconventional approach in this design uses, unlike all others, no n-well as collecting diode, but just the n++ diffusion layer. The large size of the diode, $\sim 189\,\mu m^2$, results in a capacitance of $95\,fF$. As there is no n-well allowing access to charge carriers generated in the epitaxial layer, only electrons generated in the diode itself can be collected. This leads to a rather small fill factor of $20\,\%$.

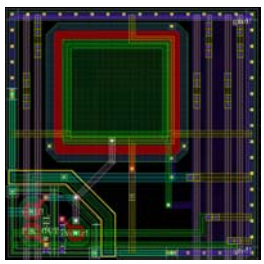

Figure 4.14: *Pixel Layout*

The limitation of the fill factor, which is defined as the sensitive area divided by the total area of a pixel, to a value less than 100 % is mostly due to the guard ring, which acts as a competitive collection path and prevents charge generated beneath the read out electronics of the pixel from reaching the collecting diode.

	Pixel 0	Pixel 1	Pixel 2	Pixel 3	Pixel 4	Pixel 5	Pixel 6	Pixel 7
diode type	C-shape	C-shape	square	square	square	square	C-shape	square
diode size [μm^2]	33,49	33,49	10.24	10.24	2.89	2.89	∼34	188.88
guard ring	yes	yes	yes	no	no	no	yes	yes
field plate	yes	no	yes	yes	no	yes	no	no
total capacitance [fF]	32	30	18	18	18	???	93	95
fill factor [%]	85	85	20-30	100	100	100	85	20

Table 4.2: *This table lists the most important properties of the 8 different pixel geometries of the SUCCESSOR-I chip.*

SUCCESSOR-II

The SUCCESSOR-II chip is slightly smaller than SUCCESSOR-I with a size of 3400*x*3600 μm^2. Its schematics and a picture of the die are shown in Fig. 4.15. It is produced in the AMS 0.35 μm technology. Instead of standard low resistivity wafers a high resistivity substrate without epitaxial layer was used for this submission.

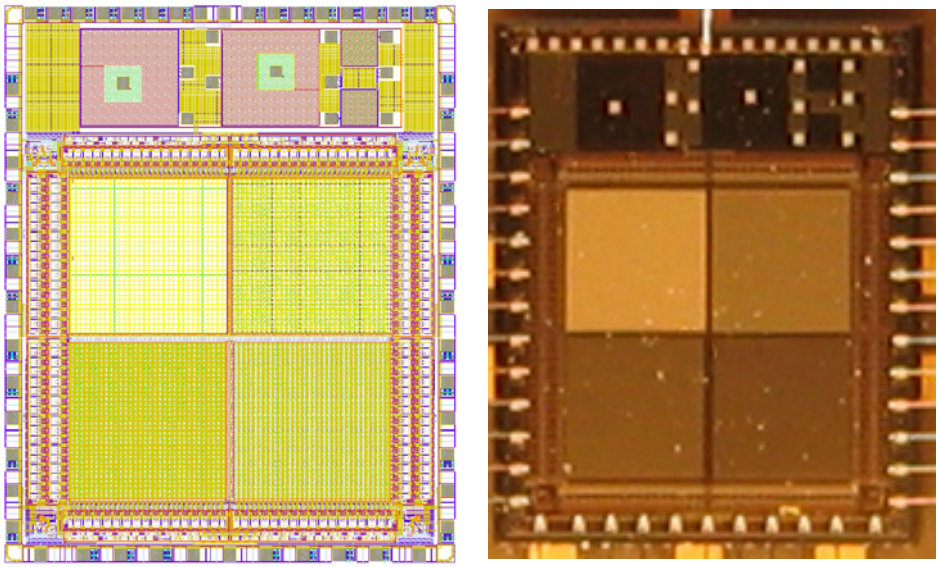

(a) Schematic (b) Die

Figure 4.15: *Schematic view of the SUCCESSOR-II CMOS sensor.*

Like its predecessor, SUCCESSOR-II features different pixel arrays, but instead of 8 different pixel matrices it has only 4. Again each of the matrices contains 32×32 pixels. The pitch of the pixels is 40 μm.

The overall chip layout is like the one of the MIMOSA-IV prototype [Dep03b]. It uses the same grouping of the pixel matrices and the same digital part including arrangement of the bond pads. The digital part is designed using radiation hard transistor layouts.

The four different pixel matrices consist of two PhotoFET pixel matrices, one self-biasing pixel matrix and one standard pixel matrix. The main difference between the two PhotoFET matrices is, that in one of them the pixels are grouped in sub-arrays.

The matrix with the standard pixels is divided into two halves. In one half the collecting diode of the pixels is $4.3 \times 3.3\,\mu m^2$ while in the other half it is $2 \times 2\,\mu m^2$. The collecting diodes have a rectangular shape. Another modification in case of the standard cells is the changed layout of the read out electronics. Like in SUCCESSOR-I source and drain of the reset transistor are swapped to eliminate a possible parasitic charge transfer path.

The last matrix, the one with the self-biasing pixels, is split into two halves like the one with the standard pixels. In the case of the self-biasing pixels the two diode sizes are $4.3 \times 3.4\,\mu m^2$ and $6 \times 6\,\mu m^2$.

The self-biasing pixel uses a second diode, which is biased in forward direction, to constantly recharge the collecting diode. Thus this pixel does not require a reset pulse to counter the discharging of the collecting diode due to leakage currents.

All 4 pixel matrices can be read out at the same time. The maximum clock frequency for reading out this chip is $40\,MHz$.

During the tests of this chip it was observed, that particle transitions through the pixels with the small standard diode generated no signal at all. The preliminary conclusion of this effect is, that there is a minimum diode for reasonable operation size depending on the feature size of the process.

SUCCESSOR-IV / MimoTERA

The SUCCESSOR-IV, also called MimoTERA, is a chip specially designed to meet the requirements of the application as a real-time beam monitor in radio therapy with hadrons. The most important features are a fast read out time and a very short dead time.

The chip, a schematic view is shown in Fig. 4.16, is produced in the AMS CAU technology with a feature size of $0.6\,\mu m$ and epitaxial layer thickness of $14\,\mu m$. It is a rather large chip with its overall dimensions of $17350 \times 19607\,\mu m^2$.

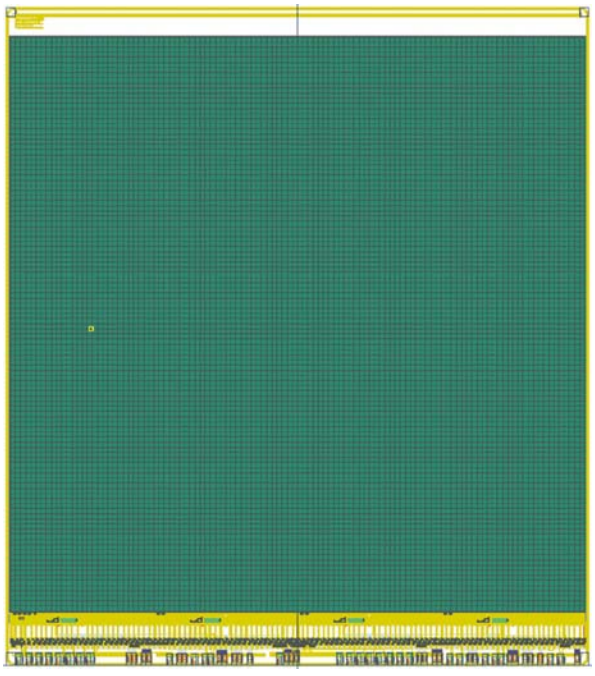

Figure 4.16: *Schematic view of the SUCCESSOR-IV / MimoTERA CMOS sensor.*

The mechanical layout of the SUCCESSOR-IV chip sticks as close as possible to that of the MIMOSA-V to allow re-usage of the masks for the back-thinning process. The main modification is the enlargement of the bond pads to $85 \times 185\,\mu m^2$ for easier access to the pads with the head of the bonding machine.

The total array contains 112×112 pixels, each sized $153 \times 153\,\mu m^2$. They are arranged in 4 sub-arrays of 28×112 pixels, which are read out in parallel. This allows to keep the integration (and read out) time below $100\,\mu s$.

To keep the dead time as small as possible, each pixel is divided into two halves, with independent front-end electronics and collecting diodes. While one half is sensitive, the other half is being read out and reset.

As the pixels are quite large, special measures have to be taken to achieve a maximum fill factor for both pixel halves. Thus each pixel half does not only have one collecting diode, but a whole set of 9×9 diodes, each $5 \times 5\,\mu m^2$ large, interleaved with those of the other half.

To cope with the requirements on the dynamic range of the pixels two in-pixel capacitors were included in the design. One has a capacitance of $0.5\,pF$, the other one $5\,pF$. Thus, by setting a switch, the dynamic range can be adjusted by a factor of 10.

The limitation on the read out and the dead time does not allow to use correlated double sampling to suppress kTC noise[17], as this would require reading at least two consecutive frames for one set of data. The kTC noise expected from the calculations is $\sim 280\,e^-(ENC)$[18], which is within the acceptable range.

Like for the SUCCESSOR-I and -II the maximum read out frequency is $40\,MHz$, which in case of this chip will also be the default value. This high frequency is required by the quasi real-time application as beam monitor which should sample the beam profile with a rate of $10\,kHz$.

The beam monitor of Tera, the main application of this chip, is a low interception system based on the secondary electron emission from thin foils, see section 4.1.2. These secondary electrons have a kinetic energy of a few eV. After acceleration and focusing the kinetic energy of the electrons is in the range of $20\,keV$.

The range of electrons with this energy in silicon is only a few μm. Thus a sensor with almost no dead layer has to be used. This is achieved by back-etching SUCCESSOR-IV to the epitaxial layer, see section 4.2.2. The only dead layer is then the passivation layer, which has a thickness of less than $200\,nm$.

4.2.3 SOI pixel detectors

There are two SOI pixel sensors, that were designed within the SUCIMA collaboration. One is a full size sensor, the other is a "baby detector", that is only one quarter of the size of the full sensor. The smaller sensor also lacks the on-chip digital part.

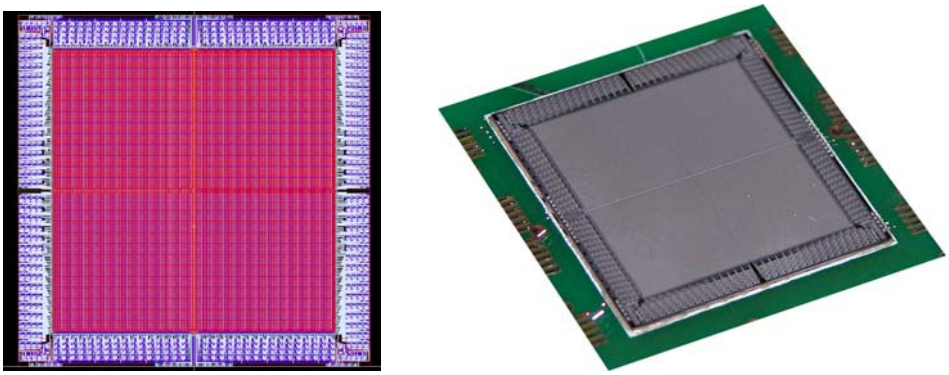

(a) Layout (b) Die

Figure 4.17: *The SOI sensor. (a) depicts the schematic layout of the sensor. Like all other prototypes it is segmented into 4 parts for a faster read out. A picture of the actual die of the sensor is shown in (b). There the sensor is mounted onto its hybrid.*

On each wafer there are 4 full size sensors, shown in Fig. 4.17, and 6 small ones plus a set of test structures. The large detectors are $2.4 \times 2.4\,cm^2$ and have 128×128 square pixels. The full size sensor is divided into 4 completely independent sectors. The baby detector is $1.2 \times 1.2\,cm^2$ large and has 48×48 square pixels.

The wafers processed using the final layout of SUCIMA were of two different types. One type is made with low-resistivity handle wafers, the other with high-resistivity ones. From the second type one would expect better detector performance, as the lifetime of the charge carriers is larger and the leakage current is smaller.

[17] The kTC noise is the noise associated with the capacitance of the device, in this case the capacitance of the diode plus that of the transistors.

[18] **ENC**: **E**quivalent input **N**oise **C**harge

Since the SOI technology is applied to full size pixel sensors for the first time, there were some problems in the first production batches, both in the analog and in the digital part. Thus the testing on the prototypes was more difficult than expected and only few results were obtained.

Further information on the SOI technology and the sensors can be found in [Mar03].

4.3 Data Acquisition System

The DAQ system of the SUCIMA collaboration was designed and built by the Cracow group. It is specially engineered to meet all requirements of the different setups. Due to its modular design it can be used to read all 3 types of detectors used in SUCIMA: CMOS, SOI and silicon micro-strip detectors. It is also able to provide the fast read out and online data processing for the usage in the Secondary emission for Low Interception Monitoring (SLIM).

After an introduction into the main PCB of the DAQ system, the repeater for the CMOS and the hybrid will be presented. At the end of this chapter the LabView software will be described together with the algorithms used for the online analysis.

4.3.1 USB2.0 Data Acquisition System

The PCB carrying the powerful Field Programmable Gate Array (FPGA) is the core of the SUCIMA DAQ system. It provides the digital control and clock signals, digitises up to 4 analog signals in parallel and handles the communication with the computer. In the SLIM application it will also do all data processing and only pass the most important information to the beam control computer. A picture of the actual PCB is shown in Fig. 4.18

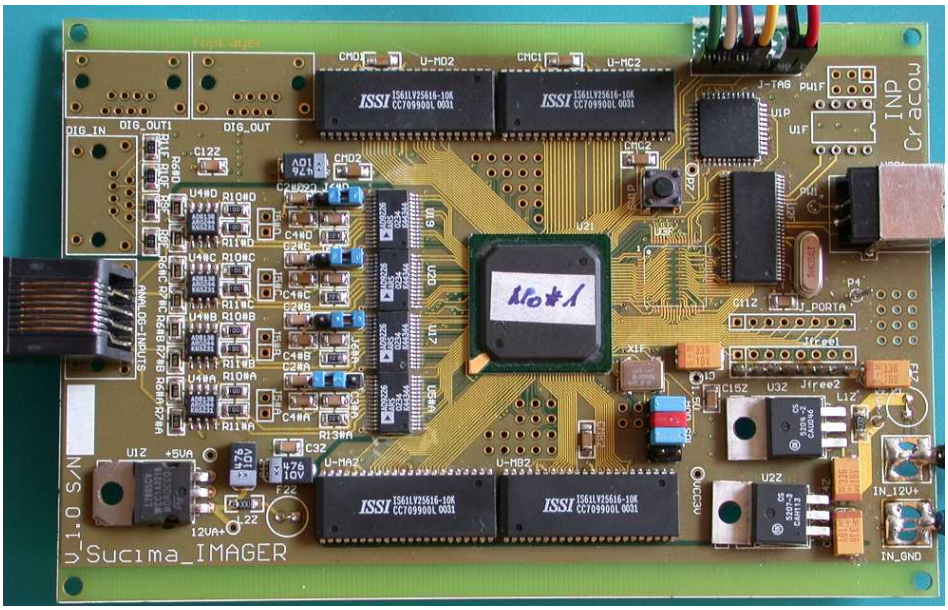

Figure 4.18: *The SUCIMA Imager card. This PCB houses an FPGA that reads analog data via 4 ADCs and generates the digital signals required by the sensor. Also located on the PCB is a USB interface chip, that handles the data transfer to and from the PC.*

In Fig. 4.19 a block diagram of the complete DAQ system is shown. One can see the sensor itself, the intermediate repeater card and the DAQ card. The main feature of the DAQ card is a Virtex II FPGA by Xilinx [Xil04]. This FPGA has 1 million system gates and runs at an internal clock rate of $420\,MHz$. Its IO pins are grouped in 8 so-called banks. Bank 0 and 1 handle the communication between the FPGA and the 4 ADCs. Bank 2, 3, 6 and 7 are used as interfaces to the 4 SRAM chips

which store the data for processing and transfer. Bank 4 and 5 are responsible for the communication with the FIFO and the IO chip.

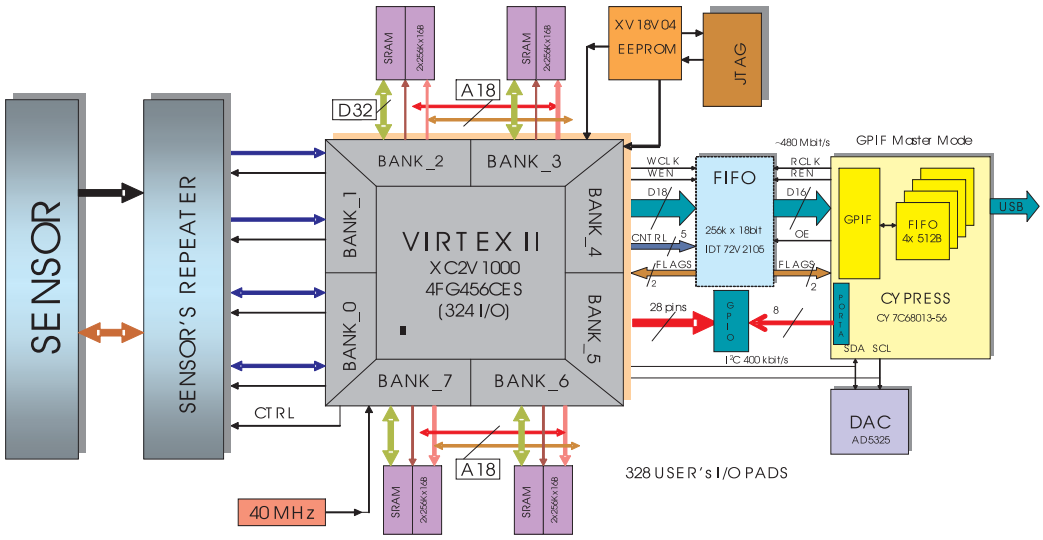

Figure 4.19: *A schematic overview of the SUCIMA DAQ system. On the left is the sensor. Next to the sensor is the so-called repeater. It is the second stage of amplification of the analogue signals. The VIRTEX FPGA is the central part of the SUCIMA USB interface card. The Cypress ASIC handles the data transfer between the FPGA and the PC.*

The 4 serial ADCs convert the analog data from the sensors with a maximum rate of $65\,MHz$ and a precision of $12\,bit$. For each of the 4 channels the data is stored in one Static RAM chip with a capacity of $256\,k\,32\,bit$ words.

The communication with the PC is done via a Cypress USB interface chip [Cyp02]. This chip uses the USB2.0 standard [Com00] to transfer up to $480\,Mbit/s$ in the synchronous mode. Even taking the overhead into account this still allows to transfer enormous amounts of data from the sensor to the computer.

The FPGA can be reprogrammed via a JTAG[19] interface. This allows to use a well adapted firmware for each detector type. This feature also allows to shorten the time needed during the development phase of the firmware code. The firmware is also stored in an EEPROM from which the FPGA automatically loads it at the time of power-up.

Two approaches were used for the firmware development. In one approach, the one used for qualifying the sensors, all data is streamed to the PC without any processing on the DAQ card. Especially during the radiation hardness measurements this was proven to be vital, as the reference voltages for the amplifiers need to be re-adjusted after every irradiation step and this is very difficult, if not even impossible, if one has only the already processed data.

The second approach is used somewhat for the MIMOSA-V and will be used to the full extent for the SLIM application. In this approach the data is pre-processed on the DAQ card. For the MIMOSA-V this is required, as the amount of raw data is too high to be handled by the PC in reasonable time. For the SLIM this is even more true, as here the quality of the beam has to be sampled with a frequency of $10\,kHz$, which is impossible, if the data processing should be done by a PC.

While for the MIMOSA-V the data processing in the DAQ card is limited to the calculation of the Correlated Double Sampling (CDS) frame, in the SLIM code the complete processing is done in the DAQ card, and only some parameters vital for the beam quality are transmitted to the PC.

A more detailed description of the DAQ system can be found in [Cze01].

[19] **JTAG**: **J**oint **T**est **A**ction **G**roup of the IEEE

4.3.2 Repeater

The repeater acts as a detector specific interface between the multi-purpose USB2.0 DAQ card and the hybrid, which carries the sensor itself. Fig. 4.20 shows the repeater for the CMOS sensors. It is mounted as a piggy back board onto the DAQ card.

The repeater has three main functionalities in the case of the CMOS sensors. It supplies the hybrid and the DAQ with power, generates the reference voltages for the amplifiers in the sensor itself and amplifies the analog signals coming from the hybrid.

The repeater is connected to 3 different voltages. From a $8.5V$ line all internal voltages are generated using standard LM317 regulators. This $8.5V$ line is also connected to the DAQ card, which has its own regulators. The other two voltages, $-1.5V$ and $-18V$, are directly connected to the cable to the hybrid. They are used to apply a bias on some of the structures on the SUCCESSOR-I sensor.

The reference voltages for the amplifiers inside the sensor can be set separately for each of the four output channels. This can be done by adjusting potentiometers in voltage dividers at the input of operation amplifiers. These then generate the reference voltage.

The connections to the DAQ card are established in two different ways. The power connections to and the digital control from the DAQ card are routed through standard pin connectors directly from PCB to PCB. The fast digital signals, clock and reset, to and the analog signals from the sensor are routed through very short twisted pair CAT5e cables using RJ45 connectors.

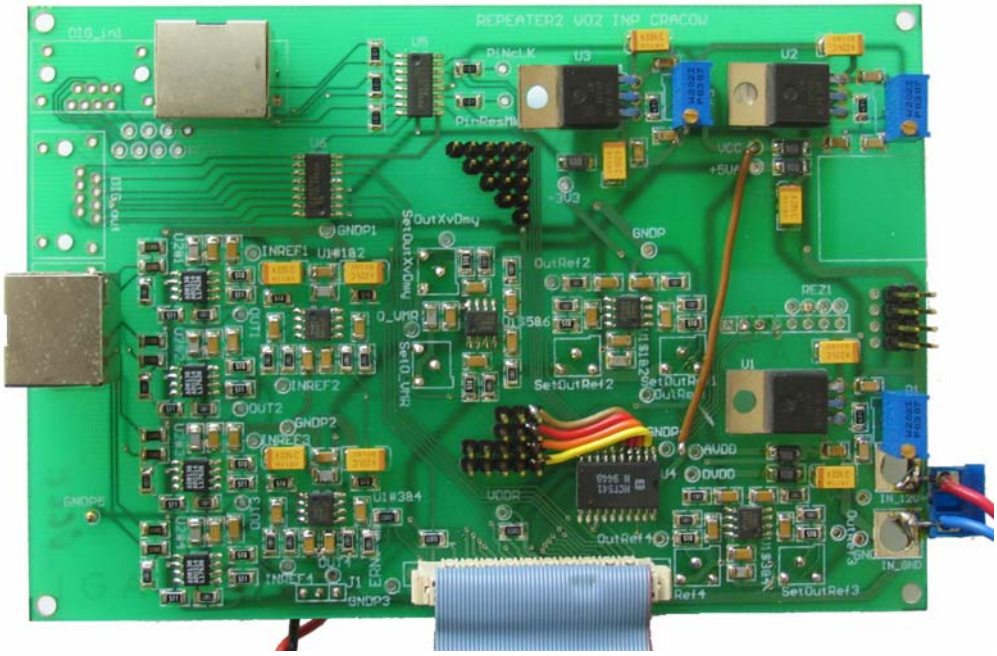

Figure 4.20: *The repeater for the SUCIMA Imager. One can see the two connectors for the fast analogue and the digital signals (top and left side), the connection to the hybrid (ribbon cable at the bottom) and the power input (on the right). The digital control signals and the power lines are routed through the interconnection pins. An additional connection allows to apply a negative bias to the oxide for some of the pixels.*

The hybrid of the detector is connected via a 50pin ribbon cable to the repeater. This cable carries all supply and reference voltages, as well as all digital and analog signals. To minimise the required space a high density connector is used.

4.3.3 Detector Hybrid

The hybrid acts as a mechanical support for the sensor itself. It is also the first external stage of the signal amplification. Besides this, it features a set of filters which smooth out any high frequency ripple on the supply voltages.

The amplifiers used, due to constraints on the available space, especially in the case of SLIM, are two-channel high bandwidth ones. With the gain set to one, they act as line drivers to ensure a good signal transmission to the repeater.

The filters on the power supply lines and the reference voltage lines use standard RC designs to suppress high frequency noise that could add to the intrinsic noise and is almost impossible to be removed by digital filters in the analysis.

There are two main designs for the SUCIMA hybrid. One is based on a standard PCB, see Fig. 4.21(a), while the other is made from ceramics, depicted in Fig. 4.21(b). The advantages of the PCB hybrids are easy to see. They are much easier to make than ceramic hybrids and thus are less expensive.

The ultra high vacuum in the beam pipe, in which the sensor is placed for the SLIM application, requires materials that are not outgassing, unlike the PCB material. One therfore has to use more sophisticated materials like ceramics. The issue of outgassing has also to be taken into account when choosing the components and the solder.

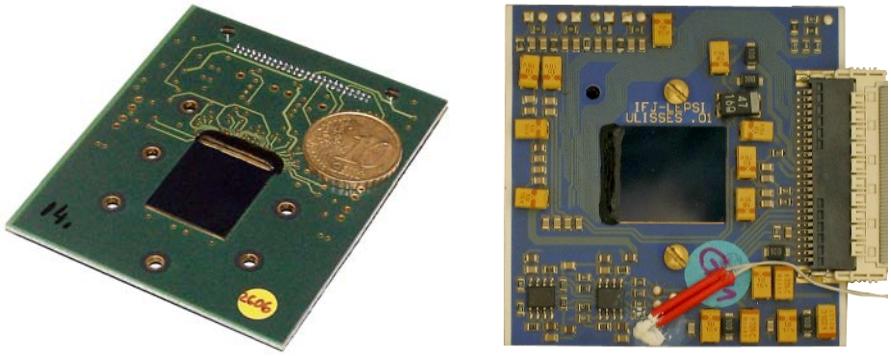

(a) standard hybrid (b) ceramics hybrid

Figure 4.21: *The two hybrids for the MIMOSA-V and the Successor-IV. The picture on the left shows the standard PCB hybrid. This hybrid is used for most of the applications. Only for the UHV applications, like the beam monitor for Tera, is it necessary to use a ceramics hybrid, shown on the right.*

4.4 LabView Software for USB-DAQ

Within the framework of this thesis a data acquisition and analysis software for LabView has been developed [Nat03][(20)]. The software was used during the development phase of the firmware of the USB-DAQ card for debugging purposes, but it is also used for the measurements on the radiation hardness of the SUCCESSOR-I chips.

In the following section the internal structure of the software will be introduced shortly. The algorithms used for the data analysis are described in the appendix D.

Fig. 4.22 shows a screenshot of the front panel of the software. The GUI is segmented into three parts. The top is used for the settings of the main processing features and the interaction with the software. In the middle is a status bar and on the bottom the parameters for the data analysis can be adjusted and the results viewed.

[(20)] Programmes written in LabView are called VI, which stands for Virtual Instrument.

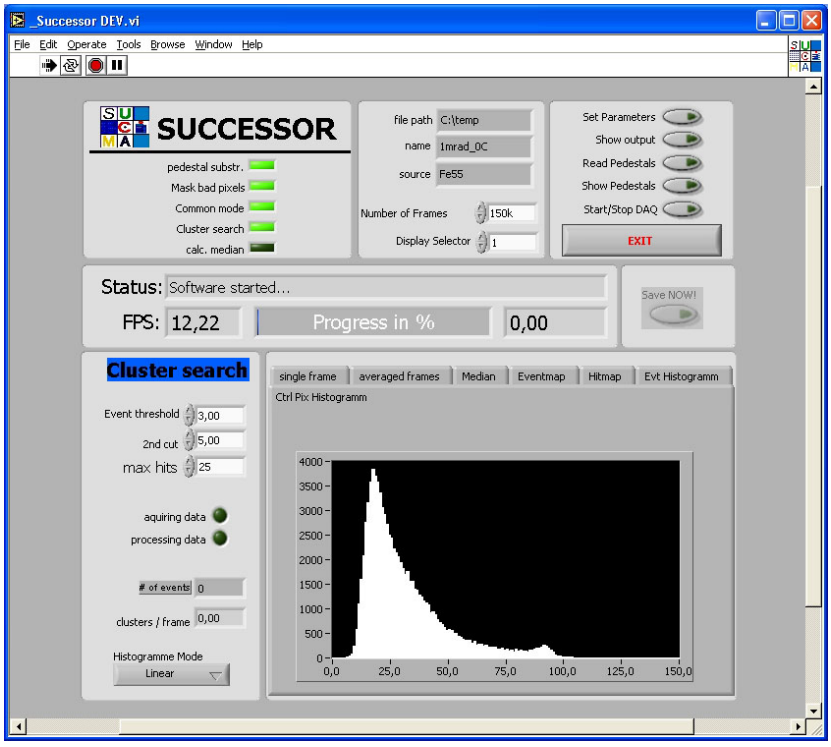

Figure 4.22: *The front panel of the SUCIMA DAQ software, written in LabView 6.1. The software allows to set all necessary parameters for the read out and the online data analysis and also displays the results of the data analysis. The diagram shows a typical histogram of a ^{55}Fe measurement with a SUCCESSOR-I sensor.*

4.4.1 Internal Structure

The internal structure of the DAQ software is shown in Fig. 4.23. The software is based on 7 modules. Five of these modules are run for every frame acquired while two of them are only run once, one at the start, one at the end.

After making the necessary settings in the corresponding window, one has to run first the “Read Pedestals” sub-programme before the main DAQ can be started. This sub-VI acquires a specified number of frames and then calculates the pedestals, the noise matrix and the bad pixel mask. These values are used as initial values during the processing of the data during the acquisition.

Once the main DAQ sequence is started, a frame will be read from the specified source, e.g. from the sensor or from a file. From this frame the pedestals will be subtracted. After this, the bad pixel mask is applied to the data. The next step in the processing is the suppression of the Common Mode noise. This is done on a per row basis, as the Common Mode spread across the sensor is too large to be fitted with a global value.

Following these steps is the cluster search, see section D for a detailed description of the used algorithms. The cluster search gives distributions of found seed pixels, clusters and their position back to the main programme. There the results are put into the histograms.

After the cluster search the found events are subtracted from the raw data and this information is used to calculate a new set of pedestals, noise matrix and bad pixel mask. With this updated set, drifts of the sensor, e.g. due to temperature changes, can be, at least partially, compensated.

When the set number of frames has been acquired and processed, the programme leaves the main loop and enters the “Save Data” module. In this module all relevant information on the run will be stored at the specified location in a set of files with a given name. Among the files, that can be selected for storage, are all histograms, the hit map, the integrated events, the integrated image and two information files. While one file is meant to be used by the software to read back the information

in case a re-processing is desired, the second file contains all information in a human-readable format.

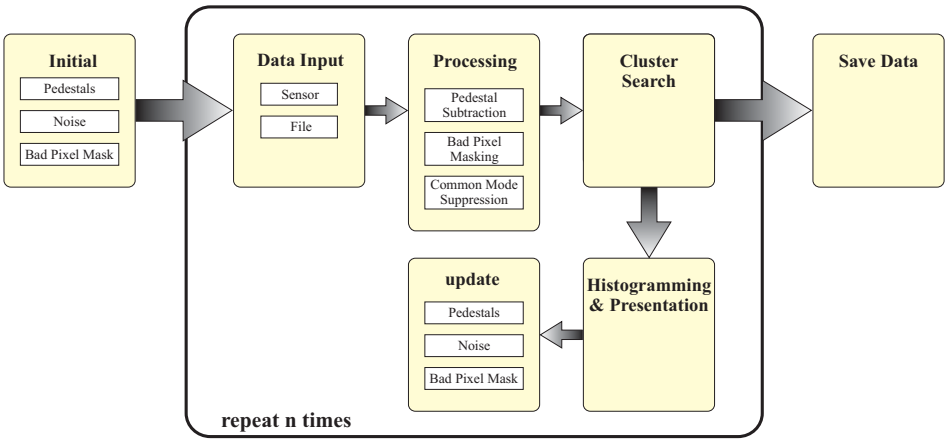

Figure 4.23: *This plot shows a schematic overview of the SUCIMA DAQ Software. The software is split into 7 different modules. While the "Initial" phase is only called once at the beginning and "Save Data" only once at the end, all other modules are used for each frame acquired.*

Some of the functionality of the software is sourced out into Dynamically Linked Libraries (DLL). For the USB2.0 interface this has to be done, as LabView is not able to acquire data directly from the USB driver of the kernel. The other two DLLs used, one reads the data in the so-called "Strasbourg-format", the other is used in the data processing, benefit from the increased performance, as the code is compiled and is not interpreted at runtime.

To make the handling of the programme easier it uses an .INI-file to "remember" the settings from the last time the software was run. In this file all settings are stored.

Chapter 5

Measurements with the SUCCESSOR-I CMOS pixel sensor

In order to select the pixel geometry suited best for the SUCIMA applications from the 8 different ones on the SUCCESSOR-I CMOS pixel sensor, detailed studies were performed on these sensors. In this chapter the setup and the measurements on the radiation tolerance, the main focus of this thesis, and their implications on the decision for the final production will be presented.

5.1 Setup & Software

To study the performance of the various pixel geometries of the SUCCESSOR-I, it was necessary to define a reproducible and reliable method for the sensor evaluation. After a short introduction into the irradiation setup at the IEKP and the measurement setup at LEPSI, the measurement procedure and the analysis methods will be presented.

5.1.1 X-Ray Irradiation Setup in Karlsruhe

The X-ray setup at the IEKP was first built to study the aging of MSGCs [Erb99]. For the irradiation of the CMOS sensors some major modifications were realised, as the requirements on the irradiation are quite different.

To achieve a smaller beam spot, an adjustable collimator was mounted in front of the X-ray tube. Also a computer controlled shutter was added to allow a more precise control of the irradiation time and thus the applied dose.

The beam profile and thus the dose applied to the sensor under study can be measured using so-called calibration diodes. These diodes were calibrated against a known X-ray system at CERN and PIN-diodes used at CERN for dosimetry. Also an integral measurement of the dose rate was performed using a certified dosimeter with an ionisation chamber as sensitive device.

The temperature inside the lead container can be monitored from the PC using a PT100 temperature sensor which is read out by a GPIB[(1)] controlled Keithley 196 DMM. The GPIB bus is also used to communicate with the motor controller of the XY-stage. This XY-stage is used for the alignment of the sensor for the irradiation, but also for scanning the beam spot using the calibration diode.

Later on the existing Cu-anode X-ray tube was replaced by a W-anode tube (FK60-04 fine focus) to eliminate the characteristic lines from the spectrum, which have a rather low energy, and to have the maximum output at a shorter wavelength. The last modification of the setup was the replacement of the HV generator with a newer model (GE Inspections Debyeflex 3003) which can be computer controlled. Both, the HV generator and the X-ray tube, are water-cooled. An overview of the system in its final configuration is shown in Fig. 5.1.

[(1)] **GPIB**: **G**eneral **P**urpose **I**nterface **B**us, IEEE 488

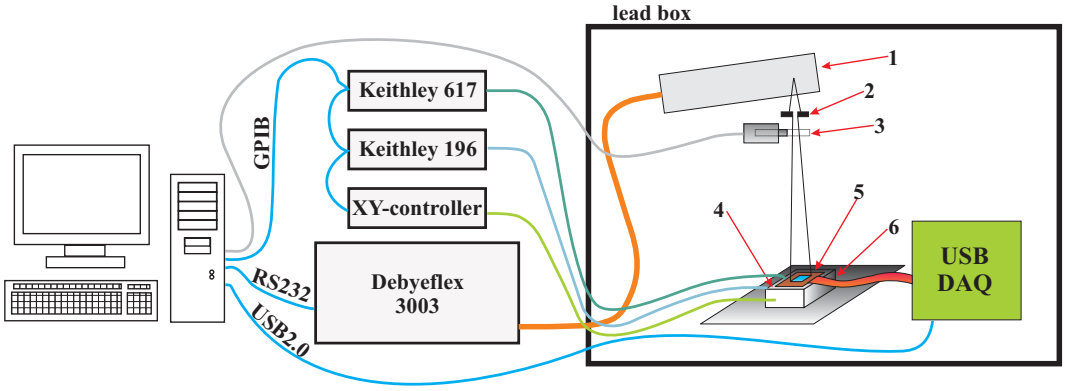

Figure 5.1: *The X-ray setup used for the irradiations of the CMOS sensors. The complete setup is controlled by a computer running LabView 6i. The parts inside the lead box are: (1) The X-ray tube, (2) an adjustable collimator, (3) shutter, (4) PT100 temperature sensor read out by the Keithley 196, (5) hybrid with sensor or calibration diode which is biased by the Keithley 617 & (6) XY-stage. The sensor is powered, clocked and read out during the irradiation via a USB DAQ board.*

Taking many dose maps of the beam profile, one example shown in Fig. 5.2, at various times before and after irradiations it was proven, that the X-ray system gives a very reproducible dose distribution and rate. Thus it was not necessary to re-evaluate the dose rate before each irradiation step.

The maximum dose rate the X-ray tube (W-anode) can deliver is $177.6\,krad/h$. As this would shorten the lifetime of the tube dramatically, it is operated at 83% of the maximum value during the irradiation process.

The diameter of the beam spot is sufficiently large ($\varnothing 16\,mm$), so that the SUCCESSOR-I sensor ($4.6 \times 3.6\,mm^2$) can be located in an area with a dose variation across the sensor of less than 5%.

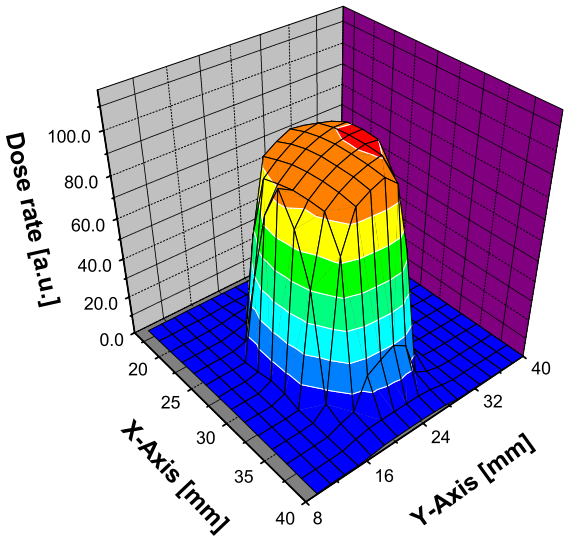

Figure 5.2: *The beam spot of the X-ray system at the height of the sensor using the circular lead collimator with the adjustable collimators fully opened.*

The adjustable collimators were also very important for the alignment of the sensor with the X-ray tube for the irradiations. They were used to create a very narrow beam spot on the sensor, see Fig. 5.4(b), which was then centered on the sensor by moving the sensor mounted on an XY-stage.

5.1.2 Measurement Setup at LEPSI

As the USB2.0 based read out system of the SUCIMA collaboration was not yet available during the time of the measurements, a VME based system located at the LEPSI in Strasbourg was used. This system, depicted in Fig. 5.3, consists of a PC which is connected to a VME crate housing a single-board computer and a so-called imager card. This imager card features two FPGAs that generate the necessary digital signals for the sensor and handle the communication with the VME backplane.

The read out is done by the single-board computer in the crate running realtime Linux. As it is disc-less, it has no possibility to store the data, which is streamed to the PC instead. The PC is also used to initialise the settings for the read out system. During the data acquisition the PC also shows

an online display of the raw data, allowing some quality control of the data. For a more detailed description of the setup refer to [Dev03].

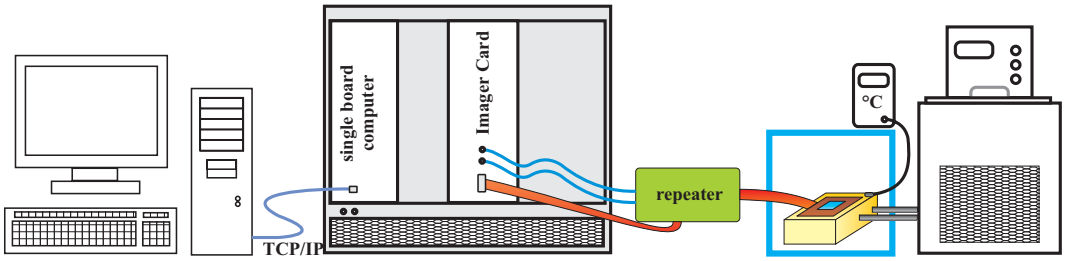

Figure 5.3: *The setup at the LEPSI, as it was used for the measurements on the CMOS sensors. Sensor is located in a temperature controlled box and connected to a repeater board. Through this board it is supplied with power and all digital signals. Also the analogue signals coming from the sensors pass through the repeater and are amplified there. The VME crate, housing the so-called imager card, is controlled by a single-board computer. The data is streamed to a Linux PC, which is also used to set the parameters for the DAQ.*

5.1.3 Measurement & Irradiation Procedure

To ensure the reproducibility of the acquired data procedures for the measurement and the irradiation were defined and applied to all measured sensors. Also the most important parameters set for the measurements were recorded. The procedures are described in the following:

- **Measurements:** There are two different types of measurements: the leakage current measurement and the recording of ^{55}Fe -spectra. Both sets of measurements are done for each of the pixel matrices.

  – Leakage Current: As the leakage currents are very small for some pixel geometries, especially before the irradiation, more frames than in the standard mode are read out between resets to achieve a longer integration time and thus higher integrated values. These values are then divided by the number of frames read to re-normalise them.

  When measuring highly irradiated devices, it was noticed, that the method mentioned above ran into saturation and was not applicable any more. Additionally, the gain of the repeater was enhanced by a factor three in comparison to measurements with other prototype chips.

  To calculate the leakage current, 10000 frames are acquired without a source above the sensor. From these frames the pedestals are calculated. The distribution of the pedestals of the sensor is fit with a Gaussian distribution.

  This method is precise enough at low doses and is still usable at high doses. The results for low doses are in very good agreement with those taken with the first method.

  The leakage current measurements are done at the temperatures $-15\,℃$, $0\,℃$, $10\,℃$ and $20\,℃$.

  – ^{55}Fe Spectra: Two things can be learned from the ^{55}Fe spectra. The first is the position of the peak generated by the $5.89\,keV$ gammas converted in the small depletion layer directly beneath the collection diode, see Fig. 3.9. As mentioned above, from the position of the peak the device can be calibrated.

  The second important characteristic is the charge collection efficiency (CCE). By comparing the spectra of the seed pixels and the clusters one can learn, wether the CCE has changed due to the irradiation of the device.

The standard amount of statistics acquired for a ^{55}Fe spectrum is $150k$ frames per run, operating the device at $2.5MHz$. As the SUCCESSOR-I chip has too high a leakage current after irradiation to doses of more than $1Mrad$ for this read out frequency, later measurements were done at $10MHz$. To get compatible statistics the number of frames per run was increased to $600k$.

^{55}Fe spectra were acquired at each dose step for all sectors at $-15\,°C$ and at $20\,°C$.

- **Irradiation:** For the irradiations the hybrid with the sensor is mounted onto an aluminum carrier, as shown in Fig. 5.4(a). The digital part of the sensor is protected by a $7mm$ copper plate which has a $4mm$ high free area in the middle for moving it over the bonds without touching them. The carrier is then in turn mounted onto the fixation inside the lead box of the X-ray system.

  To achieve a homogeneous irradiation of the sensor it has to be centered in the beam of the X-ray tube. This is done by creating a very narrow beam using the adjustable collimators in front of the tube and moving the sensor with the XY-stage so that the beam is centered on the sensor, see Fig. 5.4(b). After the alignment the collimators are opened fully to minimise edge effects.

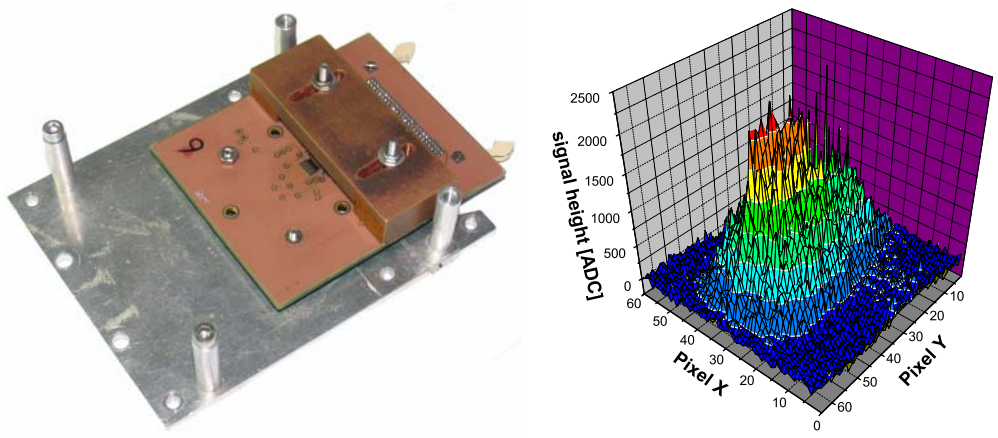

(a) Mounting (b) Alignment

Figure 5.4: *(a) A picture of a SUCCESSOR-I hybrid mounted on its aluminum carrier with the copper protection of the digital part in place. (b) The beam spot during the alignment of the chip for the irradiation. The beam is extremely collimated and then the sensor is moved to the centre of the spot. The data was taken with the central 4 pixel matrices of a SUCCESSOR-I chip.*

For the irradiations of the sensors a rather high dose rate was chosen, to keep the time required for one dose step within a sensible range. The output of the X-ray tube was set to $25mA$ at $60kV$, which corresponds to about $148krad/h$. This is $\sim 83\%$ of the maximum output, which is still considered safe for long term operation of the system.

In order to achieve an irradiation environment as close as possible to a real application, the sensor is powered and read out during the whole time of the irradiation. This is especially important as the migration of the charge carriers generated in the oxide and the interfaces depends on the applied voltage.

Using two $9V$ batteries the field plates on some of the structures of the SUCCESSOR-I chip can be supplied with the correct negative bias voltages, $-18V$ for the thick oxide and $-1.5V$ for the thin. This should lead to a removal of the positive charges trapped in the oxide after the irradiation.

Each chip is fully qualified at each dose step. Thus it is measured at $0\,krad$ and then again after each irradiation. Some chips were measured twice at a dose step to investigate possible annealing effects, see section 5.2.1 on the non-radiation hard digital part.

5.2 Radiation Tolerance Studies - Side Remarks

In this section the two most important side effects, which were observed during the irradiations of SUCCESSOR-I chips will be discussed briefly. These effects are the non-radiation hardness of the digital part of the sensor and the inhomogeneous pedestals after irradiation of the device. The measurement results will be presented in detail together with a summary in the next section.

5.2.1 Non-Radiation Hard Digital Part

In the first irradiation series the SUCCESSOR-I chips were completely exposed to the X-rays, as previous irradiations of other prototype chips were done the same way. But at $1\,Mrad$ the chip was not operational any more directly after the irradiation, even at $-15\,℃$. The chip was fully functional again after 3 weeks annealing at room temperature.

Investigations soon allowed to trace back the problems to the digital part of the sensor, which is not radiation hard. One of the major hints to this source of the problems was the dramatically increased current consumed by the digital part. This was most probably caused by the oxide charge-up during the irradiation. This effect can lead to shifted threshold voltages and parasitic charge transfer paths, rendering the device non-operational.

During all further irradiations the digital part of the SUCCESSOR-I chip was protected by a $3\,mm$ copper plate. Fig. 5.5 shows the currents of the analog and the digital part of the sensor for sensors irradiated with and without shielding.

All sensors irradiated with shielded digital part were working without any problems even after doses of $3.5\,Mrad$ and according to the results below will also work even after higher doses.

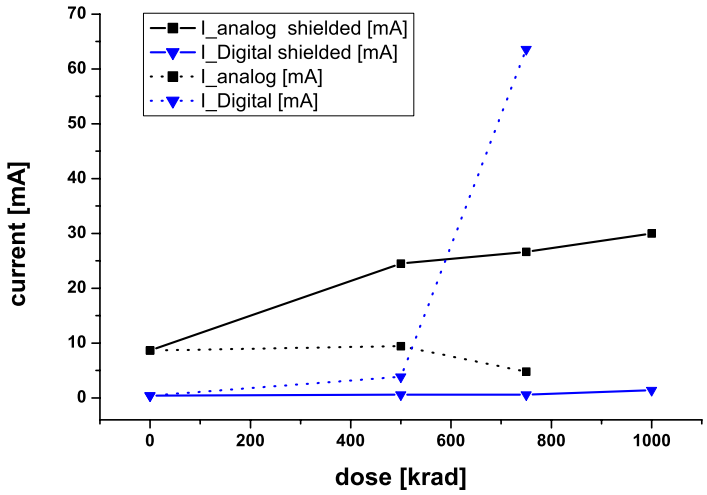

Figure 5.5: *Current consumption of the SUCCESSOR-I of both, analog and digital part, as function of the irradiation dose. The plot shows the drastic effect of the shielding of the non-radiation hard digital part.*

5.2.2 Inhomogeneous Pedestals

One of the problems of the measurements on the SUCCESSOR-I chip were the inhomogeneous pedestals. There are two effects contributing to this. One is the difference of the pixel geometries

that leads to differences in gain and leakage current. The other is the issue of the analog output driver at the end of each of the four read out sections.

These output drivers generate a certain amount of heat, which is related to the current flowing through them. Thus as the chips are irradiated to higher doses the effect gets stronger due to the higher leakage currents and becomes a limiting factor when doing measurements at room temperature and with low read out frequencies.

A second problem of this effect is the self-heating. The output buffers are heating the pixels closest to them. These in turn have a higher leakage current due to the increased temperature which then causes the buffers to produce even more heat.

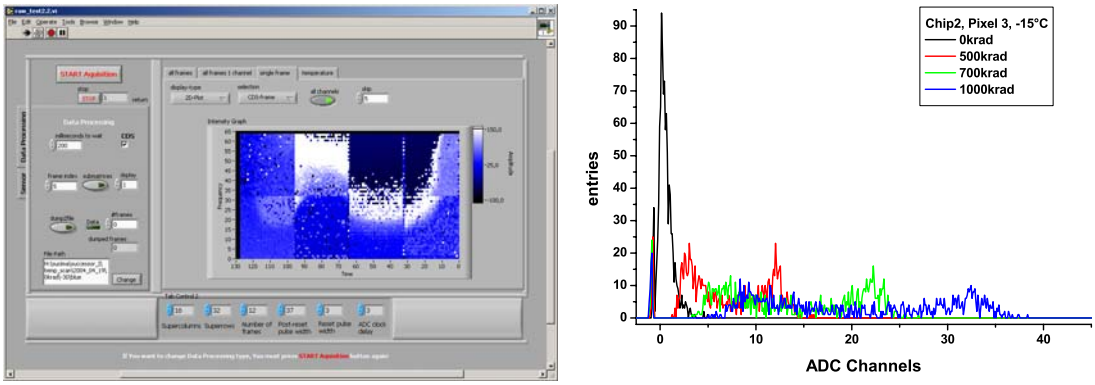

(a) Screenshot (b) Pedestal Spread

Figure 5.6: *The inhomogeneous pedestals of a SUCCESSOR-I chip. (a) shows a screenshot of the read out software with all eight sectors directly after irradiating the sensor to* $3.5\,Mrad$*. The sensor was operated at room temperature. (b) shows the spread of the pedestals of a SUCCESSOR-I chip shown for the example of pixel 3 for four different doses.*

The screenshot shown in Fig. 5.6(a) was taken directly after the irradiation of a SUCCESSOR-I to $3.5\,Mrad$. One can clearly see the very prominent effect of the inhomogeneous pedestals. This picture leads to the assumption, that buffer 2, second from the right, produces the most heat. The pixel sub-matrix affected the most by this effect is number 3. The pedestals of the aforementioned sub-matrix are shown for different doses in Fig. 5.6(b). One can easily see, that the distribution becomes much wider for higher doses. While the pedestals range from -1 to 5 for $0\,krad$, they reach values from -1 to 38 for $1000\,krad$.

To verify the hypothesis of the buffer driven heating, a picture of a sensor irradiated to $500\,krad$ was taken with a FLIR[(2)] camera. This picture is shown in Fig. 5.7. Unfortunately, the effect of the heating was dominated by the differences in the reflectivity of the surfaces. Thus it was not possible to check the validity of this hypothesis.

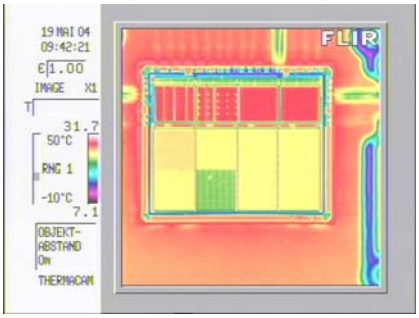

Figure 5.7: *A picture of a SUCCESSOR-I chip taken with an infra-red camera. The effect of the heating of the output buffers is not visible, as it is dominated by the differences in the reflectivity of the surface.*

[(2)]**FLIR**: **F**orward **L**ooking **I**nfraRed

5.3 Radiation Tolerance Studies - Results

In this section measurement results obtained with SUCCESSOR-I chips at different dose steps will be presented for pixels 3 and 4. The plots for all other pixels can be found in appendix E. A detailed description of each of the eight pixels can be found in section 4.2.2 on page 120. At the end of this section a summary of the measurements will be given.

All measurements presented below were done using the X-ray system described in section 5.1.1 and according to the procedure defined in section 5.1.3. The characterisations of the SUCCESSOR-I chips were done using the reference measurement system in Strasbourg, which is described in section 5.1.2.

The measurement data was analysed using the algorithms, which are summarised below and described in detail in appendix D.2. After acquiring the raw data of two consecutive frames from the sensor so-called correlated double sampling (CDS) is performed: the content of frame #1 is subtracted from frame #2. From this CDS-frame the pedestals, calculated beforehand, are subtracted. To this data set a common mode correction is applied. This step suppresses noise in the data set that is common to a complete row of pixels. The next process is the iterative search for hit clusters in the data, till no more hits are found passing the two cut levels. The cuts are set on the signal to noise ratio (SNR) of the seed pixel of the cluster and the SNR of the complete cluster.

The error in the irradiation dose applied to the sensor was estimated to be $\sim 10\,\%$. This rather high value is caused by the 5% variance of the beam intensity across the die and the uncertainty in the dose rate itself. These uncertainties originate from the different thicknesses of the sensitive volume of the devices used to measure the dose rate (PIN diode: few μm, CMS diode: $\sim 300\,\mu m$) and the thickness of the affected volume of the SUCCESSOR-I ($\sim 15\,\mu m$).

The error of the temperature measurement during the leakage current studies and the statistical error of the measurements themselves are much smaller than 5% for most of the measured values and thus are not included in the presented plots, as the error bars would be hidden by the markers for the measurement points anyway. The algorithms used to calculate the histograms, the leakage current and the errors are presented in appendix D.

As the main purpose of the radiation hardness studies presented here was to find the most robust pixel, still giving a "nice" signal, for the submission of the final device of SUCIMA, only four pixels were investigated at doses beyond $1\,Mrad$, as the others were already considered not to be worthwhile further effort. For the favoured pixels (2, 3, 4 and 5) also the measurements for $2\,Mrad$ will be presented. The measurements were done with different chips #2, #3 and #7. While chip #3 was not irradiated and was used as a reference device, chip #2 was irradiated to $500\,krad$, $750\,krad$ and $1000\,krad$. The dose steps for chip #7 were $1000\,krad$ and $2000\,krad$.

On the following pages only the ^{55}Fe spectra acquired at $-15\,°C$ will be presented, as the ones taken at $20\,°C$ are dominated by effects of the increased noise (due to the much higher leakage currents), and thus do not allow a good judgement on the performance of the pixel with respect to charge collection efficiency. As the leakage current increased strongly with the dose, the read out frequency was changed from $2.5\,MHz$ to $10\,MHz$ for doses above $1\,Mrad$ to reduce the integration time by a factor four, and thus the leakage current, to prevent a saturation of the amplifiers in the read out chain.

On the following pages only the result plots for pixels 3 and 4 will be shown, as pixel 3 is the pixel closest to the "standard" MAPS design and pixel 4, is the one chosen for the design of the final device of SUCIMA. The plots of pixels 0, 1, 2, 5, 6 and 7 can be found in appendix E.

- Seed Pixel Spectrum:
  The seed pixel spectrum is a histogram of the values of the pixel with the highest signal to noise ratio of a cluster, that passes both cuts. This histogram gives a good impression of the intrinsic gain of the pixel, which is represented by the position of the small peak. This value is needed for the conversion of the leakage current data from ADC channels to fA.

- Cluster Spectrum:
  In the cluster spectrum the sum of the nine pixels with the highest signal to noise ratio in the cluster is histogrammed. From the cluster spectra one can learn about the charge sharing between the pixels. Only the plots for a cluster size of nine pixels are shown. For this cluster size $\sim 95\,\%$ of the deposited charge is collected. Due to the used algorithm, larger cluster (> 15) sizes are affected by the noise of the matrix, which will lead to a decreased value of the sum.

- Noise Spectrum:
  The development of the noise spectrum as a function of the irradiation dose gives a good indication on the usefulness of a pixel for dosimetry applications, where a high signal to noise ratio is required to reach the necessary precision.

- Leakage Current:
  The leakage current of a pixel is also an important factor, as it imposes limits for the maximum integration time and temperature at which the device should be operated. Outside these limits the leakage current will drain the collecting diode and limit the dynamic range of the detector and it can saturate the output amplifiers.

5.3.1 SUCCESSOR-I – Pixel 3

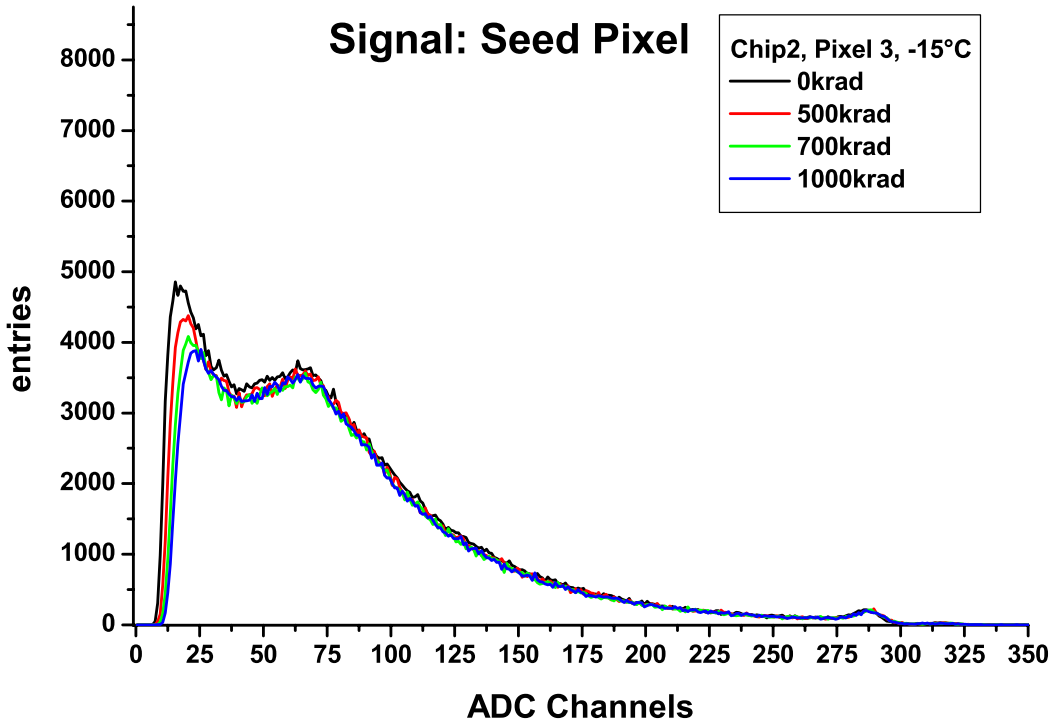

Figure 5.8: *This histogram shows the seed pixel spectrum of Pixel 3 for various doses. The measurements were done at* $-15\,℃$ *with a read out frequency of* $2.5\,MHz$.

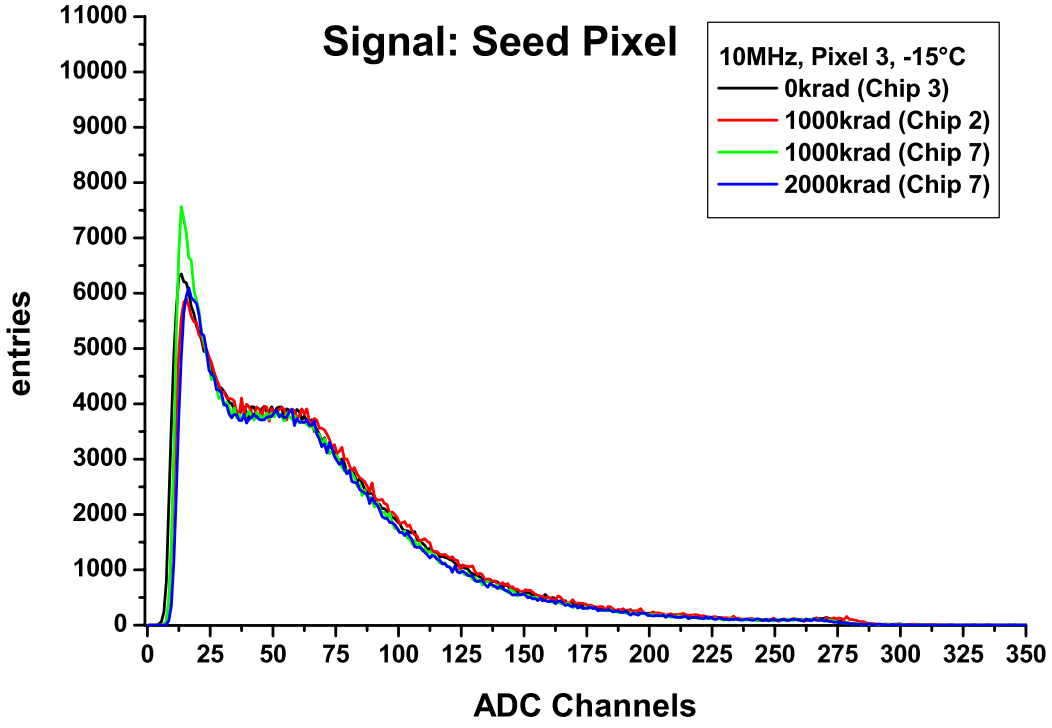

Figure 5.9: *This histogram shows the seed pixel spectrum of Pixel 3 for various doses. The measurements were done at* $-15\,℃$ *with a read out frequency of* $10\,MHz$.

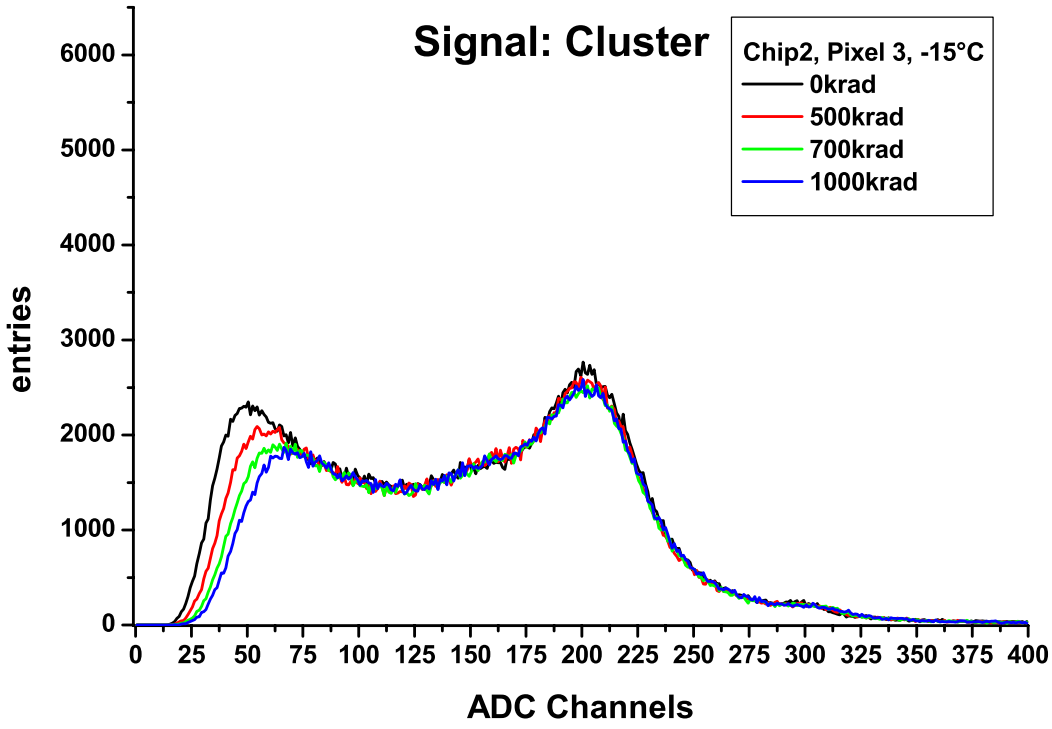

Figure 5.10: *This histogram shows the* 3×3 *cluster spectrum of Pixel 3 for various doses. The measurements were done at* $-15\,℃$ *with a read out frequency of* $2.5\,MHz$.

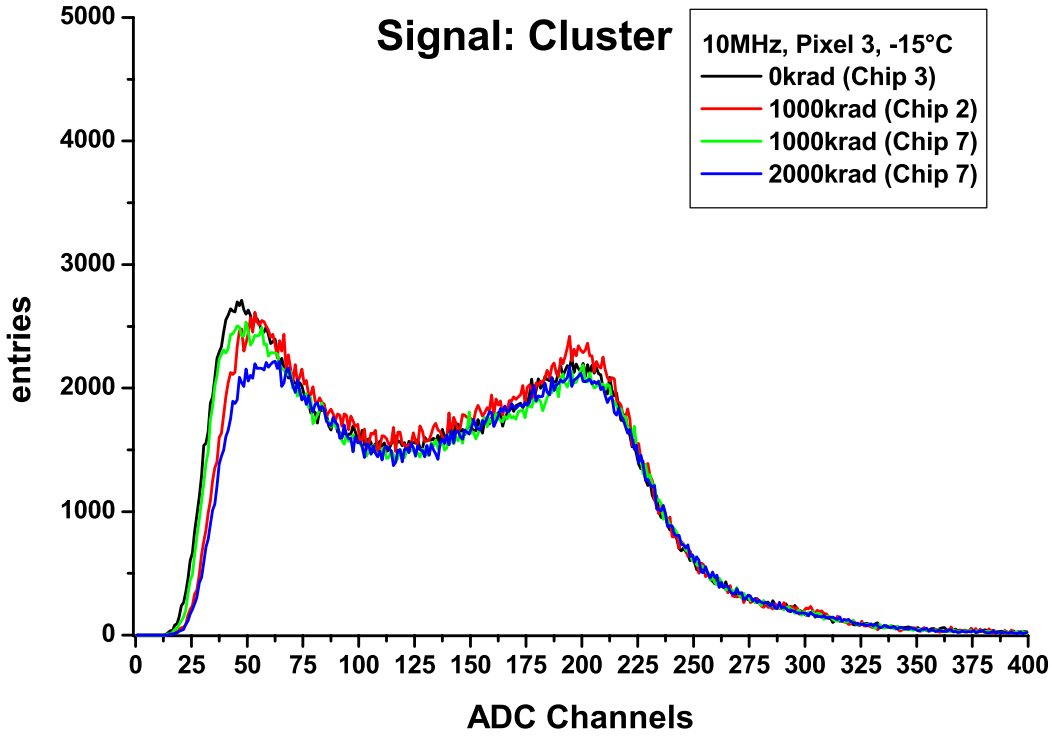

Figure 5.11: *This histogram shows the* 3×3 *cluster spectrum of Pixel 3 for various doses. The measurements were done at* $-15\,℃$ *with a read out frequency of* $10\,MHz$.

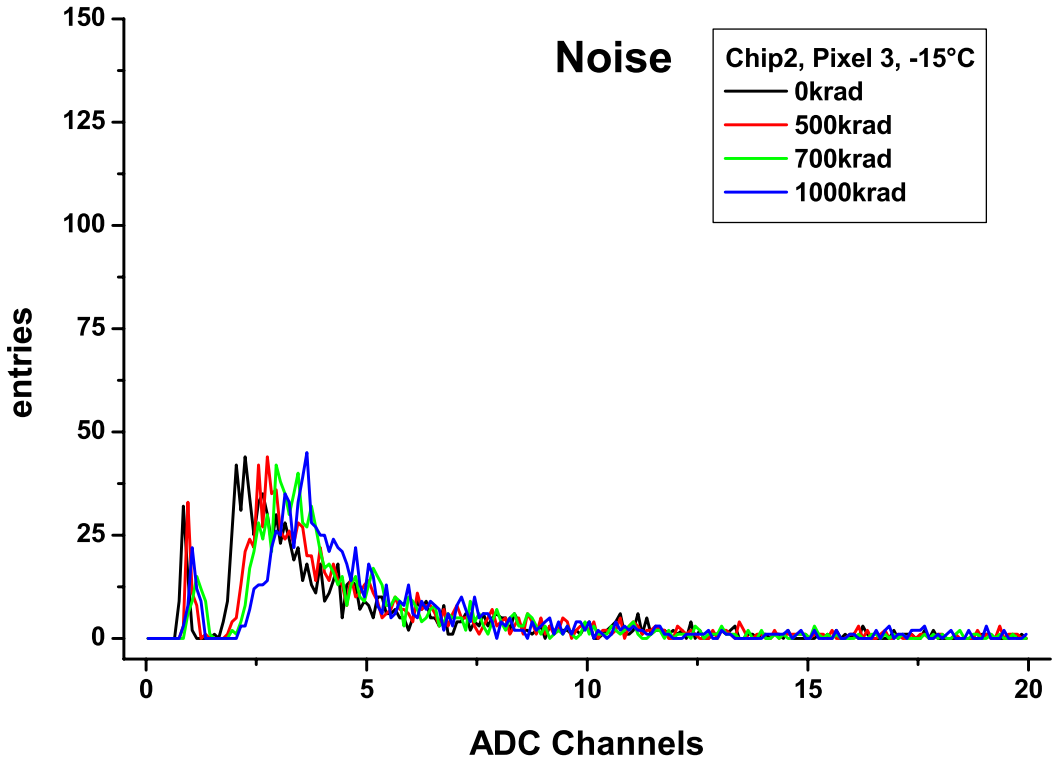

Figure 5.12: *This histogram shows the noise spectrum of Pixel 3 for various doses. The measurements were done at* $-15\,℃$ *with a read out frequency of* $2.5\,MHz$.

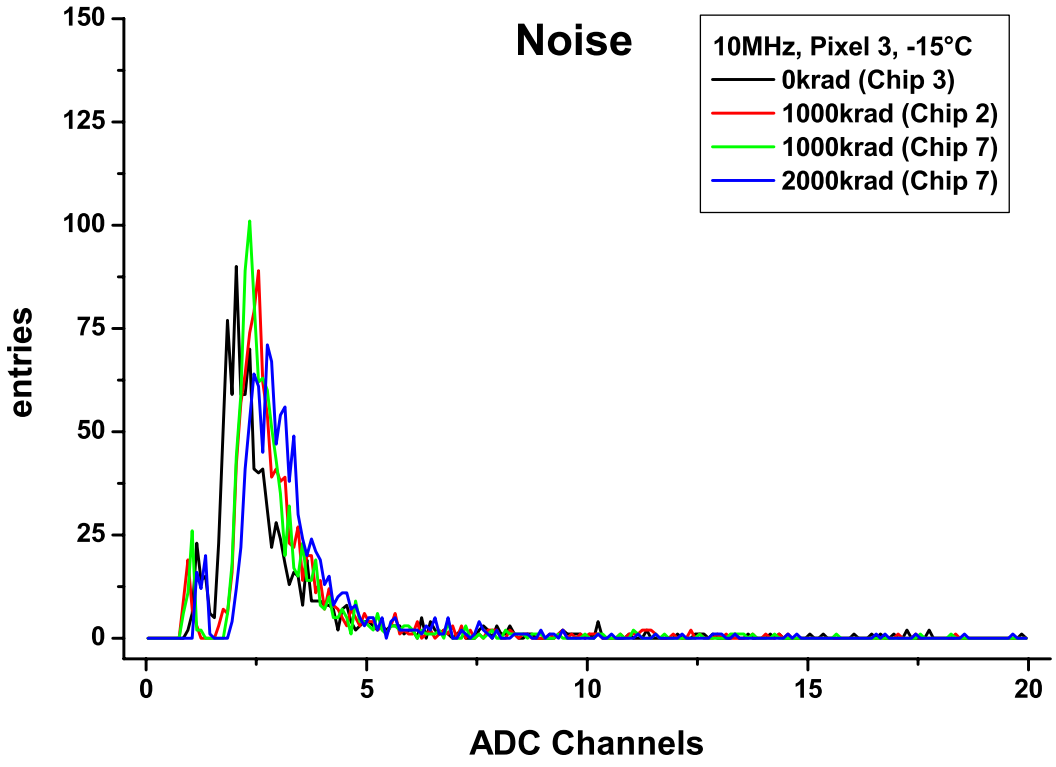

Figure 5.13: *This histogram shows the noise spectrum of Pixel 3 for various doses. The measurements were done at* $-15\,℃$ *with a read out frequency of* $10\,MHz$.

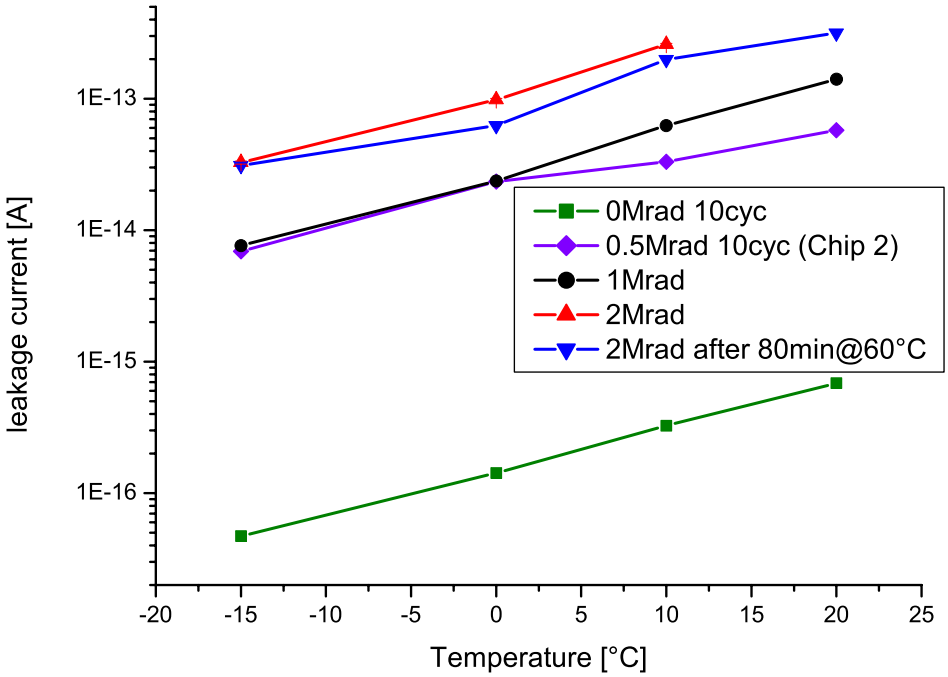

Figure 5.14: *This plot shows the leakage current of Pixel 3 for various doses as a function of the temperature.*

5.3.2 SUCCESSOR-I – Pixel 4

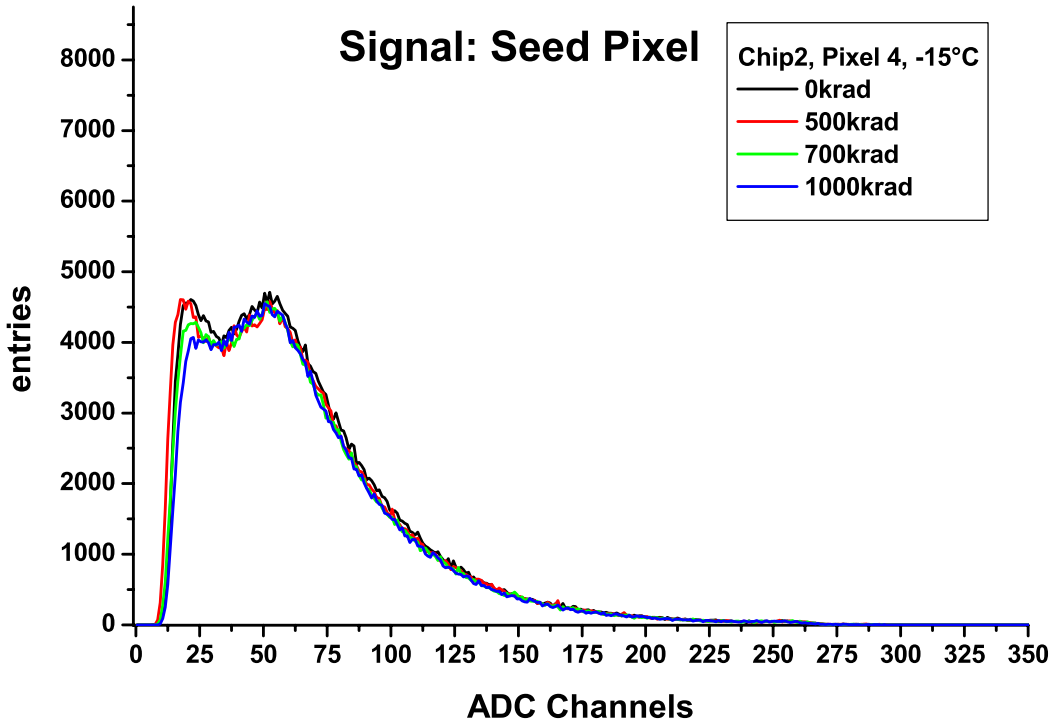

Figure 5.15: *This histogram shows the seed pixel spectrum of Pixel 4 for various doses. The measurements were done at* $-15\,℃$ *with a read out frequency of* $2.5\,MHz$.

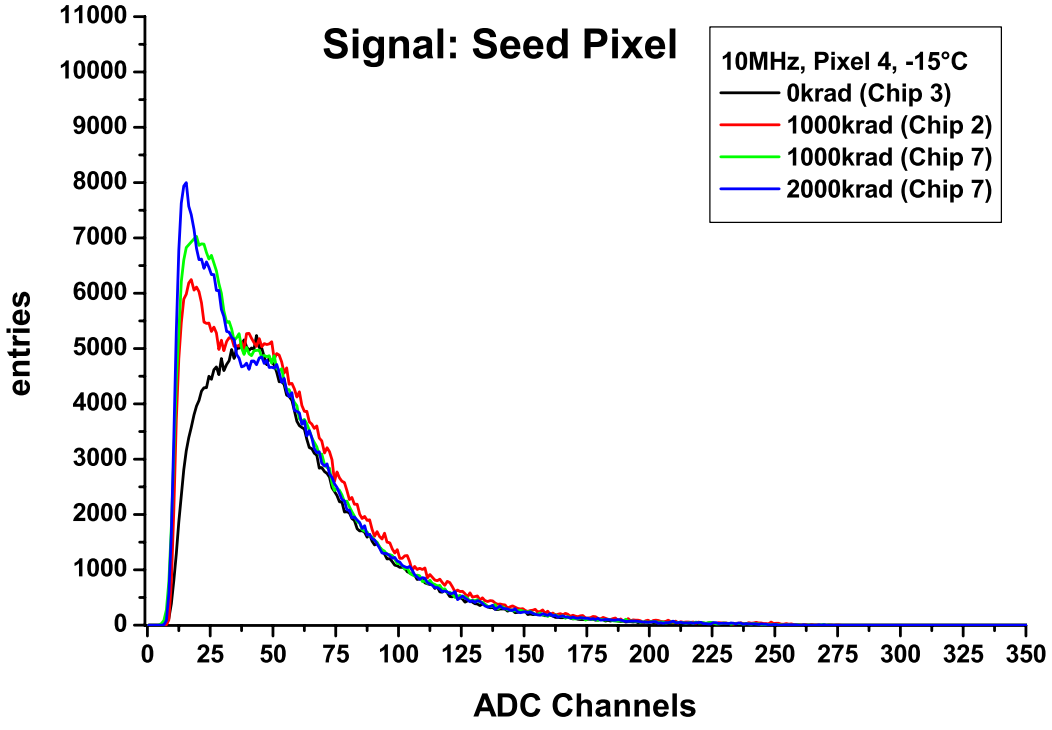

Figure 5.16: *This histogram shows the seed pixel spectrum of Pixel 4 for various doses. The measurements were done at* $-15\,℃$ *with a read out frequency of* $10\,MHz$.

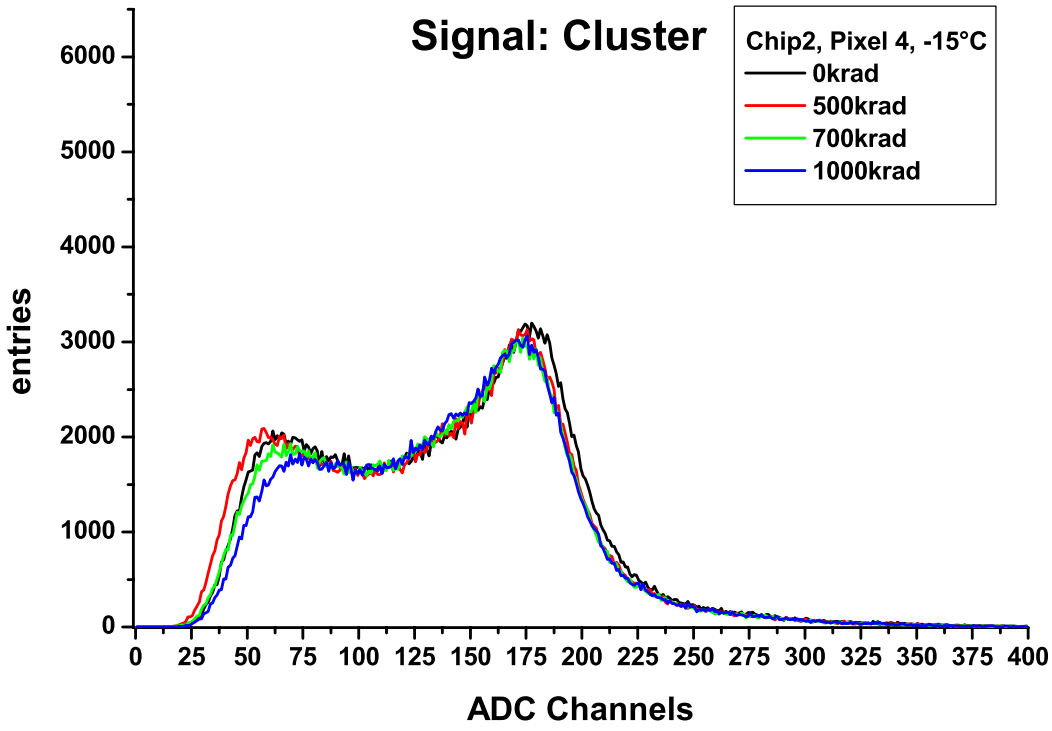

Figure 5.17: *This histogram shows the* 3×3 *cluster spectrum of Pixel 4 for various doses. The measurements were done at* $-15\,℃$ *with a read out frequency of* $2.5\,MHz$.

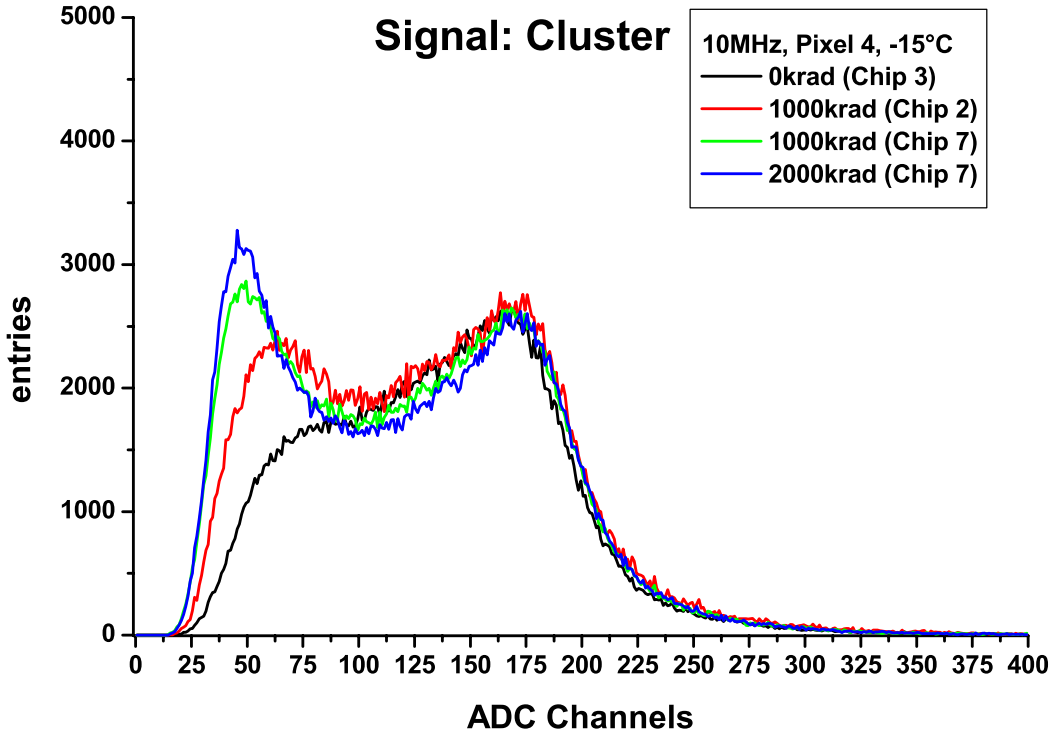

Figure 5.18: *This histogram shows the* 3×3 *cluster spectrum of Pixel 4 for various doses. The measurements were done at* $-15\,℃$ *with a read out frequency of* $10\,MHz$.

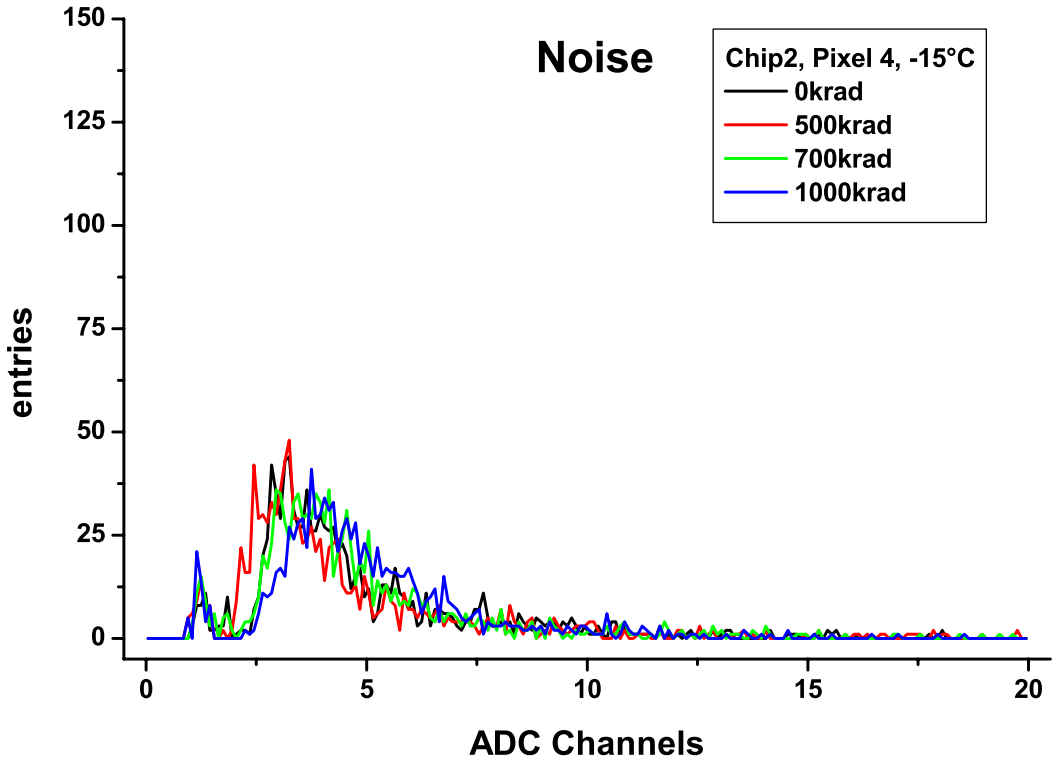

Figure 5.19: *This histogram shows the noise spectrum of Pixel 4 for various doses. The measurements were done at* $-15\,℃$ *with a read out frequency of* $2.5\,MHz$.

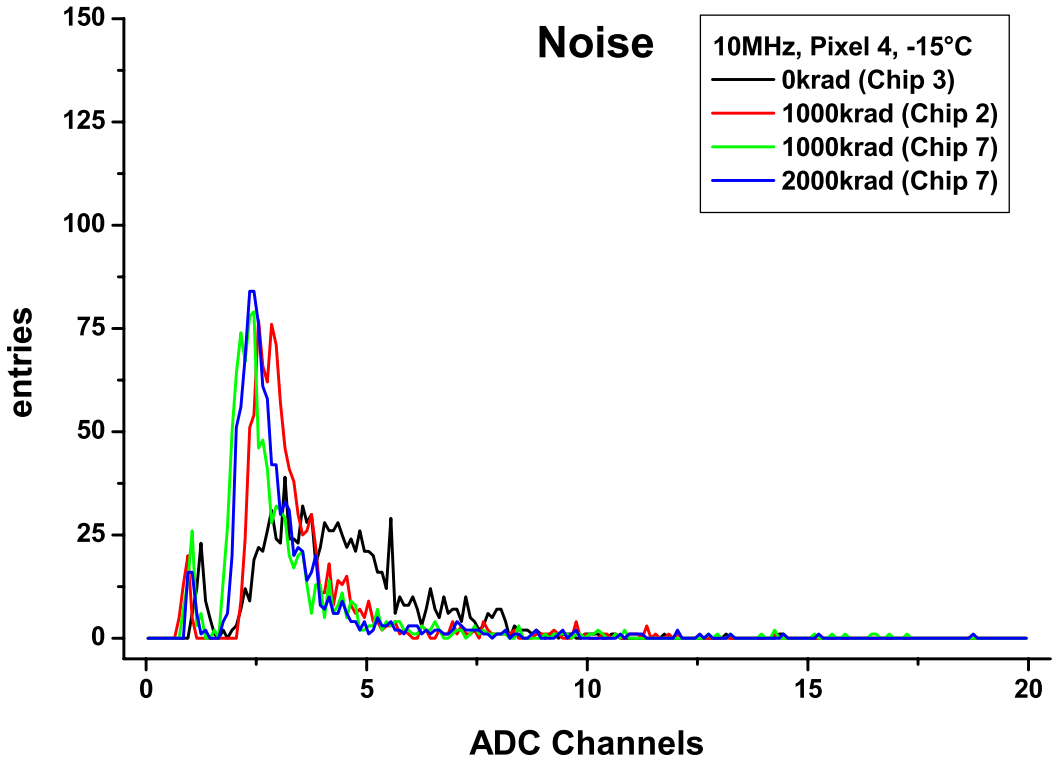

Figure 5.20: *This histogram shows the noise spectrum of Pixel 4 for various doses. The measurements were done at* $-15\,℃$ *with a read out frequency of* $10\,MHz$.

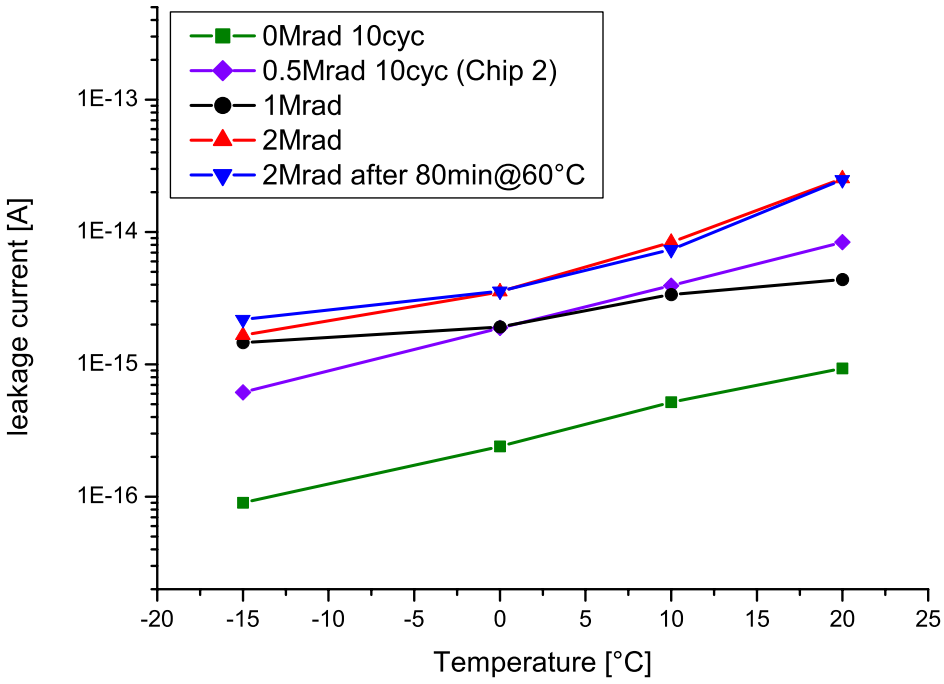

Figure 5.21: *This plot shows the leakage current of Pixel 4 for various doses as a function of the temperature.*

5.3.3 Summary

In this summary, a short comparison of the cluster and noise spectra for the four favoured pixels will be followed by a review of the results from the leakage current measurements. At the end of this section the most important criteria will be summarised in two tables. As a conclusion the choice of the pixel used in the next generation of CMOS detectors will be motivated, based on the measurements presented here.

In previous measurements on CMOS detectors, it was observed, that a substantial charge loss affected the performance of the device already at relatively low doses of $100\,krad$ [Dep02]. This effect is observable as a shift of the peak in the cluster spectrum towards lower values. The shift of the cluster peak is also observable for some of the pixels of SUCCESSOR-I at $T = -15\,℃$, but only for longer integration times and even then only to a non-significant extent ($< 2\,\%$). At higher temperatures ($T = 20\,℃$), the effect becomes more prominent, but is still much smaller than previously observed.

Another effect that was established in previous studies was the decreased gain of the amplification inside the detector [Dep02]. The effect reveals itself as a shift of the small ^{55}Fe peaks in the seed pixel spectrum towards lower values. Again, this effect was not observed with the SUCCESSOR-I detector. Even after $2\,Mrad$, the position of the small peak remains stable, within the precision of the measurement.

In the current understanding, this stability of the intrinsic gain has to be accredited to the newer CMOS processes which use a much thinner gate oxide and thus are less receptive to damage effects in the oxide, as mentioned in section 3.4.2. This also contributes to the stability of the charge collection process. An additional beneficial effect for the charge collection is the swapping of the source and the drain of the reset transistor, which removes a possible parasitic charge transfer path, see section 3.4.2.

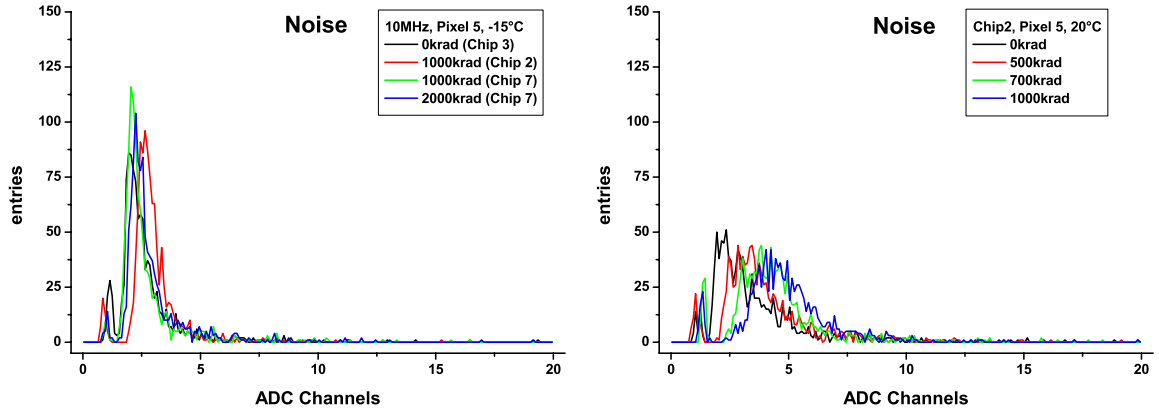

(a) $-15\,℃$, $10\,MHz$ (b) $20\,℃$, $2.5\,MHz$

Figure 5.22: *The noise spectra of pixel 5. (a) shows the noise distribution of this pixel for* $T = -15\,℃$ *and a read out frequency of* $10\,MHz$*. In (b) the noise distribution is depicted for* $T = 20\,℃$ *and* $2.5\,MHz$*. While the noise is not affected by the irradiation in plot (a), it is clearly increasing with the dose in plot (b), which is mostly caused by the increased leakage current.*

At $T = -15\,℃$ the noise of the detector, also a very crucial parameter for the evaluation, is also almost not affected by the irradiation of the detector, even up to $2\,Mrad$. This can be seen in the noise histograms of the individual pixels, one example is shown in Fig. 5.22(a) for pixel 5 ($10\,MHz$). At $T = 20\,℃$ the noise is 2 to 3 times higher and increases with the dose, which is mostly related to the increased leakage current, see Fig. 5.22(b) which shows the noise distribution of pixel 5 for a read out frequency of $2.5 MHz$ and doses up to $1\,Mrad$.

One of the most important parameters of a detector is the signal to noise ratio (SNR). In this thesis the SNR is defined as the position of the peak in the cluster spectrum divided by the most probable value of the corresponding noise distribution. In Fig. 5.23(a) the cluster spectra of the pixels 2, 3, 4 and

5 is shown for $T = -15\,℃$, a dose of $2\,Mrad$ and a read out frequency of $10\,MHz$. The corresponding noise distributions are shown in Fig. 5.23(b). One can easily see that the SNR is dominated by the intrinsic gain of the pixel (the position of the cluster peak) and not by the noise, which is comparable for all pixels. As the effect of the irradiation on the SNR is very small, only the values for $1\,Mrad$ and $2\,Mrad$ are given in Tab. 5.1 and Tab. 5.2, respectively. The increase in the SNR from $1\,Mrad$ to $2\,Mrad$ can be explained by the 4 times shorter integration time, which leads to a decreased noise, even though the dose is higher.

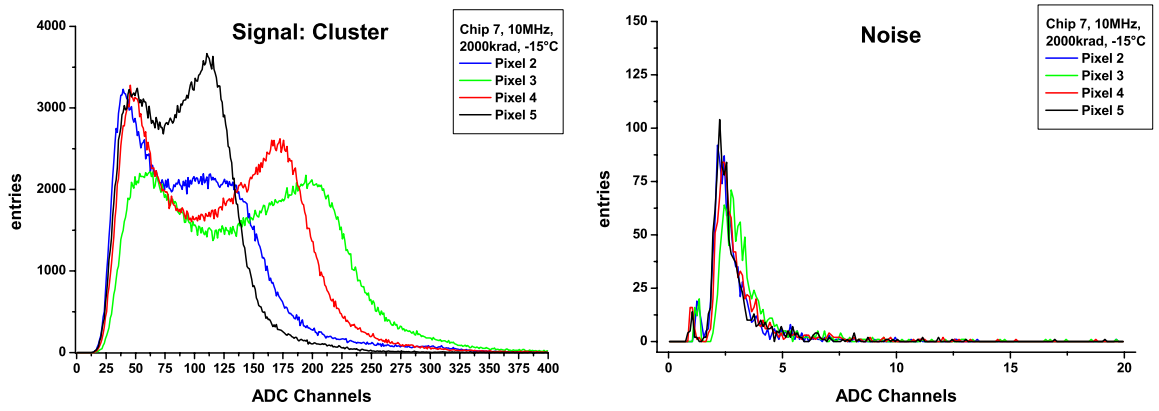

(a) Cluster Spectra

(b) Noise Spectra

Figure 5.23: *(a) shows the cluster spectra of pixels 2, 3, 4 & 5 acquired at T=−15℃. In (b) the corresponding noise histograms are depicted. These plots give a very good indication of the signal to noise ratio (SNR), defined as the position of the cluster peak divided by the most probable value of the noise. As one can easily see the SNR is dominated by the different gains due to the different capacitances of the pixel types.*

Fig. 5.24 shows the leakage current of the eight pixel types as a function of the dose for $T = -15\,℃$. As already mentioned in section 5.2.2, the inhomogeneous pedestals pose some problems for the leakage current measurements. Mostly the pixels 1, 3, 5 and 7 are affected by the heating of the output buffers. The worst effects can be observed for pixel 3, where parts of the matrix are in saturation even for low temperatures and short integration times. This effect dominates the increase of the leakage current of the matrix itself and somewhat limits the significance of the leakage current measurements as criterium for the choice of a pixel for the next generation of detectors. Still it can be said, that the leakage current increase for pixel 0, 2 and 4 is not a show stopper.

The measurement results for $750\,krad$ (pixel 1, 3, 5 and 7), which are significantly above the expected values, can be accredited again to the additional increase of the leakage current due to the buffers, as chip #2 was not annealed before the measurement unlike chip #7 at the higher doses. This annealing was done to remove excessive charges in the oxide and to thus minimise the effects from the heating digital part due to increased currents. The effect of the annealing was limited, as can be seen from the leakage current plots of the individual pixels on the pages before, where the results of the non-annealed and the annealed chip #7 are almost identical for a dose of $2\,Mrad$.

The most important parameters of the eight pixel types on SUCCESSOR-I are summarised in Tab. 5.1 and 5.2. In the first table the parameters are given for an irradiation dose of $1\,Mrad$ for all eight pixels, while in the second table they are given only for the four most favoured pixels at a dose of $2\,Mrad$.

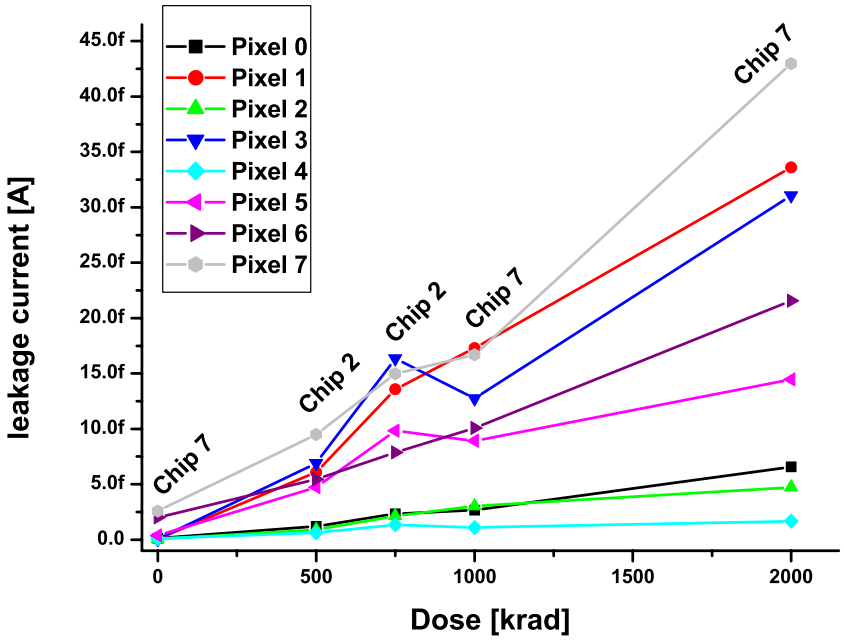

Figure 5.24: *The leakage current of all eight pixels of SUCCESSOR-I at T=−15℃ as a function of the dose. The values of the pixel 1, 3, 5, and 7 are strongly affected by the inhomogeneous pedestals, see section 5.2.2.*

	pixel 0	pixel 1	pixel 2	pixel 3	pixel 4	pixel 5	pixel 6	pixel 7
Charge Collection	n/c	n/c	n/c	n/c	n/c	n/c	n/c	n/c
Noise [ADC]	2.25	2.55	2.60	3.40	3.85	2.55	2.05	1.90
Cluster Peak [ADC]	140.5	146.5	128.0	202.0	173.5	115.0	64.0	30.5
S/N	62	58	49	59	45	45	31	16
fA/ADC (2.5 MHz)	1.82	1.72	4.28	9.26	1.30	1.55	1.09	1.08
$I_{leak}(1Mrad)/I_{leak}(0)$	23	220	67	271	12	23	5	6

Table 5.1: *Summary table of the measurement results obtained with the eight pixel types of the SUCCESSOR-I chip. All results in this table are given for an irradiation dose of* 1 $Mrad$ *and were obtained with a read out frequency of* 2.5 MHz*. (n/c = no change)*

	pixel 2	pixel 3	pixel 4	pixel 5
Charge Collection	n/c	n/c	n/c	n/c
Noise [ADC]	2.20	2.65	2.40	2.25
Cluster Peak [ADC]	123.5	201.5	171.0	111
S/N	56	76	71	49
$I_{leak}(2Mrad)/I_{leak}(0)$	104	659	18	38

Table 5.2: *Summary table of the measurement results obtained with the four favoured pixel types of the SUCCESSOR-I chip. All results in this table are given for an irradiation dose of* 2 $Mrad$ *and were obtained with a read out frequency of* 10 MHz*. (n/c = no change)*

Choosing a pixel geometry

The decision on the pixel type to be used in the next generation of CMOS pixel detectors for the SUCIMA project was taken based on the measurement results presented above. Which pixel did we choose and based on which criteria?

As can be easily seen from the presented results, the old worries of charge loss and gain variation due to irradiation of the detector did not affect any of the eight tested pixel types. Also the signal to noise ratio is well above any critical value for the pixels 1 to 5. Pixels 6 and 7 were only regarded as test structures and never really as a possible candidate for the next detector iteration.

So finally the decisive parameters were the gain and the leakage current. The gain should be neither too low (poor detection efficiency) nor too high (possible risk of saturation in high dose rate environments). But the most important issue was the leakage current, which effectively limits the operational range of the device with respect to temperature and integration time. The pixel type matching these criteria best, was pixel 4. Consequently, the design of the pixels in the SUCCESSOR-V detector is based on the geometry of pixel 4 of the SUCCESSOR-I.

This new detector, SUCCESSOR-V, will allow to make more than 10000 measurements of a brachytherapy source under worst case conditions (measurement time: $10\,s$, dose rate: $20\,rad/s$). Older pixel designs would have allow only a few hundred measurements as their performance degraded very fast with increasing dose.

5.4 CMOS Pixel Sensors in Magnetic Fields

For applications in both HEP and medicine it is necessary to study the behaviour of CMOS sensors in high magnetic fields.

For measurements within a magnetic field, the superconducting magnet *JUMBO* [Sch99] located at the *Institut für Technische Physik, Forschungszentrum Karlsruhe*, Germany, was used. This magnet, shown in Fig. 5.25 is capable of producing a magnetic field of up to 10 Tesla in our configuration. It is possible to measure at any temperature between 77K and room temperature by cooling the warm bore of the magnet with nitrogen gas. The superconducting coil consists of niob titanium and is cooled by liquid helium during operation.

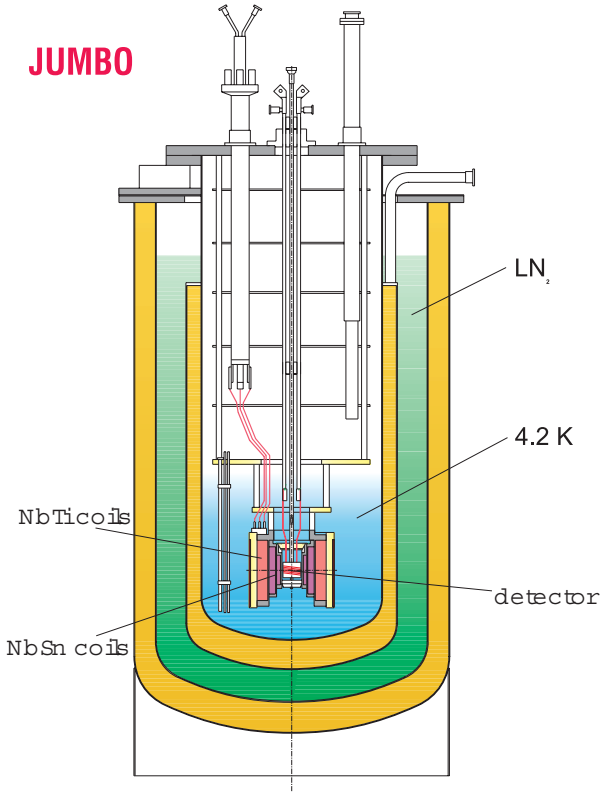

Figure 5.25: *The JUMBO magnet at the ITP, Forschungszentrum Karlsruhe*

Two different sets of measurements were done with the MIMOSA-I chip. For the first run (RUN I) the sensor surface was aligned parallel to the direction of the magnetic field, for the second run (RUN II) the sensor was aligned perpendicular to the field. In the first run, the sensor was read out 6000 times (*frames*) for each value of the magnetic field, in the second run 4000 frames were taken for each value of the field.

For a magnetic field parallel to the sensor surface Fig. 5.26(a) shows the charge distribution of the central pixel of each event. There are two peaks visible. The peak located at about 270 ADC counts is produced by events in which a photon converts within a collecting diode and thus represents 100% charge collection efficiency. The bigger peak around 70 ADC counts is produced by photons converting somewhere within the bulk material of MIMOSA where there is no electric field. Not all charges are collected because a big part of the total charge escapes to adjacent pixels.

It can be seen that the bulk peak shifts to lower ADC counts with increasing magnetic field, which means that less charge is collected by the central pixel when the field increases. Fig. 5.26(b) shows the sum of all ADC counts within a 3x3 matrix around the central pixel. The same effect, but less pronounced, as for the central pixel can be seen for the 3x3 matrix where most of the total charge

should be collected. For the 5x5 matrix the effect is even smaller.

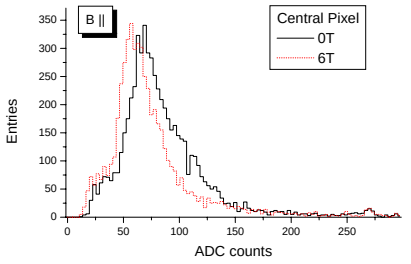

(a) central pixel

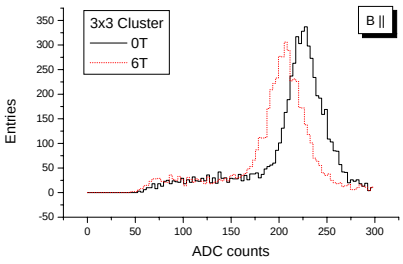

(b) 3x3 matrix

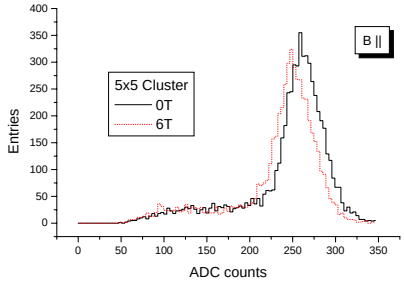

(c) 5x5 matrix

Figure 5.26: *Charge collection for parallel field. (a) central pixel, (b) 3x3 matrix, (c) 5x5 matrix*

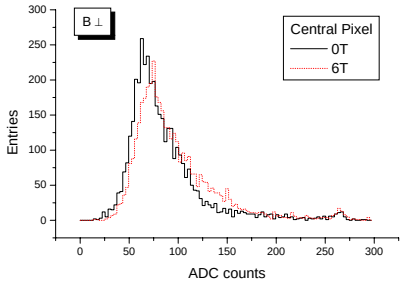

(a) central pixel

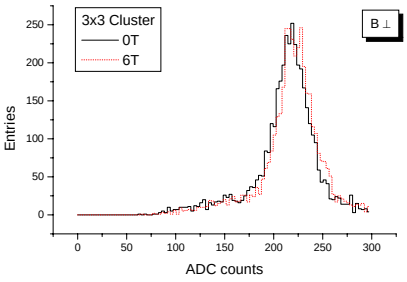

(b) 3x3 matrix

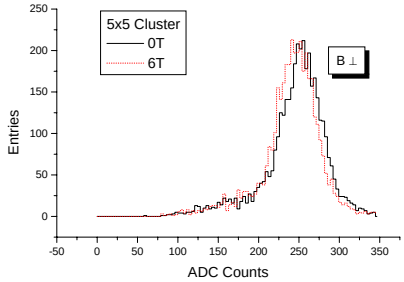

(c) 5x5 matrix

Figure 5.27: *Charge collection for perpendicular field. (a) central pixel, (b) 3x3 matrix, (c) 5x5 matrix*

This could be understood in the following way (Fig. 5.28(a)): As soon as the electrons reach the

collecting diode which is on a positive potential, they start to move towards the diode. The direction of movement is then perpendicular to the magnetic field leading to a Lorentz force pointing away from the diode. So the Lorentz force literally tries to prevent the charges from reaching the diode. This leads to a loss in charge collection efficiency.

Figs. 5.27(a) and 5.27(b) show the same histograms for a perpendicular magnetic field. It can be seen that the situation is quite different compared to the parallel field. Still, the small peak stays at the same place as expected. But the bulk peak is now shifted towards higher ADC counts i.e. higher charge collection efficiencies. Also, the peak of the 3x3 matrix sum is slightly shifted in that direction. The 5x5 matrix shows slightly less charge collection efficiency. This leads to the following understanding (Fig. 5.28(b)): The generated charge drifting to the collection diode is focused on the central pixel. The magnetic field prevents the electrons from being deflected.

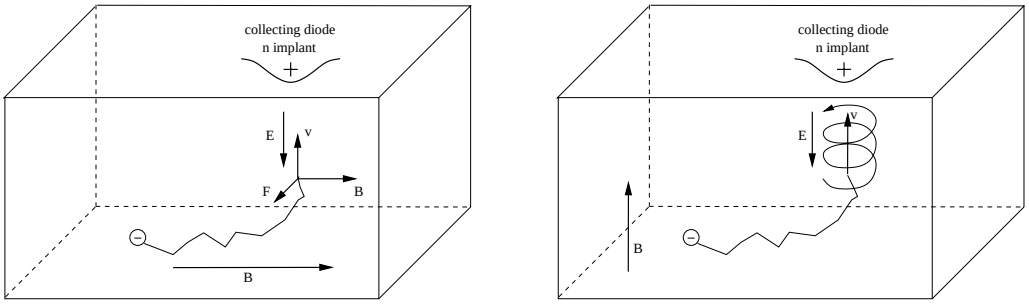

(a) Parallel Field (b) Perpendicular Field

Figure 5.28: *(a) Lorentz force tries to deflect electrons away from the collecting diode for a magnetic field parallel to the sensor surface (b) Lorentz forces focuses the collected charge for a perpendicular field*

Fig. 5.29 shows the position of the bulk peak for several values of the magnetic field. It can clearly be seen that the peak shifts to lower energies for parallel field and to higher energies for perpendicular field.

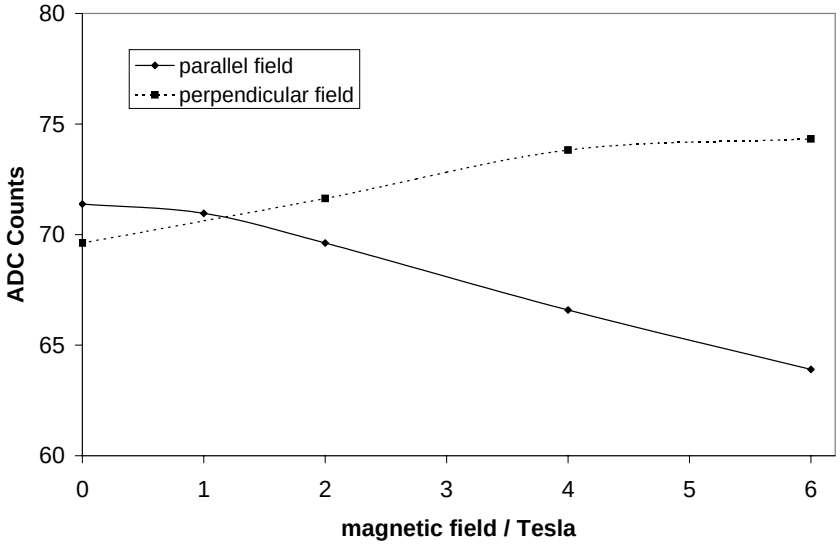

Figure 5.29: *Most probable pulse height of the central pixel as function of the magnetic field parallel and perpendicular to the surface of MIMOSA.*

Figs. 5.30(a) to 5.31(b) show the shape of the events calculated using the method described in appendix D. Cross-sections through the event shape in two directions are shown (X and Y). The X direction is the direction in which rows are read out.

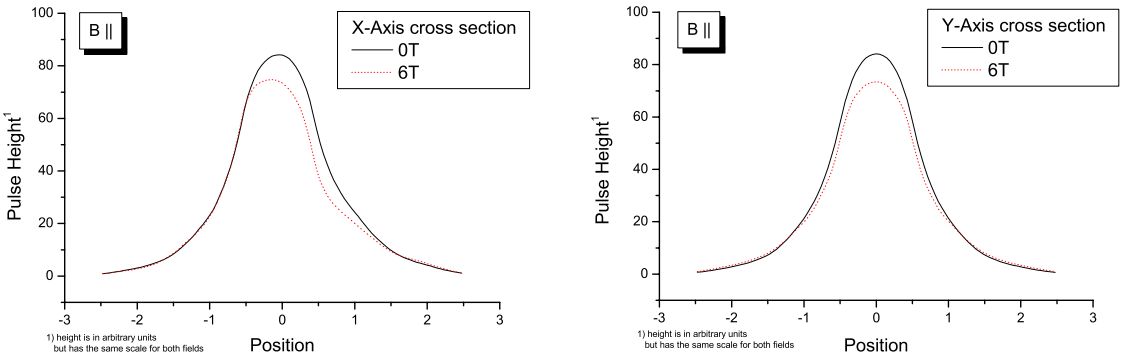

(a) X direction (b) Y direction

Figure 5.30: *Charge distribution for parallel field; (a) X direction, (b) Y direction*

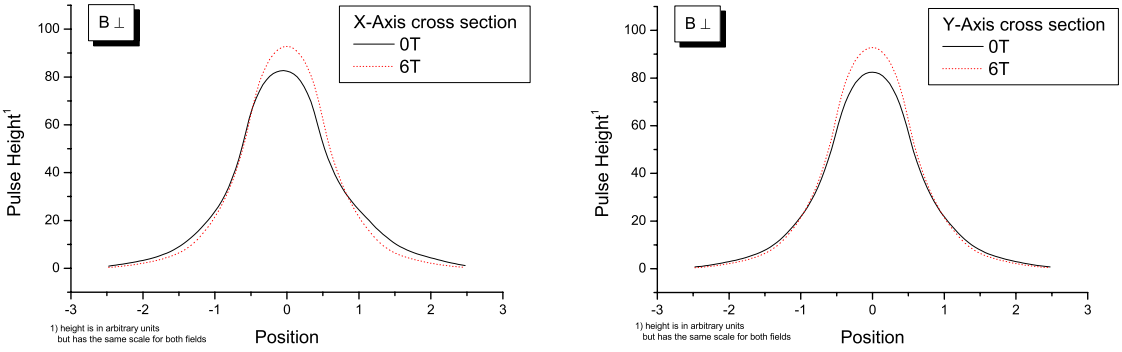

(a) X direction (b) Y direction

Figure 5.31: *Charge distribution for perpendicular field; (a) X direction, (b) Y direction*

It can be seen that the width of the events is not changing very much from zero to six Tesla. This indicates that the distribution of charge is about the same for all fields. A difference can be seen in the total amount of charge collected, represented by the area covered by the plot. For a parallel (perpendicular) field the total charge collected is clearly less (more) for six Tesla compared to zero field in agreement with the peak shifts discussed before.

Since the observed effects are small, which was expected due to the thin sensitive layer of the CMOS detectors, it can be concluded, that CMOS detectors can be used in high magnetic fields without any difficulties and only a small calibration factor is required.

Summary

In 2008 the **A**lpha **M**agnetic **S**pectrometer (AMS02) detector will be launched in a Space Shuttle to the **I**nternational **S**pace **S**tation (ISS) and will then measure the spectrum of the primary cosmic rays, consisting of charged particles and photons, there for at least three years. During this time AMS02 will collect an unprecedented amount of data with an unrivalled precision in the energy range $300\,MeV$ to $3\,TeV$. The analysis of this data will allow to refine the existing models for the acceleration and propagation of particles in the universe. With the contribution of the Transition Radiation Detector (TRD) and the Electromagnetic Calorimeter, it will be possible to measure the positron fraction with very high precision, leading to a possible verification of the theories for the nature of the Dark Matter. The data of AMS02 will also be essential for any long duration manned spaceflight outside of Earth's protective environment, as it will, for the first time, allow to measure the flux of the primary particles as a function of the time for more than a few days.

The location of the AMS02 detector on the S3 truss of the ISS inflicts very stringent requirements on the detector and electronic systems. The ability to withstand vacuum, temperature cycles on location and vibration during the transport in a Space Shuttle, but also the need to remain operational without any hardware maintenance, are among these requirements.

In the first part of this thesis the development of the electronics, from engineering level to pre-production, was discussed in detail using the example of the electronics for the TRD. This includes remarks on the general design followed throughout the complete AMS02 experiment, like the redundancy in the system to overcome zero-maintenance issues, but also detector specific items like power schemes and data flow. In this presentation of the electronics (read out, slow-control and power distribution) an emphasis was put on the development of the firmware of the data reduction card (UDR) - detector specific part -, the low voltage regulator card (UPSFE) and the controller for the DC/DC converters (S9011AU), which were programmed within the framework of this thesis.

In addition to the programming of the firmware codes for these cards, a test environment for the UPSFE has been designed, built and successfully applied during the qualification of the pre-production at the Chung-Shan Institute of Science and Technology in Taiwan. In two test periods at the Proton Synchrotron (PS-T9) facility at CERN, the performance of the electronics was successfully tested with physics data taking using data acquisition systems consisting of electronics on the engineering (October 2002) and the qualification level (October 2003).

Additionally, it was shown, that the electronics of the TRD, at single board level, meet the requirements of space-qualified electronics by testing them in thermo-vacuum, vibration and electromagnetic interference tests. The integration and functionality tests at crate level at the Institut für Experimentelle Kernphysik were finished successfully without showing any open issues. The space-qualification tests (thermo-vacuum test, vibration test and electro-magnetic interference test) will be done at crate level in the near future at the National Space Program Office (NPSO) in Taiwan.

Dosimetry applications in brachytherapy, the local treatment of human tissue with high activity radioactive sources, and other applications, both in radiotherapy and High Energy Physics, call for detection devices with a fine granularity and high tolerance with respect to the absorbed dose. Within the EU project "**S**ilicon **U**ltra fast **C**ameras for electron and gamma sources **I**n **M**edical **A**pplications" (SUCIMA) new prototype detectors were developed based on CMOS and SOI technology. The SOI option was investigated by our colleagues in Cracow and found not to be mature enough yet for large scale applications.

In addition to the detectors, a USB2.0 data acquisition system was developed in the SUCIMA collaboration by our Cracow colleagues. Together with a LabView software developed in the framework of this thesis, it was used during the irradiations to create realistic scenarios and as well as for pre- and post-irradiation measurements, which were done to characterise the detectors.

The radiation hardness studies on a prototype CMOS pixel detector, the SUCCESSOR-I, were the other main focus of this thesis and make up the second part of it. The SUCCESSOR-I detector was produced in the

AMIS 0.35 μm technology and has a 4 μm epitaxial layer. Since the SUCCESSOR-I detector was designed as a technology study, its sensitive area is segmented into eight sub-matrices, each filled with pixels of a different design. The purpose of the radiation hardness study was to find the pixel layout with the best compromise of detection efficiency and radiation tolerance.

The irradiations of the detectors were done using an X-ray system with a tungsten anode operating at an acceleration voltage of 60 kV and a dose rate of $\sim 147\,krad/h$, effectively limiting the damage effects of the radiation to charge trapping in the oxide. For all eight pixel types the most important characteristics were measured before and after the irradiation, which was done in steps of 500, 750 and 1000 $krad$ for chip #2 and 1000 and 2000 $krad$ for chip #7.

As the main purpose of the radiation hardness studies was to choose the most robust pixel layout of the eight on SUCCESSOR-I, a number of figures of merit were selected: charge collection loss, intrinsic gain, gain degradation, signal to noise ratio and leakage current.

While prototype CMOS detectors, measured in previous studies, showed serious degradation effects after doses of only 100 $krad$ [Dep02], it was proven for all eight pixel layouts of SUCCESSOR-I, that the charge collection efficiency and the intrinsic gain of the pixels are only affected in a non-significant amount, even for doses of up to 2 $Mrad$. Also the signal to noise ratio was quite stable and well above any critical value, especially at $T = -15\,°C$, where the noise performance of the device is not so much affected by the increased leakage current.

Thus the decision criteria were reduced to the gain of the pixel and the leakage current. The gain of the pixel should neither be too small (too little signal) nor be too high (limited dynamic range). The leakage current of the pixel should be rather small, otherwise it would limit the maximum possible integration time, and should not increase too much with the dose. The pixel matching these two criteria best is pixel 4, which is now also used in the final device of SUCIMA, the SUCCESSOR-V. Especially its leakage current behaviour is a big plus. The leakage current is much smaller than that of the other pixels and it only increases very slowly, by a factor 18, with increasing dose (0 $krad$ to 2000 $krad$). For comparison, the leakage current of pixel 3 increases for the same dose by a factor of almost 660!

During the radiation hardness studies two effects were observed, which need to be addressed in future devices in order not to jeopardise the long term operation of a CMOS detector. The first item is the non-radiation hard digital part of SUCCESSOR-I. This is not a big problem, as solutions for this are already known and have been proven to be successful. One remaining issue is the self-heating of the output buffers, which increases the leakage current of the pixels by rising their temperature and leads to inhomogeneous pedestals. This problem could be overcome by a modified layout of the output buffers, which is probably much quite difficult to implement.

In addition to the radiation hardness measurements, also studies on the performance of CMOS pixel detectors under the influence of strong magnetic fields ($\leq 6\,T$) were done using an older prototype CMOS detector, MIMOSA-I. Two sets of measurements were performed. In the first set the detector surface was aligned parallel to the magnetic field, in the second perpendicular to it. While for the first set the signal becomes weaker with increasing field strength, it becomes stronger in the second case. The smallness of these effects was expected, as the sensitive volume of CMOS sensors is very thin. The current understanding of this effect is based on the Lorentz force, that deflects drifting charges in magnetic fields. In the first case the Lorentz force results in a longer effective drift path hindering the electrons from reaching the collecting diode within the integration time. In the second case, the Lorentz force acts against movements away from the collecting diode and thus brings more electrons to the collecting diode.

As a summary it can be said, that a radiation hard CMOS detector was successfully developed together with a corresponding USB2.0 DAQ card. This system can be understood as a digital camera for ionising radiation, that can be easily connected to any standard PC. A system using the SUCCESSOR-V as detection device will be able to make more than 10000 measurements under worst case conditions (measurement time: 10 s, dose rate: 20 rad/s). Older designs would only last a few hundred measurements, as their performance, especially the charge collection efficiency, degraded very fast with increasing dose.

Appendix A

LeCroy Bus data word definition

LeCroy OUT			**LeCroy IN**	
bit	function	internal use	bit	function
0	1		32	0
1	parity bit (odd)		33	echo of parity bit
2	power down bit	unused	34	echo of power down bit
3	broadcast bit	unused	35	echo of broadcast bit
4	select code [7]	board address [3]	36	echo of select code [7]
5	select code [6]	board address [2]	37	echo of select code [6]
6	select code [5]	board address [1]	38	echo of select code [5]
7	select code [4]	board address [0]	39	echo of select code [4]
8	select code [3]	unused	40	echo of select code [3]
9	select code [2]	unused	41	echo of select code [2]
10	select code [1]	unused	42	echo of select code [1]
11	select code [0]	register address [3]	43	echo of select code [0]
12	read/write		44	echo of read/write
13	section address [2]	register address [2]	45	echo of section address [2]
14	section address [1]	register address [1]	46	echo of section address [1]
15	section address [0]	register address [0]	47	echo of section address [0]
16	data [15]		48	data [15]
17	data [14]		49	data [14]
18	data [13]		50	data [13]
19	data [12]		51	data [12]
20	data [11]		52	data [11]
21	data [10]		53	data [10]
22	data [9]		54	data [9]
23	data [8]		55	data [8]
24	data [7]		56	data [7]
25	data [6]		57	data [6]
26	data [5]		58	data [5]
27	data [4]		59	data [4]
28	data [3]		60	data [3]
29	data [2]		61	data [2]
30	data [1]		62	data [1]
31	data [0]		63	data [0]

Table A.1: *LeCroy bus bit function.*

Appendix B

UPSFEv2 firmware manual

This manual will give an introduction to the usage of the UPSFEv2 firmware. The various registers for commands and feedback will be described. A bit by bit review is shown in the tables at the end of this manual.

The commands to the UPSFEv2 are sent from the control centre via the JMDC and the JINJ to the JINF. For the communication from the main computer to the U-crate the AMSwire protocol is used. The AMSwire command is “translated”in the JINFv2 to a LeCroy command and sent via the backplane to the UPSFEv2.

The default power-up state of all control signals is “ON” to ensure a safe operation of the detector, even in the case of a communication loss with the UPSFEv2. To reduce power consumption in the U-crate, all unused parts should be disabled via software command as soon as the communication with the ground is established.

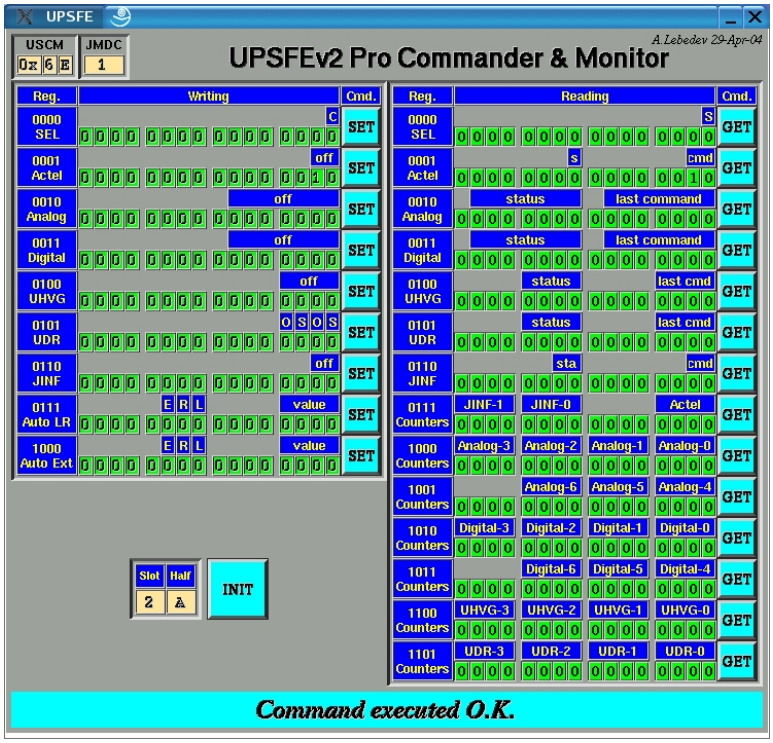

Figure B.1: *This screenshot shows the UPSFEv2 commanding software that was used during the development of the firmware and will be used during the various tests of the UPSFEv2. It will also serve as a basis for the final software, which will be used during the flight. [Software by Alexei Lebedev]*

B.1 Control Words & Feedback Registers

B.1.1 Power-up Detection

At power-on of the S9011AU the bit SEL is set to “1”. It can be read out via register *SEL* (“read 0000”), where it is bit 0. The register is automatically reset to “0” after reading it. To reset this register manually the data word “x0001” has to be written to register *SEL* (“ctrl 0000”).

B.1.2 2nd Actel

For redundancy the UPSFEv2 has two Actel Anti-Fuse FPGAs. Both of them are active after a power-on. To keep one Actel as cold redundant spare or to disable a malfunctioning Actel, one Actel can switch off its brother.

To minimise the risk of an accidental power-off of the second Actel, two signals have to be set in the *Actel* (“crtl 0001”) register. Only one combination “x0001” will switch of the second Actel, all other combinations are not relevant.

The corresponding feedback register *Actel* (“read 0001”) holds information on the actual status of the second Actel (bit 8) and the last command set for the *Actel* register (bits 1 & 0).

B.1.3 Linear Regulators Half A

The control register *LR_A control* (“crtl 0010”) is used for manipulating half A[(1)] of the linear regulators (LR) on the UPSFE. Setting a “1” in one of the lower 7 bits of the data word will switch off the corresponding linear regulator, a “0” will enable it.

The feedback register for the linear regulators half A, *LR_A* (“read 0010”), contains the information in the last command sent to the UPSFE regarding the half A of the linear regulators in the lower byte and the actual status in the upper byte.

B.1.4 Linear Regulators Half D

This is the set of registers corresponding to the above mentioned for the half D of the linear regulators. The registers are: *LR_D control* (“crtl 0011”) and *LR_D* (“read 0011”).

B.1.5 UHVG

Via the UHVG registers both halves of the two UHVGs belonging to the same power group as the UPSFE can be switched on and off. The commands are set in the register *UHVG control* (“crtl 0100”), the status and the last command regarding the UHVGs can be read back via register *UHVG* (“read 0100”). Again, a “1” disables the corresponding half of a UHVG, while a “0” enables it.

B.1.6 UDR2

The same scheme as for the UHVG is used for the UDR2s. Again, via two registers *UDR control* (“crtl 0101”) and *UDR* (“read 0101”) the commands can be set and and read back together with the actual status. Unlike the UHVG, the two control lines do not control directly the two SSFs on the UDRs, but one line disables the complete UDR and the other one switches between the two redundant halves.

[(1)] The naming of the two halves of the UPSFE *A* and *D* is a left-over from the UPSFE version 1, in which the analog (A) and digital (D) supply lines to the UFE were powered from different linear regulators.

B.1.7 JINF

For the JINF the same scheme as for the UHVG and the UDR2 is used again. The registers are *JINF control* (“ctrl 0110”) and *JINF* (“read 0110”). This feature is still available in the UPSFEv2 firmware even though it will not be used on the UBPv2, as the JUNFv2 now controls its own SSFs, like the UPSFE.

B.1.8 Linear Regulator trip counters

The UPSFEv2 features a 4*bit* trip counter for each of its linear regulators. Thus there are 2 times 7 counters. These counters can be controlled via the register *LR counter control* (“ctrl 0111”).

They can be set to a value passed in the same data word or reset to zero. An additional feature of these counters is an automatic disabling of a linear regulator that has reached the maximum allowed value (15) of trips. The feature is disabled by default and must be enabled via a command, if desired.

The values of the counters can be read via 4 registers in the UPSFEv2 firmware. These registers are *LR_A cnt 1* (“read 1000”) and *LR_A cnt 2* (“read 1001”) for half A of the linear regulators, and *LR_D cnt 1* (“read 1010”) and *LR_D cnt 2* (“read 1011”) for half D of the linear regulators. The register *LR_x cnt 1* contains the values of the counters 0 to 3 and the register *LR_x cnt 2* the values of the counters 4 to 6.

B.1.9 External monitor lines trip counters

The above mentioned 4*bit* trip counters are also implemented for the monitor lines of the 2nd Actel, the UHVGs, the UDRs and the JINF. The functionality is the same as for the counters of the linear regulators including the automatic disabling. There is only one exception to this, the counter of the 2nd Actel has no automatic disable feature.

These counters can be controlled via the register *EXT counter control* (“ctrl 1000”). The counters are grouped into various registers according to the corresponding card they monitor. There are the following registers: *Actel & JINF cnt* (“read 0111”), *UHVG cnt* (“read 1100”), *UDR cnt* (“read 1101”).

B.2 Backplane Connections - LeCroy Bus

In Tab. B.1 the LeCroy clock and data lines used by the USCM to communicate with the S9011AU are listed. Tab. B.2 gives the corresponding information for the QM2 backplane.

UPSFE ♯	backplane slot ♯	board address	clock line half A	data line half A	clock line half B	data line half B
0	2	0010	4	12	5	13
1	3	0011	4	12	5	13
2	6	0110	4	12	5	13
3	7	0111	4	12	5	13
4	11	1011	4	12	5	13
5	12	1100	4	12	5	13

Table B.1: *QM1 backplane connections of the UPSFE for the LeCroy bus.*

UPSFE ♯	backplane slot ♯	board address	clock line half A	data line half A	clock line half B	data line half B
0	2	0010	2	2	7	7
1	5	0011	2	2	7	7
2	8	0110	2	2	7	7

Table B.2: *QM2 backplane connections of the UPSFEv2 for the LeCroy bus.*

B.3 FPGA pin assignment

Figs. B.2 and B.3 show the pin assignment for both Actel A54SX32A-TQ144 FPGAs on the UPSFEv2. Due to the routing of the signal lines on the UPSFEv2, the two FPGAs have a different pin assignment.

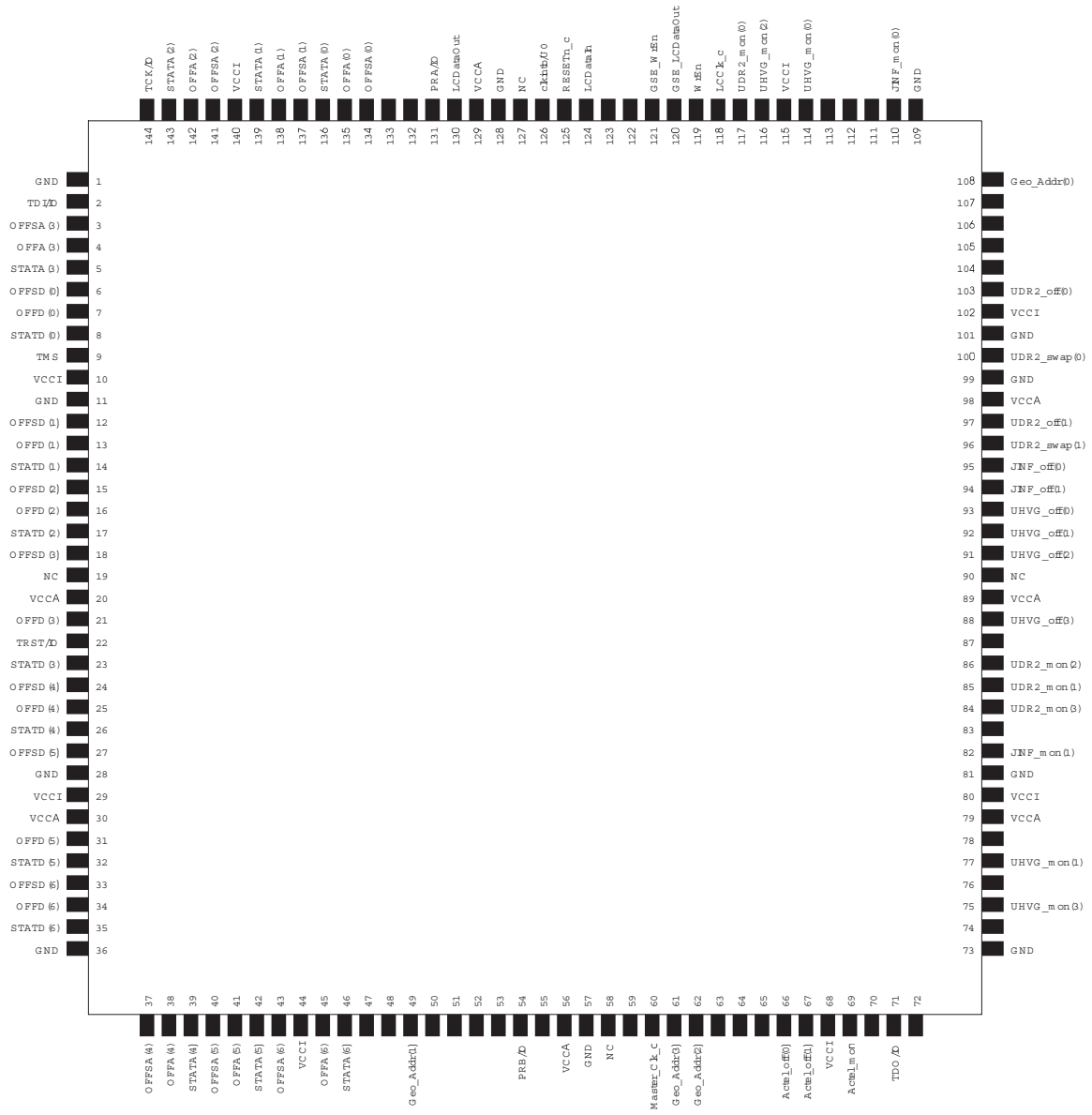

Figure B.2: *This picture shows the pin assignment for FPGA_0 (U37, top side).*

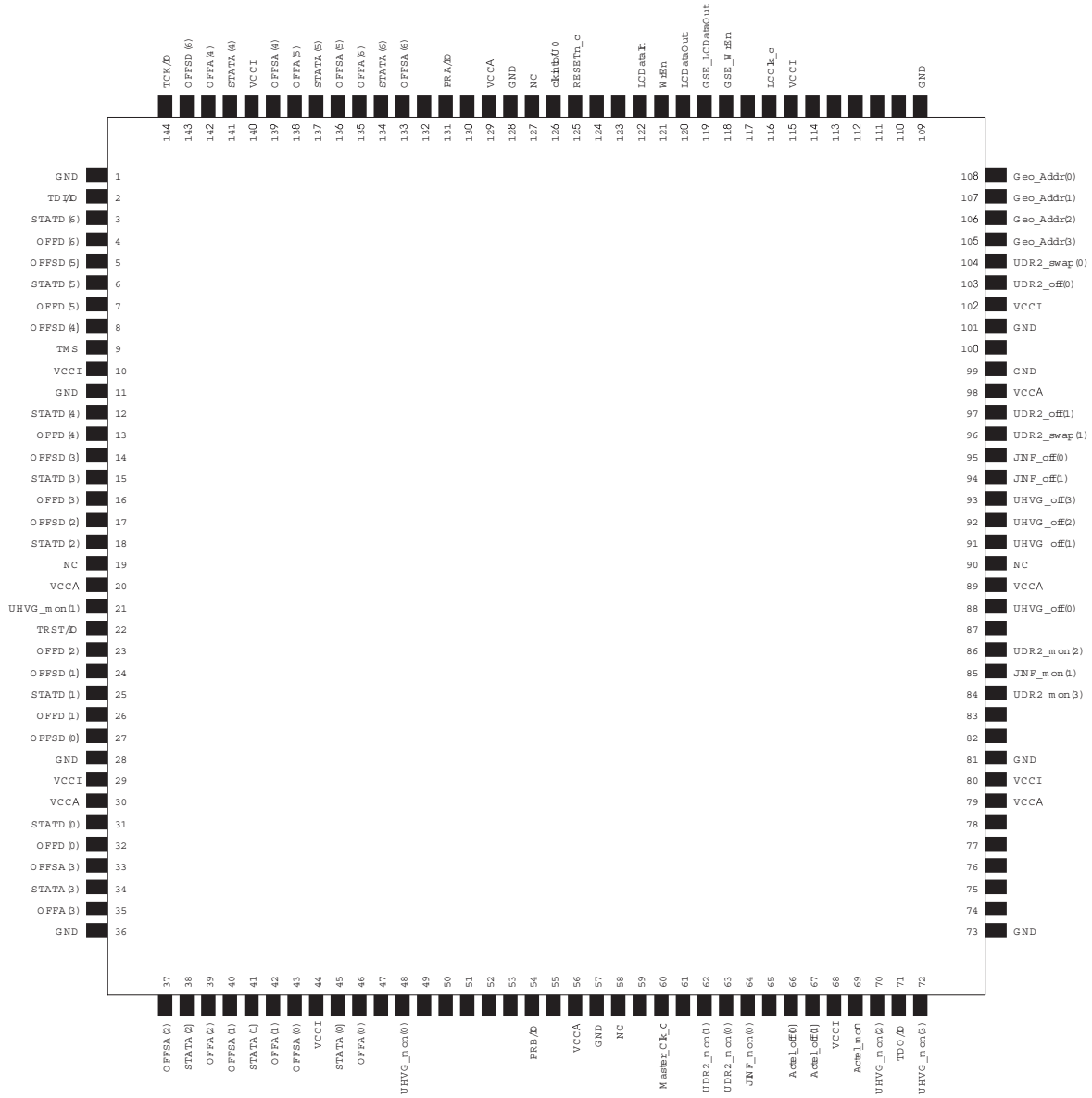

Figure B.3: *The upper picture shows the pin assignment for FPGA_0 (U37, top side), the lower picture for FPGA_1 (U56, bottom side).*

B.4 UPSFEv2 Command & Read Registers Tables

In the tables on the following pages a detailed description of the usage of the bits in the various read and write registers is given.

register	0000	0001	0010	0011	0100	0101	0110	0111	1000
name	SEL	Actel control	LR_A control	LR_D control	UHVG control	UDR control	JINF control	LR counter control	EXT counter control
data [15]	0	0	0	0	0	0	0	0	0
data [14]	0	0	0	0	0	0	0	0	0
data [13]	0	0	0	0	0	0	0	0	0
data [12]	0	0	0	0	0	0	0	0	0
data [11]	0	0	0	0	0	0	0	0	0
data [10]	0	0	0	0	0	0	0	enable auto mode	enable auto mode
data [9]	0	0	0	0	0	0	0	reset LR counter	reset EXT counter
data [8]	0	0	0	0	0	0	0	load LR counter	load EXT counter
data [7]	0	0	0	0	0	0	0	0	0
data [6]	0	0	LR_A off [6]	LR_D off [6]	0	0	0	0	0
data [5]	0	0	LR_A off [5]	LR_D off [5]	0	0	0	0	0
data [4]	0	0	LR_A off [4]	LR_D off [4]	0	0	0	0	0
data [3]	0	0	LR_A off [3]	LR_D off [3]	UHVG_off [3]	UDR_off [1]	0	value LR [3]	value EXT [3]
data [2]	0	0	LR_A off [2]	LR_D off [2]	UHVG_off [2]	UDR_swap [1]	0	value LR [2]	value EXT [2]
data [1]	0	Actel off [1]	LR_A off [1]	LR_D off [1]	UHVG_off [1]	UDR_off [0]	JINF_off [1]	value LR [1]	value EXT [1]
data [0]	clear SEL	Actel off [0]	LR_A off [0]	LR_D off [0]	UHVG_off [0]	UDR_swap [0]	JINF_off [0]	value LR [0]	value EXT [0]

Table B.3: *UPSFEv2 write commands. The data bits 0..15 correspond to bits 16..31 in Tab. A.1. If a “1” is loaded in to a register the corresponding device is disabled. To enable it, load a “0” into it. Are more detailed description is given in the sections corresponding to the registers on the preceding pages.*

register	0000	0001	0010	0011	0100	0101	0110
name	SEL	Actel	LR_A	LR_D	UHVG	UDR	JINF
data [15]	0	0	0	0	0	0	0
data [14]	0	0	LR_A status [6]	LR_D status [6]	0	0	0
data [13]	0	0	LR_A status [5]	LR_D status [5]	0	0	0
data [12]	0	0	LR_A status [4]	LR_D status [4]	0	0	0
data [11]	0	0	LR_A status [3]	LR_D status [3]	UHVG status [3]	UDR status [3]	0
data [10]	0	0	LR_A status [2]	LR_D status [2]	UHVG status [2]	UDR status [2]	0
data [9]	0	0	LR_A status [1]	LR_D status [1]	UHVG status [1]	UDR status [1]	JINF status [1]
data [8]	0	Actel status	LR_A status [0]	LR_D status [0]	UHVG status [0]	UDR status [0]	JINF status [0]
data [7]	0	0	0	0	0	0	0
data [6]	0	0	LR_A last command [6]	LR_D last command [6]	0	0	0
data [5]	0	0	LR_A last command [5]	LR_D last command [5]	0	0	0
data [4]	0	0	LR_A last command [4]	LR_D last command [4]	0	0	0
data [3]	0	0	LR_A last command [3]	LR_D last command [3]	UHVG last command [3]	UDR last command [3]	0
data [2]	0	0	LR_A last command [2]	LR_D last command [2]	UHVG last command [2]	UDR last command [2]	0
data [1]	0	Actel last command [1]	LR_A last command [1]	LR_D last command [1]	UHVG last command [1]	UDR last command [1]	JINF last command [1]
data [0]	SEL	Actel last command [0]	LR_A last command [0]	LR_D last command [0]	UHVG last command [0]	UDR last command [0]	JINF last command [0]

Table B.4: *UPSFEv2 read commands part 1: last commands (= desired value) & status bits (= actual value). A "1" corresponds to "off" or "error", while a "0" corresponds to "on" or "okay". More details on the different registers can be found in the corresponding sections on the preceding pages.*

register	0111	1000	1001	1010	1011	1100	1101
name	Actel & JINF cnt	LR_A cnt 1	LR_A cnt 2	LR_D cnt 1	LR_D cnt 2	UHVG cnt	UDR
data [15]	JINF counter_1 [3]	LR_A counter_3 [3]	0	LR_D counter_3 [3]	0	UHVG counter_3 [3]	UDR counter_3 [3]
data [14]	JINF counter_1 [2]	LR_A counter_3 [2]	0	LR_D counter_3 [2]	0	UHVG counter_3 [2]	UDR counter_3 [2]
data [13]	JINF counter_1 [1]	LR_A counter_3 [1]	0	LR_D counter_3 [1]	0	UHVG counter_3 [1]	UDR counter_3 [1]
data [12]	JINF counter_1 [0]	LR_A counter_3 [0]	0	LR_D counter_3 [0]	0	UHVG counter_3 [0]	UDR counter_3 [0]
data [11]	JINF counter_0 [3]	LR_A counter_2 [3]	LR_A counter_6 [3]	LR_D counter_2 [3]	LR_D counter_6 [3]	UHVG counter_2 [3]	UDR counter_2 [3]
data [10]	JINF counter_0 [2]	LR_A counter_2 [2]	LR_A counter_6 [2]	LR_D counter_2 [2]	LR_D counter_6 [2]	UHVG counter_2 [2]	UDR counter_2 [2]
data [9]	JINF counter_0 [1]	LR_A counter_2 [1]	LR_A counter_6 [1]	LR_D counter_2 [1]	LR_D counter_6 [1]	UHVG counter_2 [1]	UDR counter_2 [1]
data [8]	JINF counter_0 [0]	LR_A counter_2 [0]	LR_A counter_6 [0]	LR_D counter_2 [0]	LR_D counter_6 [0]	UHVG counter_2 [0]	UDR counter_2 [0]
data [7]	0	LR_A counter_1 [3]	LR_A counter_5 [3]	LR_D counter_1 [3]	LR_D counter_5 [3]	UHVG counter_1 [3]	UDR counter_1 [3]
data [6]	0	LR_A counter_1 [2]	LR_A counter_5 [2]	LR_D counter_1 [2]	LR_D counter_5 [2]	UHVG counter_1 [2]	UDR counter_1 [2]
data [5]	0	LR_A counter_1 [1]	LR_A counter_5 [1]	LR_D counter_1 [1]	LR_D counter_5 [1]	UHVG counter_1 [1]	UDR counter_1 [1]
data [4]	0	LR_A counter_1 [0]	LR_A counter_5 [0]	LR_D counter_1 [0]	LR_D counter_5 [0]	UHVG counter_1 [0]	UDR counter_1 [0]
data [3]	Actel counter [3]	LR_A counter_0 [3]	LR_A counter_4 [3]	LR_D counter_0 [3]	LR_D counter_4 [3]	UHVG counter_0 [3]	UDR counter_0 [3]
data [2]	Actel counter [2]	LR_A counter_0 [2]	LR_A counter_4 [2]	LR_D counter_0 [2]	LR_D counter_4 [2]	UHVG counter_0 [2]	UDR counter_0 [2]
data [1]	Actel counter [1]	LR_A counter_0 [1]	LR_A counter_4 [1]	LR_D counter_0 [1]	LR_D counter_4 [1]	UHVG counter_0 [1]	UDR counter_0 [1]
data [0]	Actel counter [0]	LR_A counter_0 [0]	LR_A counter_4 [0]	LR_D counter_0 [0]	LR_D counter_4 [0]	UHVG counter_0 [0]	UDR counter_0 [0]

Table B.5: *UPSFEv2 read commands part 2: trip counters. The registers contain the values of the trip counters of the monitor lines from the linear regulators and the external monitor lines. For more details please refer to the corresponding sections on the preceding pages.*

Appendix C

S9011AU firmware manual

This manual will give an introduction to the usage of the S9011AU firmware. The various registers for commands and feedback will be described. A bit by bit review is shown in the tables at the end of this manual.

The commands to the S9011AU are sent from the control centre via the JMDC and the JINJ to the JINF. For the communication from the main computer to the U-crate the AMSwire protocol is used. The AMSwire command is “translated”in the JINFv2 to a LeCroy command and sent via the backplane to the S9011AU.

The default power-up state of all control signals is “ON” to ensure a safe operation of the detector, even in the case of a communication loss with the S9011AU. To reduce power consumption in the UPD, all unused parts should be disabled via software command as soon as the communication with the ground is established.

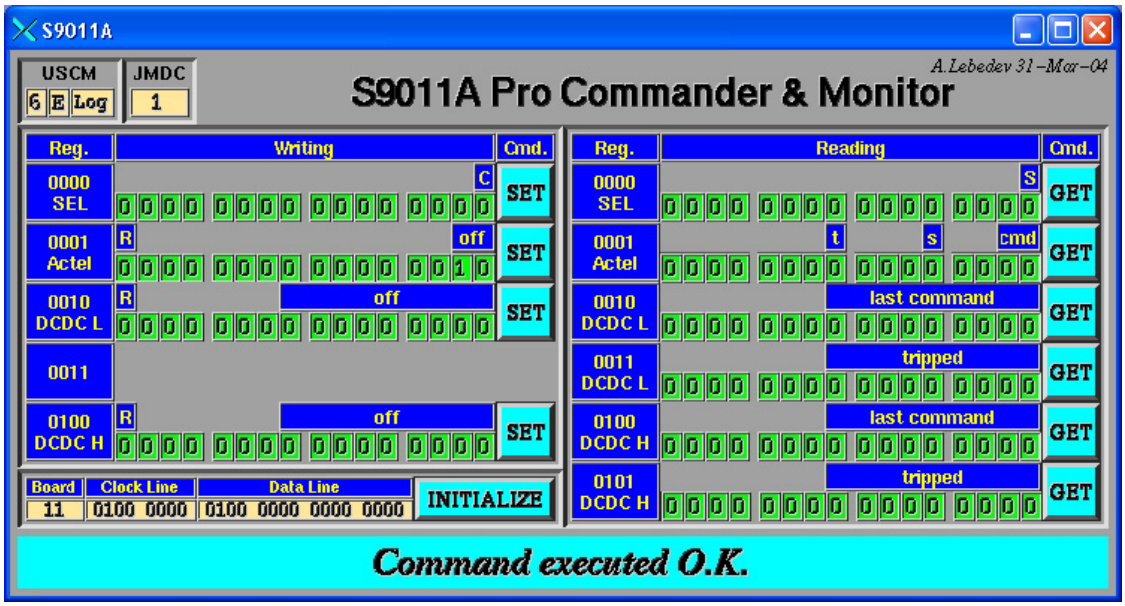

Figure C.1: *This screenshot shows the S9011AU commanding software that was used during the development of the firmware and will be used during the various tests of the S9011AU. It will also serve as a basis for the final software, which will be used during the flight. [Software by Alexei Lebedev]*

C.1 Command & Feedback Registers

C.1.1 Power-up Detection

At power-on of the S9011AU the bit SEL is set to “1”. It can be read out via register *SEL* (“read 0000”), where it is bit 0. The register is automatically reset to “0” after reading it. To reset this register manually the data word “x0001” has to be written to register *SEL* (“ctrl 0000”).

C.1.2 2nd Actel

For redundancy the S9011AU has two Actel Anti-Fuse FPGAs. Both of them are active after a power-on. To keep one Actel as cold redundant spare or to disable a malfunctioning Actel, one Actel can switch off its brother.

To minimise the risk of an accidental power-off of the second Actel, two signals have to be set in the *Actel* (“crtl 0001”) register. Only one combination “x0001” will switch of the second Actel, all other combinations are not relevant.

The corresponding feedback register *Actel* (“read 0001”) holds information on the actual status of the second Actel (bit 8), the trip detection flip-flop (bit 4) and the last command set for the *Actel* register (bits 1 & 0).

C.1.3 DC/DC converters half L

The control register *DC/DC L* (“crtl 0010”) is used for manipulating the L half of the DC/DC converters in the UPD. Setting a “1” in one of the lower 9 bits of the data word will switch off the corresponding DC/DC converter, a “0” will enable it.

There are two feedback registers for the DC/DC converter halves L. The first one, *DC/DC L last command* (“read 0010”), contains the information in the last command sent to the S9011AU regarding the L halves of the DC/DC converters. The second register, *DC/DC L trip FFs* (“read 0011”) allows to read the trip detection flip-flops for the 9 L halves.

C.1.4 DC/DC converters half H

This is the set of registers corresponding to the above mentioned for the H halves of the DC/DC converters. The registers are: *DC/DC H* (“crtl 0100”), *DC/DC H last command* (“read 0100”) and *DC/DC H trip FFs* (“read 0101”).

C.2 Backplane Connections - LeCroy Bus

In Tab. C.1 the LeCroy clock and data lines used by the USCM to communicate with the S9011AU are listed. Tab. C.2 gives the corresponding information for the QM2 backplane.

S9011AU ♯	board address	clock line half A	data line half A	clock line half B	data line half B
0	0011	6	14	7	15

Table C.1: *QM1 Backplane Connections of the S9011AU for the LeCroy Bus.*

S9011AU #	board address	clock line half A	data line half A	clock line half B	data line half B
0	0011	3	3	4	4

Table C.2: *QM2 backplane connections of the S9011AU for the LeCroy bus.*

C.3 FPGA Pin Assignment

Fig. C.2 shows the pin assignment for both Actel A54SX32A-TQ144 FPGAs on the S9011AU.

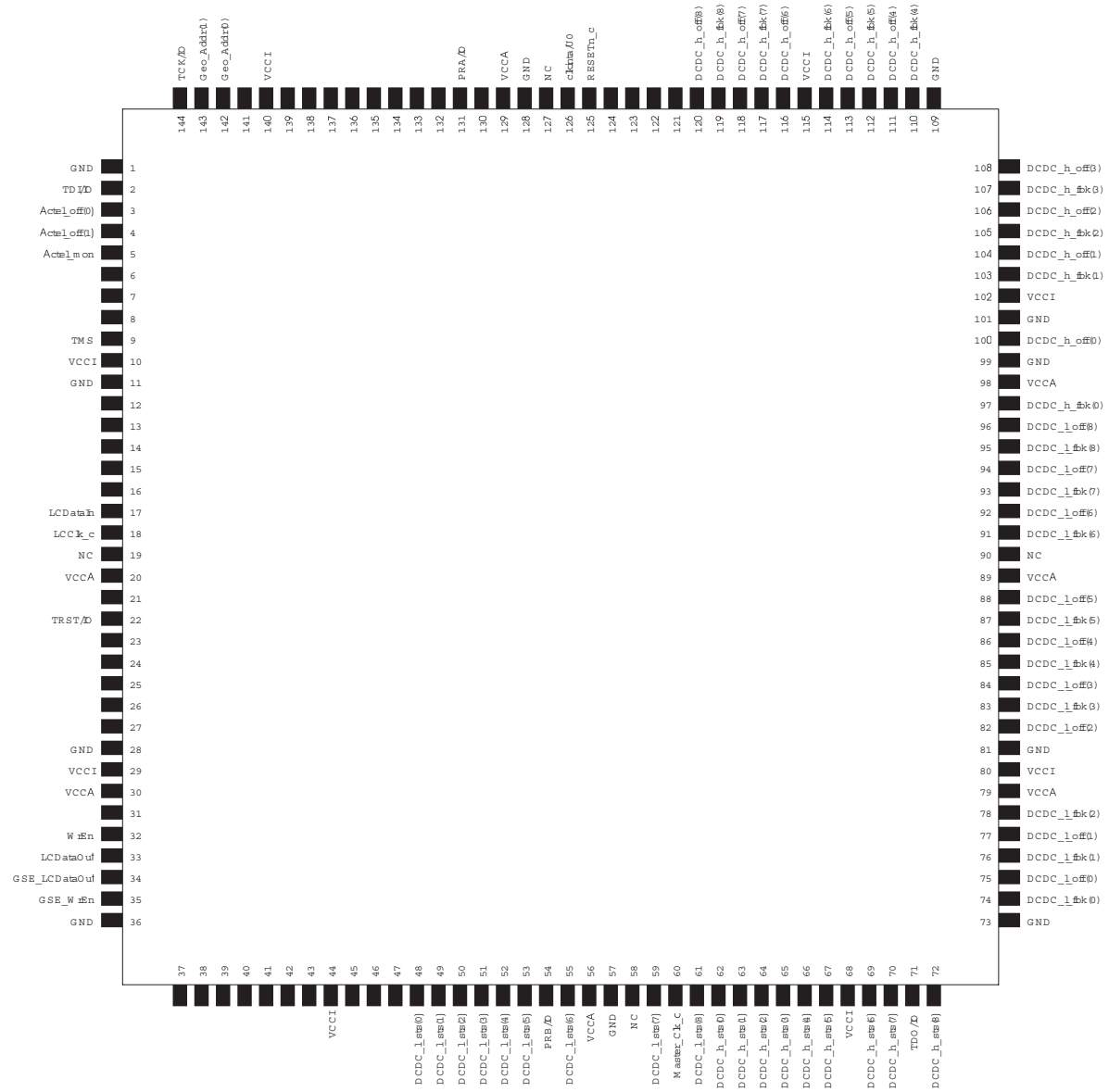

Figure C.2: *This picture shows the pin assignment for both Actel A54SX32A-TQ144 FPGAs on the S9011AU.*

C.4 S9011AU Command & Read Registers Tables

In the tables on this and on the following page, a detailed description of the usage of the bits in the various read and write registers is given.

register name	0000 SEL	0001 Actel control	0010 DC/DC L control	0100 DC/DC H control
data [15]	0	reset Actel trip FF	reset DC/DC L trip FFs	reset DC/DC H trip FFs
data [14]	0	0	0	0
data [13]	0	0	0	0
data [12]	0	0	0	0
data [11]	0	0	0	0
data [10]	0	0	0	0
data [9]	0	0	0	0
data [8]	0	0	DC/DC L off [8]	DC/DC H off [8]
data [7]	0	0	DC/DC L off [7]	DC/DC H off [7]
data [6]	0	0	DC/DC L off [6]	DC/DC H off [6]
data [5]	0	0	DC/DC L off [5]	DC/DC H off [5]
data [4]	0	0	DC/DC L off [4]	DC/DC H off [4]
data [3]	0	0	DC/DC L off [3]	DC/DC H off [3]
data [2]	0	0	DC/DC L off [2]	DC/DC H off [2]
data [1]	0	Actel off [1]	DC/DC L off [1]	DC/DC H off [1]
data [0]	clear SEL	Actel off [0]	DC/DC L off [0]	DC/DC H off [0]

Table C.3: *S9011AU write commands. The data bits 0..15 correspond to bits 16..31 in Tab. A.1. If a "1" is loaded in to a register the corresponding device is disabled. To enable it, load a "0" into it. Are more detailed description is given in the sections corresponding to the registers on the preceding pages.*

register	0000	0001	0010	0011	0100	0101
name	SEL	Actel	DC/DC L last command	DC/DC L trip FlipFlops	DC/DC H last command	DC/DC H trip FlipFlops
data [15]	0	0	0	0	0	0
data [14]	0	0	0	0	0	0
data [13]	0	0	0	0	0	0
data [12]	0	0	0	0	0	0
data [11]	0	0	0	0	0	0
data [10]	0	0	0	0	0	0
data [9]	0	0	0	0	0	0
data [8]	0	Actel trip FF	DC/DC L last command [8]	DC/DC L trip FF [8]	DC/DC H last command [8]	DC/DC H trip FF [8]
data [7]	0	0	DC/DC L last command [7]	DC/DC L trip FF [7]	DC/DC H last command [7]	DC/DC H trip FF [7]
data [6]	0	0	DC/DC L last command [6]	DC/DC L trip FF [6]	DC/DC H last command [6]	DC/DC H trip FF [6]
data [5]	0	0	DC/DC L last command [5]	DC/DC L trip FF [5]	DC/DC H last command [5]	DC/DC H trip FF [5]
data [4]	0	Actel status	DC/DC L last command [4]	DC/DC L trip FF [4]	DC/DC H last command [4]	DC/DC H trip FF [4]
data [3]	0	0	DC/DC L last command [3]	DC/DC L trip FF [3]	DC/DC H last command [3]	DC/DC H trip FF [3]
data [2]	0	0	DC/DC L last command [2]	DC/DC L trip FF [2]	DC/DC H last command [2]	DC/DC H trip FF [2]
data [1]	0	Actel last command [1]	DC/DC L last command [1]	DC/DC L trip FF [1]	DC/DC H last command [1]	DC/DC H trip FF [1]
data [0]	SEL	Actel last command [0]	DC/DC L last command [0]	DC/DC L trip FF [0]	DC/DC H last command [0]	DC/DC H trip FF [0]

Table C.4: *S9011AU read commands: last commands (= desired value) & trip flip-flops. A “1” corresponds to “off” or “error”, while a “0” corresponds to “on” or “okay”. More details on the different registers can be found in the corresponding sections on the preceding pages.*

Appendix D

Analysis Algorithms for SUCIMA

D.1 LabView

In the following the most important analysis algorithms used in the SUCIMA software will be introduced. One set of algorithms is used for the initial calculation of the pedestal, the noise and the bad pixel mask. A second set is used for the computation of the values updated after each frame. The main focus of this section will be set on the algorithms used in the cluster search.

D.1.1 Pedestals

The pedestals represent the leakage current of the pixel of the CMOS sensor. In order to achieve a correct calibration of the signal, the leakage current must be subtracted from the raw data before it is processed further.

- initial pedestals:
  For the initial calculation of the pedestals n_{max} frames are acquired from the sensor. From these frames the average is computed separately for each pixel.

$$Pedestals_{xy} = \frac{1}{n_{max}} \sum_{n=1}^{n=n_{max}} Frame_{xy}^{n} \tag{D.1}$$

- updated pedestals:
  For the updated pedestals a different algorithm is used. This is required, as the memory usage to keep the n_{max} last frames ready for recalculation would be too high, especially for the large scale sensors like MIMOSA-V. Thus an algorithm was chosen, that follows the trends slower, but uses almost no memory and is faster as well. To keep rounding errors within the tolerance, the computation is done with double precision.

$$Pedestals_{new} = \frac{Pedestals_{old} * (n_{max} - 1) + (Frame - Clusters)}{n_{max}} \tag{D.2}$$

D.1.2 Noise

The noise is defined as the fluctuations of the pedestals around their mean value. The noise matrix is used for two purposes. The first is the computing of the bad pixel mask, the second is in the cluster search.

- initial noise:
  The initial noise computation is divided into two parts. In the first part the noise is simply

calculated as the standard deviation of the fluctuation of the n_{max} frames around the pedestals.

$$Noise_{xy} = \sqrt{\frac{1}{n_{max}} \sum_{n=1}^{n=n_{max}} \left(Frame^{n}_{xy} - Pedestals\right)^2} \tag{D.3}$$

Between the first and the second iteration the BPM = Bad Pixel Mask has to be calculated, as in the second iteration the pixels above the noise threshold are masked. A further difference to the first iteration is the application of a common mode correction.

$$\begin{aligned} Noise^2_{xy} = & BPM \times \frac{1}{n_{max}} \sum_{n=1}^{n=n_{max}} \Bigg[\left(Frame^{n}_{xy} - Pedestals\right) \\ & - \frac{1}{y_{max}} \sum_{y=1}^{y=y_{max}} \left(Frame^{n}_{xy} - Pedestals\right) \Bigg]^2 \end{aligned} \tag{D.4}$$

- updated noise:
  For the evaluation of the updated noise matrix, like for the pedestals, a less memory intense and faster algorithm was chosen. The deviation of the current frame, after removing the common mode noise and the hit clusters, from the new pedestals is added quadratically to the old noise. Again these calculations are done using double precision to minimise the errors due to rounding.

$$\begin{aligned} Noise^2_{new} = & \frac{1}{n_{max}} \times \Big\{ Noise^2_{old} * (n_{max} - 1) \\ & + \left[(Frame - Pedestals - Common\ Mode - Clusters) \times BPM \right]^2 \Big\} \end{aligned} \tag{D.5}$$

D.1.3 Common Mode Noise

The common mode is a fluctuation in the signal from the sensor that is common, thus the name, to many or even all pixels. As a large common mode variation across the sensor was observed, the algorithm calculates the common mode on a per row basis.

If pixels containing "real" signals would be included in the calculation of the common mode, the value for the common mode noise would be too high. Thus pixels with a value 3 times higher than the noise are excluded from the common mode calculation.

To correct for the common mode noise, the average of the pixels of a row with values within this 3σ corridor is computed and then subtracted from all pixels in this row. This is done for all rows in the data frame.

$$CM_{xy} = \frac{1}{n} \sum_{y=1}^{y_{max}} \left[\left(Frame_{xy} - Pedestals_{xy}\right)_y \overset{!}{<} 3 \cdot Noise_{xy} \right] \tag{D.6}$$

With n = number of pixels in the row with values < 3 times the noise.

D.1.4 Bad Pixel Masking

For the computation of the initial and the updated bad pixel mask the same algorithm is used, as it is a simple and fast calculation, that simply compares the noise of a pixel to two thresholds. The lower threshold is 0, a pixel with no noise at all is regarded as "dead". The upper threshold is a cut on pixels too noisy. This is required as such pixels would spoil the energy resolution of the system.

$$BPM_{xy} = \begin{cases} 1 & 0 < Noise_{xy} \leq Threshold \\ 0 & 0 \geq Noise_{xy} \quad \vee \quad Noise_{xy} > Threshold \end{cases} \tag{D.7}$$

D.1.5 Cluster Search

The algorithm for the cluster search is divided into two parts. In the first segment the so-called seed pixel is searched and compared to a threshold, in the second a sub-matrix around the seed pixel is compared to the corresponding threshold. Once a cluster has been identified and passed both criteria, it is masked and the algorithm loops once more on the data frame.

- seed pixel:
  To find the seed pixel the array is searched for the pixel with the highest signal to noise ratio. If the pixel found has a ratio larger than the specified threshold value, the algorithm goes to the next step, the cluster analysis. If the pixel is below the threshold, there are no more seed pixels in this frame and the cluster search on the current frame is terminated.

$$Data_{xy}/Noise_{xy} \overset{?}{>} 1^{st}\ cut \tag{D.8}$$

- cluster:
  If the seed pixel has passed the first criterium, the algorithm checks if the cluster around the seed pixel passes also the second criterium, the cut on the signal to noise of the sub-matrix around the seed pixel.

  In this comparison the signal is defined as the sum of the value of all the pixels in the sub-matrix, while the noise is defined as the Root-Mean-Square (RMS) of the noise of the individual pixels in the sub-matrix.

  The size of the sub-matrix around the seed pixel can be set to 3×3, 5×5 and so on.

$$\sum_{x,y=1}^{x,y=max} Data_{xy} \overset{?}{>} 2^{nd}\ cut \times \sqrt{\sum_{x,y=1}^{x,y=max} Noise_{xy}^2} \tag{D.9}$$

- hit limit:
  As a too high number of hits in one frame could lead to an overlapping of the individual hits and thus a wrong value for the height of the cluster signal, a limit can be set on the maximum number of clusters per frame. If more clusters are found in the frame, the current frame is skipped, its results omitted and the next frame is acquired and processed. This also removes issues with “hot” frames.

D.2 Mathematica

The analysis of the data taken during the radiation hardness studies on the SUCCESSOR-I chip was done using a Mathematica 5 script written by Michael Deveaux [Dev03]. It uses basically the same algorithms as the LabView software, but there are some small differences.

- **Leakage Current I:** In principle the leakage current of the pixels can be derived from the pedestals, but for non-irradiated chips and high read out frequencies the values can be in the order of the resolution of the ADC.

  To increase the integration time by a factor of 6, and to check the time constant of the discharging, this method uses 8 consecutive frames between two resets. The first frame after the reset is discarded to allow for settling effects, from the other 7 the difference between frame #2 and frame #n is calculated.

$$CDS_i = Frame_n - Frame_2 \qquad \text{with} \quad n \in \{2..8\} \tag{D.10}$$

One measurement run consists of 500 such 8-frame sets. The first 40 of these sets were not used for the analysis, as the chip has a rather high common mode noise after starting the clock. From the other sets the mean value is computed for each CDS sample separately for each pixel.

$$M_i = \frac{1}{r_{max}} \sum_{r=r_{min}}^{r_{max}} CDS_{ir} \qquad \text{with} \quad r \in \{40..500\} \tag{D.11}$$

To these 6 data points of each of the pixels a linear fit is made, in which the slope S corresponds to the leakage current. These are then averaged over all pixels. The mean value is used for the leakage current and the deviation for the error, as the pixel to pixel spread is much larger than the error of the linear fit.

$$LC = B + S \cdot i \tag{D.12}$$

$$I_{leak} = \left(\overline{S} \pm \sigma_S\right) \cdot \frac{\nu \cdot q}{A \cdot N} \tag{D.13}$$

With ν = read out frequency, $q = e^- = 1.6 \times 10^{-19} C$, N = number of pixels (including marker pixels) = 2112 and A = calibration of the ADC.

The calibration of the ADC is derived from the position of the small peak in the ^{55}Fe spectrum as this corresponds to a well known amount of charge, that is generated in the sensor.

$$A = \frac{small\ peak\ position\ [ADC]}{E_\gamma / E_{generation}} \tag{D.14}$$

^{55}Fe has two characteristic lines, one at $5.89\,keV$ with a branching ratio of 24.4%, the other at $6.49\,keV$ (3.40%). For the calibration of the devices the $5.89\,keV$ gammas were used. The energy required to generate a electron-hole pair in silicon is $3.6\,eV$.

- **Leakage Current II:** After acquiring $n_{max} = 10000$ CDS frames without a source on the sensor, the average of these is computed for each pixel.

$$M_{xy} = \frac{1}{n_{max}} \sum_{n=1}^{n_{max}} Frame_{xy} \tag{D.15}$$

To the distribution of these values M_{xy} a Gaussian is fit. The following equation is used to calculate the leakage current in Ampere from the value of the centre of the Gaussian.

$$I_{leak} = (C) \cdot \frac{\nu \cdot q}{A \cdot N} \tag{D.16}$$

With C = Centre of the Gaussian, ν = read out frequency, $q = e^- = 1.6 \times 10^{-19} C$, N = number of pixels (including marker pixels) = 2112 and A = calibration of the ADC, see above.

The error of the value of the leakage current is given by the width of the Gaussian, as the error is dominated by the pixel to pixel variation and not by the fluctuation of the pixel value itself.

$$I = \overline{I} \pm t \cdot \frac{\sigma_{gauss}}{n} \tag{D.17}$$

Where $\overline{I}$ is the mean value for the measurement, σ_{gauss} the width of the distribution, n the number of pixels in a sub-matrix ($= 32 \times 32 = 1024$) and t the value of the Student function for a given n and given confidence level. During the evaluation of the measurements a conservative approach was used and for a confidence level of 95.8% the value of the student function was assumed to be $t = 2$.

- ^{55}**Fe -spectra:** Like in the LabView VI the algorithm searching for clusters in the data is segmented into different parts. The first part calculates the initial pedestals and noise, the second the common mode noise, the third the pedestals and noise corrected for common mode, the fourth part looks for hits and the fifth part updates the pedestals and noise. In the final part the histograms for the seed pixel and the various cluster sizes are updated.

  – Initial Pedestals & Noise: At the start of the algorithm 20 samples with 5 CDS frames each are read. From each sample the maximum value of each pixel is removed. This is done to remove any hits from the data, as they would lead to wrong values for the pedestals and the noise. After this the data is combined into one array.
  From this array one computes the pedestals:

$$Pedestals_{xy}^{init} = \frac{1}{n_{max}} \sum_{n=1}^{n_{max}} Data_{xy} \tag{D.18}$$

  and the noise:

$$Noise_{xy}^{init} = \sqrt{\frac{1}{n_{max}} \sum_{n=1}^{n_{max}} \left(Data_{xy} - Pedestals_{xy}^{init}\right)^2} \tag{D.19}$$

  with n_{max} = number of frames in the combined array $Data_{xy}$.

  – Common Mode Noise: In the common mode noise correction disturbances affecting many pixels in a frame are compensated. In a first step the pedestals are subtracted from the CDS frame.

$$F_{xy} = Frame_{xy} - Pedestals_{xy}^{init} \tag{D.20}$$

  As hits in the data would lead to wrong values for the common mode they have to be omitted from the further calculation. This is done by applying a cut on the signal to noise ratio (SNR).

$$K_{xy} = \begin{cases} F_{xy} & \text{if } F_{xy} < k \cdot Noise_{xy}^{init} \\ 0 & \text{if } F_{xy} \geq k \cdot Noise_{xy}^{init} \end{cases} \tag{D.21}$$

  In this case k was set to 5.
  If the algorithm finds too many pixels with signals above the threshold, the frame is not processed further, as there is a high probability that the data taking was disturbed.
  The common mode CM_y is then calculated on a per row basis as the average of the values K_{xy} in this row and subtracted from all pixels in this row.

$$D_{xy} = F_{xy} - CM_y^{init} \qquad \text{with} \quad CM_y^{init} = \frac{1}{y_{max}} \sum_{y=1}^{y_{max}} K_{xy} \tag{D.22}$$

  – Pedestals & Noise: To increase the precision of the pedestals and the noise both are reiterated after applying the common mode correction to the data set.

$$D_{xy} = Frame_{xy} - CM_y^{init} - Pedestals_{xy}^{init} \tag{D.23}$$

  Frames with a too high common mode are excluded from the further calculation. If there are too many frames failing this criteria, the computation is aborted.
  To this data set again a threshold ($k = 5$) on the SNR is applied to remove any possible hits, that might have been masked by a high common mode, from the calculation of the pedestals and the noise.

$$K_{xy} = \begin{cases} D_{xy} & D_{xy} < k \cdot Noise_{xy}^{init} \\ 0 & D_{xy} \geq k \cdot Noise_{xy}^{init} \end{cases} \tag{D.24}$$

The "new" pedestals and noise can be calculated as:

$$Pedestals_{xy} = Pedestals_{xy}^{init} + P_{xy} \qquad \text{with} \quad P_{xy} = \frac{1}{n_{max}} \sum_{n=1}^{n_{max}} D_{xy} \tag{D.25}$$

$$Noise_{xy} = \sqrt{\frac{1}{n_{max}} \sum_{n=1}^{n_{max}} (D_{xy} - P_{xy})^2} \tag{D.26}$$

With n_{max} = number of frames taken into account for the calculation.

– Cluster Search: When looking for hits in the data, one has first to remove the pedestals and the common mode noise from the acquired data.

$$S_{xy} = Frame_{xy} - Pedestals_{xy} - CM_y \tag{D.27}$$

where CM_y is the common mode calculated using $Pedestals_{xy}$ and $Noise_{xy}$.
For possible seed pixels it is required that

$$S_{xy}/Noise_{xy} \overset{!}{>} c_{seed} \qquad \text{with} \quad c_{seed} = 5 \tag{D.28}$$

Additionally, the seed pixel, the pixel with the highest SNR in the cluster, has to be 2 or more pixels away from the edge of the chip, as the cluster size is 5×5 pixels, with the seed pixel at the centre, and all clusters have to be complete for further processing.
In case of overlapping clusters only the one with the higher SNR is used in the further computation, the weaker one is masked. This is done by sorting the clusters found according to their SNR and starting the further processing from the cluster with the highest SNR, always keeping the addresses of the previous hits in memory and checking for possible overlays.
To the remaining clusters a second cut is applied. The summed signal of the 3×3 matrix around the seed pixel has to be 3 times larger than the Root-Mean-Square (RMS) noise of the matrix.

$$\sum_{i,j=-1}^{1} S_{x+i,y+i} \overset{!}{>} c_{cluster} \cdot \sqrt{\sum_{i,j=-1}^{1} (Noise_{x+i,y+i})^2} \tag{D.29}$$

with x,y= coordinates of the seed pixel and $c_{cluster} = 3$.

– Updated Pedestals & Noise: As the pedestals and the noise of the sensor are not constant over time, both, pedestals and noise, are updated after each frame.
In the first iteration two intermediate arrays are filled

$${}^1I_{xy} = \begin{cases} Pedestals_{xy} & \text{if } x,y \text{ inside a cluster} \\ Frame_{xy} - CM_y & \text{else} \end{cases} \tag{D.30}$$

$${}^2I_{xy} = \begin{cases} Noise_{xy} & \text{if } x,y \text{ inside a cluster} \\ Frame_{xy} - Pedestals_{xy} - CM_y & \text{else} \end{cases} \tag{D.31}$$

Using these arrays, the updated pedestals and noise can be calculated.

$$Pedestals_{xy}^{new} = \frac{1}{n}\left[(n-1) \cdot Pedestals_{xy} + {}^1I_{xy}\right] \tag{D.32}$$

$$Noise_{xy}^{new} = \sqrt{\frac{1}{n}\left[(n-1) \cdot (Noise_{xy})^2 + ({}^2I_{xy})^2\right]} \tag{D.33}$$

where n is the number of frames that should be included in the pedestal and noise calculation.

- Histograms: At the end of the analysis the following histograms presenting the data are built:
  - Seed Pixel Spectrum: For each cluster the value of the pixel with the highest SNR is entered into this histogram. This is done for all frames from the run.
  - Cluster Spectra: To build the cluster spectra, the values of the pixels in one cluster are first sorted according to their height, and then a certain number of pixels is summed. These sums are calculated for a number of pixels included from 2 to 25 and then entered into the corresponding histograms. This is done for all clusters passing the two criteria from all frames. The histograms used for the radiation hardness studies are the 9 and the 25 pixel histograms, which correspond, in most cases, to a 3×3 and a 5×5 matrix around the seed pixel.
  - Pedestal Distribution: Two histograms are built from the pedestal data. One from the initial computation and one from the last updated pedestals. This allows to check for time dependent phenomena or temperature drifts of the sensor.
  - Noise Distribution: Also for the noise two histograms are generated. Again, one from the initial calculation and one from the last updated noise. There, the same motivation as for the pedestals comes into play.

As the Mathematica script has to be run in the interpreter mode of Mathematica and cannot be compiled, due to the different commands in the two modes, the analysis has serious issues with performance and memory usage. A port of the script to ROOT was written by Götz Gaycken, but the code was not verified before the end of this thesis and thus not used for the data presented here.

Appendix E

Measurement Results SUCCESSOR-I

E.1 SUCCESSOR-I – Pixel 0

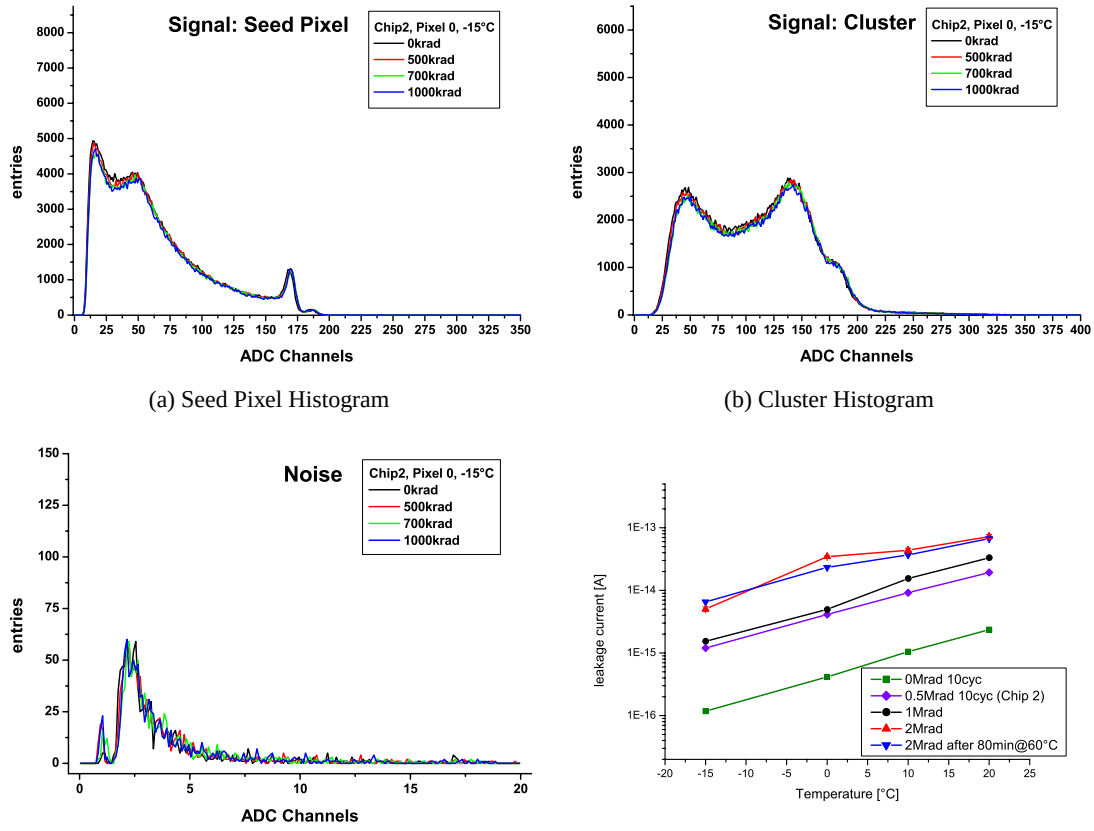

(a) Seed Pixel Histogram

(b) Cluster Histogram

(c) Noise Histogram

(d) Leakage Current

Figure E.1: *Measurement results for Pixel 0. (a) shows the seed pixel spectra of an ^{55}Fe source acquired at $T = -15\,℃$ with an read out frequency of $2.5\,MHz$ for different doses. In (b) the corresponding cluster spectrum is depicted, in (c) the noise spectrum. The leakage current of pixel 0 is shown as a function of the temperature for different doses in (d).*

E.2 SUCCESSOR-I – Pixel 1

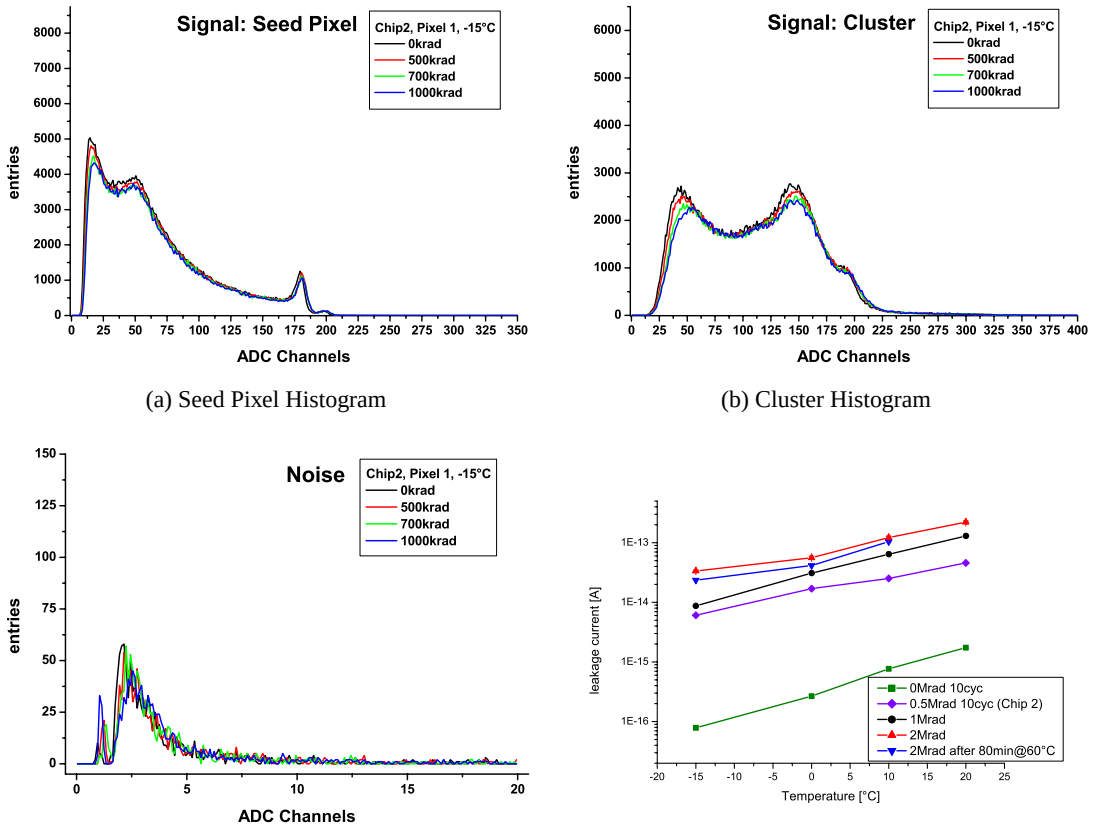

(a) Seed Pixel Histogram

(b) Cluster Histogram

(c) Noise Histogram

(d) Leakage Current

Figure E.2: *Measurement results for Pixel 1. (a) shows the seed pixel spectra of an ^{55}Fe source acquired at $T = -15\,°C$ with an read out frequency of $2.5\,MHz$ for different doses. In (b) the corresponding cluster spectrum is depicted, in (c) the noise spectrum. The leakage current of pixel 1 is shown as a function of the temperature for different doses in (d).*

E.3 SUCCESSOR-I – Pixel 2

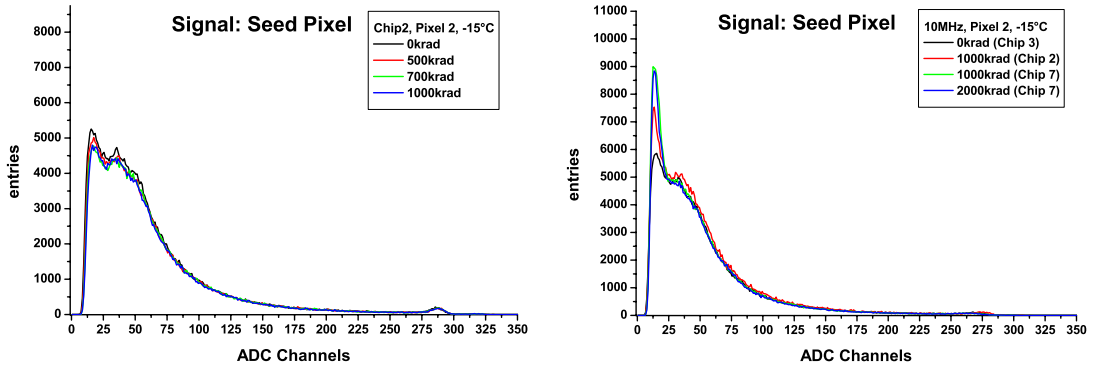

(a) Seed Pixel, $2.5\,MHz$

(b) Seed Pixel, $10\,MHz$

Figure E.3: *Measurement results for Pixel 2. (a) shows the seed pixel spectra of an ^{55}Fe source acquired at $T = -15\,°C$ with an read out frequency of $2.5\,MHz$ for different doses. In (b) the seed pixel spectra are shown for $10\,MHz$.*

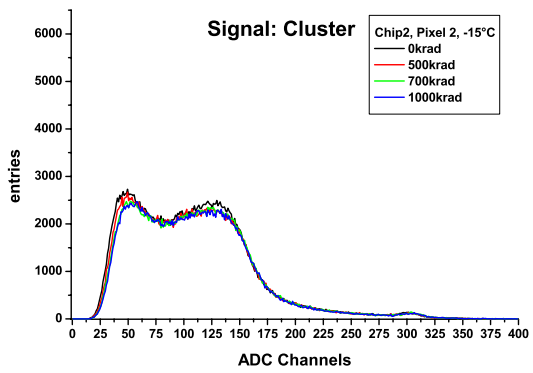

(a) Cluster Histogram, 2.5 *MHz*

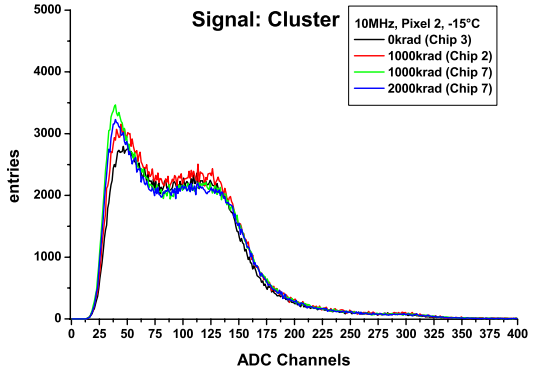

(b) Cluster Histogram, 10 *MHz*

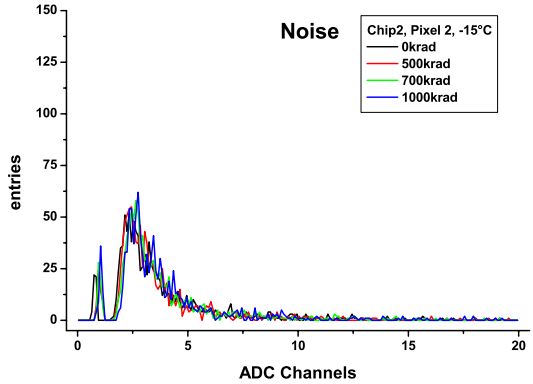

(c) Noise Histogram, 2.5 *MHz*

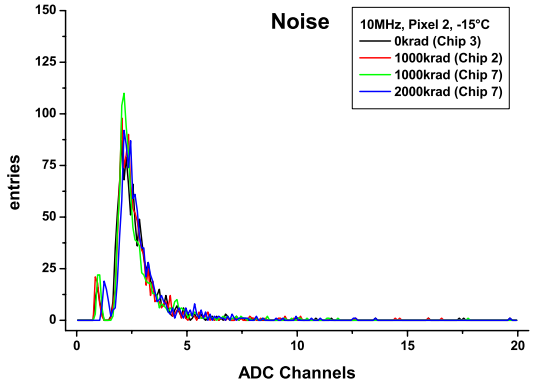

(d) Noise Histogram, 10 *MHz*

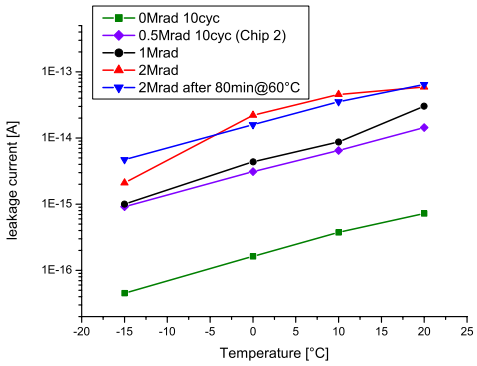

(e) Leakage Current

Figure E.4: *Measurement results for Pixel 2. (a) shows the cluster spectra of an* ^{55}Fe *source acquired at* $T = -15\,°C$ *with an read out frequency of* 2.5 *MHz for different doses. In (b) the cluster spectra are shown for* 10 *MHz. The noise spectra are depicted in (c) and (d). (e) shows The leakage current of pixel 2 as a function of the temperature for different doses.*

E.4 SUCCESSOR-I – Pixel 5

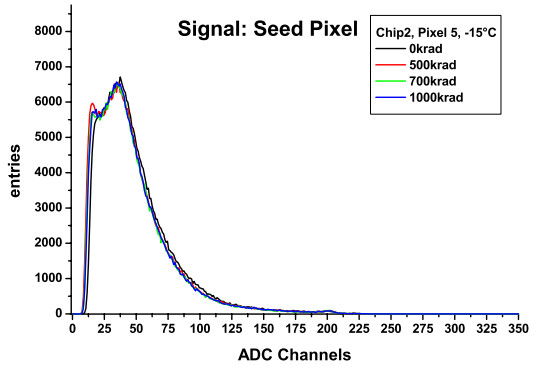

(a) Seed Pixel, 2.5 *MHz*

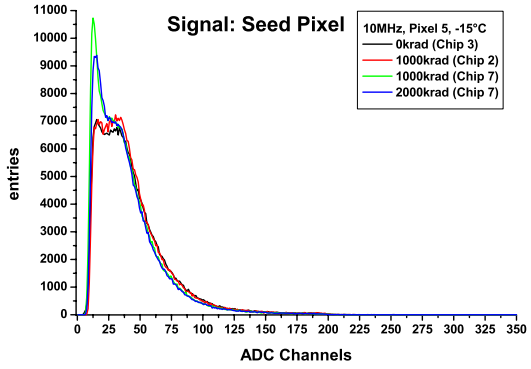

(b) Seed Pixel, 10 *MHz*

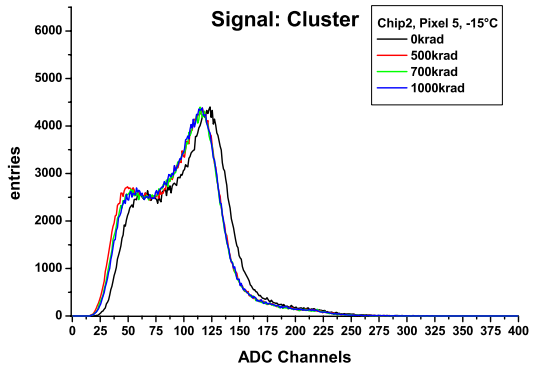

(c) Cluster Histogram, 2.5 *MHz*

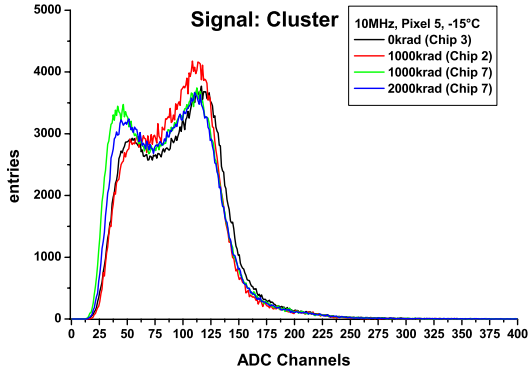

(d) Cluster Histogram, 10 *MHz*

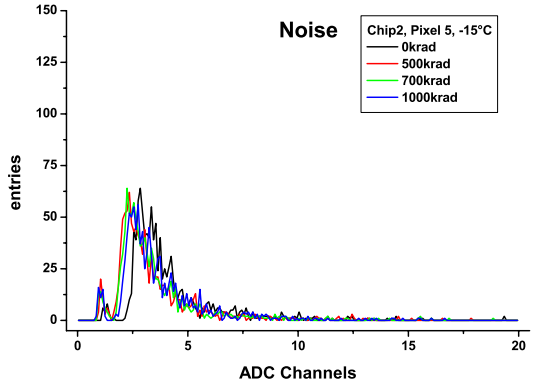

(e) Noise Histogram, 2.5 *MHz*

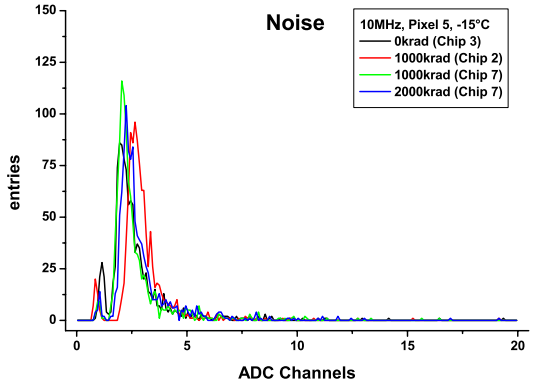

(f) Noise Histogram, 10 *MHz*

Figure E.5: *Measurement results for Pixel 2. (a) shows the seed pixel spectra of an* ^{55}*Fe source acquired at* $T = -15\,℃$ *with an read out frequency of* 2.5 *MHz for different doses. In (b) the seed pixel spectra are shown for* 10 *MHz. (c) shows the cluster spectra of an* ^{55}*Fe source acquired at* $T = -15\,℃$ *with an read out frequency of* 2.5 *MHz for different doses. In (d) the cluster spectra are shown for* 10 *MHz. The noise spectra are depicted in (e) and (f).*

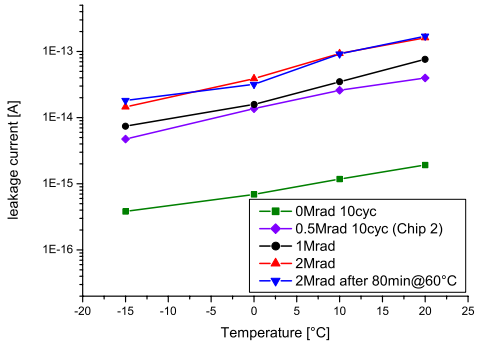

Figure E.6: *Measurement results for Pixel 5. The leakage current of pixel 5 is plotted as a function of the temperature for different doses.*

E.5 SUCCESSOR-I – Pixel 6

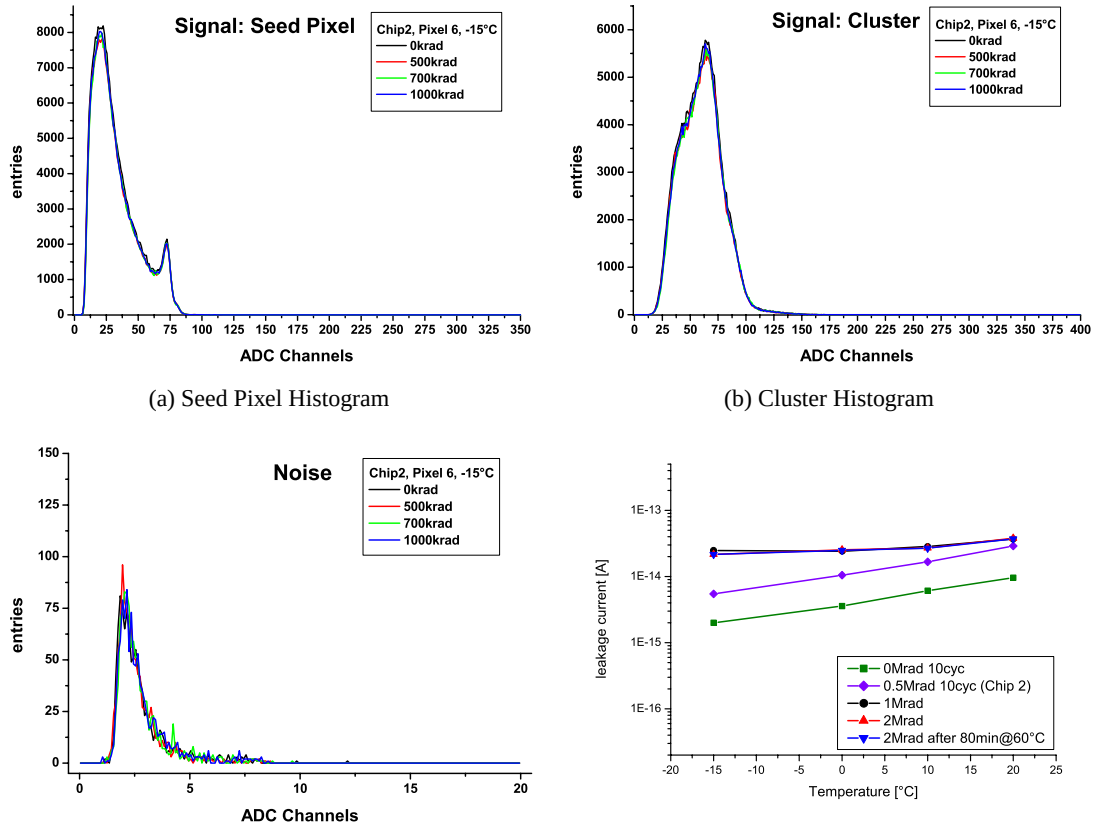

(a) Seed Pixel Histogram

(b) Cluster Histogram

(c) Noise Histogram

(d) Leakage Current

Figure E.7: *Measurement results for Pixel 6. (a) shows the seed pixel spectra of an ^{55}Fe source acquired at $T = -15\,°C$ with an read out frequency of $2.5\,MHz$ for different doses. In (b) the corresponding cluster spectrum is depicted, in (c) the noise spectrum. The leakage current of pixel 6 is shown as a function of the temperature for different doses in (d).*

E.6 SUCCESSOR-I – Pixel 7

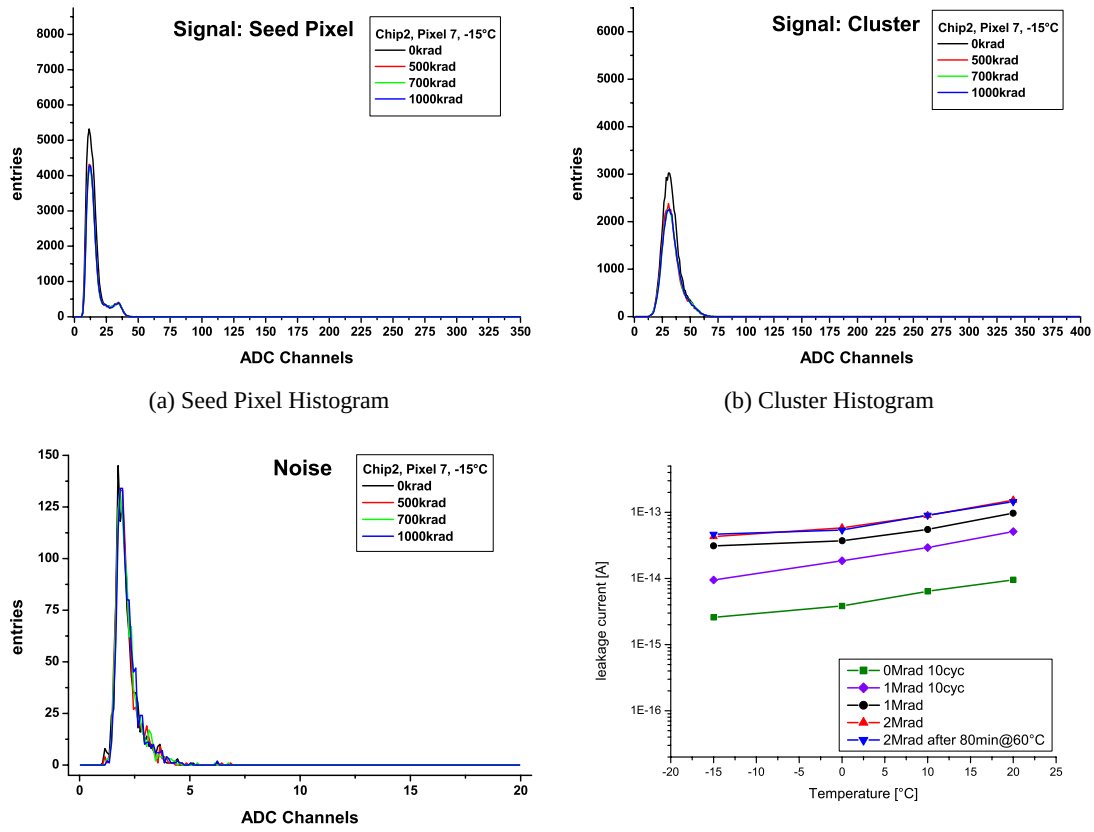

(a) Seed Pixel Histogram

(b) Cluster Histogram

(c) Noise Histogram

(d) Leakage Current

Figure E.8: *Measurement results for Pixel 7. (a) shows the seed pixel spectra of an* ^{55}Fe *source acquired at* $T = -15\,^{\circ}C$ *with an read out frequency of* $2.5\,MHz$ *for different doses. In (b) the corresponding cluster spectrum is depicted, in (c) the noise spectrum. The leakage current of pixel 7 is shown as a function of the temperature for different doses in (d).*

Acknowledgements

The broad spectrum of this thesis, covering different technologies and methods, would not have been possible without the support of my supervisors and my colleagues and the plentiful discussions with them. At this time I would like to thank all of them.
I would like to thank Prof. Wim de Boer for the great possibility he offered me with this PhD thesis, his scientific input and his support for my ideas together with his complete trust in my capabilities.
Prof. Thomas Müller honoured me with accepting the co-reference and supporting my work.
For the fruitful discussions on many topics I would like to thank the colleagues in my group. In alphabetical order: Johannes Bol, Alexander Dierlamm, Alexander Furgeri, Eugene Grigoriev, Florian Hauler, Michael Koppenhöfer & Mike Schmanau. They also contributed to the preparation and implementation of many measurements.
For her help with the construction of electronics I would like to thank Pia Steck. I am very grateful to Tobias Barvich, without his help many ideas for mechanics would never have been made real. He also acted as an interface to our great mechanical workshop.
A very special thanks goes to our administrative group: Diana Fellner-Thedens, Sven Fuchs and Edeltraud Haas. Without their support many things would not have been possible.
For his help with the day to day IT issues, and some more exotic ones, I would like to thank Hans-Jürgen Simonis.
This is also the moment to thank all the people, who were proof-reading this thesis: Jutta Bol, Frank Hartmann, Stephan Heising, Bernhard Ledermann, Jens Rehn, Marcel Stanitzki and Julia Walther.
Last but not least I'm indebted to my girlfriend Julia, my friends and of course my family for their great support during the last years.

This PhD thesis was supported by the European Community within the V (Growth) Framework. SUCIMA project – Contract no. G1RD-CT-2001-00561.

List of Figures

List of Tables

Bibliography

[Act01] ACTEL CORPORATION: *Actel A54SX32A Datasheet*. v3.0, Jun 2001

[Act02] ACTEL CORPORATION: *Actel HDL Coding Style Guide*, Jun 2002

[Ago03] AGOSTINELLI ET AL., S.: Geant4 - a simulation toolkit. In: *Nuclear Instruments and Methods in Physics Research A* 506 (2003), S. 250–303

[Agu02] AGUILAR ET AL., M.: The Alpha Magnetic Spectrometer (AMS) on the International Space Station: Part I - results from the test flight on the space shuttle. In: *Physics Reports* 366 (2002), Nr. 6, S. 331–405

[Alc99] ALCARAZ ET AL., J.: Search for Antihelium in Cosmic Rays. In: *Phys. Lett.* B (1999), Nr. 461, S. 387–396

[Ali80] ALIG, S. BLOOM AND C.W. STRUCK, R.C.: Scattering by Ionization and Phonon Emission in Semiconductors. In: *Phys. Rev. B* 22 (1980), Nr. 12, S. 5565–5582

[Alt05] ALTERA CORPORATION: *APEX 20K Device Family Architecture*, 2005. – http://www.altera.com/products/devices/apex/features/apx-architecture.html

[Ama93] AMALDI AND B. LARSSON, U.: Hadrontherapy in oncology. In: *Excerpta Medica, Elsevier International Congress Series* 1077 (1993), Oct

[Ama95] AMALDI AND M. SILARI EDITORS, U.: *The TERA Project And The Center For Oncological Hadrontherapy*. 2nd. P.O. Box 13, I-00044 Frascati (Roma) Italy : INFN - LFN Divisione Ricerca, 1995. – ISBN: 88-86409-09-5

[AMS05] AMS COLLABORATION, The: AMS on ISS Construction of a particle physics detector on the International Space Station. In: *Nuclear Instruments and Methods A* (2005), Nr. submitted

[Ane00] ANELLI, Giovanni M.: *Design and characterization of radiation tolerant integrated circuits in deep submicron CMOS technologies for the LHC experiments*, Institut National Polytechnique de Grenoble, Diss., Dec 2000

[Ash02] ASHENDEN, Peter J.: *The designer's guide to VHDL 2nd edition*. Morgan Kaufmann Publishers, 2002

[Bat99] BATTISTON, Roberto: Search for antimatter in space with the Alpha Magnetic Spectrometer. In: *astro-ph* (1999), 07, Nr. 9907152

[Bea04] BEATTY ET AL., J.J.: New Measurement of the Cosmic-Ray Positron Fraction from 5 to 15 GeV. In: *Phys.Rev.Lett.* 93 (2004), S. 241102

[Ben03] BENNETT ET AL., C. L.: First Year Wilkinson Microwave Anisotropy Probe (WMAP) Observations: Preliminary Maps and Basic Results. In: *Astrophys.J.Suppl.* 148 (2003), Nr. 1

[Boe04] BOER, W. de: Indirect Evidence for WIMP Annihilation from Diffuse Galactic Gamma Rays. In: *arXiv:astro-ph* v1 (2004), Dec, Nr. 0412620. – Invited paper at DARK2004, Texas, 3-9 October, 2004

[Bos91] BOSCH: *CAN Specification*. ver. 2.0, 1991

[Bow99] BOWER ET AL., C.R.: The HEAT-pbar Cosmic Ray Antiproton Experiment. In: *ICRC* OG.4.1.04 (1999)

[Boy70] BOYLE AND G.E. SMITH, W.S.: Charge coupled semiconductor devices. In: *Bell Syst. Tech. J.* 49 (1970), Apr, Nr. 4, S. 587–593

[Bro61] BRONSHTEIN AND B.S. FRAIMAN, I.M.: Determining the path lengths of slow secondary electrons. In: *Sov. Phys. Sol. Stat.* 3 (1961), S. 1188–1197

[Bro92] BROEILS, A. H.: The mass distribution of the dwarf spiral NGC 1560. In: *Astronomy and Astrophysics* 256 (1992), Mar, Nr. 1, S. 19–32. – ISSN 0004-6361

[Brü02] BRÜCKEL, Martin: *The Transition Radiation Detector of the AMS-02 Experiment - Development and Tests of Read-out Electronics*, Institut für Experimentelle Kernphysik, Universität Karlsruhe, Diplomarbeit, 2002

[CAE03a] CAEN: *Technical Information Manual MOD. S9048 - $\pm$2.6V DC/DC CONVERTER*. rev. 1, May 2003

[CAE03b] CAEN: *Technical Information Manual MOD. S9054 - $+$5.6V DUAL DC/DC CONVERTER*. rev. 0, Jun 2003

[CAE03c] CAEN: *Technical Information Manual MOD. S9056 - $+$3.4V DUAL DC/DC CONVERTER*. rev. 0, Apr 2003

[CAE03d] CAEN: *Technical Information Manual MOD. S9056 - $+5/+120$V DUAL DC/DC CONVERTER*. rev. 0, Sep 2003

[CAE04] CAEN: *Technical Information Manual Mod. S9011 - AMS02 TPD Electronics & Filter*. rev. 1, Mar 2004

[Cam01] CAMPS, V. COMMICHAU, K. HANGARTER, C.: *USCM3CON two slot USCM300 Motherboard*. version 1.1, Oct 2001

[Cam03] CAMPS V. COMMICHAU K. HANGARTER, C.: *Universal Slow Control Module USCM V03/S3b for AMS-II*. 2003

[Cap05] CAPPELLINI, Chiara: *Dosimetry Measurements Of Radioactive Sources For Medical Applications Using A Large Area Silicon Strip Detector*, Universita degli Studi dell'Insubria, Como, Italy, Diss., Jan 2005

[CHA] CHANDRA COLLABORATION: *CHANDRA website*

[Cha99] CHANG, K.C.: *Digital Systems Design with VHDL and Synthesis*. IEEE Computer Society, 1999

[Cho98] CHOCHULA ET AL., P.: The DELPHI Silicon Tracker at LEP2. In: *Nucl. Instrum. Methods* A (1998), Nr. 412, S. 304–328

[Coc32] COCKCROFT AND E.T.S. WALTON, J.D.: Experiments with High Velocity Positive Ions. In: *Proceedings of the Royal Society of London* A (1932), Nr. 137, S. 229–242. – ; A136 (1932) 619

[Cod03] CODE MERCENARIES: *IO-Warrior - Generic universal I/O Controller*, Feb 2003

[Col00] COLLINS ET AL., Paula: Charge Collection Efficiency and Resolution of an Irradiated Double Sided Silicon Microstrip Detector Operated at Cryogenic Temperatures. In: *Nuclear Instruments and Methods A* 440 (2000), Nr. 1, S. 17–37

[Com00] COMPAQ ET AL.: *Universal Serial Bus Specification Rev. 2.0*, Apr 2000

[Cro97] CRONIN, T.K. GAISSER, AND S.P. SWORDY, J.: Cosmic Rays at the Energy Frontier. In: *Scientific American* 276 (1997), S. 44

[Cyp02] CYPRESS: *CY7C68013 EZ-USB FX2 USB Microcontroller High-speed USB Peripheral Controller*. C, Dec 2002

[Cze01] CZERMAK ET AL., A.: Data Acquisition System for Silicon Ultra Fast Cameras. In: *Proc. 7th International Conference on Advanced Technology and Particle Physics* (2001), Oct

[Dal00] DALLAS SEMICONDUCTOR - MAXIM: *Current-Limit Switch Is Digitally Programmable (Application note for MAX890L)*, Mar 2000

[Dam81] DAMERELL ET AL., C.J.S.: Charge-coupled devices for particle detection with high spatial resolution. In: *Nucl. Inst. and Meth.* 185 (1981), S. 33

[Dep02] DEPTUCH, Gregorz: *New Generation of Monolithic Active Pixel Sensors for Charged Particle Detection*, Universite Louis Pasteur Strassbourg - University of Mining and Metallurgy Cracow, Diss., 2002

[Dep03a] DEPTUCH ET AL., G.: Development of monolithic active pixel sensors for charged particle tracking. In: *Nuclear Instruments and Methods in Physics Research A* (2003), Nr. 511, S. 240 – 249

[Dep03b] DEPTUCH ET AL., G.: Monolithic Active Pixel Sensor for Dosimetry Application. In: *Proceedings of the 33rd European Solid-State Device Research Conference*, 2003

[Dep04] DEPTUCH ET AL., G.: Tritium Autoradiography with Thinned and Back-Side Illuminated Monolithic Active Pixel Sensor Device. In: *Submitted to Computer Physics Communications* (2004)

[Dev03] DEVEAUX, Michael: *Untersuchungen zur Strahlenhärte von Monolithic Active Pixel Sensoren*, Universität Kaiserslautern, Fachbereich Physik, Diplomarbeit, Feb 2003

[Die03] DIERLAMM, Alexander: *Studies on the Radiation Hardness of Silicon Sensors*, Universität Karlsruhe, Diss., 2003

[Dul04] DULINSKI ET AL., W.: Tests of a backside illuminated monolithic CMOS pixel sensor in an HPD set-up. In: *Submitted to Computer Physics Communications* (2004)

[Dur93] DURIEU, EDITED BY D.J. SIMON, revised by L.: Secondary Beams for Tests in the PS East Experimental Area. In: *CERN PS/PA-EP Note* (1993), 8, Nr. 88-26, 93-21

[ECS03] ECSS: *ECSS-E-50-12A SpaceWire - Links, nodes, routers and networks*, Jan 2003

[Egg04] EGGERT, Rawi: *Development of a Fuse-Test Backplane for a Multi-Channel Power Supply (UPSFE) within the AMS Project*, Berufsakademie Karlsruhe, Diplomarbeit, 2004

[Ego00] EGORYTCHEV ET AL., V.: Particle identification via transition radiation and detectors. In: *Nuclear Instruments and Methods in Physics Research A* 453 (2000), S. 346–352

[Eid04] EIDELMAN ET AL., S.: *Review of Particle Physics*. Bd. 592. 2004. – 1+ S. – website: http://pdg.lbl.gov

[Erb99] ERBACHER, Thomas: *Alterungsstudien an Mikrostreifen-Gasdetektoren*. IEKP-KA/99-17, Institut für Experimentelle Kernphysik, Universität Karlsruhe (TH), Diplomarbeit, 1999

[Eri99] ERICKSON, Robert W.: Optimal Single Resistor Damping of Input Filters. In: *IEEE Applied Power Electronics Conference* (1999)

[ESA] ESA: *XMM-Newton website*

[Fer03] FERRANDO ET AL., O.: SLIM (Sem for Low Interception Monitoring) - An innovative non-destructive beam monitor for the extraction lines of a hadrontherapy centre. In: *presented at the IEEE-NSS 2003* (2003)

[Fra94] FRASER ET AL., G.W.: The X-Ray Energy Response of Silicon. In: *Nucl. Instr. and Meth. A* 350 (1994), S. 368–378

[Gar57] GARIBIAN, G. M.: Radiation of a particle moving across the interface of two media with account of multiple scattering. In: *Zh. Eksp. Teor. Fiz.* 33 (1957), S. 1403. – Translation: Soviet Physics JETP 6, 1079 (1958)

[Gin45] GINZBURG AND I.M. FRANK, V.L.: Radiation of a uniform moving electron due to its transition from one medium into another. In: *J. Phys.* 9 (1945), S. 353–362

[Goy02] GOY, Corinne: *Dark matter search potential with AMS02*. 2002

[Gro00] GROOM ET AL., D.E.: *Review of Particle Physics*. Springer Verlag, 2000. – 1–878 S

[Gru00] GRUPEN, Claus: *Astroteilchenphysik - Das Universum im Licht der kosmischen Strahlung*. Braunschweig, Wiesbaden : Vieweg Verlag, 2000. – ISBN: 3-528-03158-1

[GSI] GSI DARMSTADT: Carbon Ion Radiotherapy @ GSI / Treatment planning. In: *http://www-aix.gsi.de/~bio/RESEARCH/therapytpdev.html*

[Hau05] HAULER, Florian: *Space Qualified Electronics for the AMS-02 TRD Detector*, Institut für Experimentelle Kernphysik, Universität Karlsruhe (TH), Diss., 2005

[Hes12] HESS, V.F.: Über Beobachtungen der durchdringenden Strahlung bei sieben Freiballonfahrten. In: *Phys. Zeit.* 13 (1912), S. 1084

[IDE00] IDEAS ASA, NORWAY: *VA32-HDR12 specifications*. 1.0, 12 2000

[IEE95] IEEE STD. 1355: *Standard for Heterogeneous Inter-Connect (HIC). Low Cost, Low Latency, Scalable Serial Interconnect for Parallel System Construction*, 1995

[Isr04] ISRAEL, Martin H.: Isotopic Composition of Cosmic Rays. In: *19th European Cosmic Ray Symposium* (2004)

[Jac98] JACKSON, John D.: *Classical Electrodynamics*. 3rd. Wiley, 1998. – ISBN: 047130932X

[Jun02] JUNGERMANN ET AL., L.: Measurements with a CMOS pixel sensor in magnetic fields. In: *Nucl. Instr. and Meth.* A (2002), Nr. 487, S. 163–169

[Kem87] KEMMER AND G. LUTZ, J.: New semiconductor detector concepts. In: *Nucl. Instr. and Meth.* A (1987), Nr. 253, S. 365

[Kir02] KIRN, Thomas: AMS TIM and General Meeting - Status of AMS TRD. In: *Johnson Space Center* (2002), Oct

[Kle73] KLEBESADEL; IAN B. STRONG; ROY A. OLSON, Ray W.: Observations of Gamma-Ray Bursts of Cosmic Origin. In: *Astrophysical Journal* 182 (1973), Jun, S. L85–88

[Kra04] KRAMMER, M.: The silicon sensors for the Inner Tracker of the Compact Muon Solenoid experiment. In: *Nucl. Instrum. Methods* A (2004), Nr. 531, S. 238–245

[LeC97] LECROY: *Preliminary Users Manual LeCroy MHV100*, 1997

[Lin02] LIN, X. CAI, C. H.: *AMSWIRE PCI BOARD DESIGN SPECIFICATION*, May 2002

[LIN03] LIN, C.H.: *AMS WIRE - AMS-II DAQ LINK PROTOCOL*. ver. 3.1, Jun 2003

[Lut99] LUTZ, Gerhard: *Semiconductor Radiation Detectors*. Springer-Verlag, 1999 (Device Physics). – ISBN 3-540-64859-3

[Mar03] MARCZEWSKI, J.: SOI Active Pixel Detectors of Ionizing Radiation - Technology & Design Development. In: *Nuclear Science Symposium 2003*, 2003

[Mar04] MARCZEWSKI, J.: *Bulk Silicon Detectors of Ionizing Radiation - The role of the depletion layer*. IET, 2004. – ISBN 83-914179-5-6

[Mey03] MEYER, Carsten: Draht nach draußen - USB-Interfacing mit Custom-Chips. In: *c't* (2003), Aug, S. 204

[NAS] NASA: *Website of the International Space Station*

[Nat03] NATIONAL INSTRUMENTS: *LabView User Manual*. 7.0 & 7.1, Apr 2003. – Part Number 320999E-01

[Pet03] PETER FORTESCUE, JOHN STARK, GRAHAM SWINERD: *Spacecraft Systems Engineering*. 3rd. NewYork, Chichester, Brisbane, Toronto : John Wiley and Sons, 2003 (0-471-61951-5)

[Phi00] PHILIPS SEMICONDUCTORS: *THE I2C-BUS SPECIFICATION*. version 2.1, Jan 2000

[Pir99] PIRAN, Tsvi: Gamma-ray Bursts and the Fireball Model. In: *Physics Reports* 314 (1999), Oct, S. 575–667. – arXiv:satro-ph/9810256 v1 16 Oct 1998

[Sch99] SCHNEIDER, F. HORNUNG, A. RIMIKIS, Th.: High Field Magnet Facilities and Projects at the Forschungszentrum Karlsruhe. (1999)

[Sch01] SCHWERING, Georg: The Transition Radiation Detector of the AMS-2 Experiment. In: *7th International Conference on Advanced Technology and Particle Physics* (2001), Oct

[Sie00] SIEDENBURG, Th.: ISS Orbit Parameters. In: *presented at the AMS02 Technical Interchange Meeting* (2000), Jul

[Sil00] SILL, A.: SVX-II: CDF Run II Silicon Tracking Projects. In: *Nucl. Instrum. Meth.* A (2000), Nr. 447, S. 1–8

[Sim03] SIMON FOR THE PAMELA COLLABORATION, M.: Status of the PAMELA Experiment On-board of the Resurs DK-1 Spacecraft. In: *XXVIII International Cosmic Ray Conference* OG 1.5 (2003), Nr. 2117

[Tav03] TAVANI ET AL., M.: The AGILE Instrument. In: *Proceedings of the SPIE* 4851 (2003), S. 1151–1162

[Tex03] TEXAS INSTRUMENTS: *Suitable LVDS Architectures - Application Report SLLA147*, Sep 2003

[TRA] TRACER COLLABORATION: *TRACER website*

[Tur01] TURCHETTA ET AL., R: A monolithic active pixel sensor for charged particle tracking and imaging using standard VLSI CMOS technology. In: *Nuclear Instruments and Methods in Physics Research* A (2001), Nr. 458, S. 677–689

[Ver01] VERIN ET AL., V.: Endoluminal Beta-Radiation Therapy for the Prevention of Coronary Restenosis after Balloon Angioplasty. In: *New Engl. Jou. Med.* 344 (2001), Jan, S. 243

[Wak04] WAKELYA, S. PLEWNIAB, D. MÜLLER, J.R. HÖRANDEL, F. GAHBAUER, S.P.: Transition radiation detectors for energy measurements at high Lorentz factors. In: *Nuclear Instruments and Methods in Physics Research A* 531 (2004), Apr, S. 435–444

[Wan02] WANG ET AL., J. Z.: Measurement of Cosmic-Ray Hydrogen and Helium and Their Isotopic Composition with the BESS Experiment. In: *The Astrophysical Journal* 564 (2002), 01, Nr. 1, S. 244–259

[Xil04] XILINX: *Virtex-II Platform FPGAs: Complete Data Sheet*. 3.3, Jun 2004

Glossary

A

ACOP AMS Crew Operations Post.

ADC Analog to Digital Converter.

AGILE Astro-rivelatore Gamma a Immagini LEggero.

AMICA Astro Mapper for Instrument Check of Attitude.

AMS Alpha Magnetic Spectrometer.

B

BOX Buried OXide.

C

CAEN Costruzioni Apparecchiature Elettroniche Nucleari spa.

CAN Controller Area Network, μController interconnection standard defined by Bosch AG.

CARSO Center for Advanced Research in Space Optics.

CCD Charge Coupled Device.

CCE Charge Collection Efficiency.

CDDC Command Distributor & Data Concentrator.

CDF the Collider Detector at Fermilab.

CDP Common Digital Part.

CDS Correlated Double Sampling.

CERN Conseil Européen pour la Recherche Nucléaire.

CMOS Complementary Metal Oxide Semiconductor.

CMS Compact Muon Solenoid.

cPCI Compact Peripheral Component Interface.

CSIST Chung-Shan Institute of Science and Technology.

D

DAC Digital to Analog Converter.

DAQ Data Acquisition.

DELPHI DEtector for Lepton, Photon and Hadron Identification.

DEPFET DEpleted P-channel Field Effect Transistor.

DLL Dynamically Linked Library.

DMM Digital Multi Meter.

DSP Digital Signal Processor.

E

ECAL Electromagnetic CALorimeter.

EM Engineering Module.

EMI Electro-Magnetic Interference.

ENC Equivalent input Noise Charge.

ESA European Space Agency.

ESS Environmental Stress Screening.

F

FET Field Effect Transistor.

FIFO First In First Out, a memory architecture.

FLIR Forward-Looking InfraRed.

FM Flight Module.

FPGA Field Programmable Gate Array.

FS Flight Spare module.

G

GCR Galactic Cosmic Rays.

GPIB General Purpose Interface Bus, IEEE 488.1, IEC60625.1, first introduced by Hewlett Packard as HPIB in the late 1960's.

GPS Global Positioning System.

GRB Gamma Ray Burst.

GSE Ground Support Equipment.

GUI Graphical User Interface.

H

HPD Hybrid Photo Detector.

HV High Voltage.

I

I2C IIC, Intra Integrated circuit (-bus), defined by Philips.

IEKP Institut für Experimentelle Kernphysik, Universität Karlsruhe (TH), Germany.

J

J-Crate main computer and interface crate.

JINF J INterFace.

JINFv2 J Interface, version 2, re-designed after the weight reduction.

JLV1 J Level 1 Trigger card.

JT-Crate Trigger & DAQ crate.

JTAG Joint Test Action Group of the IEEE. Defining test interfaces for integrated circuits, for example a boundary scan interface for digital ICs in the IEEE 1149.1 standard, also called JTAG interface.

L

LEPSI Laboratoire d'Electronique et de Physique des Systemes Instrumentaux, Strasbourg, France.

LHC Large Hadron Collider, a storage ring for protons and ions being built at CERN in the old LEP tunnel.

LVDS Low Voltage Differential Signal.

LVTTL Low Voltage Transistor to Transitor Logic.

M

MACHO MAssive Compact Halo Object.

MAPS Monolithic Active Pixel Sensors.

MIMOSA Minimum Ionising particle MOS Active pixel sensor.

MIP Minimum Ionising Particle.

MLI Multi Layer Insulation.

MOSFET Metal-Oxide-Semiconductor Field Effect Transistor.

MSSM Minimal SuperSymmetric Model.

mSUGRA MSSM with supergravity inspired symmetry breaking.

MWPC Multi-Wire Proportional Chamber.

N

NASA National Aeronautics and Space Administration, USA.

NSPO National Space Programme Office, Taiwan.

P

PCB Printed Circuit Board.

PMT Photo Multiplier Tube.

Q

QM Qualification Module.

R

RICH Ring Image CHerenkov detector.

RMS Root Mean Square.

S

S9011AU Control electronics board for the DC/DC converters. Located in the UPD.

S9011B 28V input filter of the UPD.

S9043 see UDR.

S9048 DC/DC converter, $\pm 2.6V$.

S9053U DC/DC converter, $3.7V$.

S9056 DC/DC converter, $5V$ & $120V$.

S9058 See UBP.

S9070 see UPSFE.

SDR Scintillation Data Reduction card (TOF).

SIMOX Separation by IMplanted OXygen.

SLIM Secondary emission for Low Interception Monitoring.

SNR Signal to Noise Ratio.

SOI Silicon-On-Insulator.

SSF Solid State Fuse.

STS Space Transport System, aka Space Shuttle.

SUCCESSOR SUCIMA ChargE SenSOR.

SUCIMA Silicon Ultra fast Cameras for electron and gamma sources In Medical Applications.

T

TOF Time Of Flight.

TRD Transition Radiation Detector.

TVT Thermo Vacuum Test.

U

U Übergangsstrahlungsdetektor (= transistion radiation detector), used as short form in the naming convention of the AMS electronics, as “T” is already used by the Tracker.

U-Crate TRD electronics crate.

UBP U BackPlane.

UBPv2 U Backplane, version 2, re-designed after the weight reduction.

UDR U Data Reduction card.

UFE U Front-End.

UG-Crate U Gas electronics crate.

UHVD U High Voltage Distributor.

UHVG U High Voltage Generator.

UPD U Power Distribution box.

UPSFE U Power Supply for Front-End card.

UPSFEv2 U Power Supply for Front-End, version 2, re-designed after the weight reduction.

USB Universal Serial Bus.

USCM Universal Slow Control Module.

USS Unique Support Structure.

UTE U Tube End.

V

VI Virtual Instrument, name of a programme in LabView.

VME Versa Module Europa.

W

WAMP Wilkinson Microwave Anisotropy Probe.

WIMP Weakly Interacting Massive Particle.

X

xDR x Data Reduction card, where x stands for all possible subdetectors.

Index